PLEASE TYPE

UNIVERSITY OF NEW SOUTH WALES

Thesis/Project Report Sheet

Surname or Family name: BOURKE

First name: TYLER Other name/s: J. LEONARD

Abbreviation for degree as given in the University calendar: PhD

School: PHYSICS (ADFA) Faculty: N/A

Title: SELECTED STUDIES OF SOUTHERN MOLECULAR CLOUDS

Abstract 350 words maximum: (PLEASE TYPE)

This thesis presents the results of distinct but related studies of selected Southern Molecular Clouds.

In the first part of the thesis we present the first results of a program to measure the line-of-sight magnetic field strength in southern molecular clouds with the Parkes radiotelescope, through the Zeeman effect in OH. For 18 clouds observed we detected the Zeeman effect in one cloud associated with RCW38, with a field strength of 38 ± 3 μG, and possibly in a cloud associated with RCW57, with a strength of -203 ± 25 μG. A comparison with field strengths estimated from a simple spherical cloud model indicates that our results are consistent with large scale cloud support against gravitational collapse being due to the magnetic field. The results are also consistent with the observed line-widths being due to hydromagnetic wave motions.

In the second part of the thesis we present the results of a detailed study of the proto-stellar molecular outflow originating in the Bok globule BHR71. This outflow is driven by a very young low mass proto-stellar object, and lies almost in the plane of the sky, with bipolar outflow lobes extended up to 0.3 pc from the protostar. The abundances of a number of molecular species are enhanced within the outflow, compared to the values determined within the globule. The species carbon sulphide, silicon monoxide and methanol all show abundance enhancements, of up to 400 in the case of silicon monoxide. These large enhancements are most likely due to the release from dust grains of ice mantles and silicon bearing species, via shocks produced by the interaction of the outflow and the stationary gas of the globule in the presence of a magnetic field. However, we find that the abundance of the formyl ion is decreased by a factor of 20 in the outflow. All these results are in agreement with predictions from the most advanced C-shock models available.

Finally, in the main appendix we report on a mid-infrared study of the southern HII region RCW38. Our observations are consistent with the region containing IRS1 being due to a ridge or shell of material surrounding a cavity of about 0.1 pc radius centred on the exciting hot massive young star(s) IRS2. The derived dust temperature in the IRS1 ridge is remarkably uniform, a result which is best explained as due to heating by resonantly trapped Lyman alpha photons, rather than by direct stellar heating. We deduce the effective temperature of IRS2 to be about 45,000 K, consistent with an O5 ZAMS star.

Declaration relating to disposition of project report/thesis

I am fully aware of the policy of the University relating to the retention and use of higher degree project reports and theses, namely that the University retains the copies submitted for examination and is free to allow them to be consulted or borrowed. Subject to the provisions of the Copyright Act 1968, the University may issue a project report or thesis in whole or in part, in photostate or microfilm or other copying medium.

I also authorise the publication by University Microfilms of a 350 word abstract in Dissertation Abstracts International (applicable to doctorates only).

Signature Witness 19/4/99 Date

The University recognises that there may be exceptional circumstances requiring restrictions on copying or conditions on use. Requests for restriction for a period of up to 2 years must be made in writing to the Registrar. Requests for a longer period of restriction may be considered in exceptional circumstances if accompanied by a letter of support from the Supervisor or Head of School. Such requests must be submitted with the thesis/project report.

FOR OFFICE USE ONLY Date of completion of requirements for Award:

Registrar and Deputy Principal

THIS SHEET IS TO BE GLUED TO THE INSIDE FRONT COVER OF THE THESIS

Selected Studies of Southern Molecular Clouds

by
Tyler Leonard Bourke
BSc. (Hons), Australian National University
MSc., Univ. New South Wales

Thesis submitted in accordance with the regulations for the
Degree of Doctor of Philosophy

School of Physics
University College
The University of New South Wales

April 1998

I hereby declare that this submission is my own work and to the best of my knowledge it contains no material previously published or written by another person, nor material which to a substantial extent has been accepted for the award of any other degree or diploma at UNSW or any other educational institution, except where due acknowledgment is made in the thesis. Any contribution made to the research by colleagues, with whom I have worked at UNSW or elsewhere, during my candidature, is fully acknowledged.

I also declare that the intellectual content of this thesis is the product of my own work, except to the extent that assistance from others in the project's design and conception or in style, presentation and linguistic expression is acknowledged.

Tyler Bourke

To my parents, and to Lyman.

The alchemists detect in the sexual activity of man a correspondence with the world's creation, with the growth of plants, and with mineral formation. When they see the union of rain and earth, they see it in an erotic sense, as copulation. And this extends to all natural realms of matter. For they can picture love affairs of chemicals and stars, a romance of stones, or the fertility of fire.

Jim Morrison

"Snow Emergency" is a form of martial law. Boston drivers have no rights and may be treated very arbitrarily and without appeal. The behaviour of the authorities is erratic in snow emergency situations. Most of the time, they will plow around you if you leave your car parked on a snow emergency street, leaving you with a big shoveling job to get your car but not any other inconvenience. Occasionally the plows will deliberately bury your car with all the excess snow on the street. You will have to shovel the equivalent of a driveway full of snow to free your car. In this case you will have so much snow to shovel you may as well wait until spring.

The Boston Driver's Handbook

"Acknowledgments"

To acknowledge is to rave on about all the people who have had some 'good' influence on you during your time as a student, including the guy you bought you that last drink at Toad when you had no money left and Brooke wanted you out! Well, if you have ever looked through the numerous PhD theses out there you could be forgiven for believing that this is the main definition.

I spent the best part of the last 4 years at the Harvard-Smithsonian Center for Astrophysics (CfA – no, not the Country Fire Authority), while also a student at UNSW (ADFA Campus, and no, ADFA is not Australian Dairy Farmers Association, though I sometimes wonder...). Good deal, eh? I had a great time in Boston both professionally and socially, and my far flung advisors, Phil Myers, Garry Robinson, and Harry Hyland, are to be thanked for getting me there. In particular Phil looked after my interests in Boston, and Garry kept things smooth in Canberra. This thesis would not have been possible without them. Thanks all, I hope I was worth the trouble.

When a student money is always a concern, but thanks to financial support through a Smithsonian Predoctoral Fellowship and a top up from Phil when that ran out, money was something I didn't have to worry too much about.

Well the CfA was great, 'nuff said. If there was somewhere to buy meat pies and a pub nearby then perfection was within reach, in spite of the snow. To stay there I not only needed to convince Phil of my worth but also my in-house committee of Alyssa Goodman and Mark Reid. Somehow I managed that. A place to "work" is only as good as the people there. At the risk of leaving people out due to oversight, those who readily come to mind are João (Benny from ABBA?), Paola (a better friend is hard to imagine), David W., Merce, Ted, Jonathan (always nice to have a pom around for some verbal jousting), Hua, Mark G. (Cable Guy), Mario, Diego, Hector, Jose (part of the Espanol crowd), Kenny, Eric, and of course the Barflies (see you at Grendels). If I've left you out sorry, let me buy you a beer. The admin were superb 'cause the job always got done with minimum fuss, so hats off to Tom, Dave, Judy, Jean, Nancy, Greg

(Mr insomniac), and Jamie over the summers.

No, I didn't spend all my time at the CfA. I was very fortunate to stay with great friends Linda & Brian during my whole time in Cambridge MA. Sorry Linda, that none of the setups worked! They introduced me to other great people, in particular Pattie & Brad, and Ali & Adi. Plenty of others kept me distracted from astronomy. I won't try to mention everyone...oh, ok, I will. A few seemed to corrupt me more than others, particularly the Toad crowd highlighted by Mark (yes, you GP!), Vonnie, PJ, Mel, Mary, Di, "the Swedes", Jan-Eric & Stein, and Jacque La-la. Then there was the unique international crew, including Ina, Claire, Trish, Ian, Jan, Jeanne, Christine, Charlie, João, Meli, Lisie, Danni, Carlos, Antonio, Barbara, Sean & May, Leslie, and a host of others. Bet I've missed someone there. A special mention to Betty for fine Italian distractions. I couldn't survive without my volleyball, particularly those Sundays in the park over summer (and Grendels afterwards). It was always great to play with Lloyd, Nat, Pat, Jurek, Mark, Karl, Kevin, Linda, Beth, Greg, Hanna, and last (but certainly not least) Heather, amongst others. The score never really mattered.

Wider afield, a motivating factor in my move to Bean Town was Michelle in NYC. Thanks for sharing the dream.

Any Aussie living OS is a good hotel for travelling Aussies, and I was no exception. "Mates" to visit included Sam & Raylee, Jeppo, Phil, Stacy, and Jodie & Greg. The same is true for ISU friends. I'll mention only the DC team of Greg & Kathy and ankle-biters, and Patricia from Houston. Always great to see them. Of course Aussies tend to congregate wherever they go and I helped to prop up a few bars with fellow local Aussies and wannabes. Yes, I'm talking about sometimes-Glen (MÀTE, Mate, mate), Ang, Vince, Peter B. (Barnsie!), Annie, Robbo, Shaun, Coral (yahoo!) and the house that Adam destroyed.

Ok, we're almost done. I can't forget Sonia, nor Divya, for extra spark and words of wisdom (and gossip) from afar. My other 'international connections' always amazed Phil and resulted in some fruitful collaborations in places like Chile (Guido), Germany (Ralf), Finland (Kimmo), Italy (Paola), Germany/Holland

(Chris, mate!), and back home in Oz (many). The willingness of others to share data always amazed me. A pretty good bunch, those astronomers! The support staff at the different observatories I visited were also great, in particular Harry and Euan at Parkes during the difficult times.

Of course, thanks to my parents for just being themselves and always being there. Their support is unquestioned.

My main source of sanity and inspiration near the end of my time in Boston came from a very special woman by the name of Regula. She is anything but her namesake!

Well, that wasn't too bad was it. I'm sure I forgot some people. Sorry. Ok, you've got this far, time to settle into a quiet corner of a pub somewhere with a pint (don't forget to tip in the USA!) and read on. Maybe you'll learn something. Probably not! Cheers.

Abstract

In the first part of this thesis (Chapter 2), we present the first results of an extended program to measure the line-of-sight magnetic field strength toward southern molecular clouds with the ATNF Parkes radiotelescope, using the Zeeman effect, primarily through observations of OH absorption lines against background continuum sources (H II regions). From 18 Gaussian components observed toward 9 sources, we definitely detected the Zeeman effect in the molecular gas associated with the H II region RCW 38, with a field strength of 38 $\pm$ 3 μG, and possibly in the molecular gas associated with the H II region RCW 57, with a field strength of -203 ± 25 μG. The molecular clouds were also observed in the ^{13}CO $J = 1 \rightarrow 0$ transition to determine their the physical properties (e.g., clouds size and mean column density). Comparison of the observed magnetic field strengths and sensitive upper limits with those estimated from a simple spherical model of a molecular cloud without surface terms indicates that the results are consistent with large scale cloud support being due to either the mean magnetic field or turbulent motions associated with magnetohydrodynamic waves. Our results cannot rule out either scenario. However, in about half of the clouds studied the kinetic energy density alone is insufficient to provide large scale cloud support to the clouds, and an additional means of support is required. A comparison of the magnetic field strengths (including upper limits) and line widths show that the results are consistent with the supersonic line widths being due to hydromagnetic wave motions, resulting from perturbations of the mean magnetic field.

In the second part of this thesis (Chapters 3 & 4) we present the results of a study of the highly collimated outflow from the Bok globule BHR 71, which shows abundance enhancements of SiO and CH_3OH within the outflow. These results are best explained as being due to destruction of grain mantles in C-shocks.

In Chapter 3, we report on observations of the southern Bok globule BHR 71 in the $J = 1 \rightarrow 0$ and $J = 2 \rightarrow 1$ lines of ^{12}CO, the $J = 1 \rightarrow 0$ lines of ^{13}CO

and $C^{18}O$, and $(J,K) = (1,1)$ and $(2,2)$ inversion lines of NH_3 made with angular resolution of $\sim 20''$ to $\sim 9'$. We also report 1.3 mm continuum observations made with SEST with $\sim 20''$ resolution. The low angular resolution molecular observations indicate that the globule has a diameter of ~ 0.5 pc, a kinetic temperature of 11 K, a total mass of $\sim 40\ M_\odot$, and an average molecular density of $\sim 9 \times 10^3$ cm^{-3}. The high angular resolution observations reveal the presence, near the center of the globule, of a highly collimated bipolar outflow with lobes extending by ~ 0.3 pc in opposite directions from a strong 1.3 millimeter continuum source. The morphology and velocity structure of the flow is well described by a biconical outflow that is inclined from the line of sight at an angle of $\sim 84°$, has a semi-opening angle of 15°, and in which the gas moves outwards with an approximate constant radial velocity (with respect to the cone apex) of ~ 28 km s^{-1}. The outflow appears to be driven by a very young stellar object with $L_{bol} \sim 9\ L_\odot$, whose characteristics at infrared and millimeter wavelengths are similar to those of the so-called Class 0 sources.

In Chapter 4 we report on observations of the $J = 3 \rightarrow 2$ and $J = 2 \rightarrow 1$ transitions of SiO and CS, the $J_k = 3_k \rightarrow 2_k$ and $J_k = 2_k \rightarrow 1_k$ transitions of CH_3OH, and the $J = 1 \rightarrow 0$ transition of HCO^+, made with SEST, toward the highly collimated bipolar outflow BHR 71. Broad wing emission was detected toward the outflow lobes in all the observed molecular lines. The shape of the profiles are strikingly different from molecule to molecule. For CS and HCO^+ the emission from the outflowing gas appears as a weak broad feature superposed upon a strong narrow emission from the quiescent ambient gas. For CH_3OH the intensity of the broad emission feature is considerably stronger than that of the narrow component, while for SiO the broad feature completely dominates the emission spectra.

The spatial distribution of the integrated wing emission is considerably extended, and broadly similar in all the observed molecular transitions, showing well separated blue and red shifted lobes with FWHM angular sizes of $2\farcm4 \times 1\farcm3$ and $2\farcm4 \times 1\farcm4$, respectively. We find that the abundance of methanol and silicon monoxide in the outflow lobes is enhanced with respect to that of the ambient

cloud by factors of up to $\sim$ 40 and 350, respectively. The large enhancements of methanol and silicon monoxide in the outflow lobes are most likely due to the release from grains of ice mantles and Si-bearing species via C-shocks produced by the interaction between the outflow and dense ambient gas in the presence of a magnetic field. On the other hand, we find that the abundance of HCO^+ in the outflowing gas is smaller than that in the ambient gas by roughly a factor of 20, a decrease consistent with theoretical predictions of C-shock models.

Finally, in the main appendix, we report on an initial study of the RCW 38 H II region via mid-infrared imaging and spectroscopy. We determine the dust colour temperature from both our spectrum and images at 10 and 20 μm, and deduce the gas excitation from an image in the S IV fine structure line, as well as spectra of the Ar III, S IV and Ne II fine structure lines. Our observations are consistent with a complex of sources associated with the RCW 38 IRS1 region which represent knots of material in a shell, or ridge, surrounding a cavity of about 0.1 pc in radius, which is itself created by the stellar wind of the hot young source IRS2. The dust temperature does not peak closest to IRS2, but rather along the centre of the ridge, and is remarkably uniform over the extent of our image. From photoionisation models for the observed line ratios at IRS1 we deduce a stellar effective temperature and gas density of about 43 000–48 000 K and 10^4 cm^{-3} respectively. Whilst the star, or star cluster, IRS2 is ultimately responsible for the observed thermal and ionic emission, the relatively uniform dust temperature implies that the bulk of the dust heating in the region is provided by resonantly trapped Lyman α photons, rather than direct stellar photons. This then also implies that the dust is depleted with respect to the gas by a factor of at least 100 from its normal interstellar value. The small scale spatial variations in the continuum emission and temperature can be explained by changes in the density and/or gas–to–dust mass ratio. However, positional offsets between the peaks of S IV and dust emission may imply that the sulfur abundance is locally enhanced, possibly due to grain destruction via shocks.

Contents

Chapter 1

Introduction

Though magnetic fields are believed to be important in all aspects of star formation, from large scale support of molecular clouds, through the regulation of the star formation rate, to the driving of bipolar molecular outflows and jets from protostars, and the interactions of these outflows with the parent molecular clouds through shocks, they are extremely difficult to observe directly, and their strength is almost impossible to measure.

1.1. Importance of Magnetic Fields in Molecular Cloud Physics

In their review of radio radiation from interstellar molecules, Zuckerman & Palmer (1974) noted that the expected star formation rate from the free-fall collapse of molecular clouds should be $> 30 M_{\odot}$ yr^{-1}, compared to the observed rate of only $\sim 4 M_{\odot}$ yr^{-1}. Clearly, molecular clouds are not collapsing to form stars on free-fall times; some mechanism of support against gravity must be present. Myers et al. (1986) estimated the star formation efficiency in the first Galactic quadrant at $\sim 2\%$ by comparison of far-infrared (FIR) emission, CO $J = 1 \rightarrow 0$ emission and 6 cm continuum emission, which supports the view that molecular clouds are not in free-fall. Three processes are proposed to provide

the support to molecular clouds against gravitational free-fall collapse; rotation, hydrodynamic turbulence, and magnetic fields (see review by Shu, Adams & Lizano 1987; hereafter SAL). The gas temperatures of molecular clouds, typically 10 – 30 K, are too low to provide support via thermal pressure for all but the lowest mass molecular cloud cores (Myers 1995 and references therein).

Rotation rates for molecular cloud envelopes and cores are typically ≈ 1 $\mathrm{km\,s^{-1}\ pc^{-1}}$ (Goldsmith & Aquilla 1985; Goodman et al. 1993; SAL). There appears to be little correlation between the rotation direction and either the major or minor axes of the clouds or the plane of the Galaxy, suggesting that rotation is dynamically unimportant. A comparison of cloud kinetic energy (assuming solid body rotation) with the gravitational energy indicates that the ratio of kinetic to gravitational energy is < 0.1 in almost all cases. Rotation cannot be important for cloud support.

The observed line widths from molecular clouds are highly supersonic (SAL). For a molecular cloud at a temperature of 10 – 30 K the thermal line width of the CO $J = 1 \rightarrow 0$ is only 0.1 – 0.2 $\mathrm{km\,s^{-1}}$, compared to values typically observed of > 1.0 $\mathrm{km\,s^{-1}}$. This result is suggestive of some type of supersonic turbulent motion within the clouds. However, supersonic hydrodynamic motions are highly dissipative (due to the creation of shocks) and will dampen quickly, on a timescale much less than that inferred for the lifetime of individual molecular clouds, and so some mechanism for replenishment of these fluctuations is required for hydrodynamic turbulence to be a viable explanation. No such mechanism has been identified to date.

In contrast, magnetic fields can provide support to molecular clouds in two ways (see e.g., the review by Crutcher 1994). Pressure from large scale static magnetic fields can provide cloud support perpendicular to the field, provided the ions within the cloud are well coupled to the neutrals. Long wavelength magnetohydrodynamic (MHD) waves, which can persist for a significant fraction of the cloud lifetime, can provide support both parallel and perpendicular to the field direction, provided they are smaller than the cloud and travel at sub-Alfvènic (but supersonic) speeds, so that shocks are not formed.

Theoretical models for magnetic fields within molecular clouds have identified the magnetic flux-to-mass ratio, Φ_B/M, as the crucial parameter in determining whether magnetic fields are important in cloud dynamics (e.g., Mouschovias & Spitzer 1976; McKee et al. 1993). If this ratio is below a certain value (inferred via virial considerations or detailed numerical modelling), the critical value, then the cloud is said to be in a magnetically supercritical state and the magnetic field cannot support the cloud against dynamical collapse. Clouds with values of Φ_B/M above this critical value are magnetically subcritical and the field can provide support against dynamical collapse, but the cloud may still contract quasi-statically via ambipolar diffusion until such time when Φ_B/M approaches the critical value, after which dynamical collapse takes place. This occurs because the density, and hence the mass, will increase faster than the magnetic field strength during ambipolar diffusion. The magnetic flux-to-mass ratio can be transformed into the observable quantity B/N_H for a range of models (e.g., Crutcher et al. 1993) which may then be compared to the observed values of magnetic field strength B and column density N_H for molecular clouds (see Chapter 2).

Arons & Max (1975) first suggested that the observed supersonic line widths in molecular clouds could be due to long lived MHD waves. For a molecular cloud in approximate equilibrium between its kinetic, magnetic and gravitational energy densities, it can be shown that the line widths $\Delta v_{\rm virial}$ for simple cloud models are similar to those observed toward molecular clouds over a very large range of sizes, and that the line width follows the observed 'scaling law' of $\Delta v_{\rm obs} \propto R^{0.5}$, where R is the cloud size (e.g., Myers & Goodman 1988a). These simple models also imply that the line widths should be approximately equal to the Alfvén speed, $v_{\rm A} \equiv B/4\pi\rho$, where ρ is the density, so that $\Delta v_{\rm obs} \sim \Delta v_{\rm virial} \sim v_{\rm A}$. Myers & Goodman (1988a) show that for a large sample of molecular clouds ($\sim$ 120) this relationship holds if $B \sim 5 - 100$ μG, which is consistent with available magnetic field strength measurements (Crutcher 1994; but the current available field strengths only sample a limited range of density).

Whether the mean magnetic field or fluctuations of the mean field is the

dominant mechanism for molecular cloud support is unknown (assuming the support is magnetic in origin). If the mean field is the dominant form, then we would expect to see highly flattened molecular clouds over many size scales with their short axis parallel to the field. On large scales (a few parsecs or more) molecular clouds are observed to be filamentary and highly elongated, but no correlation between the direction of the large scale magnetic field and the cloud axes is found, though large-scale uniform fields are observed (Heiles et al. 1993). On small scales, i.e. $\sim$ 0.1 pc, molecular cloud cores with aspect ratios of around 2:1 are common (Myers et al. 1991). Highly flattened structures are found only at the smallest size scales within molecular clouds (a few thousand AU or less), when elongated disk-like structures are observed (Ohashi et al. 1997). If magnetic fields are important they probably provide support through both the mean field and the MHD fluctuations (e.g., Brogan et al. 1998).

1.2. Observational Studies of Magnetic Fields

A comprehensive review of observations of magnetic fields in molecular clouds is given by Heiles et al. (1993; see also Crutcher 1994). In simple terms, linear polarization studies of thermal radiation due to aligned dust grains (predominantly at far-infrared and millimetre wavelengths) reveal the direction of the magnetic field on the plane of the sky (Goodman 1996), but nothing about its strength. Studies of the Zeeman effect through observations of the circular polarization of spectral lines, mainly at radio wavelengths, allow the determination of the line-of-sight magnetic field strength, and whether the line-of-sight component of the magnetic field, averaged over the beam, is directed toward or away from the observer. No information about the orientation of the magnetic field with respect to the plane of the sky is available via the Zeeman effect. In theory it is possible to determine the full three dimensional stucture of the field by a combination of linear polarization observations and Zeeman observations with a suitable model (Myers & Goodman 1991), but in practice it is extremely difficult to accumulate the required observations and has been undertaken for only one

cloud.

Other methods for investigatng magnetic fields, such as Faraday rotation and polarization of spectral lines due to radiative transfer effects, are generally not practical for the study of fields within molecular clouds, due to the effects being almost undetectably small leading to ambiguous results. For example, long path lengths are generally required for detection of Faraday rotation, and an independent determination of the electron density along the path is needed to infer the magnetic field strength. The electron density is extremely difficult to measure in any molecular cloud; it requires the determination of the ionization fraction via indirect observational methods (observations of molecular ions) together with detailed chemical modelling (e.g., Caselli et al. 1998; Williams et al. 1998; Bergin et al. 1998b).

We concentrate here on observational studies of the Zeeman effect on spectral lines, mainly the OH lines near 1.6 GHz. The Zeeman effect is described in detail in Chapter 2. Though it is almost 30 years since the detection of the Zeeman effect in OH toward Orion B (Verschuur & Turner 1970) and 15 years since the confirmation of this result (Crutcher & Kazès 1983), there are still only 11 different molecular clouds, excluding masers (where the physical conditions are difficult to determine) in which the Zeeman effect has been detected (Crutcher & Kazés 1983; Kazés & Crutcher 1986; Heiles & Stevens 1986; Troland, Crutcher & Kazés 1986; Crutcher, Kazés & Troland 1987; Kazés et al. 1988; Crutcher et al. 1993; see also reviews by Troland 1990 and Crutcher 1994). There are many more upper limits, both published and unpublished (T. Troland, private communication).

Observations of the Zeeman effect in OH with single dish radiotelescopes has been the primary method used for measuring magnetic field strengths in molecular clouds over the past 15 years. These observations mainly sample the envelope regions of molecular cloud cores, with densities $\sim 10^3$ cm^{-3} (Heiles et al. 1993; Crutcher 1994), and the results are generally consistent with the clouds being approximately magnetically critical and the observed line widths being due to MHD wave motions (Crutcher et al. 1993; Crutcher 1994), though

more detections are clearly required. As an example, the magnetic field strength in the low mass molecular cloud B1 has been measured at two different spatial scales (Goodman et al. 1989; Crutcher et al. 1993) and detailed modelling has been undertaken (Crutcher et al. 1994). Initial input parameters to the model are the observed cloud mass (600 $M_{\odot}$) and the magnetic field strength on the large scale (16 μG), which can be well represented by a model cloud in exact magnetohydrostatic equilibrium. The comparison of the evolution of the model with observations of the column density and density profile at different spatial scales shows an excellent agreement between theory and observations, providing good evidence for the importance of magnetic fields in molecular cloud physics.

Interferometric observations of the Zeeman effect in both OH and H I with the VLA show considerable structure in the magnetic field (e.g., Roberts et al. 1993, 1995). With additional information provided by studies of the far-infrared polarized emission from dust grains, the three dimensional structure of the magnetic field may be inferred (Roberts et al. 1996). In the case of W3 (Roberts et al. 1993) an hourglass morphology is inferred for the three dimensional structure of the field, with the pinch occurring at the location of the protostar W3-IRS5, which is suggestive of an evolved self-gravitating cloud threaded by an initially uniform magnetic field. At the waist the magnetic flux-to-mass ratio suggests the core is approximately magnetically critical.

Gradually the number of high resolution studies is increasing, but there are still a number of single dish observations to be made, both in the northern and southern skies, with OH and other molecules, to increase the detection statistics and provide very sensitive upper limits in non-detection cases. The high demand for time on the interferometric telescopes limits the number of sources which can be studied with these instruments. In addition, follow-up observations with a suitable molecular tracer are required to determine the properties of the molecular gas in which the Zeeman effect has been measured. Crutcher et al. (1996) have begun a very difficult program to investigate magnetic field strengths in molecular cloud *cores* with densities 10^5 – 10^6 cm^{-3} via the Zeeman effect in CN at 113 GHz (Heiles et al. 1993). The results from their study will be very

important in determining whether the expected (on theoretical grounds) $B - n$ scaling relationship holds, and to fully confront the many theoretical studies in more than an approximate manner.

1.3. Outflows in Molecular Clouds

Bipolar outflows from young stars and protostars are a ubiquitous phenomenon. Their observational manifestataions are observable over a wide range in wavelength, and consist of molecular, atomic and ionized components. Important reviews are given by Lada (1985) and Bachiller (1996), and our current understanding is well described in the proceedings from IAU Symposium 182 "Herbig-Haro Flows and the Birth of Low Mass Stars" (1997). These outflows can be quite energetic and are capable of sweeping up the ambient gas surrounding the protostar, which is clearly shown by observations of e.g., the ^{12}CO $J = 1 \rightarrow 0$ and $J = 2 \rightarrow 1$ transitions at 115 & 230 GHz. The outflow velocities are supersonic and shocks result, which in some cases are observed to have a remarkable effect on the chemistry of the ambient gas (Bachiller 1996).

Even the youngest protostars, the "Class 0" sources (André, Ward-Thompson, & Barsony 1993), have outflows, indicating that this phenomenon must arise relatively early in the evolution of a protostar. In fact some of the most spectacular features of outflows are only seen toward the Class 0 sources, possibly because of their youth. Such features include a high collimation (perhaps because the outflow has not had time to sweep up a significant fraction of the ambient gas), extremely fast molecular bullet-like features (Bachiller et al. 1991), which may later evolve into the optically visible Herbig-Haro objects, and abundance enhancements of a number of molecular species, such as SiO and CH_3OH, probably due to shocks destroying grain mantles and the sputtering of grain cores in the (previously unshocked) ambient medium, and the resulting high temperature chemistry.

At present models of bipolar outflows are just beginning to confront the

detailed observations which have recently become available for a number of outflows (e.g., Lada & Fich 1996; Padman et al. 1997; Eislöffel 1997). The important questions that remain to be answered are: how are outflows formed and how are they driven; how do they evolve; and what role do they play in the observed supersonic line-widths within molecular clouds and the dispersal of the gas infalling onto the protostar?

The outflows from the Class 0 protostars are possibly the best laboratory for their study, since their early time evolution allows for the study of the interaction of the underlying jet or disk-driven wind with the ambient medium from which the molecular outflow is formed (through some as yet unknown entrainment mechanism). They also allow the investigation of the chemical changes that occur when the shocks in the outflow interact with the ambient gas, at a time when previous outflow events have not disturbed the surrounding gas.

1.3.1. Shocks in Outflows

Due to the observed high Mach numbers in outflows, shocks naturally form when the outflow ploughs into the surrounding ambient medium. Two types of shocks are possible, J- and C-shocks (Draine & McKee 1993; Hollenbach 1997). Molecular clouds, due to their low ionization ($x_e \sim 10^{-7}$; Caselli et al. 1998; Williams et al. 1998; Bergin et al. 1998b) but dynamically important magnetic fields, can be thought of as a two-fluid medium (neutrals and ions/electrons), with significant coupling between the two fluids. In J-shocks, the transition region from the bulk flow upstream (in the shock reference frame) of the shock to the post-shock region of random thermal motions is spatially very small, of the order of the mean free path of the neutrals, hence the term J- or Jump shock. In a C-shock the size of the transition zone is of the same order as the cooling zone, and they are essentially co-spatial. This is because the ions and neutrals in the presence of a magnetic field are differentially accelerated, since the sound speed and Alfvén speed differ significantly in molecular clouds. The ions downstream from the shock thus have an advance warning of its arrival, and

through ion-neutral collisions can transmit this information to the neutrals. In effect the neutral gas is continuously heated and compressed before the arrival of the shock, and the transition from the pre- to post-shock conditions occurs in a continuous manner. A combination of the continuous transformation of the flow variables and ion-neutral slip provides a mechanism to convert the kinetic energy of the shock into heat at a rate slow enough to keep the temperature low through radiative cooling. Hence the emission from C-shocks appears mainly in the form of molecular spectral lines such as the vibrational lines of H_2 near 2 μm, since the gas is not dissociated (Hollenbach 1997, and references therein). J- and C-shocks obey the overall jump (Rankine-Hugoniot) conditions despite their different scale lengths.

Observable manifestations of shocks within outflows include Herbig-Haro objects (seen at optical and near-infrared wavelengths as small nebulous knots of emission), molecular "bullets" seen in e.g., CO and SiO emission at millimetre wavelengths, and large bow shaped structures seen in the optical (Hα and [S II] emission), near-infrared (vibrational lines of H_2), and millimetre wavelegths (CO, SiO, and NH_3). These observations have been modelled with varying degrees of success as being due to J-shocks (e.g., Gredel 1994), C-shocks (e.g., Davis & Smith 1995), or some combination of the two (e.g., Noriega-Crespo & Garnavich 1994). In almost all cases some form of C-shock is required to explain at least part of the observations, e.g., the widespread H_2 emission in the near-infrared. One simple picture involving both types of shock is that of a supersonic jet (neutral and ionized) propagating from the protostar into the molecular cloud and creating a wide bow shock, with J-shocks near its head and C-shocks further back on the bow, where the flow becomes more oblique, resulting in the intense H_2 emission (e.g., Hollenbach 1997). Such a simple picture is able to explain many of the morphological aspects of molecular outflows before any detailed modelling is undertaken.

Modelling of protostellar outflows is difficult, and various approaches have been taken. One approach is to model the underlying jet, which is often observable directly in [S II], or indirectly in H_2, without attempting to include in the

model the lower velocity molecular outflow which has been swept up by the jet through some entrainment mechanism (see the contributions in IAU Symposium 182, e.g., Cabrit, Raga & Gueth, p163). Another approach is to concentrate mainly on the outflow properties, with little regard to the origin of the driving source, instead studying such aspects as the entrainment mechanisms and how they compare with observations (e.g., Chernin & Masson 1995; Stahler 1994). More recently the theoretical studies of Smith et al. (1997 and references therein) have produced promising results which reproduce the morphology and energetics of the underlying jet-like phenomenon (as observed in H_2 emission in the near-infrared) and the morphology and dynamics of the swept up molecular outflow (as seen in the rotational transitions of CO).

1.3.2. Chemistry

To date, none of the detailed dynamical models for jets or outflows have included any significant chemical effects. Yet with the high temperatures and pressures associated with shocks it is expected that high temperature chemistry will significantly change the nature of the molecular gas and the dust in the ambient medium (e.g., Bergin et al. 1998a). Preliminary simple modelling of specific species has been performed (e.g., silicon – Schilke et al. 1997; Caselli et al. 1997; sulphur – Pineau des Forêts et al. 1993), but such aspects as oblique shocks (i.e., as expected in a bow shock), oblique magnetic fields, or the spatial distribution of the chemical species are yet to be investigated. This is one area of outflow study where observations are lacking. For only one molecular outflow (the outflow from the Class 0 protostar in the L1157 molecular cloud) are observations available against which coupled time-dependent chemical and dynamical models can be tested. There exists for L1157 molecular line maps in a number of species that have been affected by shocks in the outflow, and complementary maps of species which remain unperturbed (Bachiller & Pérez Gutiérrez 1997). An observational sample of one is insufficient to motivate detailed theoretical models (as a general rule!). Observations are needed of rotational transitions for a number of molecules toward the Class 0 outflows, where the most interesting chemistry

is observed, as well as maps of some of the chemically interesting species, such as SiO. However, merging a complicated two dimensional outflow model with a complicated chemical model is no easy task.

The "shock chemistry" which results from the passage of a protostellar jet or wind through the surrounding ambient medium manifests itself through strong emission in the rotational transitions of molecular species such as SiO and CH_3OH (Bachiller 1996). Due to evaporation of ice mantles, destruction of grain cores, and high temperatures driving endothermic reactions, a number of species normally frozen out onto dust grains (CH_3OH), tied up in grain cores (Si), or prevented from forming in the gaseous phase due to high activation barriers (H_2O) become important in the study of shocks. As some of the processes and reactions are fast, and the post shock cooling times short, the chemistry can be strongly time dependent (e.g., Bergin et al. 1998a). The study of the different chemical species (molecular and ionic) can potentially be used to probe the state of evolution of the outflow and the driving source. Moreover, the interaction of J-shocks with the ambient medium will have an observably different effect on the resulting shock chemistry than C-shocks, and the study of the post shock chemistry can be used to probe the nature of the shocks.

1.4. Outline of the thesis

This thesis is divided into three main chapters, with two appendices. The chapters describe the investigation of magnetic fields in molecular clouds in two very different ways.

In Chapter 2 we attempt to study magnetic fields directly by measuring their strength via the Zeeman effect. No serious attempt has previously been made to detect the Zeeman effect in the 18 cm ground state transitions of OH with radio telescopes in the southern hemisphere. In the northern hemisphere the telescopes at Green Bank (NRAO), Hat Creek, and Nançay have been used extensively to observe those sources with the best chance of success in detecting

the Zeeman effect. Followup studies have been successfully performed with the VLA. The clear need for more *detections* of the Zeeman effect and the great potential for doing so with the Parkes radio telescope has resulted in the study presented in Chapter 2, where we report the results of our observations of nine southern molecular clouds for the Zeeman effect. We clearly detect the Zeeman effect toward the bright H II region RCW 38, and possibly toward another bright H II region RCW 57. These represent the *first detections of the Zeeman effect in molecular clouds with the Parkes radio telescope*, and the *first detection of the Zeeman effect in southern molecular clouds* not visible to northern telescopes. Our results are consistent with previous findings, namely that magnetic fields do appear to be important in regulating star formation, either through pressure provided by static magnetic fields, or through MHD turbulence provided by a fluctuating component of the field (Alfvén waves), or both. However, this is more of a consistency argument than a definitive proof.

In Chapters 3 and 4 we report the results of a study of a very spectacular outflow being driven by the low mass protostellar candidate IRAS 11590–6452 in the Bok globule BHR 71. IRAS 11590–6452 is a classic example of a Class 0 protostar, the youngest protostars we have yet identified, and its outflow is one of an even smaller group of outflows identified to date which show abundance enhancements of such species as SiO and CH_3OH, and where the temperature of the molecular gas swept up into the outflow is clearly higher than in the surrounding ambient gas into which it is travelling. The type of chemistry observed in this outflow is most likely the result of C-shocks ramming an oblique magnetic field. As discussed above, these C-shocks do not exist without the presence of a magnetic field of about the strength required to be important in other aspects of the molecular cloud dynamics. In Chapter 3 we study the global aspects of the parent molecular cloud, in this case a well isolated Bok globule, and we derive the bulk properties of the outflow through observations of CO. We also determine the nature of IRAS 11590–6452 through a combination of IRAS and mm observations. In Chapter 4 we look at the outflow as traced in some less abundant molecular species such as SiO and CH_3OH, and find that their abun-

dances have been greatly affected by the outflow and differ significantly from their ambient cloud values. Their spatial distribution does not clearly allow us to decide between the jet-driven and wind-driven outflow models, and actually suggests that we may be seeing a combination of the two.

Finally, in Appendix A we present the results of a mid-infrared study of RCW 38, which is the beginning of a larger study of this source to complement the detection of the Zeeman effect toward it. We observe a ridge of dust emission associated with the bright mid-infrared source IRS1 which is being heated and evaporated by the hot young star(s) associated with IRS2. Using photoionisation models we are able to determine the stellar effective temperature of IRS2 to be 43 000–48 000 K, consistent with a zero-age main sequence (ZAMS) star of spectral type O5.5–O4.5. The photoionisation models also allow us to estimate the gas density in the IRS1 dust ridge to be $\sim 10^4$ cm^{-3}. The dust temperature in the ridge is observed to be relatively uniform, an observation which is best explained as due to heating by resonantly trapped Lyman α photons, which in turn implies that the dust is depleted by a factor of $\sim$100 with respect to its interstellar value.

In future studies, to complement our single-dish Zeeman observations and mid-infrared study, we aim to obtain high resolution Zeeman observations and addition molecular line observations of the dense gas associated with RCW 38, to obtain a more complete picture of this region.

The scripts used in the analysis of the Zeeman data are included for reference in Appendix B.

1.5. Contribution to published papers

Chapter 2 is entirely due to the candidate. It has not yet been submitted for publication in a refereed journal.

Chapter 3 has been published in the Astrophysical Journal (Bourke et al., 1997, 476, pp781-800, plus one colour plate) in the form presented in this the-

sis, with the exception that Figure 3.14 has been added to the Chapter. The candidate's contribution to the published paper is estimated to be ~65%.

Chapter 4 has been accepted for publication in the Astrophysical Journal in the form presented in this thesis, with the exception that Figure 4.7 has been added to the Chapter. The candidate's contribution to the journal article is estimated to be ~40%, with the remainder of the paper being due mainly to Garay and Kohnenkamp. The collaboration with Garay is continuing and future papers are planned.

Appendix A has been accepted for publication in the Monthly Notices of the Royal Astronomical Society (MNRAS) in a slightly modified version to that presented in this thesis. Section A.4.3 was removed from the version submitted to MNRAS due to its speculative nature. The candidate's contribution to the journal article is estimated to be ~25%. Since the candidate's contribution is significantly less than his contribution to the other papers presented in this thesis this work is included as an appendix rather than a main chapter.

REFERENCES

André, P., Ward-Thompson, D., & Barsony, M. 1993, ApJ, 406, 122

Arons, J., & Max, C. E., 1975, ApJ, 196, L77

Bachiller, R. 1996, ARA&A, 34, 111

Bachiller, R., Martín-Pintado, J., & Fuente, A. 1991, A&A, 243, L21

Bachiller, R., & Pérez Gutiérrez, M., 1997, in IAU Symp. 182, Herbig-Haro Flows and the Birth of Low Mass Stars, ed. B. Reipurth & C. Bertout (Dordrecht: Reidel), 153

Bergin, E. A., Melnick, G. J., & Neufeld, D. A. 1998a, ApJ, in press

Bergin, E. A., Plume, R., Williams, J. P., & Myers, P. C., 1998b, ApJ, in press

Bourke, T. L., Garay, G., Lehtinen, K. K., Köhnenkamp, I., Launhardt, R., Nyman, L-Å, May, J., Robinson, G., & Hyland, A. R. 1997, ApJ, 476, 781 (Chapter 3)

Brogan, C., Troland, T. H., Roberts, D. A., & Crutcher, R. M., 1998, submitted to ApJ

Caselli, P., Hartquist, T. W., & Havnes, O. 1997, A&A, 322, 296

Caselli, P., Walmsley, C. M., Terzieva, R., & Herbst, E., 1998, ApJ, in press

Chernin, L. M., & Masson, C. R., 1995, ApJ, 455, 182

Crutcher, R. M., 1994, in ASP Conf. Ser. 65, Clouds, Cores, and Low Mass Stars, ed. D. P. Clemens & R Barvainis (San Fransisco: ASP), 87

Crutcher, R. M., & Kazès, I., 1983, A&A, 125, L23

Crutcher, R. M., Kazès, I., & Troland, T. H., 1987, A&A, 181, 119

Crutcher, R. M., Troland, T. H., Goodman, A. A., Heiles, C., Kazès, I., & Myers, P. C., 1993, ApJ, 407, 175

Crutcher, R. M., Mouschovias, T. Ch., Troland, T. H., & Ciolek, G. E., 1994, ApJ, 427, 839

Crutcher, R. M., Troland, T. H., Lazareff, B., & Kazès, I., 1996, ApJ, 456, 217

Davis, C. J., & Smith, M. D., 1995, ApJ, 443, L41

Draine, B. T., & McKee, C. F., 1983, ARA&A, 31, 373

Eislöffel, J., 1997, in IAU Symp. 182, Herbig-Haro Flows and the Birth of Low Mass Stars, ed. B. Reipurth & C. Bertout (Dordrecht: Reidel), 93

Goldsmith, P. F., & Arquilla, R., 1985, in Protostars and Planets II, ed. D. C. Black & M. S. Matthews (Tucson: Univ. Arizona Press) 137

Goodman, A. A., Crutcher, R. M., Heiles, C., Myers, P. C., & Troland, T. H., 1989, 338, L61

Goodman, A. A., Benson, P. J., Fuller, G. A., & Myers, P. C., 1993, ApJ, 466, 528

Goodman, A. A., 1996, in ASP Conf. Ser. 97, Polarimetry of the Interstellar Medium, ed. W. G. Roberge & D. C. B. Whittet (San Fransisco: ASP), 325

Gredel, R., 1994, A&A, 292, 580

Heiles, C., & Stevens, M., 1986, ApJ, 301, 331

Heiles, C., Goodman, A. A., McKee, C. F., & Zweibel, E. G., 1993, in Protostars and Planets III, ed. E. H. Levy & J. I. Lunine (Tucson: Univ. Arizona Press), 279

Hollenbach, D. 1997, in IAU Symp. 182, Herbig-Haro Flows and the Birth of Low Mass Stars, ed. B. Reipurth & C. Bertout (Dordrecht: Reidel), 181

IAU Symposium 182, Herbig-Haro Flows and the Birth of Low Mass Stars, ed. B. Reipurth & C. Bertout (Dordrecht: Reidel)

Kazès, I., & Crutcher, R. M., 1986, A&A, 164, 328

Kazès, I., Troland, T. H., Crutcher, R. M., & Heiles, C., 1988, ApJ, 335, 263

Lada, C. J., 1985, ARA&A, 23, 267

Lada, C. J., & Fich, M., 1996, ApJ, 459, 638

McKee, C. F., Zweibel, E. Goodman, A. A., & Heiles, C., 1993, in Protostars and Planets III, ed. E. H. Levy & J. I. Lunine (Tucson: Univ. Arizona Press), 327

Mouschovias, T. Ch., & Spitzer, L., 1976, ApJ, 210, 326

Myers, P. C., 1995, in Molecular Clouds and Star Formation, ed. C. Yuan & J. You (Singapore; World Scientific), 47

Myers, P. C., & Goodman, A. A., 1988a, ApJ, 326, L27

Myers, P. C., & Goodman, A. A., 1991, ApJ, 373, 509

Myers, P. C., Dame, T. M., Thaddeus, P., Cohen, R. S., Silverberg, R. F., Dwek, E., & Hanser, M. G., 1986, ApJ, 301, 398

Myers, P. C., Fuller, G. A., Goodman, A. A., & Benson, P. J., 1991, ApJ, 376, 561

Noriega-Crespo, A., & Garnavich, P. M., 1994, Rev. Mex. Astron. Astrophy., 28, 173

Ohashi, N, Hayashi, M., Ho, P. T. P., Momose, M., Tamura, M., Hirano, N., & Sargent, A. I., 1997, ApJ, 488, 317

Padman, R., Bence, S., & Richer, J. 1997, in IAU Symp. 182, Herbig-Haro Flows and the Birth of Low Mass Stars, ed. B. Reipurth & C. Bertout (Dordrecht: Reidel), 123

Pineau des Forêts, G., Roueff, E., Schilke, P., & Flower, D. R. 1993, MNRAS, 262, 915

Roberts, D. A., Crutcher, R. M., Troland, T. H., & Goss, W. M., 1993, ApJ, 412, 675

Roberts, D. A., Crutcher, R. M., & Troland, T. H., 1995, ApJ, 442, 208

Roberts, D. A., Crutcher, R. M., & Troland, T. H, 1996, in ASP Conf. Ser. 97, Polarimetry of the Interstellar Medium, ed. W. G. Roberge & D. C. B. Whittet (San Fransisco: ASP), 527

Schilke, P., Walmsley, C.M., Pineau des Forêts, G., & Flower, D.R. 1997, A&A, 321, 293

Shu, F. H., Adams, F. C., & Lizano, S., 1987, ARA&A, 25, 23 (SAL)

Smith, M. D., 1992, ApJ, 390, 447

Smith, M. D., 1993, ApJ, 406, 520

Smith, M. D., Völker, R., Suttner, G., & Yorke, H. W., 1997, in IAU Symp. 182, Herbig-Haro Flows and the Birth of Low Mass Stars, ed. B. Reipurth & C. Bertout (Dordrecht: Reidel), 303

Stahler, S. W., 1994, ApJ, 422, 616

Troland, T. H., 1990, in Galactic and Intergalactic Magnetic Fields, ed. R. Beck, P. P. Kronberg, & R Wielebinski (Dordrecht: Kluwer), 293

Troland, T. H., Crutcher, R. M., & Kazès, I., 1986, ApJ, 304, L57

Verschuur, G. L., & Turner, B. E., 1970, ApJ, 162, 341

Williams, J. P., Bergin, E. A., Caselli, P., Myers, P. C., & Plume, R., 1998, ApJ, 503, 689

Zuckerman, B., & Palmer, P., 1974, ARA&A, 12, 279

Chapter 2

OH Zeeman Observations of Southern Molecular Clouds

ABSTRACT

In this Chapter we present the first results of an extended program to measure the line-of-sight magnetic field strength toward southern molecular clouds, using the Zeeman effect, with the Australia Telescope National Facility (ATNF) Parkes radiotelescope, through observations of OH absorption lines against background continuum sources (H II regions). From 18 Gaussian components observed toward 9 sources, we definitely detected the Zeeman effect in the molecular gas associated with the H II region RCW 38, with a field strength of 38 ± 3 μG, and possibly in the molecular gas associated with the H II region RCW 57, with a field strength of -203 ± 25 μG. The molecular clouds were also observed in the ^{13}CO $J = 1 \rightarrow 0$ transition to determine their the physical properties (e.g., cloud sizes and mean column density). Comparison of the observed magnetic field strengths and sensitive upper limits with those estimated from a simple spherical model of a molecular cloud without surface terms indicates that the results are consistent with large scale cloud support being due to either the mean magnetic field and/or turbulent motions associated with magnetohydrodynamic waves. Our results cannot rule out either scenario. However, in about half of the clouds studied the kinetic energy density alone is insufficient to provide large scale support to the clouds, and an additional means of support is required. A comparison of the magnetic field strengths (including upper limits) and line widths show that the results are consistent with the supersonic line widths being due to hydromagnetic wave motions, resulting from perturbations of the mean magnetic field.

2.1. Introduction

As discussed in Chapter 1, magnetic fields are widely believed to support molecular clouds against large-scale gravitational collapse, and to explain the supersonic line widths seen in all interstellar molecular spectral lines (see reviews by Heiles et al. 1993; McKee et al. 1993; and references therein). Yet these central ideas in molecular cloud and star formation physics are supported by remarkably few measurements of magnetic field strengths, due to the difficulty in measuring the Zeeman effect in molecular lines such as the 18 cm lines of OH. Excluding masers, for which the velocity dispersion and gas density are very uncertain, there are only 11 clouds in which the OH Zeeman effect has been detected above 3σ (Crutcher, Kazés & Troland 1987; Crutcher & Kazés 1983; Kazés & Crutcher 1986; Heiles & Stevens 1986; Troland, Crutcher & Kazés 1986; Kazés et al. 1988; Crutcher et al. 1993; see also reviews by Troland 1990 & Crutcher 1994). Six of these detections are from molecular clouds associated with H II regions (warm clouds), and five from other molecular clouds ("cold clouds"), with most of the detections resulting from absorption line studies. The mean values for the line-of-sight magnetic field strength B_{los} determined from these studies are ~ 75 μG for the warm clouds, and ~ 10 μG for the cold clouds (including 10 upper limits reported by Crutcher et al. 1993). Since progress in this field clearly requires more observations, we have undertaken OH Zeeman observations of molecular clouds in the relatively unexplored southern hemisphere.

The key question we wish to investigate is, to what extent do magnetic fields provide large-scale support to molecular clouds? By careful measurement of line-of-sight field strength B_{los}, statistical uncertainty $\sigma_{B_{los}}$ (or upper limit $B_{los,3\sigma}$), cloud size R, column density N, and line width (or velocity dispersion) Δv, we aim to test the measurements for the observed clouds against the following hypotheses, discussed in more detail below:

(a) *Clouds are supported primarily by the mean magnetic field.* If so, equating the magnetic and gravitational energy densities leads to the equipartition field strength $B_{\mathcal{MG}} \sim G^{1/2}N$, and clouds with a magnetic field strength

$B > B_{\mathcal{MG}}$ may be supported by the mean field.

(b) *Clouds are supported primarily by the turbulent motions associated with magnetohydrodynamic (MHD) waves.* If so, equating the magnetic, kinetic, and gravitational energy densities leads to the equipartition field strength $B_{\mathcal{MKG}} \sim G^{-1/2}\Delta v^2/R$, and clouds with $B > B_{\mathcal{MKG}}$ may be supported by MHD waves.

(c) *Clouds are supported primarily by turbulent motions unrelated to the magnetic field.* If so, the equipartition column density $N_{\mathcal{KG}} \sim \Delta v^2/GR$, is independent of B.

It has not been possible to answer these questions very well to date, because of the paucity of data on magnetic field strengths (see Fig 2.1). Fig. 2.1 does not include clouds with only upper limit measurements of B, and so while it is consistent with hypothesis (b), lack of column density data means that hypothesis (a) cannot be ruled out for these clouds. By comparing our observations against the hypotheses (a) – (c), we will attempt to determine (1) is magnetic support consistent with all available observations, *including upper limits*, and (2) for clouds with evidence of magnetic support, does the evidence favour support by the mean field, by waves, or by an approximately equal combination?

2.1.1. Molecular Cloud Energetics

In this section we discuss in more detail the hypotheses outlined above. We start with an idealised spherical molecular cloud of uniform density, for which we can write down the expressions for the gravitational, kinetic and magnetic energy densities exactly. We then rewrite these expressions in terms of observable quantities. We are then able to express the hypotheses outlined in the previous section in a more quantitative form, keeping in mind the assumptions we have made for our idealised model cloud. The analysis in this section borrows heavily from Myers (1995), Myers & Goodman (1988b), and McKee et al. (1993).

We start with the assumption of a spherical molecular cloud with mass M,

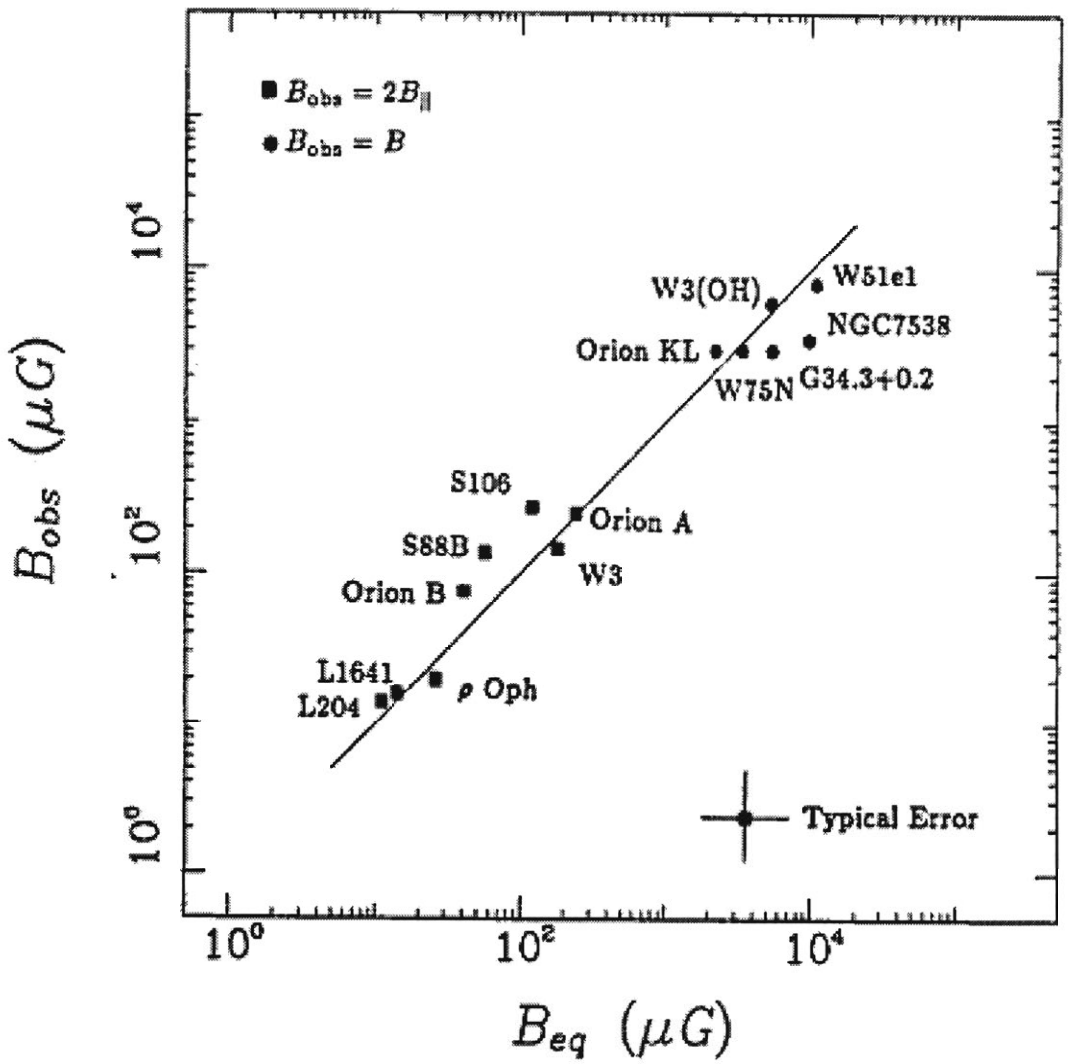

Figure 2.1.— Observed (B_{obs}) and predicted (B_{eq}) magnetic field strengths in 14 molecular clouds and molecular cloud cores, taken from Myers & Goodman 1988a. The observed field strength is equal to either twice the line-of-sight component, $2B_{\|}$ (filled squares) or the total field strength (filled circles). The predicted field strength is based on eqn. (2.9) (given in a slightly different form in Myers & Goodman, since they assume $\mathcal{M} \approx \mathcal{K} \approx \mathcal{G}$). The solid line indicates $B_{los} = B_{\mathcal{MKG}}$ (see text below for definition of terms).

uniform mass density ρ, velocity dispersion σ, and magnetic field strength B, inside a radius R. We denote the gravitational, kinetic, and magnetic energy densities by $\mathcal{G}$, $\mathcal{K}$, and $\mathcal{M}$, respectively. The cloud is truncated at R so that the energy terms go to zero at distances greater than R. With this assumption, we may write:

$$\mathcal{G} = -\frac{3}{5}\frac{GM\rho}{R} \quad , \tag{2.1}$$

$$\mathcal{K} = \frac{3}{2}\rho\sigma^2 \quad , \tag{2.2}$$

$$\mathcal{M} = \frac{B^2}{8\pi} \quad , \tag{2.3}$$

where G is the gravitational constant.

A molecular cloud is in virial equilibrium when, on average, the outward forces due to magnetic and kinetic pressure balance the inward forces due to gravity, so that

$$\mathcal{G} + 2\mathcal{K} + \mathcal{M} = 0 \quad . \tag{2.4}$$

We have ignored surface terms in this equation. The assumption of a uniform magnetic field in a spherical cloud, and hence an anisotropic magnetic pressure, is at odds with the variation expected for the gravitational and kinetic pressures, which are isotropic. However, the uncertainties in determining any of these quantities for real clouds means our assumption of a uniform field is accurate enough for our purposes (Heiles et al. 1993; Zweibel & McKee 1995).

This virial model has been successfully used by Myers & Goodman (1988a,b) to show that a combination of thermal and magnetic support against gravity fits the observed line-width relationships (that is, "Larson's Laws", $\sigma \propto R^{0.5}$ and $\rho \propto R^{-1}$: Larson 1981; Myers 1983; Dame et al. 1986; Caselli & Myers 1995) for cloud sizes from 0.1 to 100 pc provided the magnetic field strength is of order 5 – 100 μG, consistent with the data on field strengths then available. This model makes use of the concept of "equipartition" of the different forms of energy defined above, equipartition meaning that they are approximately equal, since well coupled forms of energy will tend to equilibrate (Myers 1995). Myers (1995) suggests that, due to our limited knowledge in determining $\mathcal{G}$, $\mathcal{K}$, and $\mathcal{M}$, and the use of this idealized model, in practice we cannot distinguish between

equipartition and virial values of $\mathcal{K}$ or $\mathcal{M}$ in a self gravitating system (cf., Zweibel & McKee 1995).

The defining equations for $\mathcal{G}$, $\mathcal{K}$, and $\mathcal{M}$ can be related to the observable quantities N, R, Δv, T (kinetic temperature), and B_{los}:

$$\begin{aligned} \mathcal{K} &= \frac{9mN}{8R}\left[\sigma_{NT}^2 + \frac{m}{m_{\rm obs}}\sigma_T^2\right] \\ &= \frac{9mN}{8R}\left[\frac{\Delta v^2}{8\ln 2} + \frac{kT}{m_{\rm obs}}\right] \end{aligned} \tag{2.5}$$

$$\mathcal{G} = \frac{\pi G}{5}\left(\frac{3mN}{2}\right)^2 \tag{2.6}$$

where σ_{NT} and σ_T are, respectively, the non-thermal and thermal velocity dispersions, m is the mean molecular mass, and $m_{\rm obs}$ is the mass of the molecular tracer used. For the magnetic component, we need to consider the mean field $<B>$ and the three dimensional rms field σ_{Brms}. The magnetic field we measure with Zeeman experiments is the line-of-sight component of $<B>$, which we have denoted by B_{los}. For an isotropic distribution of mean field strengths, $3{B_{los}}^2 = <B>^2$, and Myers & Goodman (1991) show that $\sigma_{Brms} \sim <B>$ from comparison of optical polarizations studies with H I Zeeman observations, so that

$$\begin{aligned} \mathcal{M} &= \left(1 + \left\{\frac{\sigma_{Brms}}{<B>}\right\}^2\right)\left(\frac{<B>}{B_{los}}\right)^2 \frac{{B_{los}}^2}{8\pi} \\ &= \frac{3{B_{los}}^2}{4\pi} \end{aligned} \tag{2.7}$$

We are now in a position to evaluate in a quantitative manner the hypotheses outlined in the previous section.

Clouds are supported primarily by the mean magnetic field

If the primary agent in molecular cloud support is the mean magnetic field then we can ignore the kinetic energy term, and equate $\mathcal{M}$ with $\mathcal{G}$. Combination of eqs (2.7) and (2.6) then implies

$$\begin{aligned} B_{\mathcal{MG}} &\approx \pi m\left(\frac{3G}{5}\right)^2 N \\ &= 2.5\left(\frac{N}{10^{21}\ {\rm cm}^{-2}}\right)\mu{\rm G} \end{aligned} \tag{2.8}$$

Thus, clouds with $B_{los} > B_{\mathcal{MG}}$ may be supported by the mean magnetic field.

Clouds are supported primary by the turbulent motions associated with MHD waves

If the turbulent motions associated with MHD waves are the primary support mechanism for molecular clouds, then we expect to have equipartition between the gravitational, kinetic and magnetic energy densities, so that $\mathcal{G} \approx 2\mathcal{K} \approx \mathcal{M}$ and eqs (2.5) – (2.7) imply

$$\begin{aligned} B_{\mathcal{MKG}} &\approx \left(\frac{15}{G}\right)^2 \frac{1}{16\ln 2}\frac{\Delta v^2}{R} \\ &= 4.4\left(\frac{\Delta v}{\mathrm{km\,s^{-1}}}\right)^2\left(\frac{R}{\mathrm{pc}}\right)^{-1}\mu\mathrm{G} \end{aligned} \tag{2.9}$$

Thus, clouds with $B_{los} > B_{\mathcal{MKG}}$ may be supported by motions associated with MHD waves.

Clouds are supported primarily by turbulent motions unrelated to the magnetic field

If the magnetic field is unimportant in cloud support, then we can ignore the magnetic term in eqn (2.4) so that $\mathcal{G} \approx 2\mathcal{K}$, and hence eqs (2.5) – (2.6) imply

$$\begin{aligned} N_{\mathcal{KG}} &\approx \frac{5}{\pi m G}\frac{1}{8\ln 2}\frac{\Delta v^2}{R} \\ &= 3.6\left(\frac{\Delta v}{\mathrm{km\,s^{-1}}}\right)^2\left(\frac{R}{\mathrm{pc}}\right)^{-1}\times 10^{21}\ \mathrm{cm^{-2}} \end{aligned} \tag{2.10}$$

independent of B. Thus, clouds with $N > N_{\mathcal{KG}}$ may be supported by non-magnetic turbulent motions.

2.2. Observational Technique

In order to test the hypotheses outlined above, we require information on the magnetic field strengths in molecular clouds. As discussed in detail in the reviews by Heiles et al. (1993) and Crutcher (1994), the only known way to obtain this

information is via the detection of the Zeeman effect in radio spectral lines, in particular the OH transitions at 1665 and 1667 MHz.

2.2.1. The OH Molecule

In this section we outline the properties of the OH molecule which make it the preferred molecule for "large scale" ($\gtrsim$ 1 pc) magnetic field strength measurements in molecular clouds. More detailed discussions of OH may be found in Townes & Schawlow (1975), Elitzur (1992), and Rohlfs & Wilson (1996). Hydroxyl (OH) is an open shell molecule with an unpaired electron (and therefore is known as a *radical*) resulting in a net electronic angular momentum, so it possesses paramagnetic properties. The 1665 and 1667 MHz transitions arise from hyperfine transitions within the "Λ doublet" of the ground vibrational state of the $^2\Pi_{3/2}$ ground electronic state (see Fig. 2.2). The projection of the electronic angular momentum **L** onto the z-axis (the inter-nuclear axis), L_z (usually written as Λ), is denoted by Σ, Π, and Δ for $L_z = 0$, 1, and 2, respectively (higher values are permissible). The total angular momentum **J**, excluding nuclear spin (**I**), is

$$\mathbf{J} = \mathbf{K} + \mathbf{L} + \mathbf{S}$$

where **K** is the end-over-end rotation ($K_z = 0$), and **S** is the electronic spin ($\pm$ $^1/_2$). So $J_z = 1 \pm {}^1/_2$ for the Π state and in this configuration two rotational ladders are possible, $^2\Pi_{1/2}$ and $^2\Pi_{3/2}$, where the superscript refers to the two possible electron configurations about the rotation axis (Fig. 8.3 of Townes & Schawlow). The interaction of the electronic orbital angular momentum with the next electronic state removes the degeneracy of the $\pm J_z$ levels, and "Λ doublet" splitting results, which refers to the fact that the splitting is due to effects on Λ (see Townes & Schawlow, section 7.5). Furthermore, hyperfine interactions with the nuclear spin, **I**, ($= \pm {}^1/_2$), causes further splitting of the Λ doublet into 4 levels according to parity ($\pm$) and the total angular momentum, **F** ($=$ **J** $+$ **I**), with $\Delta F = 0, \pm 1$ allowed ($0 \rightarrow 0$ is forbidden). The 1665 and 1667 MHz transitions are the "main-line" transitions corresponding to $\Delta F = 0$, while the satellite lines at 1612 and 1720 MHz correspond to $\Delta F = \pm 1$ respectively, as

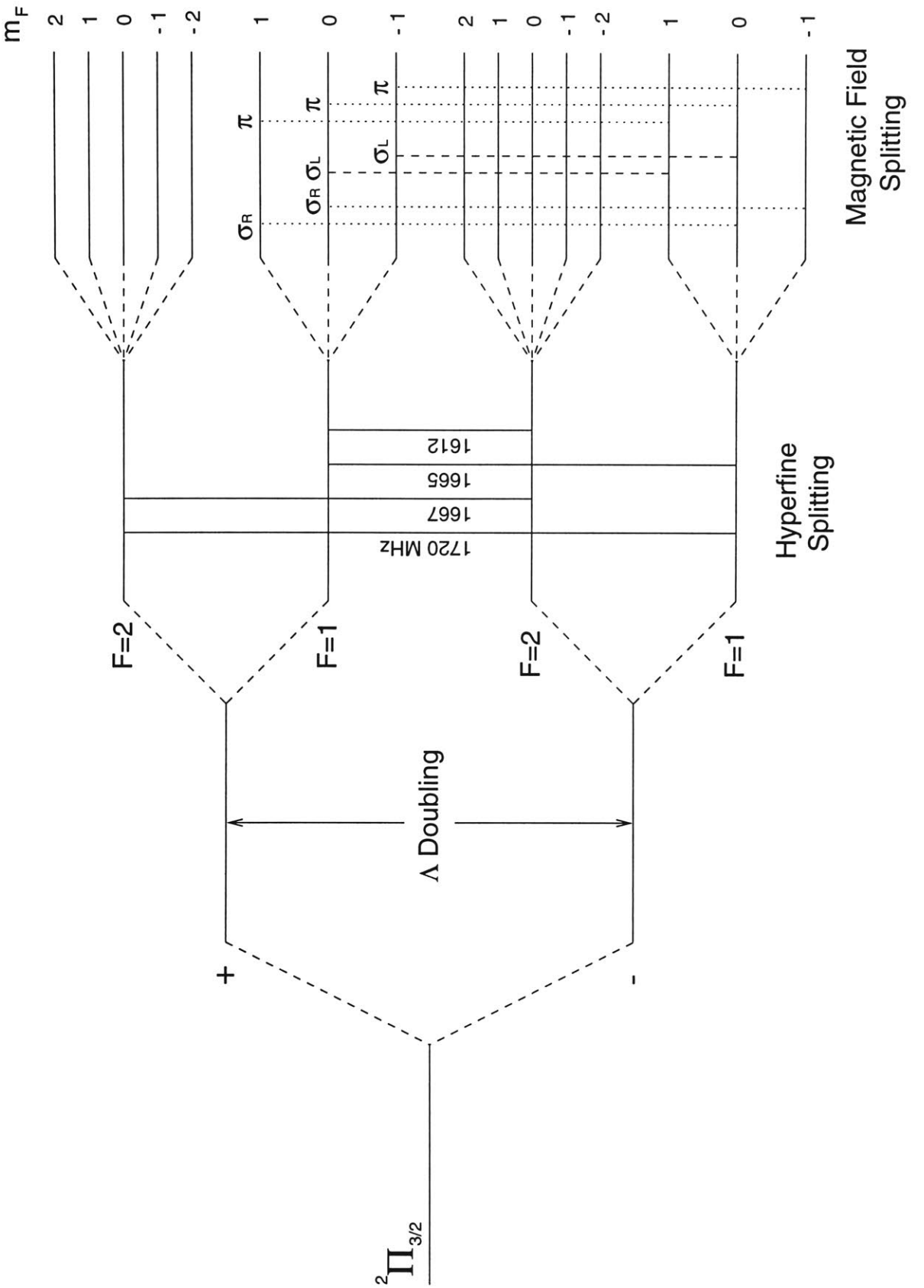

Figure 2.2.— Energy level diagram for the ground state of OH ($^2\Pi_{3/2}$, $J = {}^3/_2$). The relative splitting of the levels are not drawn to scale. The allowed π and σ components for the 1665 MHz are shown.

shown in Fig. 2.2.

External Magnetic Fields

The total angular momentum **F** is degenerate with a $2F+1$ degeneracy, which is removed with the introduction of an external magnetic field, resulting in Zeeman splitting, first observed by Zeeman (1895) in the laboratory (see Chapter 11 of Townes & Schawlow 1975). This splitting is identified by the quantum number m_F, as shown in Fig 2.2. The separation in energy of the magnetic hyperfine levels from the unsplit level of the zero magnetic field case is given by

$$\Delta E = -\mu_B \, m_F \, g \, B$$

where μ_B is the Bohr magneton, B the magnetic field strength, and g is the Landé g-factor, given by

$$g = g_J \frac{F(F+1) + J(J+1) - I(I+1)}{2F(F+1)}$$

and $g_J \approx 0.935$ for the $^2\Pi_{3/2}$ level as derived experimentally by Radford (1961).

The selection rules for the magnetic hyperfine transitions are $\Delta m_F = 0$, ± 1, $\Delta F = 0$, and parity $+ \longleftrightarrow -$. For the OH main-line transitions only three Zeeman components are generated. Transitions with $\Delta m_F = 0$ are known as $\pi - components$, while the $\Delta m_F = \pm 1$ transitions are known as $\sigma - components$. Note that for the $\pi-$components, there is no shift in frequency relative to the unsplit hyperfine line.

2.2.2. The Zeeman Effect

The most successful observational technique available for determining the magnetic field strength in molecular clouds is the Zeeman effect (Heiles et al. 1993; Crutcher 1994), which we have described briefly for OH. In Zeeman experiments, the magnetic field reveals itself as small frequency shifts, ν_z, in the right and left circularly polarized (RCP and LCP, respectively) components of the spectral

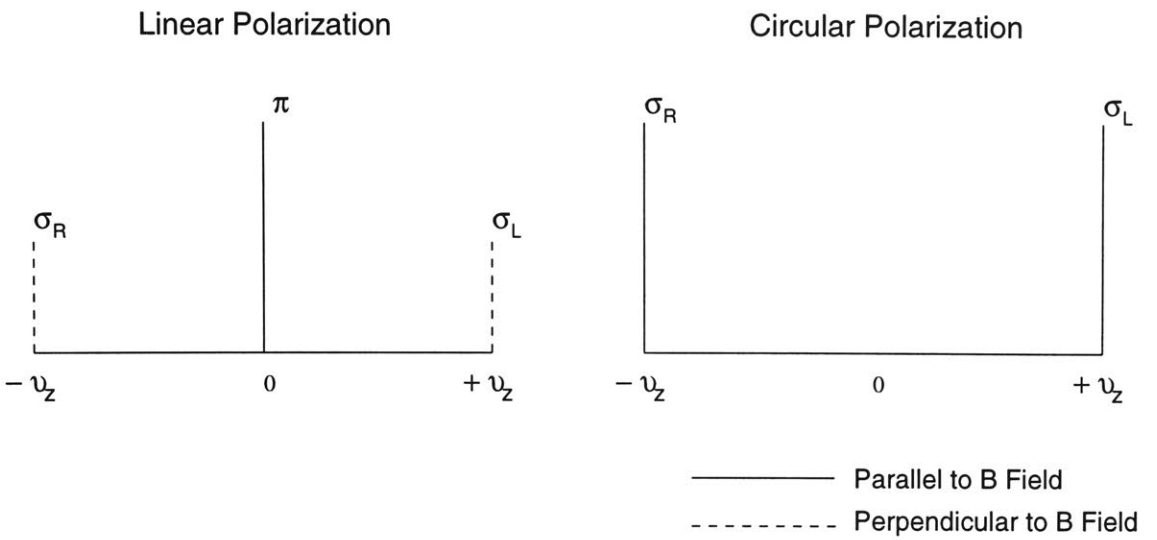

Figure 2.3.— Relative strength and polarization of the π and σ components with respect to the orientation of the magnetic field in the special cases when the field is orientated perpendicular to the line-of-sight (linear polarization – left figure) and when the field is aligned parallel to the line-of-sight and points away from the observer, so the field is positive (circular polarization – right figure).

line with respect to the frequency in the zero field case, ν_o. The frequency shift is given by

$$\begin{aligned} \nu_z &= \frac{\mu_B \, m_F \, g \, B}{h} \\ &= \frac{b}{2} B \end{aligned} \tag{2.11}$$

where h is Planck's constant. The "Zeeman factor", $b = 2\mu_B m_F g/h$ is equal to 3.27 and 1.96 Hz $\mu\mathrm{G}^{-1}$ for the 1665 and 1667 MHz transitions of OH, respectively. The observed RCP and LCP spectral line components, I_{RCP} and I_{LCP} respectively, are sums of the $\pi-$ and $\sigma-$components of the magnetic hyperfine transitions, as given in Table 2.1. The intensity of the $\pi-$ and $\sigma-$components varies as a function of the angle θ between the direction of the magnetic field and the line-of-sight. Table 2.1 is similar to that given in Goodman (1989; see also Crutcher et al. 1993). In Fig 2.3 we show schematically the Zeeman effect for the simple cases where θ is 0 or 90°.

The magnetic field strength is determined from the Stokes V spectrum,

$$V(\nu) = I_{RCP}(\nu) - I_{LCP}(\nu)$$

where $I(\nu)$ is the line profile as a function of frequency ν. Using the identities

Table 2.1. Zeeman components

Polarized Intensities	Zeeman Components		
	$\nu - \nu_z$	ν	$\nu + \nu_z$
I_{RCP}	$\sigma_{\mathrm{R}}, -$	$\pi_{\mathrm{R}}, 0$	$\sigma_{\mathrm{R}}, +$
I_{LCP}	$\sigma_{\mathrm{L}}, -$	$\pi_{\mathrm{L}}, 0$	$\sigma_{\mathrm{L}}, +$

Note. — Component Definitions.

$$
\begin{aligned}
\sigma_{\mathrm{R}}, - &= I(\nu - \nu_z)\left[\frac{1+\cos^2\theta}{4} - \frac{\cos\theta}{2}\right] \\
\pi_{\mathrm{R}}, 0 &= I(\nu)\frac{\sin^2\theta}{2} \\
\sigma_{\mathrm{R}}, + &= I(\nu + \nu_z)\left[\frac{1+\cos^2\theta}{4} + \frac{\cos\theta}{2}\right] \\
\sigma_{\mathrm{L}}, - &= I(\nu - \nu_z)\left[\frac{1+\cos^2\theta}{4} + \frac{\cos\theta}{2}\right] \\
\pi_{\mathrm{L}}, 0 &= I(\nu)\frac{\sin^2\theta}{2} \\
\sigma_{\mathrm{L}}, + &= I(\nu + \nu_z)\left[\frac{1+\cos^2\theta}{4} - \frac{\cos\theta}{2}\right]
\end{aligned}
$$

in Table 2.1 it is straightforward to show that

$$V(\nu) = \cos\theta\,[I_{\rm o}(\nu + \nu_z) - I_{\rm o}(\nu - \nu_z)] \tag{2.12}$$

where $I_{\rm o}$ is the Stokes I spectrum for $\nu_z = 0$ and is equal to $(I_{RCP} + I_{LCP})/2$.

Under most astrophysical conditions, $\nu_z \ll \Delta\nu$, where $\Delta\nu$ is the full width at half maximum of the spectral line (the exceptions are masers, see e.g., Reid & Silverstein 1990), and so detecting the shift between the RCP and LCP components due to the the Zeeman effect is difficult, and complete information about the magnetic field direction and magnitude is not obtainable. In this situation, the Stokes V spectrum allows only for the determination of the line of sight component of the field strength, B_{los} $(= B\cos\theta)$, and its sign (i.e., toward or away from the observer). It is then reasonable to approximate the difference term in eqn. (2.12) by the derivative of $I_{\rm o}$, so that eqn. (2.12) can be rewritten

$$V = 2\nu_z \cos\theta \frac{dI_{\rm o}}{d\nu} + \beta I_{\rm o} \tag{2.13}$$

where we have included the gain term $\beta I_{\rm o}$ which introduces a replica of the $I_{\rm o}$ spectrum scaled by the factor β into the V spectrum (e.g., Troland & Heiles 1982). This gain term is required since in a real experimental setup the sensitivity to the RCP and LCP components will not be identical, and this difference appears in the V spectrum as a scaled version of the I spectrum.

The Zeeman effect reveals itself in the V spectrum in the small splitting approximation as the characteristic sideways "S", or "Zeeman pattern" (see below). Substituting eqn. (2.11) into eqn. (2.13) gives

$$\begin{aligned} V &= bB\cos\theta \frac{dI_{\rm o}}{d\nu} + \beta I_{\rm o} \\ &= bB_{los} \frac{dI_{\rm o}}{d\nu} + \beta I_{\rm o} \end{aligned} \tag{2.14}$$

and by least-squares fitting the right hand side of eqn. (2.14) we are able to simultaneously determine B_{los} and β.

In Fig. 2.4 we present the results of a theoretical simulation of the Zeeman effect to illustrate the analysis presented above. In this simulation the RCP & LCP spectra are represented by Gaussians of intensity 10 arbitrary units (i.e.,

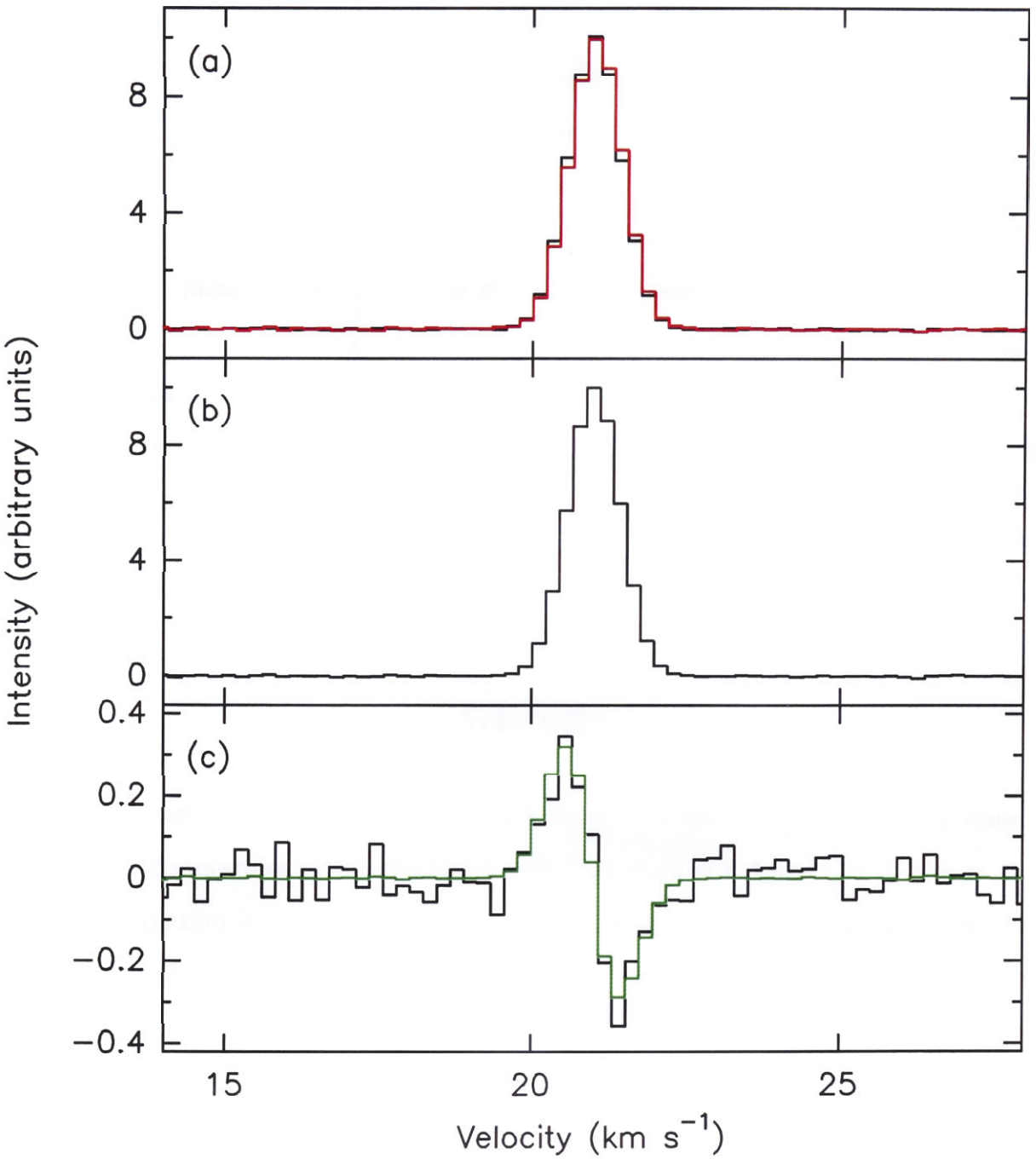

Figure 2.4.— Simulation of the Zeeman effect. In panel (a) we show theoretical RCP and LCP spectra, where the spectra have intensities of 10 units (arbitrary) and FHWM of 1.0 km s^{-1} (where the velocity resolution is 0.22 km s^{-1}), with random Gaussian noise of 0.03 units. The RCP component is plotted in black and the LCP component in red. In panel (b) we show the recreated Stokes I spectrum, which is the sum of the RCP and LCP spectra divided by 2. In panel (c) we show the V spectrum (black spectrum), which is the LCP spectrum subtracted from the RCP spectrum, overlayed with the least-squares fit of the form $bB\frac{dI}{d\nu} + \beta I$ (green spectrum).

emission lines) and full-width at half-maximum (FWHM) of 1.0 $\mathrm{km\,s^{-1}}$ (assuming a velocity resolution of 0.22 $\mathrm{km\,s^{-1}}$ for the simulation), with Gaussian random noise of 0.03 units. The separation between the RCP and LCP components is 0.02 $\mathrm{km\,s^{-1}}$, which if we were observing the 1665 MHz OH transition would correspond to a total magnetic field strength of $B = -34$ μG. In Fig. 2.4 the top panel shows the RCP and LCP spectra. The slight difference between them, due to their frequency offset, is evident on the low velocity side of the profiles where $I_{RCP} > I_{LCP}$, and on the high velocity side where $I_{LCP} > I_{RCP}$. The middle panel shows the recreated I spectrum, and the bottom panel shows the V spectrum with the characteristic sideways "S" indicative of the Zeeman effect. The bottom panel also shows the fit of $dI/d\nu$ (green line) to the true V spectrum, using eqn. (2.14). From this analysis we would derive a magnetic field strength of $B = -40 \pm 3$ μG, with a gain term $\beta = 2.6 \times 10^{-3}$.

Why OH?

The best astrophysical species for the detection of the Zeeman effect are those atoms and molecules with large Landé g-factors, such as H I and OH (Heiles et al. 1993). Another important factor to consider when choosing a Zeeman probe is that the *frequency offset* due to the Zeeman effect is *independent* of the line frequency, whereas the *Doppler broadened line width* is *proportional* to the line frequency. The ratio of the Zeeman effect to the line width decreases as the frequency of the line increases, and so low frequency lines are preferred (i.e., those in the centimetre wavelength region). The high sensitivity of centimetre wavelength telescopes and their receivers, and the transparency of the atmosphere at these wavelengths, are further points in favour of centimetre wavelength transitions as probes of the Zeeman effect. For molecular clouds the thermal transitions of OH at 1665 and 1667 MHz, which trace densities $\sim 2 \times 10^3$ $\mathrm{cm^{-3}}$ and sizes $\sim$ 1 pc (e.g., Crutcher 1979; Myers et al. 1978) are by far the best probes of the Zeeman effect currently available.

There are two serendipitous advantages of using OH. First the fact that the 1665 and 1667 MHz lines lie so close together in frequency means that they

may be observed simultaneously in the one receiver passband with modern day systems, and so they provide a consistency check on any possible Zeeman detections. By requiring that the same field strength be inferred from both OH lines allows for the elimination of possible spurious detections resulting from, for example, beam squint (see below). Second, since the ratio of line strengths of the two transitions in the optically thin regime at local thermodynamic equilibrium (LTE), $I(1667)/I(1665) \sim 9/5$, is approximately equal to the inverse of their Zeeman factors, 1.96/3.27, the two lines are equally sensitive to the Zeeman effect, which results in an effective halving of the integration time required to detect the effect in one line only. This is an important saving, since detecting the Zeeman effect in non-maser OH lines requires extremely long integration times (of the order of 10 hours).

2.3. Observations

The OH Zeeman observations were undertaken in 1995 July and 1996 October with the ATNF[1] Parkes 64-m radiotelescope. The receiver used was a HEMT (High Electron Mobility Transistor) receiver equipped with dual linear polarization feeds, mounted at the prime focus of the telescope. Cold sky system temperatures of $\sim 20 - 25$ K were recorded with this system. The outputs from the linear feeds were amplified in the low-noise amplifiers (LNAs) of the receiver, and the amplified outputs passed into a two-input, two-output "hybrid", where each linear polarization was split into two paths and a quarter cycle phase shift was introduced into one path of each polarization. Circular polarization was produced by combining the output from one linear polarization with the output from the other linear polarization with the quarter cycle phase shift introduced. The hybrid therefore acts as the electronic equivalent of a quarter-wave plate. This is shown schematically in Fig 2.5.

---

[1]The Australia Telescope is funded by the Commonwealth of Australia for operation as a National Facility managed by CSIRO

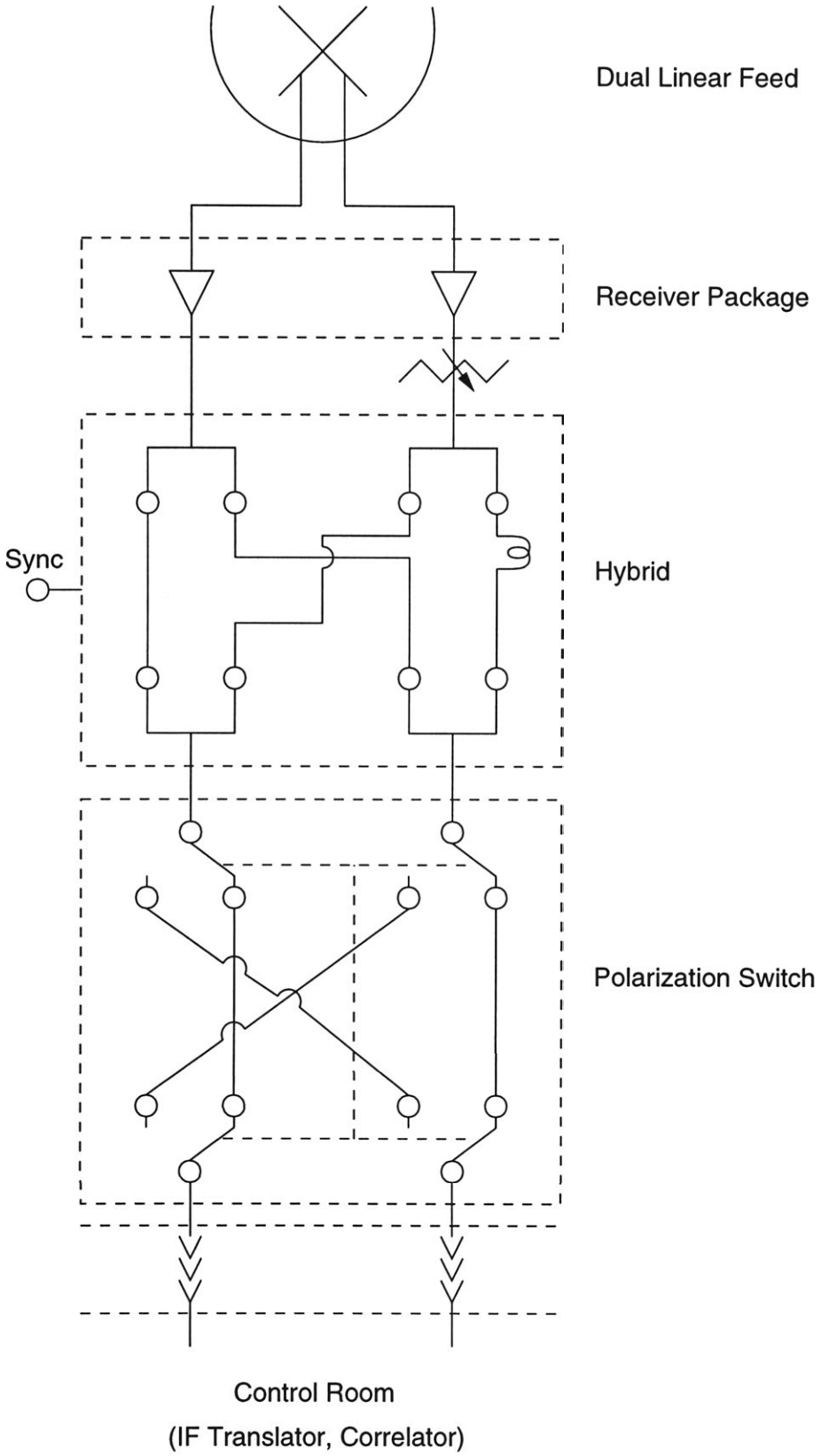

Figure 2.5.— Block diagram of the circular polarimetry setup used at Parkes, with a linear dipole feed (top). The hybrid is located immediately after the receiver package, and the polarization switch follows immediately.

The effects of instrumental polarization and gain differences between the two senses of circular polarization can be large, so to minimise these effects the signal paths of the two polarizations were interchanged at regular intervals (e.g., Crutcher et al. 1993). To achieve this, the outputs from the hybrid were passed through a double-pole, double-throw polarization switch, which allowed the separate paths the two circularly polarized signals take through the rest of the electronic system to the autocorrelator to be interchanged. The path switching was controlled by the autocorrelator and was performed every 10 seconds (the cycle time of the autocorrelator). The signals were finally passed into the Parkes 16384-channel digital autocorrelator. In order to obtain the maximum spectral resolution while observing both OH lines simultaneously the autocorrelator was configured with two 4 MHz bandpasses of 8196 channels each, with each band centred on 1666.380435 MHz. This arrangement provided a spectral resolution of 488.28 Hz (0.087 $\mathrm{km\,s^{-1}}$). The OH ground state transitions at 1665.40184 and 1667.35901 MHz were observed simultaneously in each circularly polarized bandpass, and the centre bandpass frequency was switched by $\pm$ 0.25 MHz every 4 minutes. Both senses of circular polarization were observed and recorded simultaneously. The intensity scale of the OH data presented in the remainder of this chapter is corrected antenna temperature T_A^*, as defined by Kutner & Ulich (1981). At 18 cm the main beam dish efficiency of the Parkes radiotelescope is ~ 0.7 (Caswell, private communication), and so the conversion from T_A^* to main beam brightness temperature is $T_{mb} \sim 1.4 T_A^*$.

As a test of the polarization purity of the experimental arrangement we undertook Zeeman observations of the deep OH absorption line toward Orion B (NGC 2024). The Zeeman effect in OH has previously been observed toward Orion B (see Fig. 2.6 taken from Crutcher & Kazès 1983; hereafter CK83). The signal due to the Zeeman effect in the Stokes V spectrum of Orion B is very clear, making Orion B the default "standard calibrator" for single dish Zeeman studies. In both observing periods we were able to reproduce the results of CK83 for Orion B after an on-source integration time of $\sim$ 5 hours, inferring values of 21 $\pm$ 2 μG in 1995 and 24 $\pm$ 2 μG in 1996 for the subcomponent identified

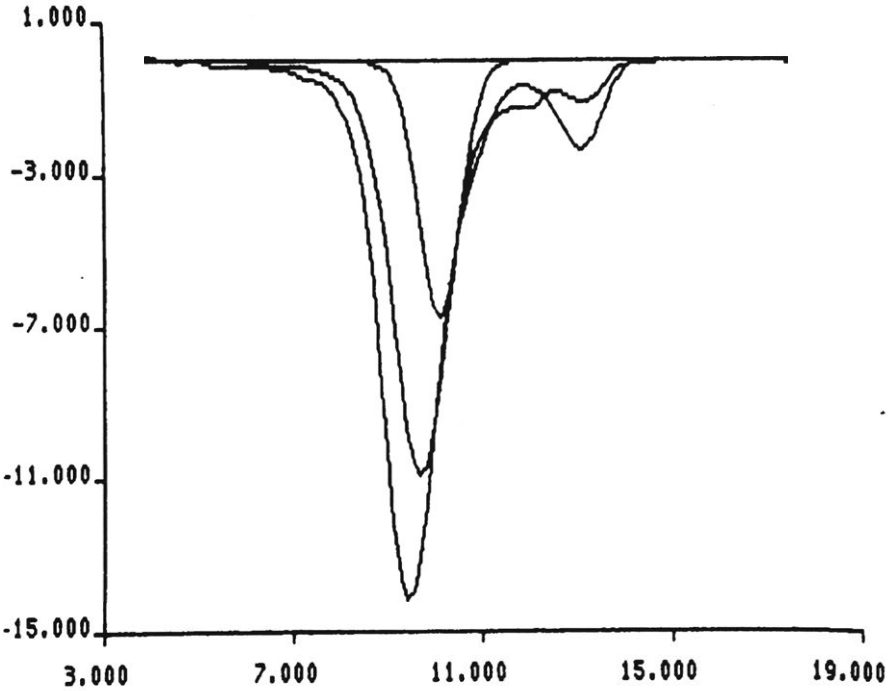

Fig. 1. Spectra of the 1667 (strongest) and 1665 lines observed for $13^h\ 18^m$ toward NGC 2024 (RA/DEC [1950.0] $05^h\ 39^m\ 14\overset{s}{.}3$ / -01° 55' 57"). The weakest line is the assumed gaussian component used for Zeeman analysis.

The abscissa scale in all figures is the same and is given in km s^{-1} relative to the LSR. The ordinate scale in °K antenna temperature is correct except that displacements of zero have been made in most figures.

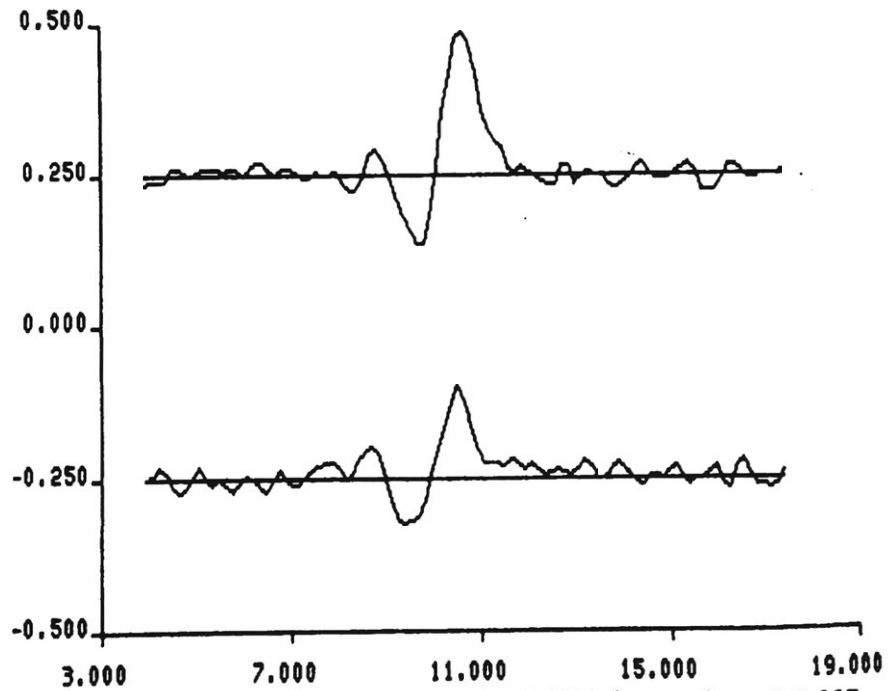

Fig. 2. Stokes V spectra of the 1665 (upper) and 1667 (lower) lines.

Figure 2.6.— The Zeeman effect in Orion B, as observed by Crutcher & Kazés 1983. Note that their V spectrum represents $I_{LCP} - I_{RCP}$.

by CK83 as the source of the Zeeman pattern, essentially independent of hour angle. These values are less than the value found by CK83 (38 $\pm$ 1 μG) using the Nançay telescope, most likely due to the different beam sizes of the two telescopes. The beam size of the Nançay telescope at the OH frequencies is 3′ $\times$ 19′.5, while the Parkes beamsize is 13′ at the same frequencies. Note that CK83 determined the sign of the field incorrectly, originally stating the field as –38 μG. This error was pointed out by Heiles & Stevens (1986), and our observations agree in sign with theirs.

Beam Squint

"Beam squint", the separation of the RCP & LCP telescope beam patterns on the sky, can introduce a fake Zeeman effect into the V spectrum if the direction of the squint is aligned with a significant systematic velocity gradient within the source being observed (Troland & Heiles 1982). In principle the fake Zeeman pattern can be identified, since the resultant frequency splitting observed in the Stokes V spectrum is equal for the two OH lines, and would result in different determinations of the magnetic field strength for the two lines, in the ratio of their b factors.

To determine the magnitude of the beam squint we mapped a strong continuum point source at the start of each observing session, mapping a region around the continuum source much large than the primary beam size of 13′. The RCP and LCP beam maps contructed in this manner were fitted with two dimensional Gaussians and the magnitude and direction of the squint was derived by comparison of the two maps. The polarized beam map (RCP – LCP) for July 1995 is shown in Fig 2.7. In July 1995 we measured the squint to be 12″ at P.A. 198°, while in October 1996 the squint was measured to be 16″ at P.A. 71°. To the experienced Zeeman observer these will appear as rather large squints, $\sim$ 2% of the primary beam FWHM. However, for our observations there is evidence to suggest that beam squint was not a problem. First, our observations of Orion B reproduce the results of CK83, in that we need to infer a Gaussian subcomponent with the same velocity and line width as CK83 to fit

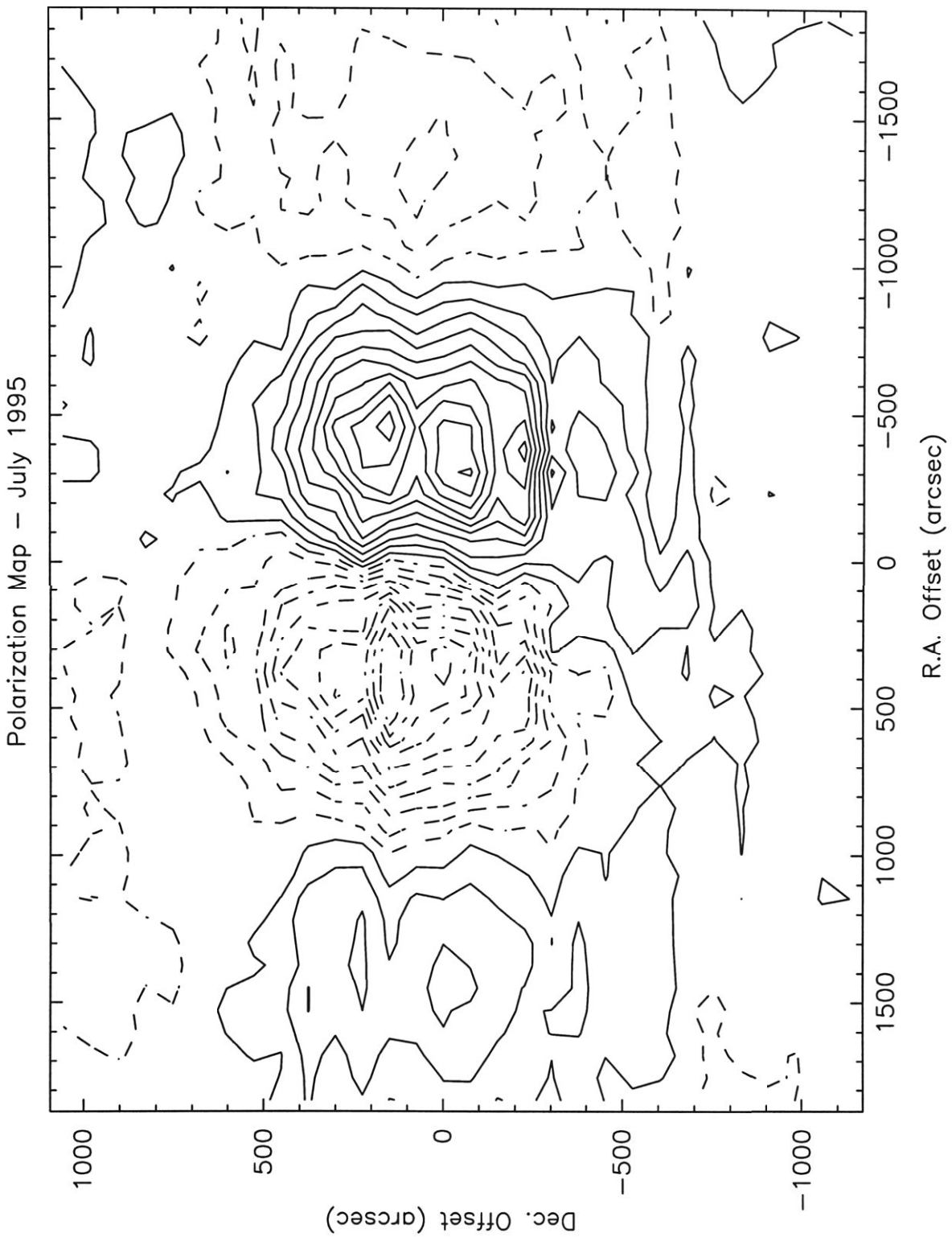

Figure 2.7.— Polarized beam pattern (RCP – LCP) as measured for Parkes, July 1995. The levels are –95, –85, ..., 85, 95% of the peak height of 0.029 (where the peak of the individual maps is normalized to 1.0). The dashed contours represent the negative levels.

our V spectrum, the value of the magnetic field strength determined for each OH line are in agreement, and our results for Orion from the two observing periods are the same. Second, Parkes is an altitude-azimuth telescope, and so the direction of squint will rotate on the sky as the hour angle changes. Since we observed our sources over large range of hour angles any beam squint effects will be greatly reduced in the overall integration, and any fake Zeeman pattern will modulate with hour angle, as the angle between the velocity gradient and squint direction changes. By examining subsets of our data obtained over small hour angles, for sources with and without evidence for Zeeman splitting, we find no evidence for (a) modulation of the Zeeman pattern in those sources showing the Zeeman effect, only an increase in the noise in a Gaussian manner, or (b) fake Zeeman patterns in those sources for which the total integration shows no Zeeman pattern. In case (b) a fake Zeeman pattern would only appear in part of the data.

Data Reduction

The data were recorded in the ATNF single dish format. Since Zeeman observations require very careful data reduction and non-standard reduction techniques, each 4 minute scan was converted to FITS format files and then to the GILDAS single-dish format for further data reduction and analysis, using the GILDAS data reduction package developed for the IRAM 30-m telescope (http://iram.fr). This package offers a flexibility not available in the ATNF single dish package 'SPC', and a number of scripts for the data reduction pipeline and Zeeman analysis were written by the candidate for use with the GILDAS single dish reduction package CLASS. The reduction pipeline is described below, and the scripts are listed in Appendix B.

After the FITS files were created a Unix shell script (`create-cfits`; see Appendix B) was used to prepare the data to be converted to a single GILDAS format file containing the multiple spectra. At this point it was necessary to inspect each spectrum by eye, to determine the sense of polarization. Since it was not possible to synchronise the autocorrelator and the polarization switch

at the start of each 4 minute integration, there was no way *a priori* to determine the sense of polarization for either channel. In the SPC data format, the different polarization switch positions are stored as "signal" or "reference" spectra, respectively. It was possible to configure the old Parkes autocorrelator for two intermediate frequencies (IFs), or "quadrants" (Q) in the local terminology, and we use this terminology here. However, only two IFs are available with the new autocorrelator we used, hence we only used two quadrants. With our experimental setup, the position of the polarization switch was not reset to the same position after each integration, so that it was not possible to always have e.g., Q1 always receiving RCP data when the data was stored as a "signal" spectrum. Thus, the "signal" spectrum in Q1 could be RCP for one integration, and then LCP for the next, or remain as RCP. In order to determine the sense of polarization being observed, a test tone generated by a small helical feed mounted at the (unused) Cassegrain focus, and pointing towards the Prime focus, was used to introduce a signal of known circular polarization. By observations of strongly polarized masers (Caswell, Haynes & Goss 1980; Caswell & Haynes 1983a,b; Caswell & Haynes 1987) it was determined that this feed produced mainly RCP polarization[2] over a very narrow frequency range (a few channels), which we centred at 1666 MHz in the middle of the bandpass, away from the OH frequencies. The level of this signal was adjusted so that it appeared only in the RCP band. Unfortunately, it was not possible to automatically identify this signal in CLASS, requiring that the polarization of each spectrum be identified and tagged manually offline. However, the inspection of each spectrum had the benefit of allowing for the possibility of rejecting bad spectra, e.g., due to inteference at the OH frequencies.

After the data were converted to GILDAS format, the identification of the

[2]The notation used here to distinguish RCP and LCP polarization is the IEEE notation, used throughout radio astronomy, where a magnetic field which points *towards* the observer is defined to be *negative*. Observationally, if the RCP component is observed at a higher frequency than the LCP component, the line-of-sight component of the magnetic field points toward the observer, i.e. the field is negative.

polarization of each spectrum as either RCP or LCP was performed, and then the spectra for each frequency switched position and polarization were averaged together (`sum-spectra.class`). Since the frequency switching of ± 25 MHz was not performed in a traditional way, no frequency switching information was contained in the file headers, so it was necessary at this stage to shift and average together the two separate frequency offsets positions used (`fold-spc.class`). This step also naturally corrected for the bandpass response of the system and produced almost flat baselines in most cases. For convenience in further analysis the two OH lines were then transferred to separate data files (`line-sep.class`) and any residual baselines were subtracted. For each individual source the same line-free channels in the spectrum were used to subtract residual baselines from both the RCP and LCP data. The Stokes V ($I_{RCP} - I_{LCP}$) and I [$(I_{RCP} + I_{LCP})/2$] spectra were then constructed as outlined above (`produce-v.class`). The fitting of the Stokes V spectra for each source to derive the magnetic field strength is described in §2.4.2.

Source Selection

Our initial search for suitable Zeeman candidates centred on the OH studies of Robinson, Goss & Manchester (1970), Goss, Manchester & Robinson (1970), Manchester, Robinson & Goss (1970), Robinson, Caswell & Goss (1971), Caswell & Robinson (1974), and Turner (1979). The spectral resolution of these earlier studies, many undertaken with the Parkes radiotelescope, was generally insufficient to detect weak, narrow maser features which may interfere with the sensitive observations we are attempting, and so we reobserved all our potential targets with the experimental setup described above. We also reobserved a number of other sources from these lists with a greater velocity coverage, as well as some sources from Chan, Henning & Schreyer (1996). We thus reobserved ~ 80 sources drawn from these lists to assess their suitability as Zeeman candidates. None of the surveyed sources from these lists showed any significant OH absorption that was not previously known, though a few previously unknown narrow line masers were found. The OH absorption mapping of the Carina Nebula by

Dickel & Wall (1974) was also consulted, as was the OH emission line mapping of the Chamaeleon I dark cloud by Toriseva, Höglund & Mattila (1985).

To determine our primary candidate list we used the "sensitivity estimator" given in Goodman (1989; see also Troland 1990) to estimate the integration time required per source to reach our target sensitivity of $3\sigma \sim 30$ μG. If we approximate the line profile as a Gaussian, then the maximum amplitude of the Stokes V spectrum occurs at the points where the second derivative of the line profile is equal to zero, which occurs at the standard deviation points of the Gaussian, $\nu_o - \nu = \pm\sigma$ (where ν_o is the unshifted line frequency and σ is the standard deviation). The maximum amplitude in the Stokes V spectrum, z, is therefore

$$z = \left|\frac{dI(\nu_o)}{d\nu}\right|_{\pm\sigma} bB\cos\theta = \frac{1.43T_A^*}{\Delta\nu} bB_{los}, \tag{2.15}$$

where T_A^* is the observed antenna temperature of the source, and $\Delta\nu$ is the line FWHM ($= \sigma\sqrt{8\ln 2}$). The rms noise T_{rms} in the spectrum after an integration time t in seconds is given by

$$T_{rms} = \frac{c_1 T_{sys}}{\sqrt{c_2 \Delta f\, t}}, \tag{2.16}$$

where c_1 depends on the type of correlator, c_2 is the weighting factor applied to the data, T_{sys} is the system temperature (including the background temperature), and Δf is the channel spacing in Hz. For the Parkes 2-bit autocorrelator, $c_1 = 1.14$ (Rohlfs & Wilson 1996, p103), and c_2 is set to 2 for Hanning weighting. For a 3σ detection ($z = 3T_{rms}$), the integration time in seconds is

$$t_{3\sigma} = \left(\frac{1.7T_{sys}\Delta\nu}{T_A^*\, bB_{los}}\right)^2 \frac{1}{\Delta f} \tag{2.17}$$

for T_{sys} and T_A^* in K, and $\Delta\nu$ and Δf in Hz.

In order to have the greatest sensitivity to the Zeeman effect, the spectral line profiles of the selected sources should be narrow and strong against a weak continuum source, and free of maser emission. Using these criteria we chose nine sources for our primary candidate list, selecting those sources with the lowest integration times required to reach the target sensitivity.

Table 2.2. Source List

Source	R.A. (B1950) $h\ m\ s$	Dec. (B1950) $^\circ\ '\ ''$	$I(1667)$ (K)	V_{lsr} ($\mathrm{km\,s^{-1}}$)	ΔV ($\mathrm{km\,s^{-1}}$)	T_S (K)	t_{int} (hr)
RCW 38	08 57 14	−47 19 42	−12.0	2.2	5.9	94	14.0
Carina	10 41 14	−59 22 24	−2.2	−25.4	5.8	82	12.5
Cham I	11 09 00	−77 08 00	0.9	4.4	1.0	–	16.4
RCW 57	11 09 50	−61 01 42	−6.1	−25.6	4.6	45	6.8
G326.7+0.6	15 41 01	−53 57 54	−1.4	−44.8	6.5	32	14.5
			−2.7	−21.6	2.0		
			−0.5	−13.3	2.0		
			−0.8	−1.9	2.0		
G327.3–0.5	15 49 06	−54 27 06	−4.1	−49.0	5.4	35	5.8
G343.4–0.0	16 55 43	−42 31 54	−1.9	5.7	0.6	7	8.5
			−0.2	−27.2	4.7		
NGC6334	17 16 55	−35 44 02	−6.9	−3.8	4.9	82	6.5
			−7.6	6.3	1.2		
G8.1+0.2	18 00 00	−21 48 12	−1.0	17.4	3.1	12	4.3

The sources observed for the Zeeman effect are listed in Table 2.2. In this table, column (1) lists the source name, columns (2) & (3) the source position, and columns (4) – (6) list, respectively, the approximate antenna temperature for the 1667 MHz transition of OH, velocity V_{lsr}, and line width ΔV of the major absorption components, as determined by fitting a Gaussian to the line profile. In three sources the line profile is clearly non-Gaussian and so the parameters listed here are illustrative only. In column (7) we give the temperature T_S of the background continuum source where appropriate, assuming a system temperature of 25 K. Column (8) lists the actual on-source integration time.

2.4. Results & Analysis

We first briefly discuss the raw V and I spectra, and provide some background information on each source. Many of these sources have appeared in the large molecular line surveys of southern sources undertaken in the 70's and early 80's (e.g., Whiteoak & Gardner 1974; Gardner & Whiteoak 1978; Whiteoak & Gard-

ner 1978; Bachelor, McCulloch & Whiteoak 1981; Whiteoak, Otrupcek & Rennie 1982; Whiteoak et al. 1985; Peng & Whiteoak 1992), and in the extensive recombination line survey of Caswell & Haynes (1987). Later we describe the Zeeman analysis for each source. In the sections below we use the notation V_{1665} and I_{1665} to denote respectively the V and I spectra for the 1665 MHz transition of OH. Similar notation is used for the 1667 MHz transition.

2.4.1. Individual Sources

Orion B: Though Orion B is used as a test source in this study, we include it in our results since the technique we use on Orion B here, and by CK83, will also be used to analyse some of the other sources in our study.

The I and V spectra from the July 1995 observing session are shown in Fig. 2.8 and the spectra for the October 1996 session are presented in Fig. 2.9. Note that the absolute calibration between the two sessions is different. The V_{1665} spectrum is similar to that of CK83, keeping in mind that their V spectra should be inverted. The V_{1667} spectrum shows a maximum at the same location as the V_{1665} spectrum, but has no clear minimum. The maximum occurs at a similar velocity to the peak absorption of the I spectrum, and so, when attempting to fit the V spectra using eqn. (2.14), the gain term dominates and thus the fit to the Zeeman pattern is poor. It is not clear why we see a well defined Zeeman pattern in the V_{1665} spectrum but not in the V_{1667} spectrum in the July 1995 observations. In the October 1996 observations the characteristic sideways "S" of the Zeeman effect is clearly seen in the V spectra for both lines, with almost identical properties. As discussed in CK83, the Zeeman effect appears to arise from a subcomponent of the overall line profile, a result which seems to be confirmed by recent VLA observations (Crutcher et al. 1998).

RCW 38: RCW 38 is a bright H II region located at a distance of 1.7 kpc. It is discussed at length in Appendix A, where we report on a mid-infrared study of the region. It is the only source other than Orion B observed during both Zeeman observing periods. Fig. 2.10 shows the V and I spectra from the

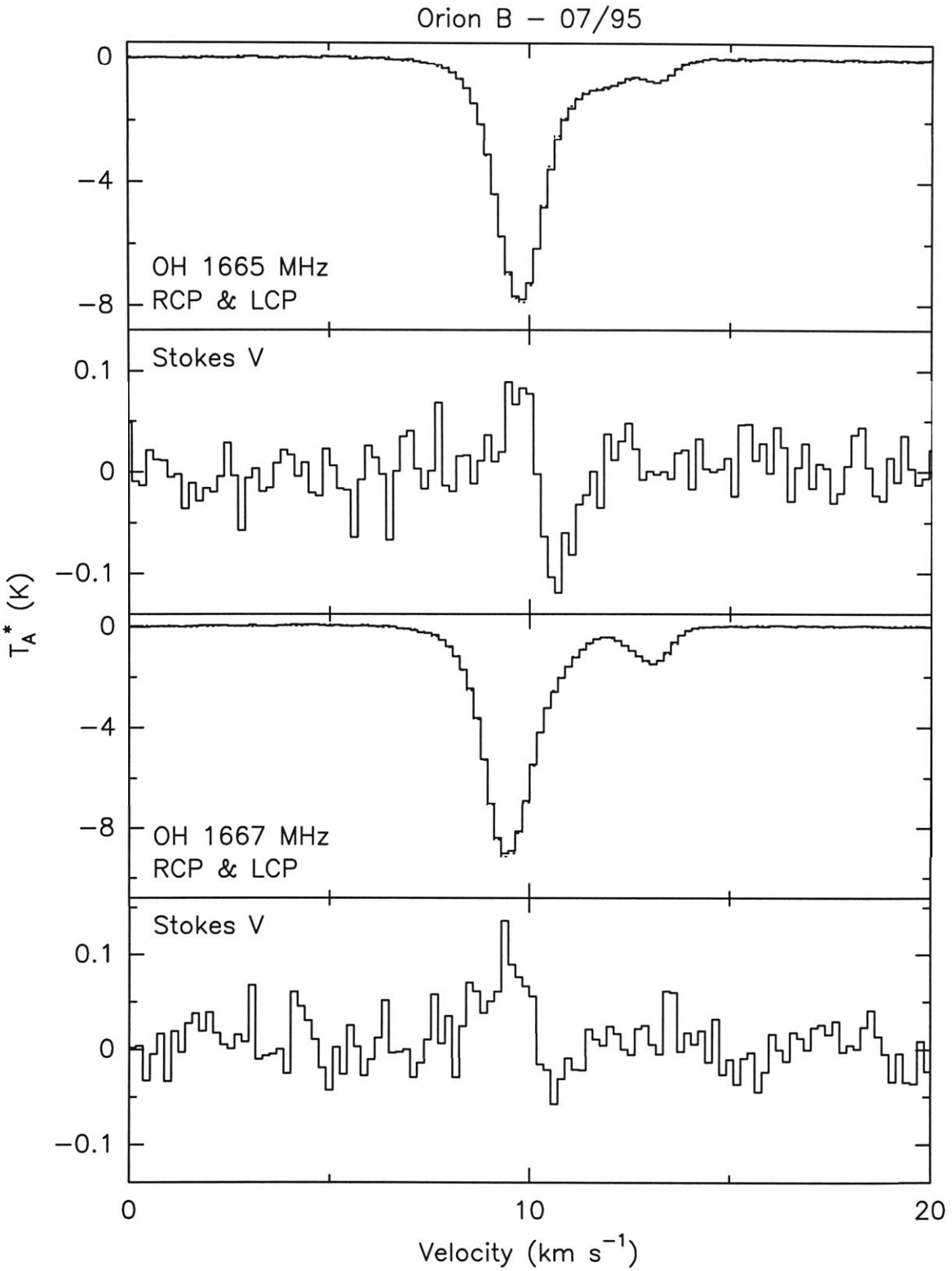

Figure 2.8.— Observed OH RCP (solid), LCP (dotted) and V spectra for Orion B (July 1995). The upper two panels show the results for the OH 1665 MHz transition, while the lower two panels show the results for the OH 1667 MHz transition. Note the barely discernable difference between the RCP and LCP absorption line spectra.

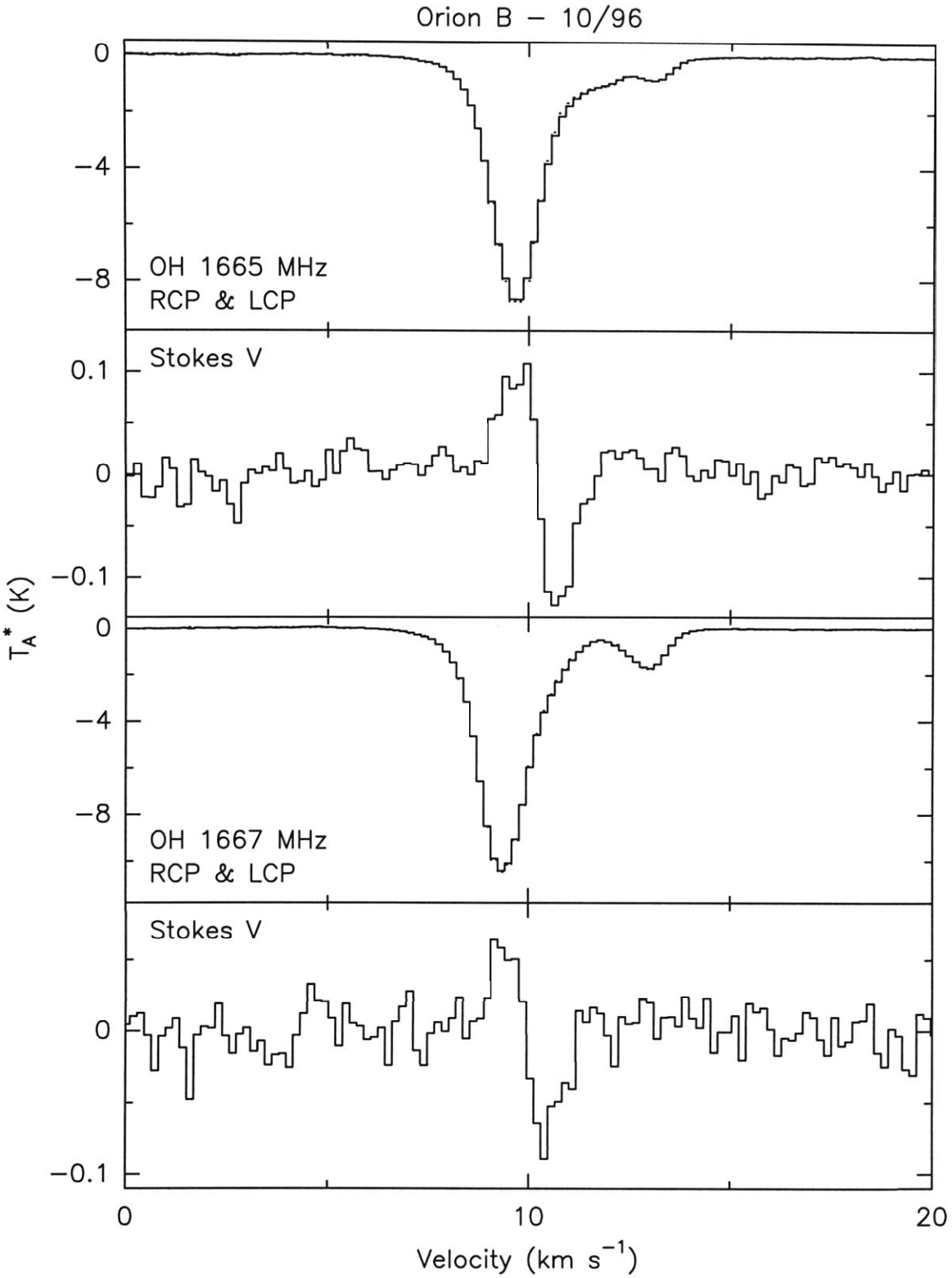

Figure 2.9.— Observed OH RCP (solid), LCP (dotted) and V spectra for Orion B (October 1996). The upper two panels show the results for the OH 1665 MHz transition, while the lower two panels show the results for the OH 1667 MHz transition. Note the barely discernable difference between the RCP and LCP absorption line spectra.

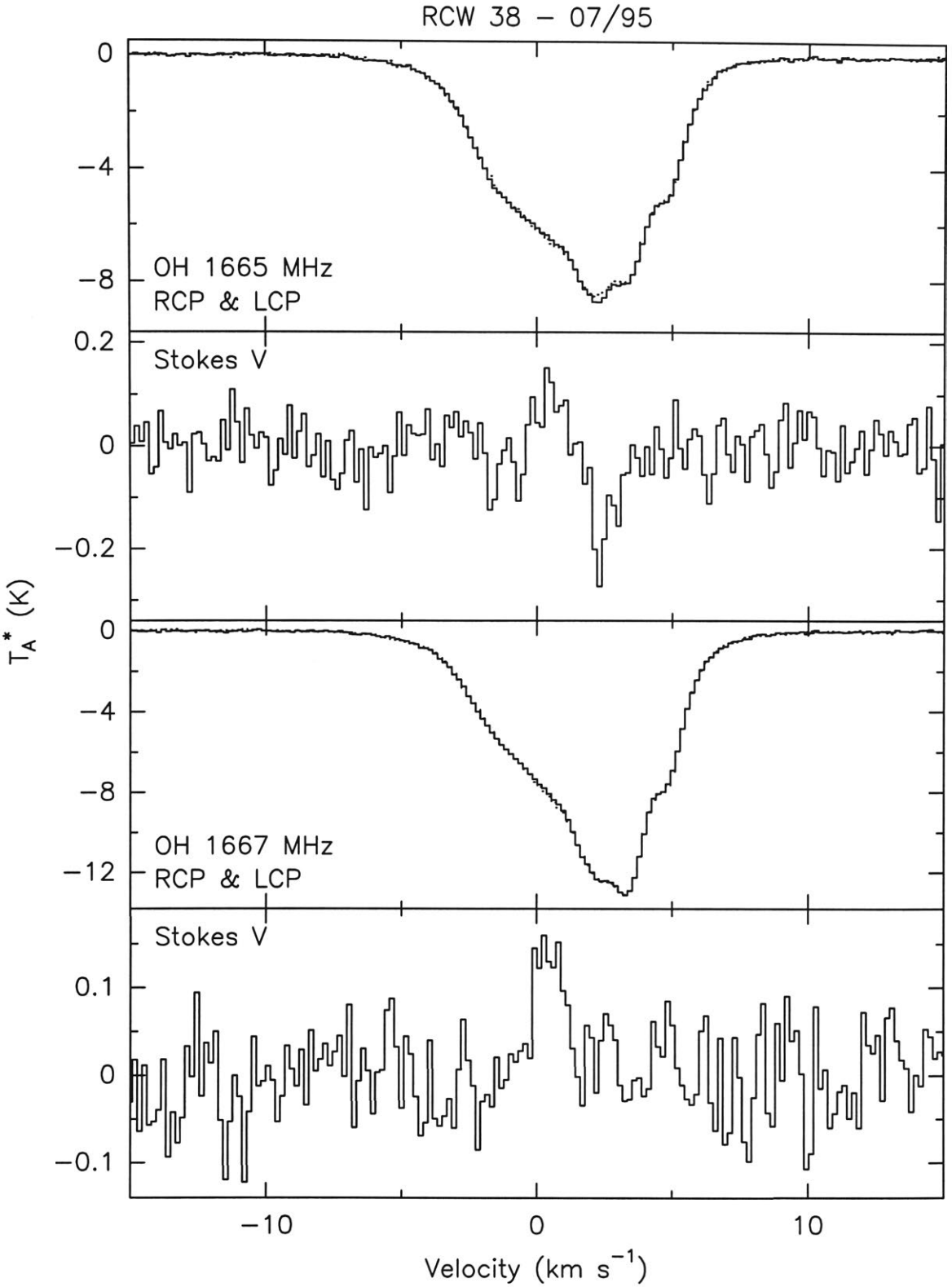

Figure 2.10.— Observed OH RCP (solid), LCP (dotted) and V spectra for RCW 38 (July 1995). The upper two panels show the results for the OH 1665 MHz transition, while the lower two panels show the results for the OH 1667 MHz transition. Note the barely discernable difference between the RCP and LCP absorption line spectra.

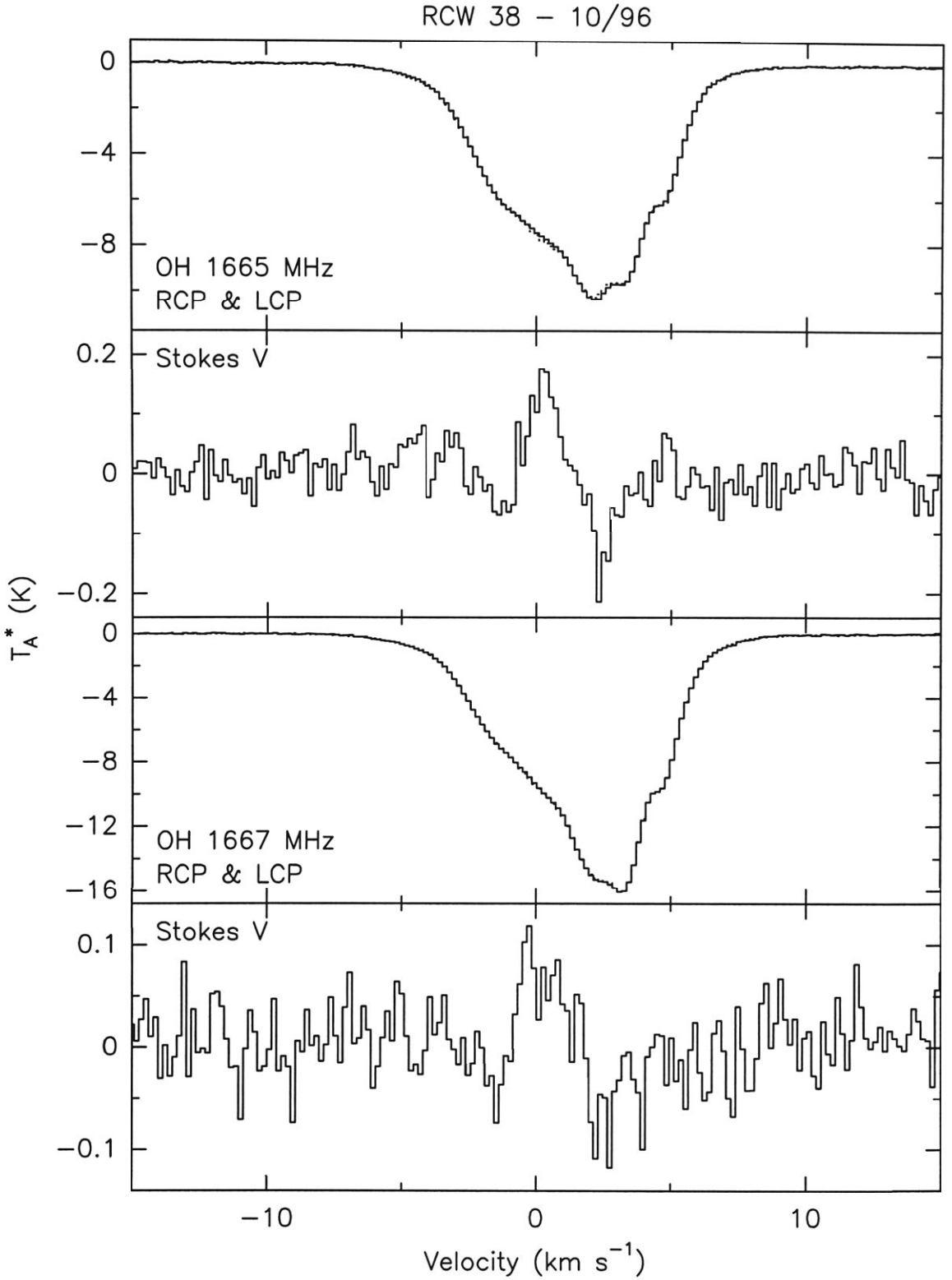

Figure 2.11.— Observed OH RCP (solid), LCP (dotted) and V spectra for RCW 38 (October 1996). The upper two panels show the results for the OH 1665 MHz transition, while the lower two panels show the results for the OH 1667 MHz transition. Note the barely discernable difference between the RCP and LCP absorption line spectra.

July 1995 session. The I profile is clearly non-Gaussian, and is most likely a composition of line profiles arising from individual molecular clumps within the 13′ beam. The V_{1665} profile shows what appears to be a Zeeman pattern, which like Orion B cannot arise from the entire I_{1665} profile. The V_{1667} spectrum is similar to Orion B, in that we see a clear counterpart to the maximum seen in the V_{1665} spectrum, but no minimum, suggesting a common cause for the differences observed in the V_{1665} and V_{1667} spectra for both Orion B and RCW 38 during the observations in July 1995. The spectra obtained during the October 1996 observing period are shown in Fig. 2.11. The V_{1665} spectrum is very similar to that obtained in July 1995. The V_{1667} spectrum now has both a clear maximum and minimum, and the V spectra are similar, suggesting that we have found evidence for the Zeeman effect in at least one component of the molecular gas associated with RCW 38.

Carina Molecular Cloud: The Carina Molecular Cloud has been mapped in OH by Dickel & Wall (1974), who found two peaks in the absorption, closely corresponding to the dark lanes either side of the optical emission associated with Eta Carina. The position we have observed is the western peak. In Fig. 2.12 there is no evidence in either the 1665 or 1667 line for the Zeeman effect. In the 1665 line we see evidence for some interference at the low velocities, but it appears only on the very edge of the line. The line profile is quite simple, and can be well fitted with two Gaussians. Despite the fact that the nebula is the host to the famous star Eta Carina, the associated molecular cloud has not been well studied. CO observations have been undertaken by Graauw et al. 1981, Whiteoak & Otrupcek 1984, and Grabelsky et al. 1988. Megeath et al. 1996 obtained molecular line and infrared continuum images of a region to the east of our Zeeman position and found evidence for ongoing star formation in a bright rimmed globule associated with the molecular cloud. Brooks is currently undertaking a multi-wavelength study of the Carina Molecular Cloud, and preliminary results from this study have been reported (Brooks, Whiteoak & Storey 1998). The distance has been determined by Tapia et al. (1988) to be 2.5 kpc.

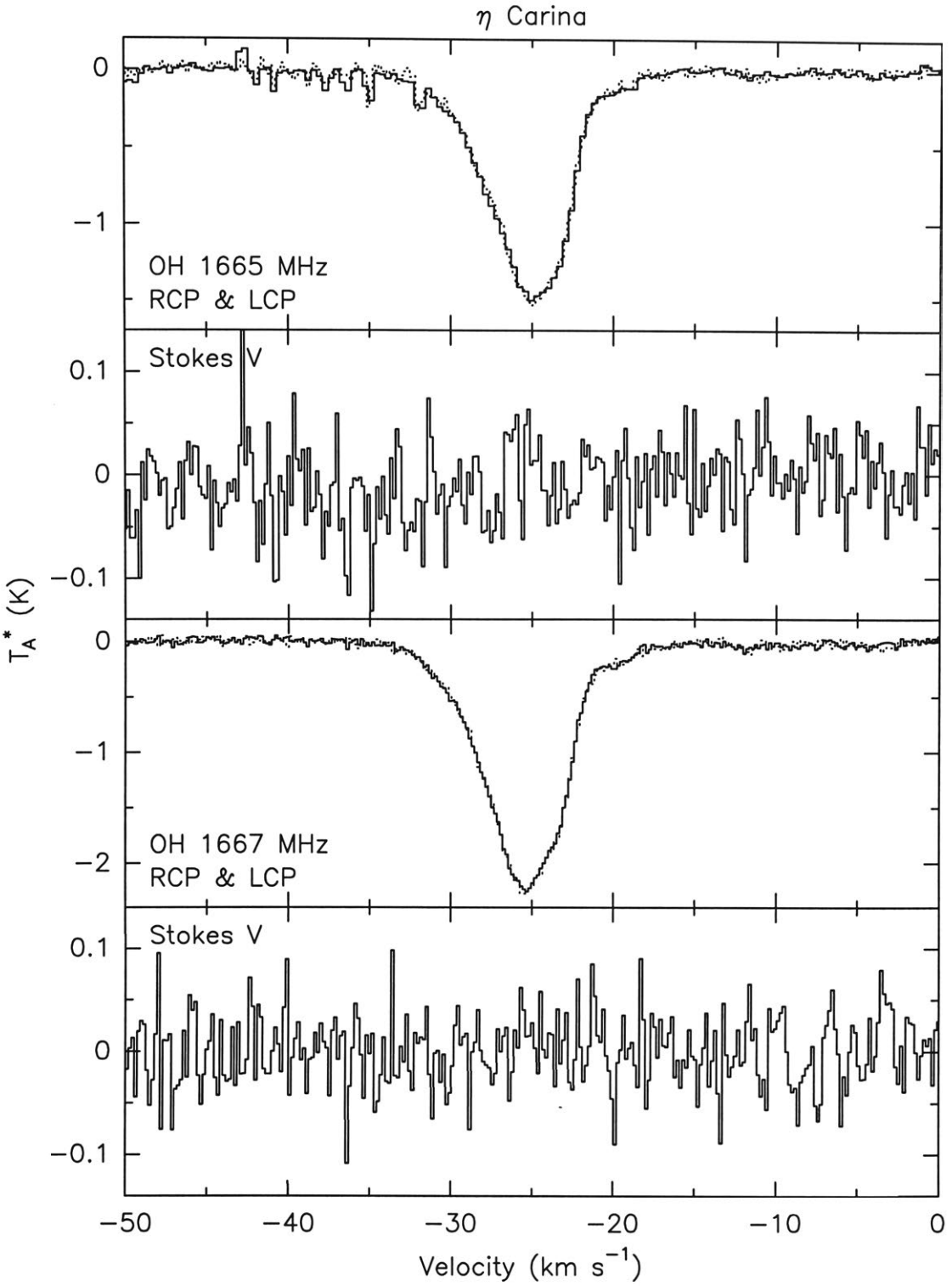

Figure 2.12.— Observed OH RCP (solid), LCP (dotted) and V spectra for the Carina Molecular Cloud. The upper two panels show the results for the OH 1665 MHz transition, while the lower two panels show the results for the OH 1667 MHz transition. Note the barely discernable difference between the RCP and LCP absorption line spectra.

Chamaeleon I: Chamaeleon I is a well studied molecular cloud forming mainly low-mass stars, located at a distance of 160 pc (see e.g., the review by Schwartz 1991). Though it is easier to detect the Zeeman effect in strong absorption lines from molecular clouds associated with H II regions, there is a clear need for more measurements of the magnetic field strength in cold molecular clouds such as Chamaeleon (Crutcher et al. 1993), which is why it has been included in this study. There is evidence for a large scale ordered magnetic field in the region (McGregor et al. 1994), and this together with the bright OH lines (at least for a thermal emission source) makes Chamaeleon I a prime Zeeman candidate among dark clouds. The cloud has been mapped in OH with the Parkes radiotelescope by Toriseva et al. (1985) and the extinction has been determined throughout the entire cloud by Cambresy et al. (1997) using near infrared colours. The V and I spectra are presented in Fig. 2.13, and show no evidence for the Zeeman effect. The line profile is well represented by a single Gaussian.

RCW 57: Located at a distance of 3.6 kpc (kinematic, e.g., Caswell & Haynes 1987) or 2.4 kpc (Persi et al. 1994, based on the possible association of HD 97499 with the molecular cloud), RCW 57 is an H II region with ongoing star formation (e.g., Persi et al. 1994). The few studies of this region that have been published suggest it is a "typical" H II region and with an associated Giant Molecular Cloud (GMC). The OH line profiles are presented in Fig. 2.14, and show deep absorption in the I profiles with a red-shifted "wing". Each OH line is well fitted by two Gaussian components. Two weak RCP masers are evident in the 1665 line, which unfortunately were not seen in our preliminary survey. There is no clear evidence in either V spectrum for the Zeeman effect, though some structure appears in the V_{1667} spectrum, but no corroborating evidence is seen in the V_{1665} spectrum. Whiteoak & Gardner (1974), observed the 5 GHz transition of H_2CO in absorption toward RCW 57 with a $4'.2$ beam, and found two velocity components with almost identical properties to the components we fitted to our OH data, suggesting that at least part of the OH absorption arises in somewhat denser gas (10^4 cm^{-3}) than is usually sampled by OH (10^3 cm^{-3}).

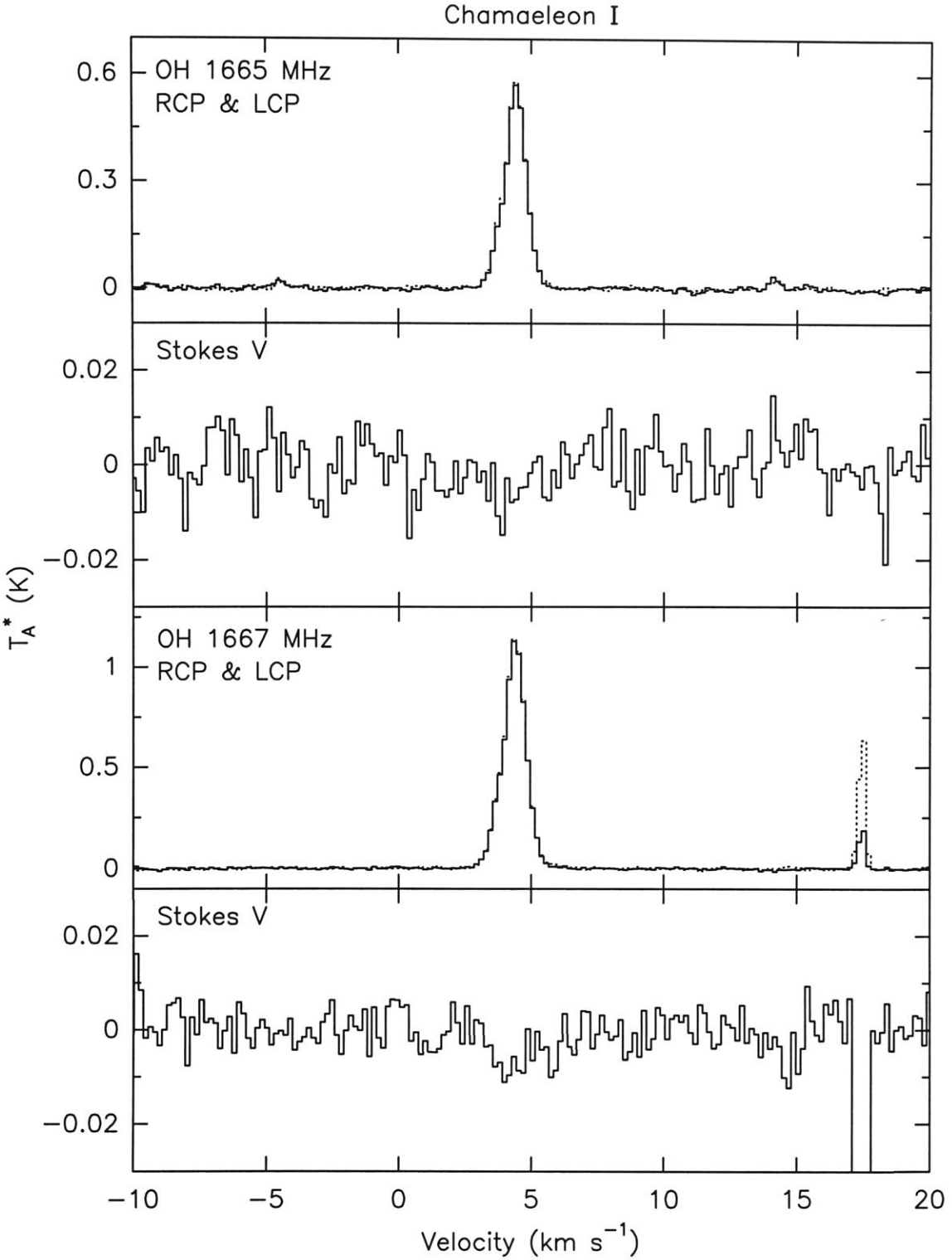

Figure 2.13.— Observed OH RCP (solid), LCP (dotted) and V spectra for Chamaeleon I. The upper two panels show the results for the OH 1665 MHz transition, while the lower two panels show the results for the OH 1667 MHz transition. Note the barely discernable difference between the RCP and LCP emission line spectra.

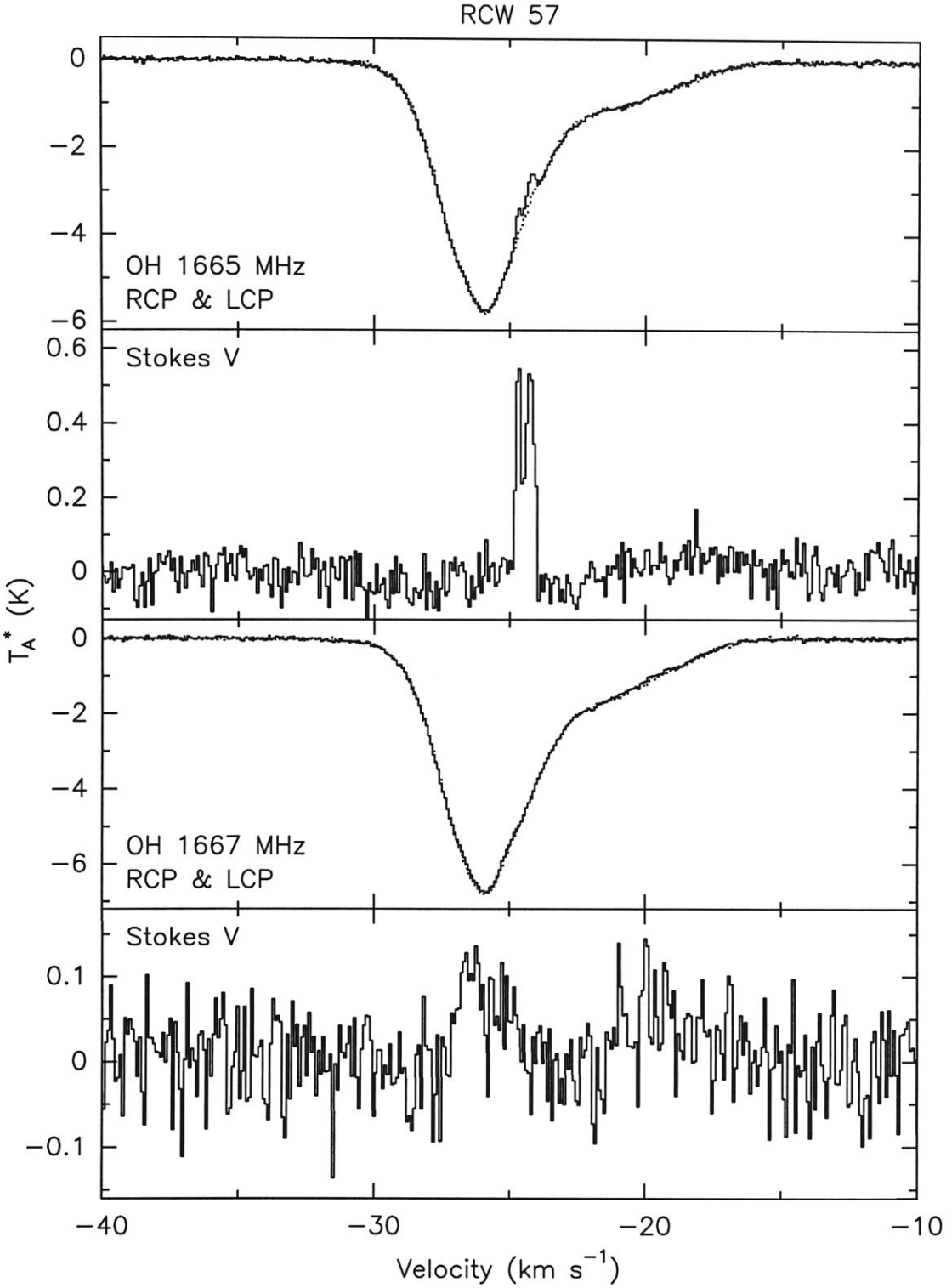

Figure 2.14.— Observed OH RCP (solid), LCP (dotted) and V spectra for RCW 57. The upper two panels show the results for the OH 1665 MHz transition, while the lower two panels show the results for the OH 1667 MHz transition. Note the barely discernable difference between the RCP and LCP absorption line spectra.

G 326.7+0.6: Very little is known about this H II region. It is probably associated with the optical H II region RCW 95. Fig. 2.15 shows that four main absorption components are seen along the line of sight to the thermal continuum source, whose recombination line velocity is near -44 km s^{-1} (Caswell & Haynes 1987). The kinematic distances for the three lowest velocity clouds at $V_{lsr} = -44$, -22, and -13 km s^{-1} are estimated to be 3.0, 1.5 and 1.0 kpc, respectively. The -2 km s^{-1} velocity component is at the solar galactocentric distance and is probably very local. Using the method of Schwartz, Gee & Huang (1988) we estimate the distance of the -2 km s^{-1} component to be $\sim$ 150 pc. The V profiles presented in Fig. 2.15 show no evidence for the Zeeman effect for any component. The 1665 MHz profile of the -44 km s^{-1} component is badly affected by interference.

G 327.3–0.5: Possibly associated with RCW 97 at a kinematic distance of $\sim$ 3.3 kpc, the only detailed study of the molecular gas associated with G 327.3–0.5 has been reported by Brand et al. (1984) who mapped the cloud in the ^{12}CO $J = 2 \rightarrow 1$ transition, and found a massive ($\sim 10^4$ $M_\odot$) cloud associated with a number of infrared sources (Frogel & Persson 1974), and a possible bipolar molecular outflow associated with the southern-most group of infrared sources. The OH profiles presented in Fig 2.16 show single deep absorption lines near -50 km s^{-1}, and a red "wing" extending to > -40 km s^{-1}. Circularly polarized masers are present in both OH lines, and unfortunately extend well into the blue side of the main OH absorption line. The Zeeman effect is clearly seen in three of the masers present in the 1667 line. However, since the properties of the molecular gas associated with masers is poorly understood we simply state that the magnetic field strengths we infer from the observed splitting (Reid & Silverstein 1990) are +1.3, +2.9, and +7 mG, for the -80, -68 and -52 km s^{-1} components, respectively, though the identification of the Zeeman pair for the -52 km s^{-1} component is not certain.

G 343.4–0.0: Another southern H II region which has not been studied, G 343.4–0.0 is not clearly associated with any RCW region. We somewhat arbitrarily assign the near kinematic distance of 2.8 kpc to this region. Unlike the

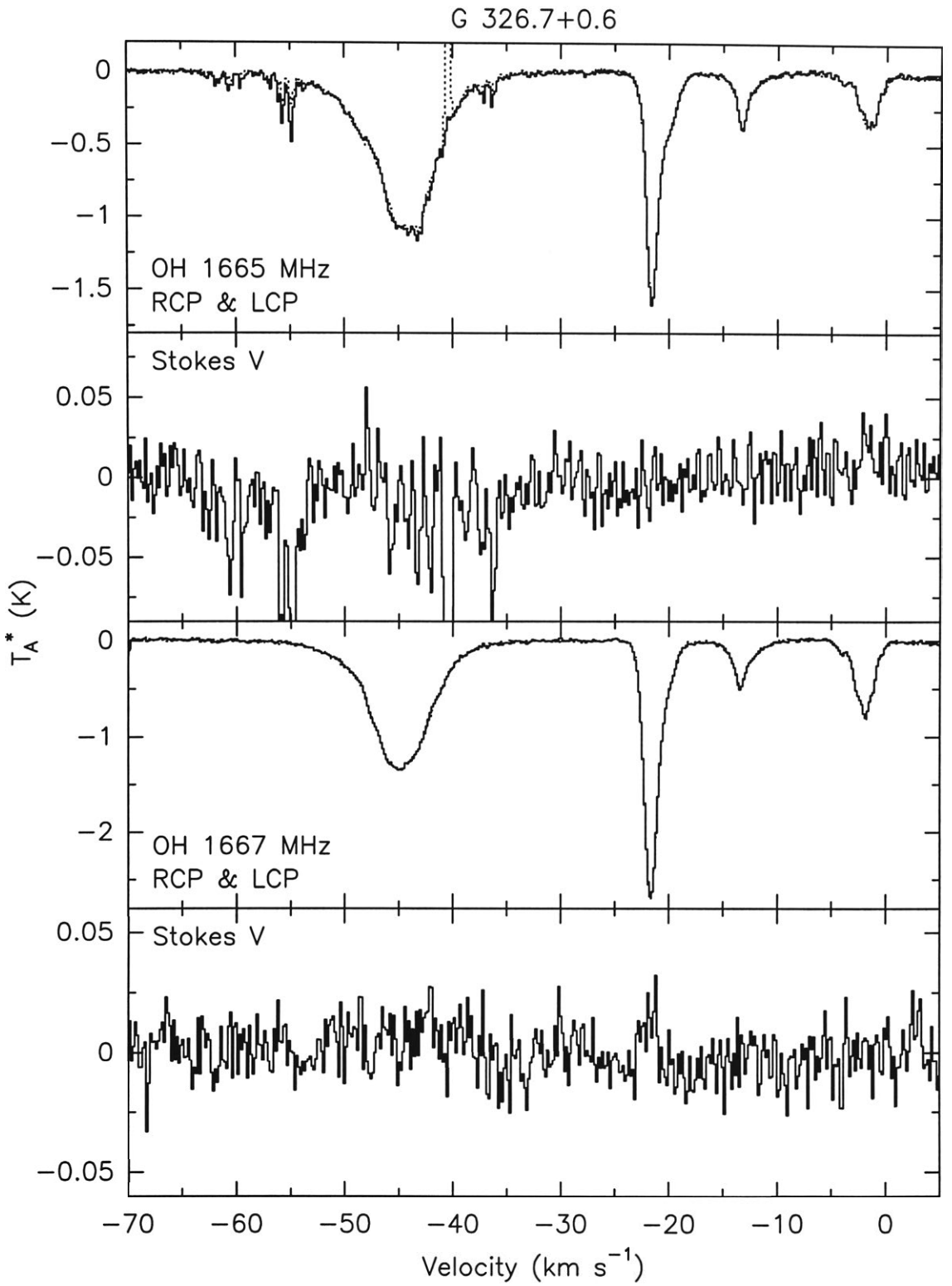

Figure 2.15.— Observed OH RCP (solid), LCP (dotted) and V spectra for G 326.7+0.6. The upper two panels show the results for the OH 1665 MHz transition, while the lower two panels show the results for the OH 1667 MHz transition. Note the barely discernable difference between the RCP and LCP absorption line spectra.

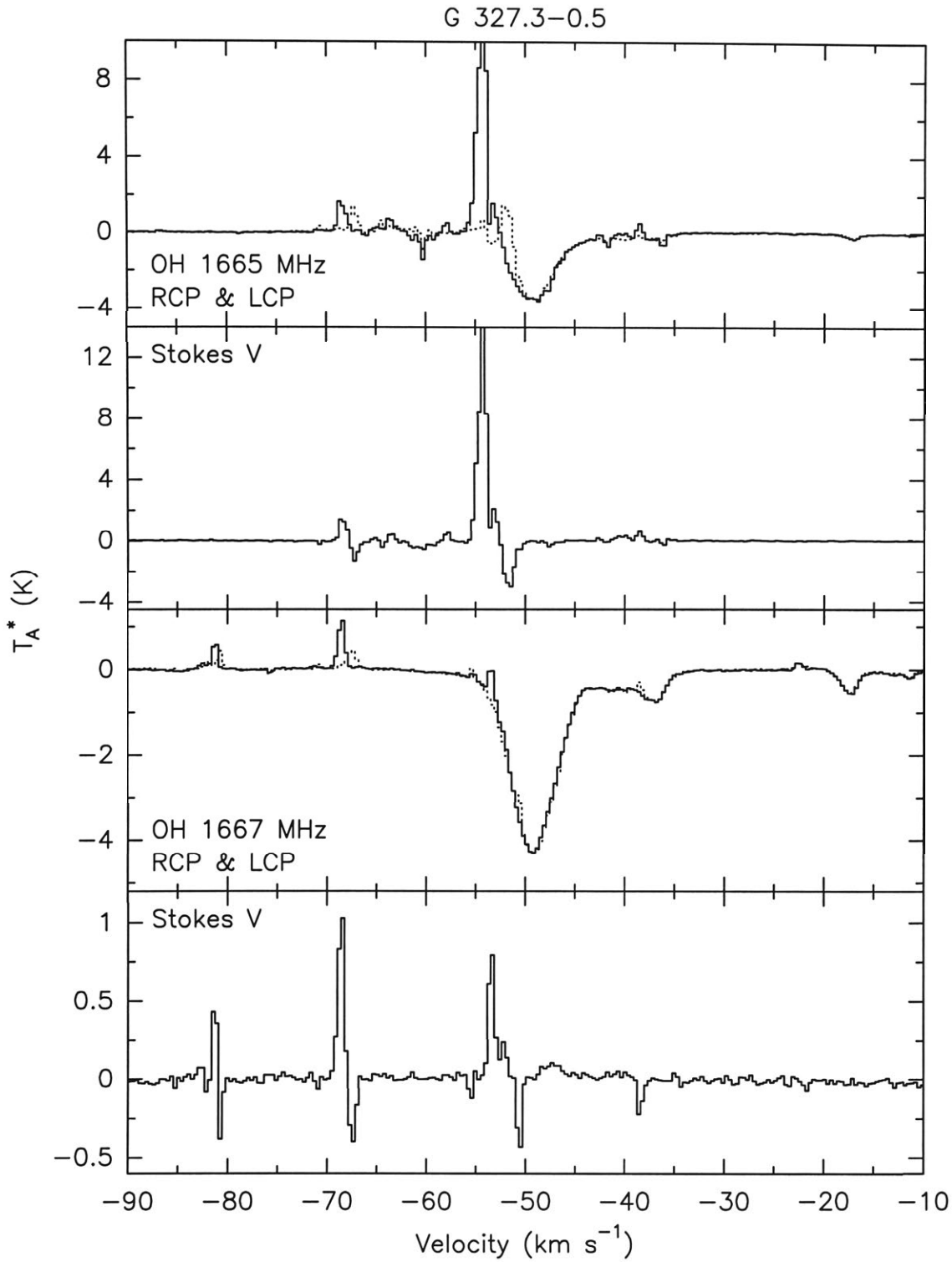

Figure 2.16.— Observed OH RCP (solid), LCP (dotted) and V spectra for G 327.3–0.5. The upper two panels show the results for the OH 1665 MHz transition, while the lower two panels show the results for the OH 1667 MHz transition. Note the barely discernable difference between the RCP and LCP absorption line spectra.

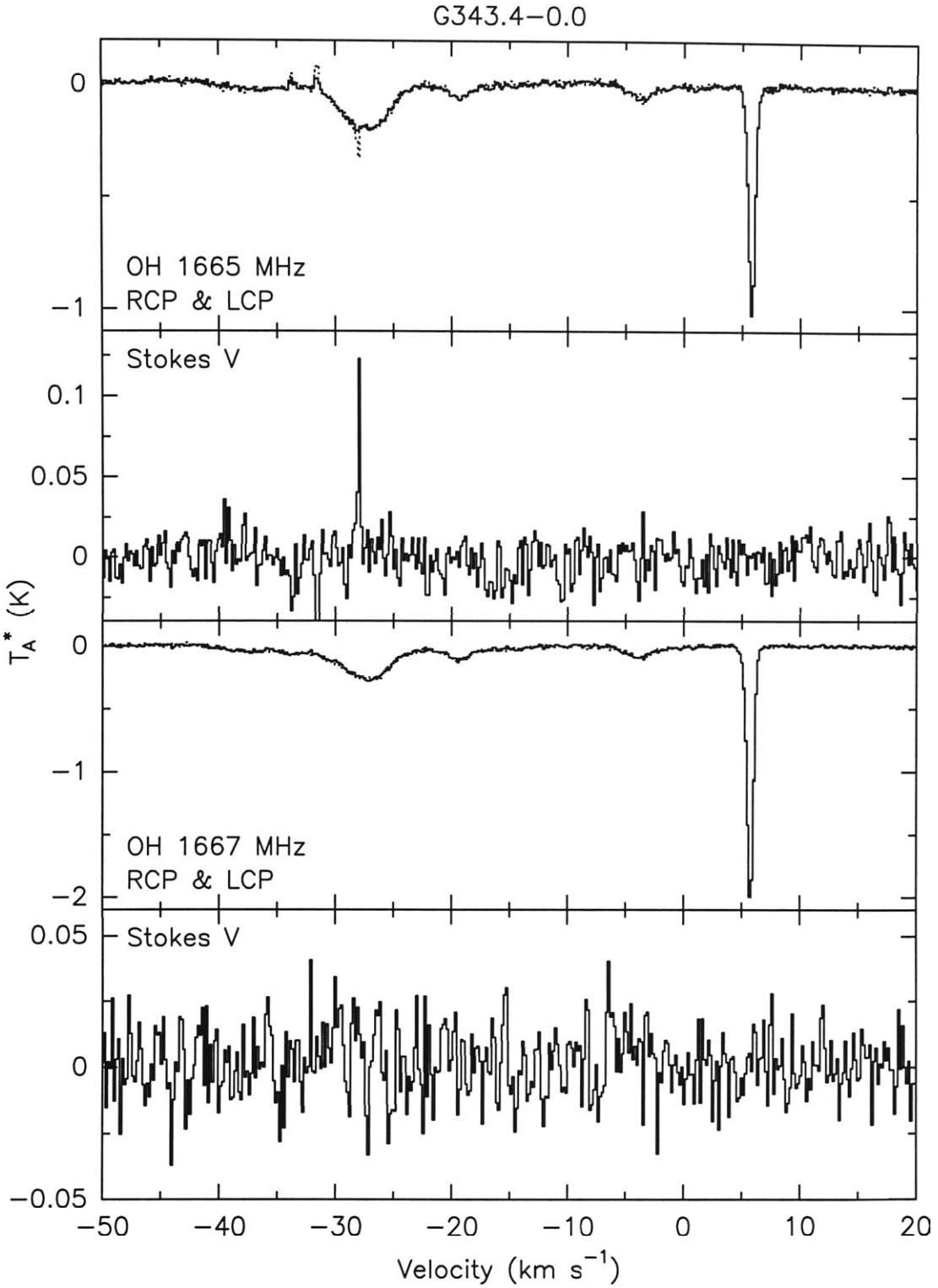

Figure 2.17.— Observed OH RCP (solid), LCP (dotted) and V spectra for G 343.4–0.0. The upper two panels show the results for the OH 1665 MHz transition, while the lower two panels show the results for the OH 1667 MHz transition. Note the barely discernable difference between the RCP and LCP absorption line spectra.

sources discussed above, G 343.4–0.0 has not even been included in many of the major molecular line surveys and maser surveys of the southern galactic plane. Whiteoak & Gardner (1974) observed the 6 $\mathrm{km\,s^{-1}}$ component in formaldehyde absorption, and OH absorption observations were reported in the extensive OH survey by Turner (1979). The Stokes I and V spectra are presented in Fig. 2.17. The two main absorption features are at -27 $\mathrm{km\,s^{-1}}$ (near the recombination line velocity) and the narrow, deep lines near 6 $\mathrm{km\,s^{-1}}$. Other weak absorption lines are seen, but their depth is less than 10 times the rms noise in the I spectra, so they are not considered in the Zeeman analysis below. There is no obvious indication in either V spectra for the Zeeman effect. The 6 $\mathrm{km\,s^{-1}}$ cloud is clearly local, and may be associated with the Lupus clouds, which have a similar velocity and lie about 10° above the plane at a similar galactic longitude. It may also be associated with the 6 $\mathrm{km\,s^{-1}}$ component seen toward NGC 6334 and NGC 6357 (W22; Kazés & Crutcher 1986; Crutcher et al. 1987; Massi, Brand & Felli 1997) near longitude 351°. Kazés & Crutcher (1986) detected the Zeeman effect in the 6 $\mathrm{km\,s^{-1}}$ component toward NGC 6357 (W22B) with a magnetic field strength of -18 ± 1 μG, while Crutcher et al. (1987) claim a detection at a nearby position (W22A) with a field strength of -32 ± 9 μG. The large scale CO maps made with the Columbia 1.2 m radiotelescope (e.g., Bronfman et al. 1989; Bitran et al. 1997), suggest an association between all the clouds near 6 $\mathrm{km\,s^{-1}}$.

NGC 6334: NGC 6334 is a well studied H II region located at 1.7 kpc (Neckel 1978). Visually it is very prominent, with numerous nebulous spots, and forms a fine pairing with the nearby NGC 6357 (W22). Important studies include the CO observations of Dickel, Dickel & Wilson (1977), the OH observations by Brooks (1995) and the recent PhD thesis by Kramer (1998), who studied [O I], [C II], and CO, CS and ammonia throughout the star-forming molecular "ridge". Fig. 2.18 shows all the features seen in the I spectrum, including the masers and absorption features. The strong masers are potentially harmful to our Zeeman observations, but since they occur only on one side of the deep absorption line at -3 $\mathrm{km\,s^{-1}}$ it is still possible to extract useful information from the absorption

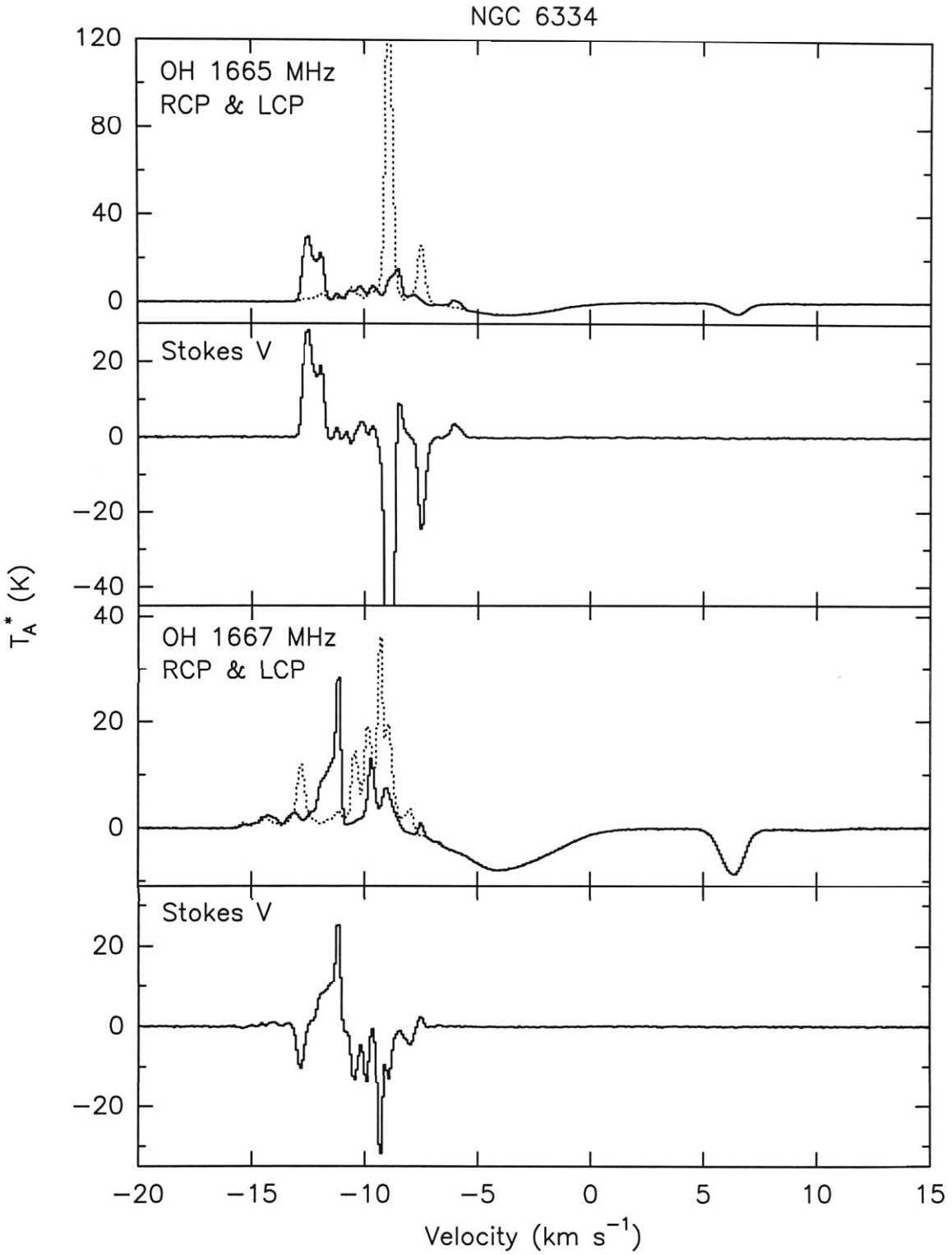

Figure 2.18.— Observed OH RCP (solid), LCP (dotted) and V spectra for NGC 6334. The upper two panels show the results for the OH 1665 MHz transition, while the lower two panels show the results for the OH 1667 MHz transition. Note the barely discernable difference between the RCP and LCP absorption line spectra.

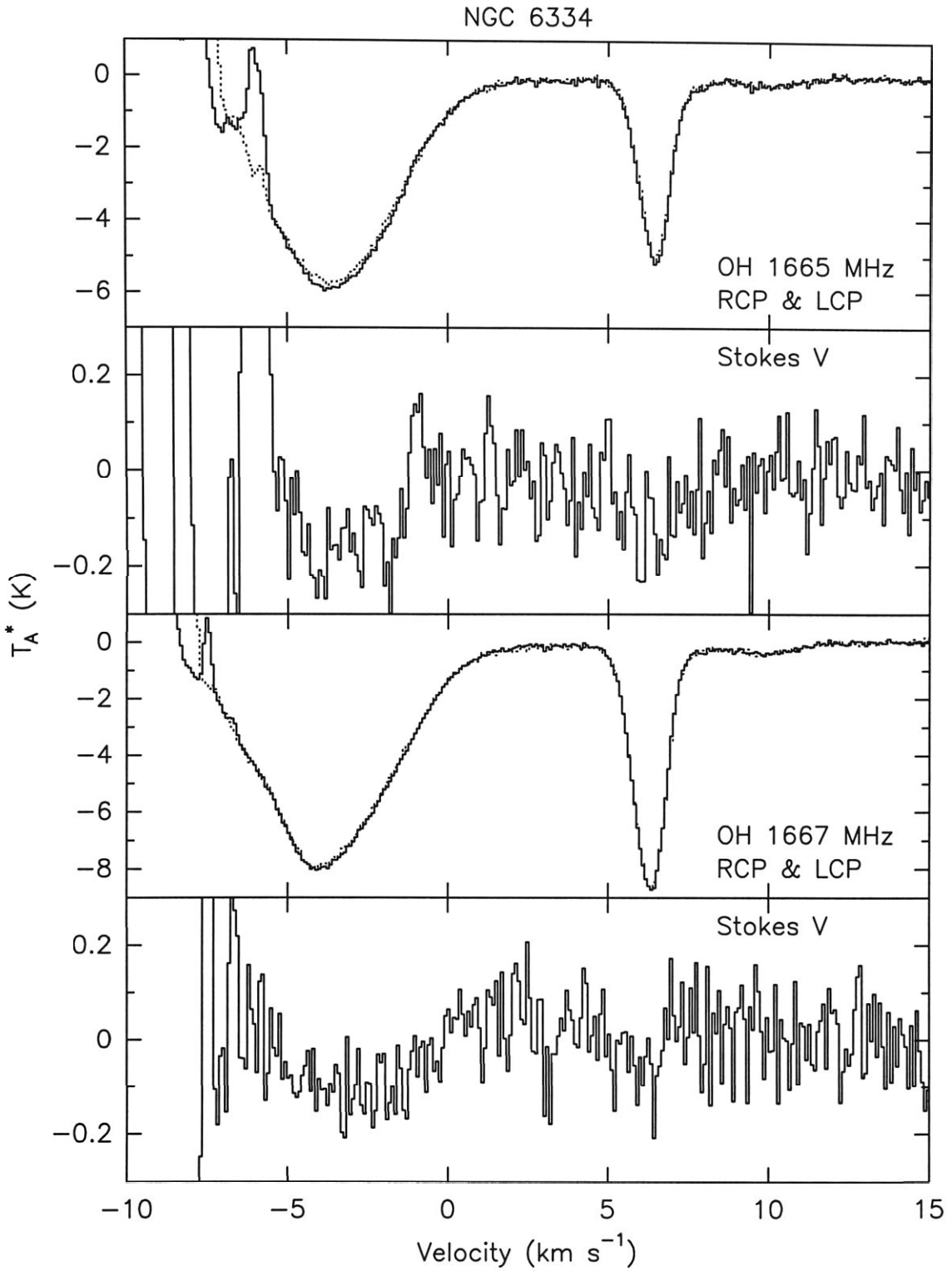

Figure 2.19.— Observed OH RCP (solid), LCP (dotted) and V spectra for the absorption components toward NGC 6334. The upper two panels show the results for the OH 1665 MHz transition, while the lower two panels show the results for the OH 1667 MHz transition. Note the barely discernable difference between the RCP and LCP absorption line spectra.

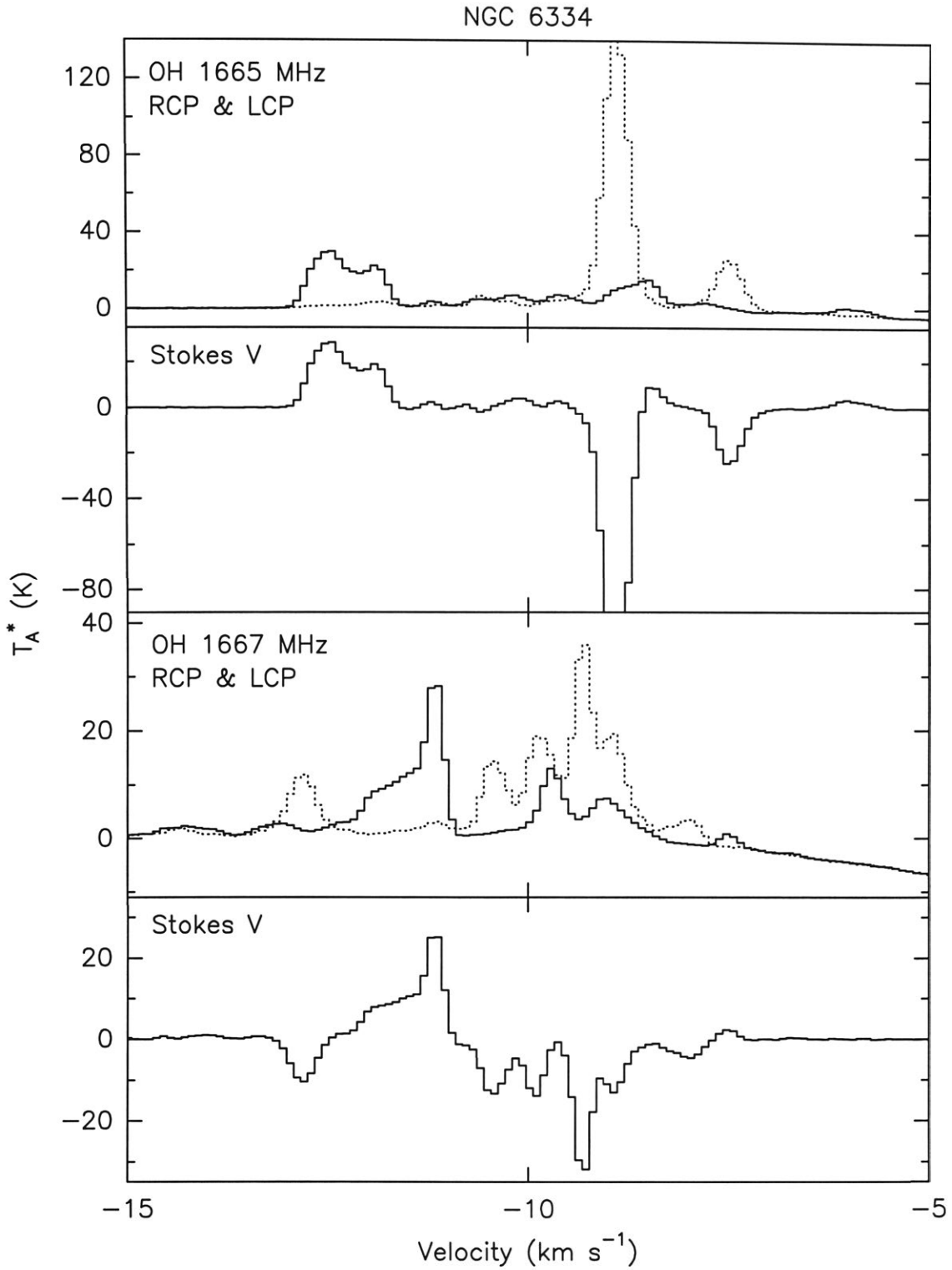

Figure 2.20.— Observed OH RCP (solid), LCP (dotted) and V spectra for the maser components toward NGC 6334. The upper two panels show the results for the OH 1665 MHz transition, while the lower two panels show the results for the OH 1667 MHz transition.

line. The absorption lines are highlighted in Fig. 2.19, which shows the feature associated directly with the H II region at -3 km s^{-1}, and the unassociated foreground cloud at 6 km s^{-1}. There is no clear evidence in the V spectra for the Zeeman effect, but some structure is present that may be due to instrumental gain differences. As discussed above for G 343.4–0.0, the 6 km s^{-1} component is local and covers a large area, but has not been studied in any detail and its distance and properties are not well known. Troland and co-workers (Troland 1995, private communication) have searched for the Zeeman effect toward NGC 6334 with the Nançay telescope and report a 3σ upper limit for the 6 km s^{-1} component of ~ 20 μG. For the -3 km s^{-1} component their observations taken during different observing periods give conflicting results, due to problems caused by the masers. In Fig. 2.20 we present an expanded view of the masers.

G 8.1+0.2: The recombination line velocity for the G 8.1+0.2 H II region is ~ 20 km s^{-1}, which implies a kinematic distance of ~ 3.5 kpc. The spectra presented in Fig. 2.21 show two velocity components near 13 and 17 km s^{-1} respectively, and a circularly polarized maser pair near 22 km s^{-1}. No obvious Zeeman effect is seen in the V spectra for the absorption lines, though it is clearly seen in the maser lines, from which we can infer a magnetic field strength in the masering region of $\sim +3$ mG. No detailed study of this H II region has been reported.

2.4.2. Fitting $dI/d\nu$ to V

In Table 2.3 we present the results of our attempts to fit the derivative of the whole I spectrum to the V spectrum for the separate velocity features in each source, excluding any masers from the fit (see `zfit.class`, Appendix B). In this Table column (1) lists the source name, column (2) the velocity of the OH feature, column (3) the magnetic field strength determined from the 1665 MHz OH transition with its one sigma uncertainty, column (4) as for column (3) but for the 1667 MHz OH transition, and column (5) the weighted mean field strength B_w (found by combining the results for the 1665 & 1667 lines) and its

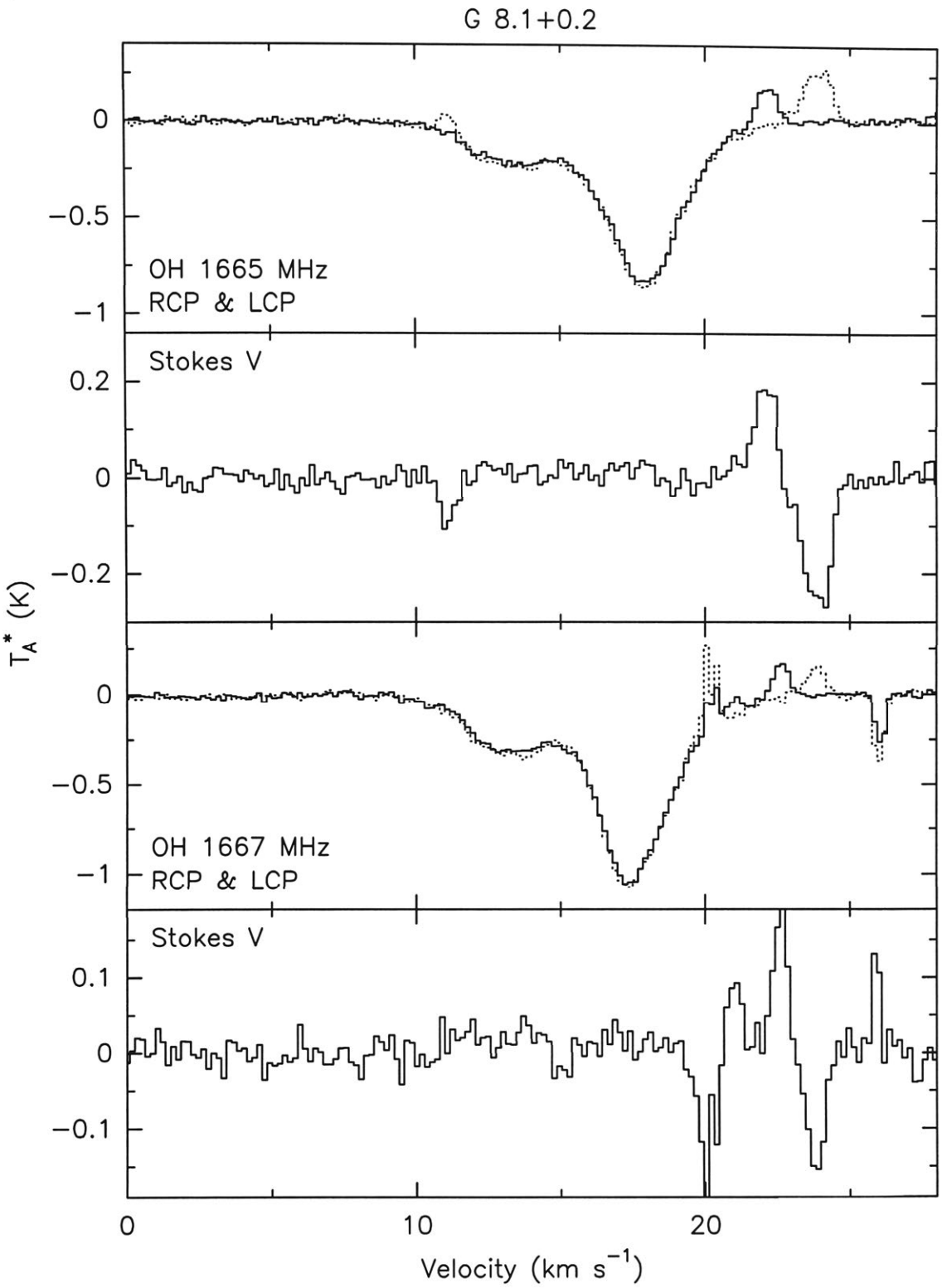

Figure 2.21.— Observed OH RCP (solid), LCP (dotted) and V spectra for G 8.1+0.2. The upper two panels show the results for the OH 1665 MHz transition, while the lower two panels show the results for the OH 1667 MHz transition. Note the barely discernable difference between the RCP and LCP absorption line spectra.

weighted one sigma uncertainty σ_w. The results in this Table suggest that we have detected the Zeeman effect in RCW 38, RCW 57, and G 8.1+0.2 at greater than the 3σ level. However, as discussed below, better fits are found for RCW 38 and RCW 57 by inferring that the Zeeman effect arises from a subcomponent of the line, while for G 8.1+0.2 an inspection of the V spectrum and the fit (Figs. 2.21 and 2.37(b), see below) suggest that it is not a real detection.

Table 2.3. Results from Fitting Entire Line Profile to V

Source	V_{lsr}	B_{los} (μG)		
	(km s^{-1})	1665 MHz	1667 MHz	$B_w \pm \sigma_w$
RCW 38	2.2	14 ± 5	14 ± 4	14 ± 3
Carina	−25.4	3 ± 22	-25 ± 27	-8 ± 17
Cham I	4.4	4 ± 5	4 ± 5	4 ± 4
RCW 57	−25.6	-15 ± 5	-12 ± 8	-14 ± 4
G326.7+0.6	−44.8	i[a]	-31 ± 23	—
	−21.6	-10 ± 7	5 ± 6	-1 ± 5
	−13.3	-5 ± 33	-18 ± 33	-12 ± 23
	−1.9	7 ± 34	-9 ± 21	-5 ± 18
G327.3–0.5	−49.0	m[a]	-60 ± 15	—
G343.4–0.0	−27.2	24 ± 37	110 ± 66	45 ± 32
	5.7	-1 ± 5	-5 ± 4	-3 ± 3
NGC 6334	−3.8	36 ± 9	14 ± 8	24 ± 6
	6.3	-2 ± 6	-11 ± 6	-7 ± 4
G8.1+0.2	17.4	57 ± 22	41 ± 26	50 ± 17

[a]Masers (m) or interference (i) preclude a meaningful fit.

2.4.3. Gaussianizing

As indicated above, not all profiles can be well represented by a single Gaussian profile, suggesting that in those cases the I profile may consist of a blend of Gaussian components at the observed position. In this case the V spectrum may be modelled as the sum of the derivatives of these Gaussians, with unique values of B_{los} assigned to each component (a technique known as "Gaussianizing" – see Heiles 1988; Goodman & Heiles 1994).

In Orion B, CK83 proposed that the observed Zeeman pattern in the V spectra might arise from a Gaussian subcomponent of the I spectra. By integrating the V spectra they were able to derive the line centre velocity and line FWHM of this component for each OH transition (hereafter we refer to this as the $V \rightarrow I$ method). They determined essentially the same line centre velocity and FWHM for this component from the V_{1665} and V_{1667} spectra, and were able to determine consistent values of the magnetic field strength from the two V spectra. Heiles (1988) and Goodman & Heiles (1994) observed the Zeeman effect in Galactic H I in emission, resulting in non-Gaussian line profiles and very complicated V spectra. They assumed that their I profiles were a blend of overlapping Gaussian components, and performed a least squares fit of multiple Gaussian components to their I spectra at each observed position. They assumed nothing *a priori* about the nature of the components making up the I spectra. To determine the magnetic field strengths they simultaneously fitted the derivatives of all the Gaussian subcomponents of their I spectra to the observed V spectra (hereafter the $I \rightarrow V$ method), obtaining meaningful results for a number of components.

For almost all the sources observed in the present study the $I \rightarrow V$ approach has been used to identify subcomponents of the I profiles. In RCW 38 (Fig 2.11) there is evidence for the Zeeman "S" in the V spectra, and for this source the $V \rightarrow I$ method is used. The results are given in Table 2.4. In this Table column (1) lists the source name, column (2) the line intensity of the Gaussian subcomponent for the 1667 MHz line, columns (3) and (4) list the line centre velocity V_{lsr} and line FWHM ΔV of the Gaussian subcomponent respectively,

column (5) lists the magnetic field strength and one sigma uncertainty derived for the subcomponent of the 1665 MHz OH line, column (6) is the same as column (5) but for the 1667 MHz OH line, and column (7) lists the weighted mean field strength B_G for the Gaussian component and its weighted one sigma uncertainty σ_G. In Table 2.4 we have attempted to identify whether the magnetic field determined from the Gaussian fitting is a detection or an upper limit. For a detection we require $\mid B_G \mid > 3\sigma_G$ and $\mid B_{1665} - B_{1667} \mid < \sigma_G$, where B_G is the weighted mean field strength determined from the 1665 and 1667 MHz lines.

Table 2.4. Magnetic Field Stengths for Gaussian Components

Source	Gaussian parameters			B_{los}		
	$I(1667)$ (K)	V_{lsr} (km s^{-1})	ΔV (km s^{-1})	B_{1665} (μG)	B_{1667} (μG)	$B_G \pm \sigma_G$[a] (μG)
Test Source						
Orion B	−7.0	10.0	1.2	26 ± 2	21 ± 2	24 ± 2
Detection[b]						
RCW 38	−8.9	1.4	2.3	38 ± 3	37 ± 5	38 ± 3
RCW 57	−1.8	−22.6	6.5	−199 ± 33	−209 ± 38	−203 ± 25
Upper Limits						
Cham I	1.1	4.4	1.0	8 ± 5	5 ± 4	6 ± 3
G 343.4–0.0	−2.0	5.7	0.7	−1 ± 5	−4 ± 4	3 ± 3
RCW 57	−5.8	−26.1	3.4	−17 ± 5	−2 ± 9	−13 ± 4
NGC 6334	−8.6	6.3	1.2	−2 ± 6	−10 ± 6	−6 ± 4
G 326.7+0.6	−2.1	−21.6	1.7	−15 ± 8	−8 ± 6	−11 ± 5
NGC 6334	−7.8	−3.8	4.9	−19 ± 15	13 ± 17	−5 ± 11
G 8.1+0.2	−1.1	17.5	3.0	60 ± 29	18 ± 25	45 ± 15
G 326.7+0.6	−0.8	−20.8	2.5	31 ± 29	92 ± 23	68 ± 18
G 326.7+0.6	−0.7	−1.9	2.0	−22 ± 40	3 ± 24	−4 ± 21
G 326.7+0.6	−1.3	−44.8	6.5	—	−31 ± 23	(−31 ± 23)[c]
G 326.7+0.6	−0.4	−13.3	2.0	−2 ± 38	−47 ± 39	−24 ± 27
Carina	−1.2	−24.9	4.0	151 ± 42	31 ± 42	91 ± 30
G 327.3–0.5	−4.3	−49.0	5.4	83 ± 99	−185 ± 38	−150 ± 35
Carina	−1.2	−26.2	6.8	−273 ± 65	−116 ± 54	−180 ± 42
G 343.4–0.0	−0.3	−27.4	4.7	−44 ± 61	234 ± 93	40 ± 51
G 8.1+0.2	−0.4	13.3	3.3	73 ± 70	83 ± 75	78 ± 51

[a] B_G is the weighted mean field strength for the Gaussian component, and σ_G is the weighted uncertainty in B_G

[b] Requires $\mid B_G \mid > 3\sigma_G$ *and* $\mid B_{1665} - B_{1667} \mid < \sigma_G$

[c] Because the field strength could not be derived for the 1665 MHz line, the value quoted for B_G is actually B_{1667}

Table 2.4 indicates that we have definitely detected the Zeeman effect in

RCW 38, and possibly in RCW 57. In addition, we have 16 upper limit detections. For RCW 38 we used the $V \rightarrow I$ to determine the Gaussian subcomponents, while for all other sources we used the $I \rightarrow V$ method. The mean field strength we determine for RCW 38 is 38 $\pm$ 3 μG. The RCW 57 profile is well fitted by two overlapping Gaussians, a "main" component ($V_{lsr} = -26.1$ km s^{-1}) and a "wing" component ($V_{lsr} = -22.6$ km s^{-1}), which could represent either two cloud components associated with RCW 57, or one cloud and an outflow wing, analogous to what is seen in the H II region S106 (Roberts, Crutcher & Troland 1995). The ^{13}CO $J = 1 \rightarrow 0$ mapping results presented for RCW 57 in Appendix 2A suggests that the "wing" component is a separate molecular cloud associated with RCW 57. The Zeeman detection listed in Table 2.4 of -203 $\pm$ 25 μG is for the component at $V_{lsr} = -22.6$ km s^{-1}. The H_2CO absorption profile for RCW 57 obtained by Whiteoak & Gardner (1974) can be fitted by two Gaussian components with similar line centre velocities and line widths.

The fitting of eqn. (2.14) to the V spectra of each source is discussed below, and the fits are presented in Figs. 2.22 to 2.37.

Orion B: In Fig. 2.22 we present the fits to the July 1995 data for Orion B. Panel (a) shows the Stokes I spectra, with the Gaussian subcomponent responsible for the Zeeman "S" in the V spectra shown as the dashed line. Panel (b) shows the fit of the derivative of the whole I spectrum to the V spectrum for each OH transition. The fit is poor for both OH lines. Panel (c) shows the fit of the derivatives of the Gaussian subcomponents shown in panel (a) to the gain-corrected V spectra. The parameters of the Gaussians have been estimated by integrating the V_{1665} spectrum, and the same Gaussian parameters are used for the 1667 line. While this method allows us to determine V_{lsr} and ΔV for the Gaussian, we do not know its line intensity for either line, so following CK83 we allow the line intensity to be the maximum possible which is consistent with the real I spectra. The value of B_{los} inferred by fitting the derivative of this Gaussian is thus a lower limit. In panel (d) we plot the residual of the fit shown in panel (c).

Fig. 2.23 is similar to Fig. 2.22 but for the October 1996 data. In the

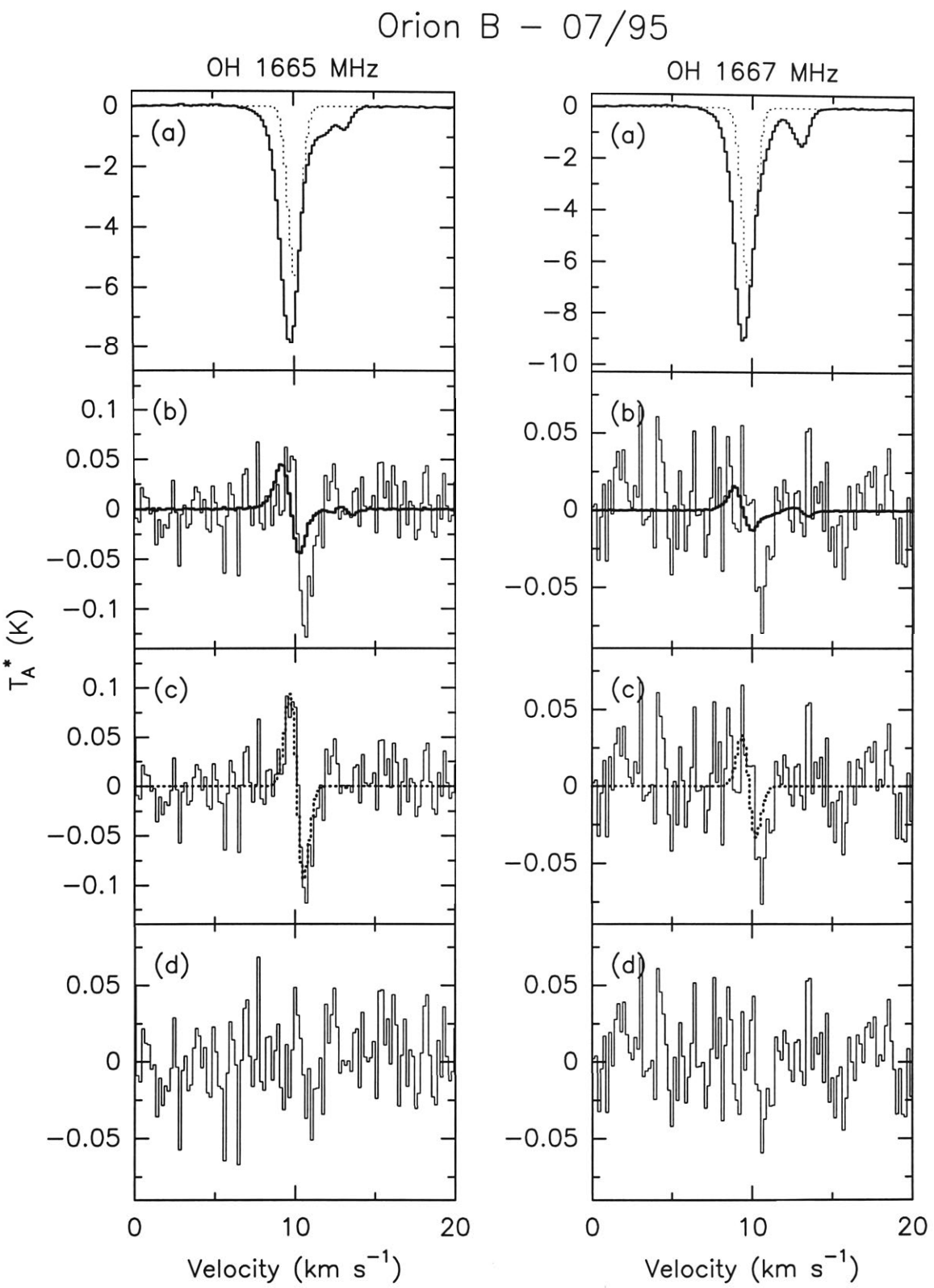

Figure 2.22.— Fitting the V spectra for Orion B. Panel (a) shows the I spectra (solid) with the Zeeman Gaussian subcomponent (dotted); panel (b) shows the fits of the derivative of I to V; panel (c) shows the fits of the derivative of the Zeeman Gaussian component to the gain-subtracted V spectra; panel (d) shows the residual of the fits in (c).

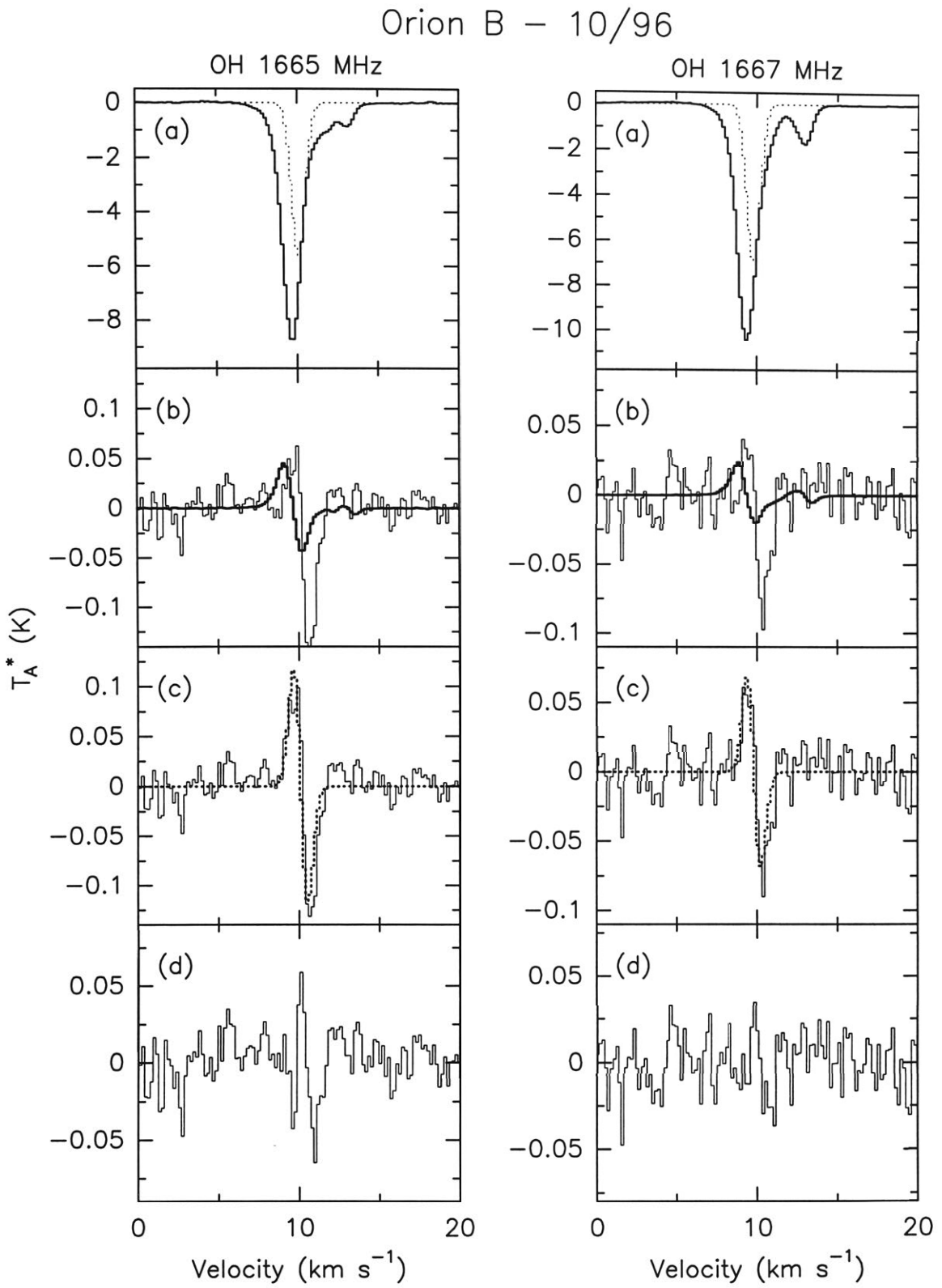

Figure 2.23.— Fitting the V spectra for Orion B. Panel (a) shows the I spectra (solid) with the Zeeman Gaussian subcomponent (dotted); panel (b) shows the fits of the derivative of I to V; panel (c) shows the fits of the derivative of the Zeeman Gaussian component to the gain-subtracted V spectra; panel (d) shows the residual of the fits in (c).

October 1996 data for Orion B we see a clear Zeeman signal in both the V_{1665} and V_{1667} spectra, so we are able to integrate them independently to infer the parameters of the Gaussian subcomponent responsible for the observed Zeeman effect. For the 1665 line we find $V_{lsr} = 10.1$ km s^{-1}, $\Delta V = 1.0$ km s^{-1}, while for the 1667 line we find $V_{lsr} = 9.8$ km s^{-1}, $\Delta V = 1.0$ km s^{-1}, with $I_{1665} = -5.6$ K and $I_{1667} = -7.0$ K, being the greatest absorption line intensities allowed by the data. The field strengths inferred for these Gaussian components are 26 ± 2 μG for the 1665 line, and 21 ± 2 μG for the 1667 line. The ratio of the magnetic field strengths $B_{1665}/B_{1667} = 1.24$ is equal to the inverse ratio of the line intensities $I_{1667}/I_{1665} = 1.25$. For the values of $B_{los}$to agree requires $I_{1667}/I_{1665} = 1$, which is the result obtained by CK83, who inferred the same intensity for the Gaussian subcomponent of both lines, and obtained the same value for B_{los} from both OH lines. Our result is therefore consistent with CK83 if we assume, as they did, that $I_{1667}/I_{1665} = 1$ for the Gaussian subcomponent responsible for the Zeeman effect. Recently, Crutcher et al. (1998) report the detection of the Zeeman effect in Orion B in OH using the VLA. The sub-component in which they detect the Zeeman effect has $V_{lsr} = 10.2$ km s^{-1} which they claim is also present in $C^{18}O$ $J = 1 \rightarrow 0$ data.

RCW 38: Fig. 2.24 shows the RCW 38 data for October 1996, in the same manner as the Orion B data in Fig 2.23. Panel (a) shows the Stokes I spectra, with the Gaussian subcomponent responsible for the Zeeman "S" in the V spectra shown as the dashed line. The fit of the derivative of the entire Stokes I spectra to the V spectra is shown in panel (b), which results in very poor fits. In panel (c) we show the fits of the derivative of the Gaussian subcomponent to the V spectra. The parameters of this subcomponent are found by integrating the V spectrum for each OH line. For I_{1665} we find $V_{lsr} = 1.4$ km s^{-1}, $\Delta V = 2.2$ km s^{-1}; for I_{1667} we find $V_{lsr} = 1.4$ km s^{-1}, $\Delta V = 2.4$ km s^{-1}. Since we have no way of determing the line intensity of this component, we assume the intensity is the maximum allowed by the real I data, as was done for Orion B. We find that $I_{1665} = -8.9$ K and $I_{1667} = -12.1$ K, which then implies $B_{1665} = 38 \pm 3$ μG and $B_{1667} = 28 \pm 3$ μG. These are the fits shown in panel (c), while the

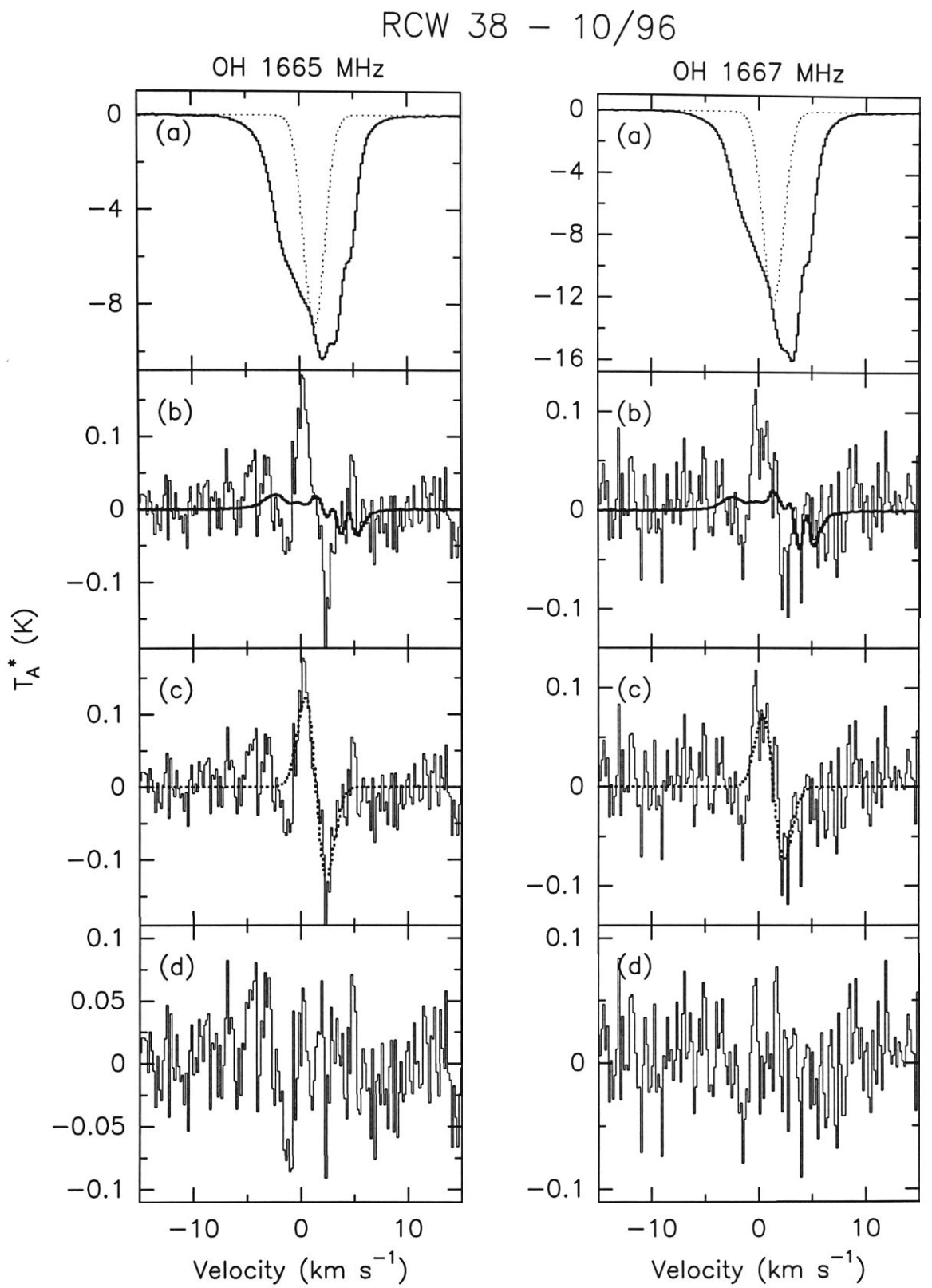

Figure 2.24.— Fitting the V spectra for RCW 38. Panel (a) shows the I spectra (solid) with the Zeeman Gaussian subcomponent (dotted); panel (b) shows the fits of the derivative of I to V; panel (c) shows the fits of the derivative of the Zeeman Gaussian component to the gain-subtracted V spectra; panel (d) shows the residual of the fits in (c).

residuals of the fits are shown in panel (d). Clearly there is no overlap at the 1σ level between the two values for B_{los}. If instead we require the line intensity of the Gaussian for both OH lines to be equal at -8.9 K, then we find that B_{1667} $= 37 \pm 5$ μG, in better agreement with the result for the 1665 line of $B_{1665} =$ 38 ± 3 μG. If the ratio of the line intensities is truly equal to one, then the OH component in which we detect the Zeeman effect is optically thick. The values of B_{los} for RCW 38 reported in Table 2.4 are for the case $I_{1665} = I_{1667}$ for the Gaussian subcomponent. We emphasise that this value of B_{los} is a lower limit due to the assumption we have made about the line intensity of the Gaussian subcomponent responsible for the Zeeman effect.

Carina Molecular Cloud: Fig. 2.25 shows the Zeeman fitting for the molecular cloud associated with the Eta Carina nebula. Panel (a) show the I spectra (solid line), and the result of fitting two Gaussians to the spectra. Both I_{1665} and I_{1667} are well fitted by two Gaussians, with similar parameters for both OH lines. The fits of the derivative of the I spectra to the V spectra are shown in panel (b). In panel (c) we show the fits of the derivatives of the Gaussians to the V spectra. The derivatives of the Gaussians are fitted simultaneously with the gain term, and the overall fits (i.e., the sum of the derivatives of the Gaussians) are shown in panel (d), with the gain terms removed.

Chamaeleon: Since the I spectra are well fitted by a single Gaussian, as shown in panel (a) of Fig. 2.26 (the dashed line is the Gaussian fit), we do not show the fitting of the derivative of this Gaussian to the V spectra. In panel (b) we show the fits of the derivative of I to V, and in panel (c) the residual of these fits.

RCW 57: The data for RCW 57 are very interesting as there is a hint of the Zeeman effect in part of the data. In panel (a) of Fig 2.27 we show the I spectra (solid lines), together with the two Gaussians whose sum best fits the I spectra. In panel (b) we show the fits of the derivative of the I spectra to the V spectra. In panel (c) we show the derivatives of the two Gaussians fitted to the V spectra, where the V spectra shown have had a gain term subtracted. The Gaussian derivatives and the gain terms were fitted simultaneously. The

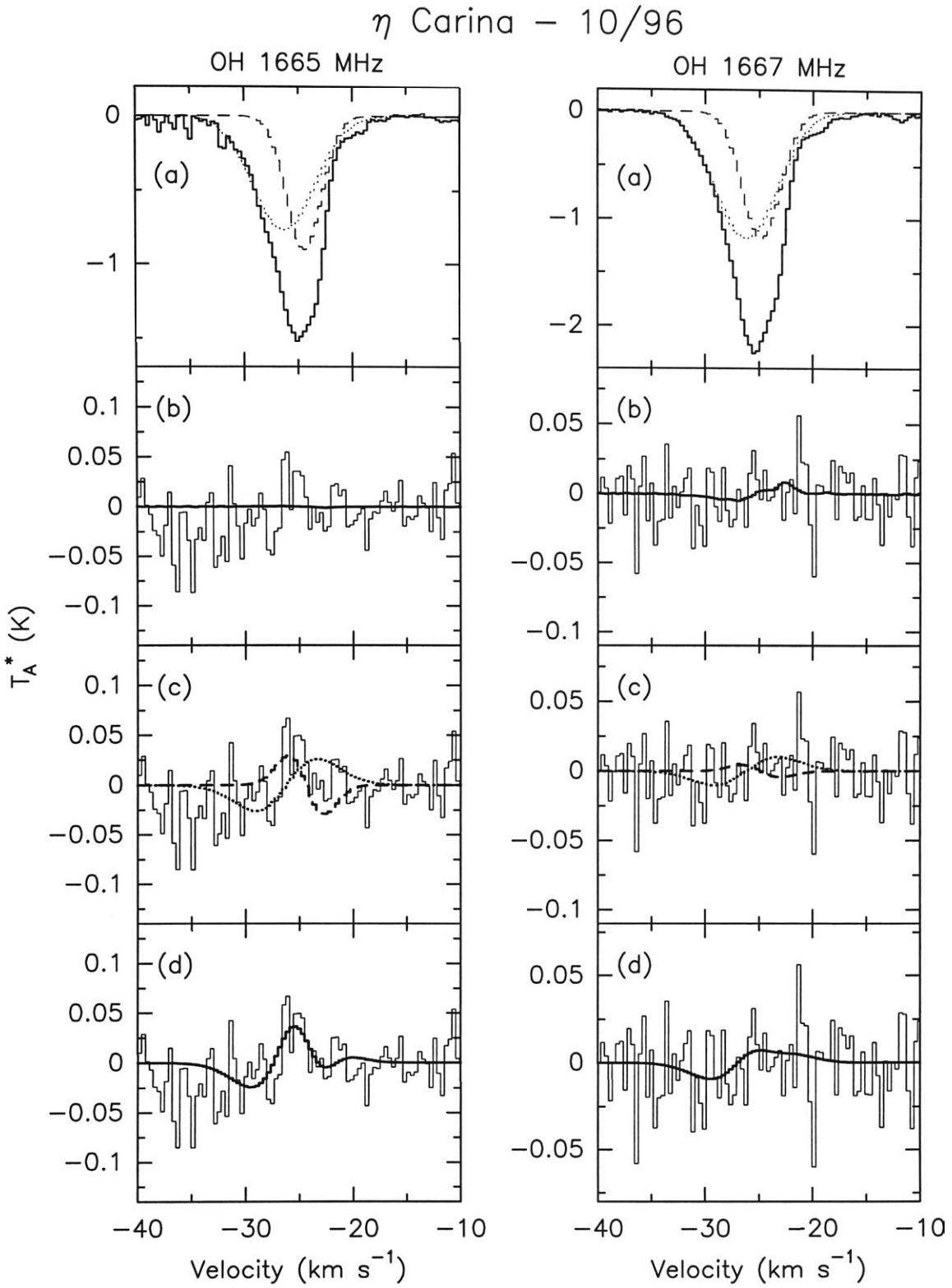

Figure 2.25.— Fitting the V spectra for Carina. Panel (a) shows the I spectra (solid) with the Gaussian subcomponents (dashed & dotted); panel (b) shows the fits of the derivative of I to V; panel (c) shows the individual fits of the derivatives of the Gaussian components to the gain-subtracted V spectra; panel (d) shows the sum of the derivatives of the Gaussian components overlayed on the V spectra.

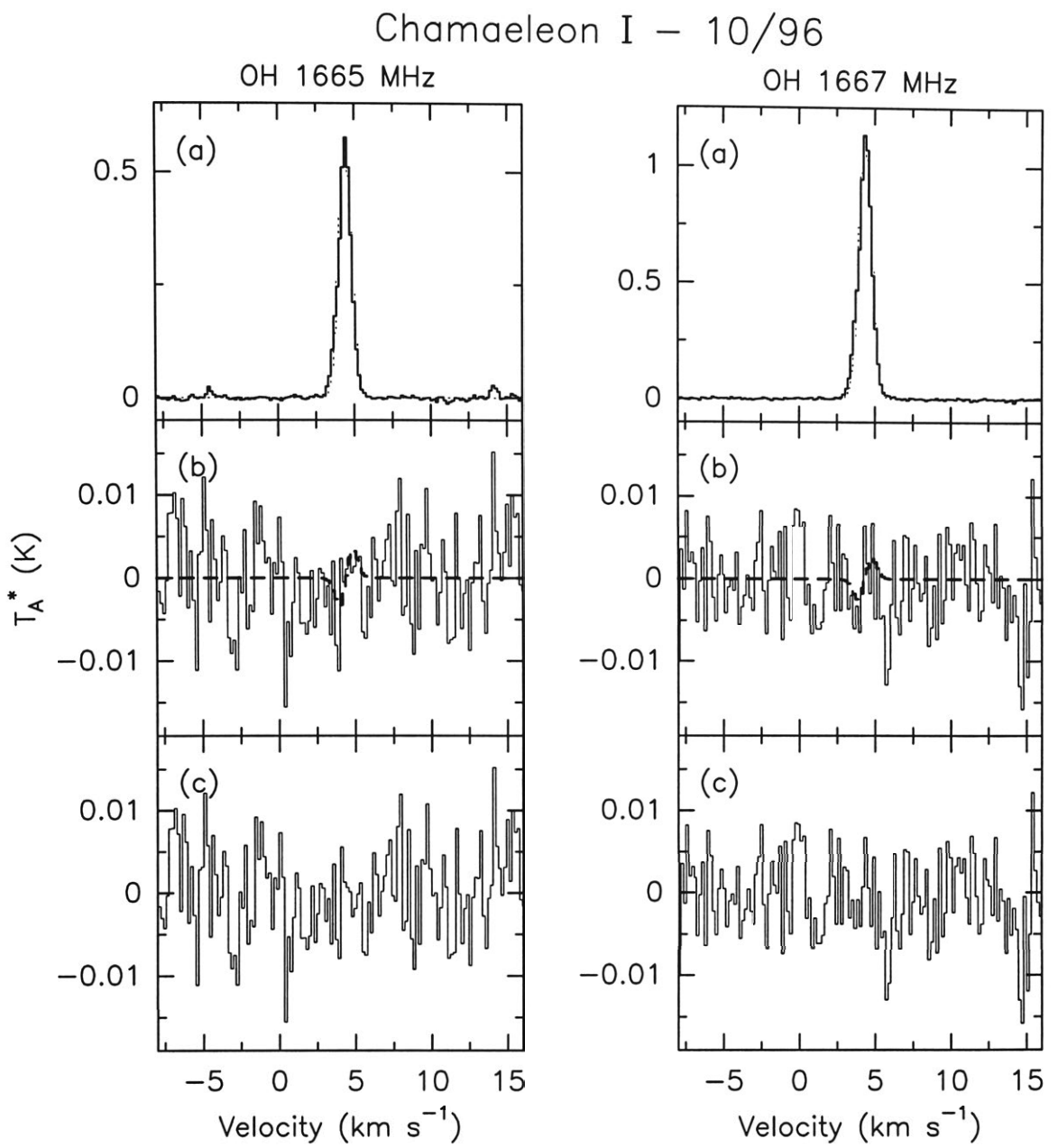

Figure 2.26.— Fitting the V spectra for Chamaeleon I. Panel (a) shows the I spectra (solid) with the Gaussian component (dotted); panel (b) shows the fits of the derivative of I to V; panel (c) shows the residual of these fits.

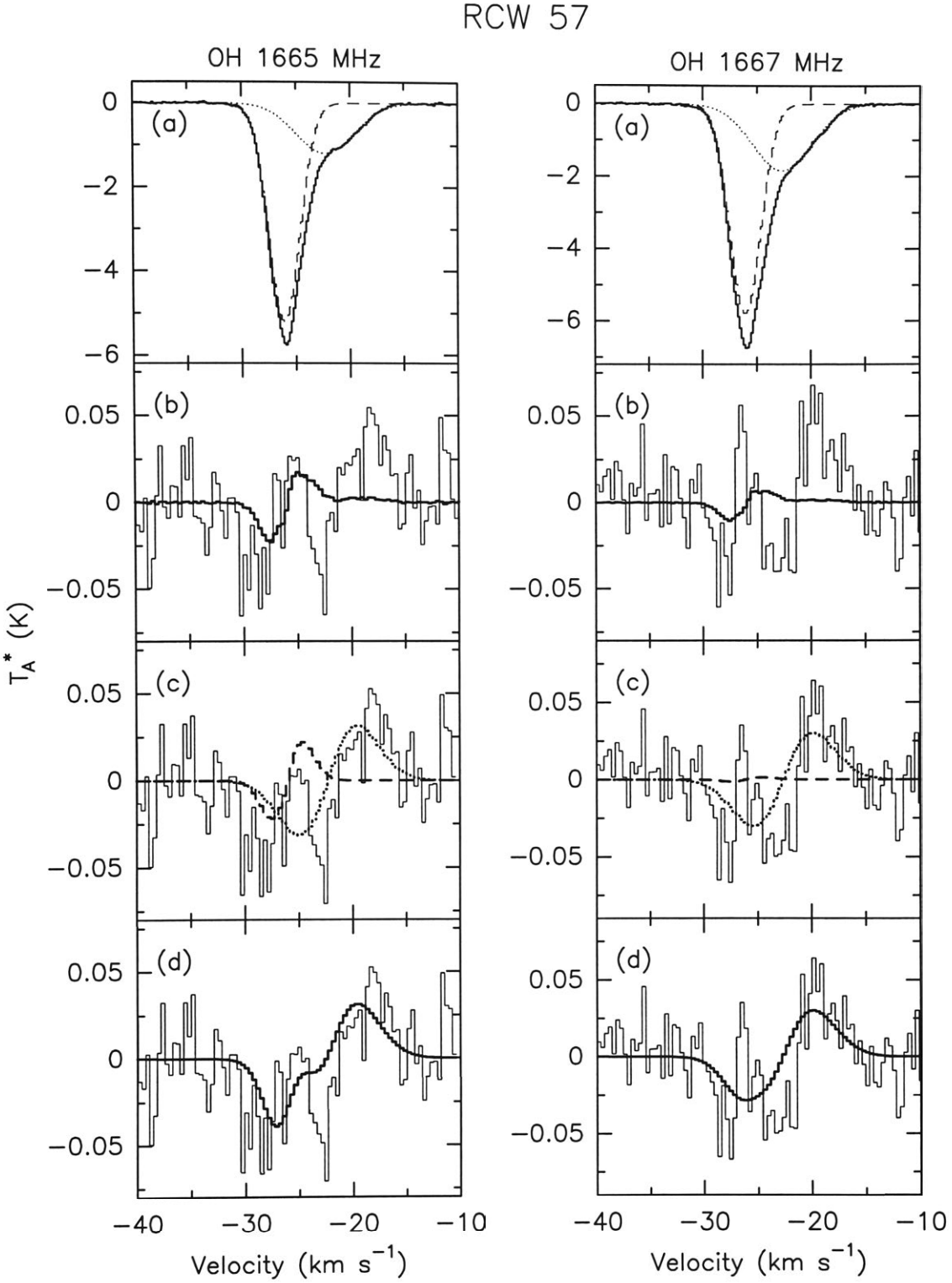

Figure 2.27.— Fitting the V spectra for RCW 57. Panel (a) shows the I spectra (solid) with the Gaussian subcomponents (dashed & dotted); panel (b) shows the fits of the derivative of I to V; panel (c) shows the individual fits of the derivatives of the Gaussian components to the gain-subtracted V spectra; panel (d) shows the sums of the derivatives of the Gaussian components overlayed on the V spectra.

gain-subtracted V spectra are similar, in particular the increase in intensity for velocities > -20 km s^{-1}, which is well fitted by the derivative of the higher velocity Gaussian ($V_{lsr} = -22.6$ km s^{-1}). Panel (d) shows the sums of the two Gaussian derivatives displayed in panel (c) overlayed on the gain-subtracted V spectra. For RCW 57 we have used the $I \rightarrow V$ method, and so nothing is assumed *a priori* about the nature of the two Gaussians that are fitted to I. Note that the masers appearing in the I_{1665} RCP spectrum have been fitted and subtracted before deriving the V_{1665} spectrum shown.

While the formal results indicate that we have detected the Zeeman effect in the -22.6 km s^{-1} component with a magnetic field strength of -203 ± 25 μG, we claim this as a tentative result only. The ^{13}CO $J = 1 \rightarrow 0$ data presented in the appendix to this chapter clearly shows two spatially distinct molecular components, whose spectral properties (i.e., velocity and line width) are similar to those inferred for the OH Gaussian subcomponents. Interferometric OH Zeeman observations of RCW 57 are required to confirm our Zeeman detection, so that the OH absorption components may be spatially separated.

G 326.7+0.6: The modelling of the V spectra for G 326.7+0.6 is shown in Figs. 2.28 – 2.31. Each velocity component was fitted separately over the velocity range shown in each figure. In Fig. 2.28 we show the component near -44 km s^{-1}. Panel (a) shows the I spectra (solid line) with a single component Gaussian fit (dashed line), panel (b) the derivatives of the Gaussian fitted to the V spectra, and panel (c) the residual of these fits. Since the V spectrum for the 1665 line is badly affected by interference, the data are not presented as the fits are meaningless. Fig. 2.29 shows the results for the -22 km s^{-1} component, which as shown in panel (a) is well fitted by two Gaussian components, similar to RCW 57. Panel (b) shows the fits of the whole I spectra to the V spectra, while panel (c) shows the derivatives of the individual Gaussian components resulting from simultaneously fitting these components and a gain term to the V spectra. The gain term inferred from these fits has been subtracted from the displayed V spectra. Panel (d) shows the sums of the Gaussian derivatives from (c) overlayed on the gain-subtracted V spectra. Figs. 2.30 and 2.31 are similar

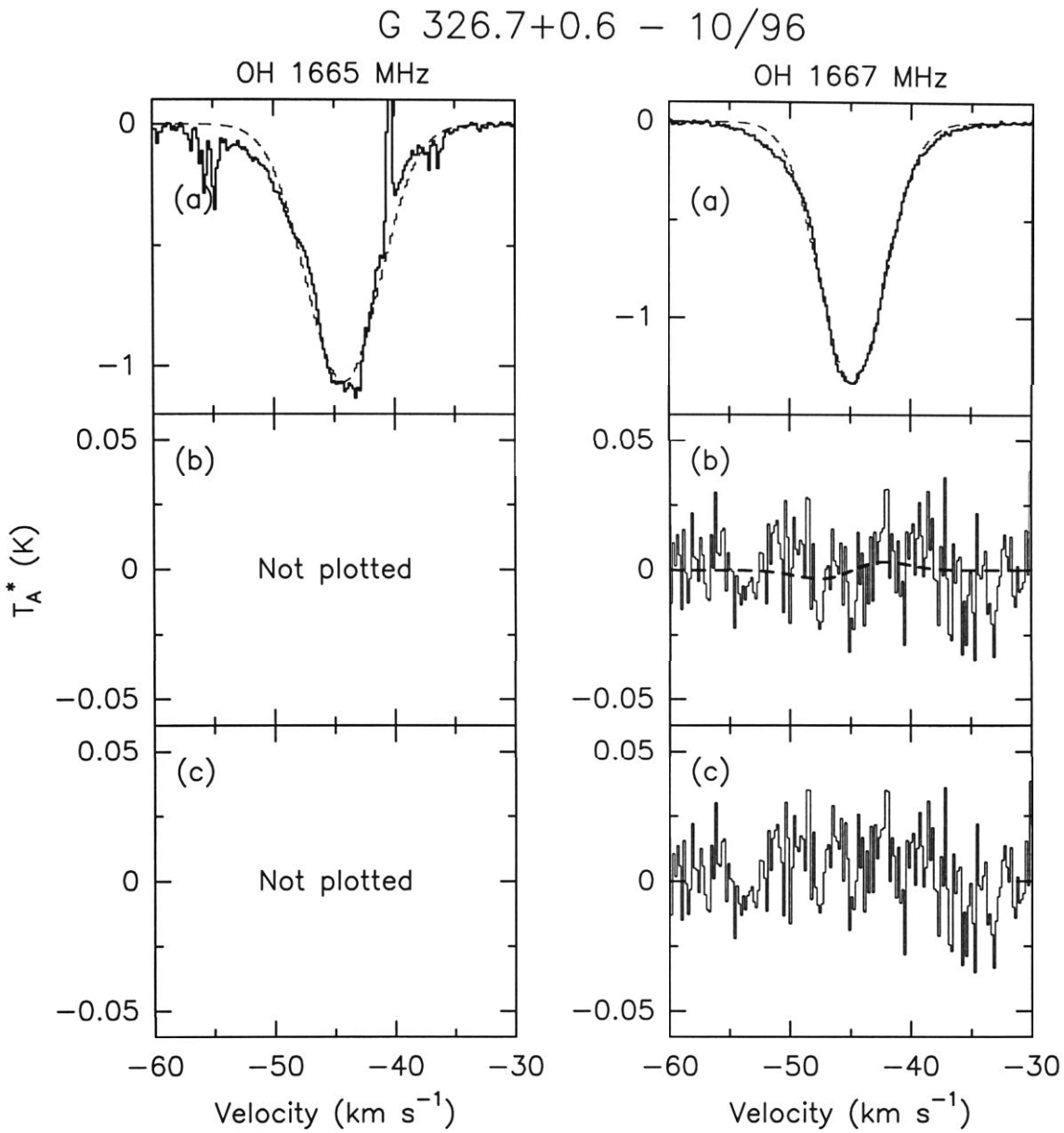

Figure 2.28.— Fitting the V spectra for the -44 km s^{-1} component of G 326.7+0.6. Panel (a) shows the I spectra (solid) with the Gaussian component (dashed); panel (b) shows the fits of the derivative of I to V; panel (c) shows the residual of these fits.

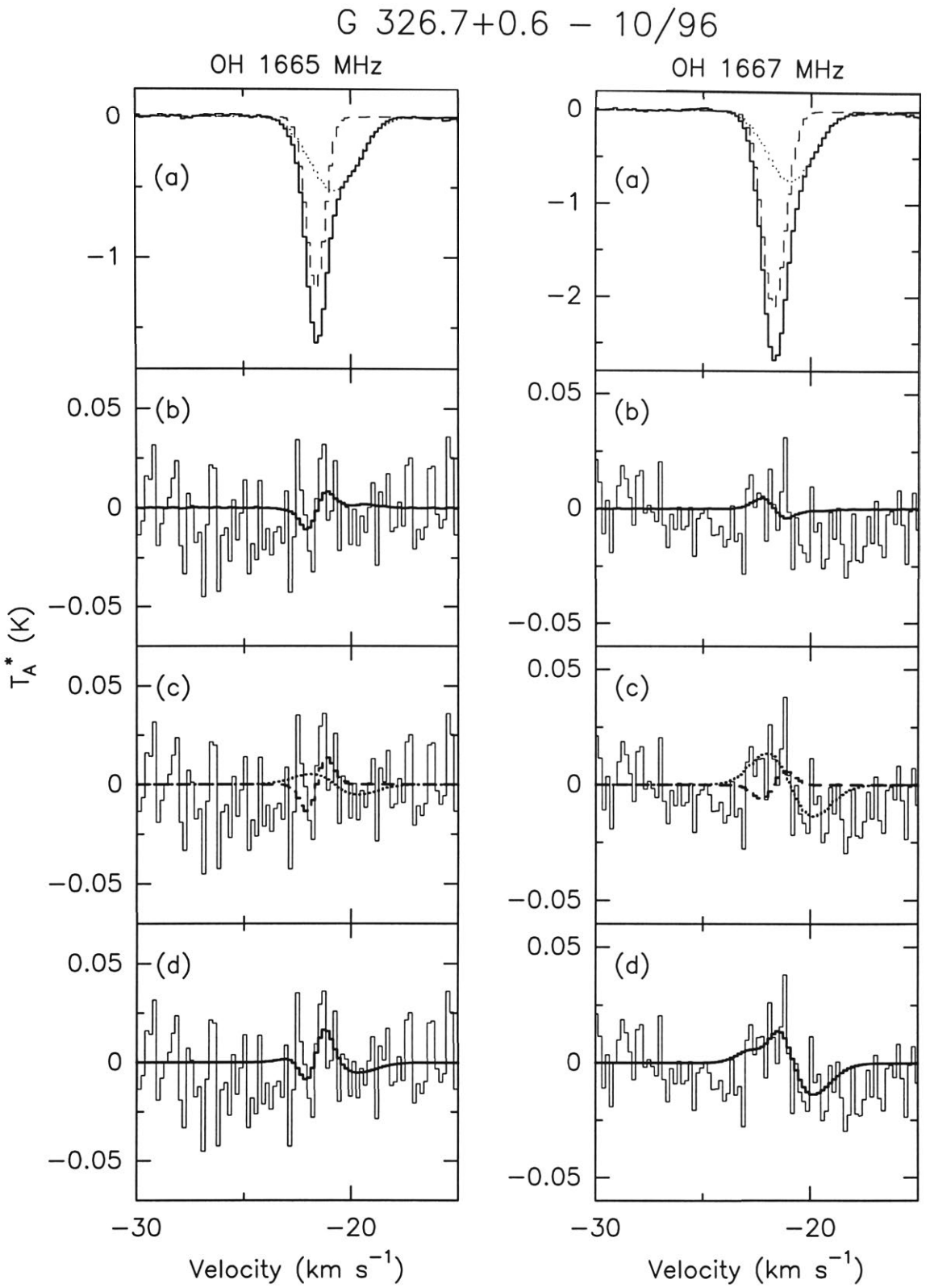

Figure 2.29.— Fitting the V spectra for the -22 km s^{-1} component of G 326.7+0.6. Panel (a) shows the I spectra (solid) with the Gaussian subcomponents (dashed & dotted); panel (b) shows the fits of the derivative of I to V; panel (c) shows the individual fits of the derivatives of the Gaussian components to the gain-subtracted V spectra; panel (d) shows the sums of the derivatives of the Gaussian components overlayed on the V spectra.

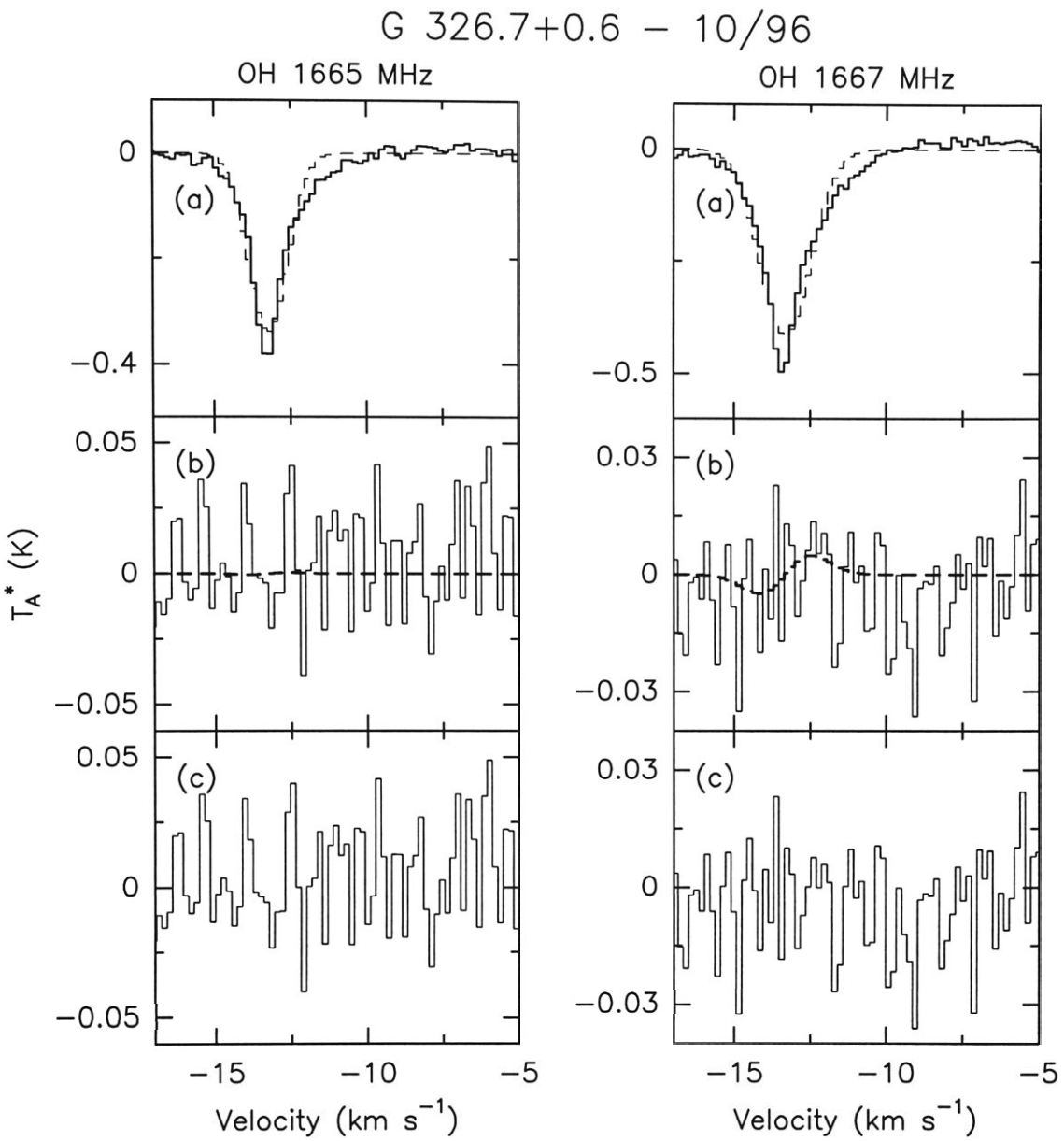

Figure 2.30.— Fitting the V spectra for the -13 km s^{-1} component of G 326.7+0.6. Panel (a) shows the I spectra (solid) with the Gaussian component (dashed); panel (b) shows the fits of the derivative of I to V; panel (c) shows the residual of these fits.

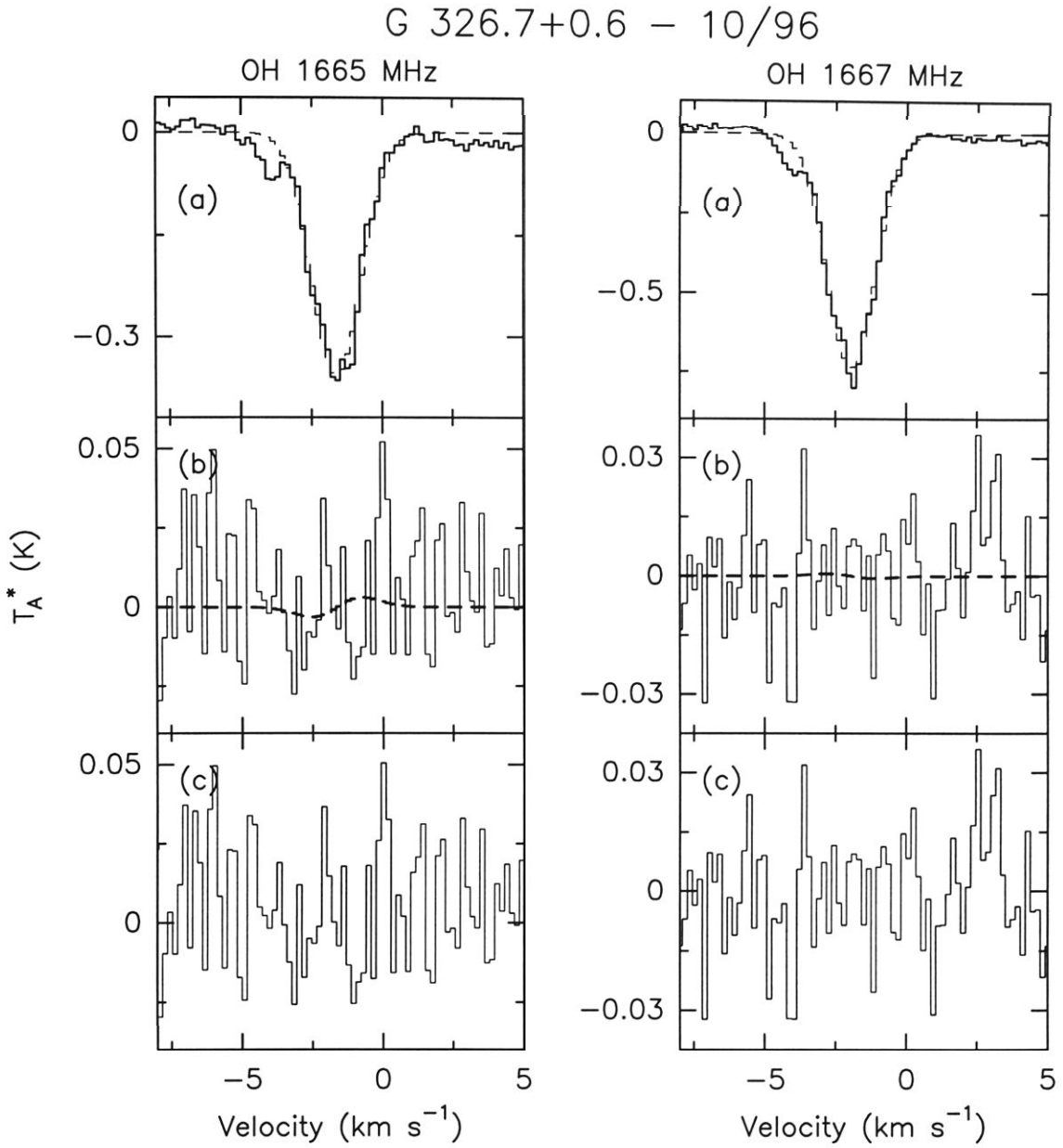

Figure 2.31.— Fitting the V spectra for the -2 km s^{-1} component of G 326.7+0.6. Panel (a) shows the I spectra (solid) with the Gaussian component (dashed); panel (b) shows the fits of the derivative of I to V; panel (c) shows the residual of these fits.

to Fig 2.28 except they show the results for the components at -13 and -2 $\mathrm{km\,s^{-1}}$, respectively.

G 327.3–0.5: Fig. 2.32 shows the results for G 327.3–0.5. Unfortunately the low velocity side of the main absorption line for both I_{1665} and I_{1667} is affected by masers. We have thus restricted our fitting to the velocity range indicated in panels (b) – (d) of this figure. The fitting of the Gaussian indicated in panel (a) (dashed line) was done over a much large velocity range with the masers excluded from the fit. Panel (b) shows the fits of the derivative of the I spectra to the V spectra. There is some structure in the V_{1667} profile which is suggestive of the Zeeman effect. Panel (c) shows the result of fitting the derivatives of the Gaussian fit to the V spectra. The V spectra in this panel have had the gain terms subtracted. The fit to V_{1667} is very good, as indicated by the residual shown in panel (d). However, the presence of the masers makes it unclear whether we are truly seeing the Zeeman effect, and corroborative evidence from the 1665 line is not available. High angular resolution OH Zeeman observations of G 327.3–0.5 are required to attempt to spatially separate the masers from the absorption components.

G 343.4–0.0: Figs. 2.33 and 2.34 show the results for the two main components of G 343.4–0.0 near -27 and 6 $\mathrm{km\,s^{-1}}$, respectively. Panel (a) of Fig. 2.33 shows the I spectra with Gaussian fits to the main absorption component at -27 $\mathrm{km\,s^{-1}}$, panel (b) shows the derivative of the entire I spectra over the velocity range shown fitted to the V spectra, while panel (c) shows the derivatives of the Gaussians from (a) fitted to the V spectra, and panel (d) the residuals of these fits. No Zeeman effect is evident in the V spectra. Fig. 2.34 shows that the 6 $\mathrm{km\,s^{-1}}$ component is well fitted by a single Gaussian (dashed line in panel (a)). Panel (b) shows the fit of the derivative of this Gaussian to the V spectra, and (c) the residuals of these fits. The results of fitting the derivative of I to V are essentially the same.

NGC 6334: Figs. 2.35 and 2.36 show the results for the two deep absorption lines seen toward NGC 6334. Both lines are well fitted by single Gaussians, and the results are shown for these Gaussian fits. Fig 2.35 shows the results

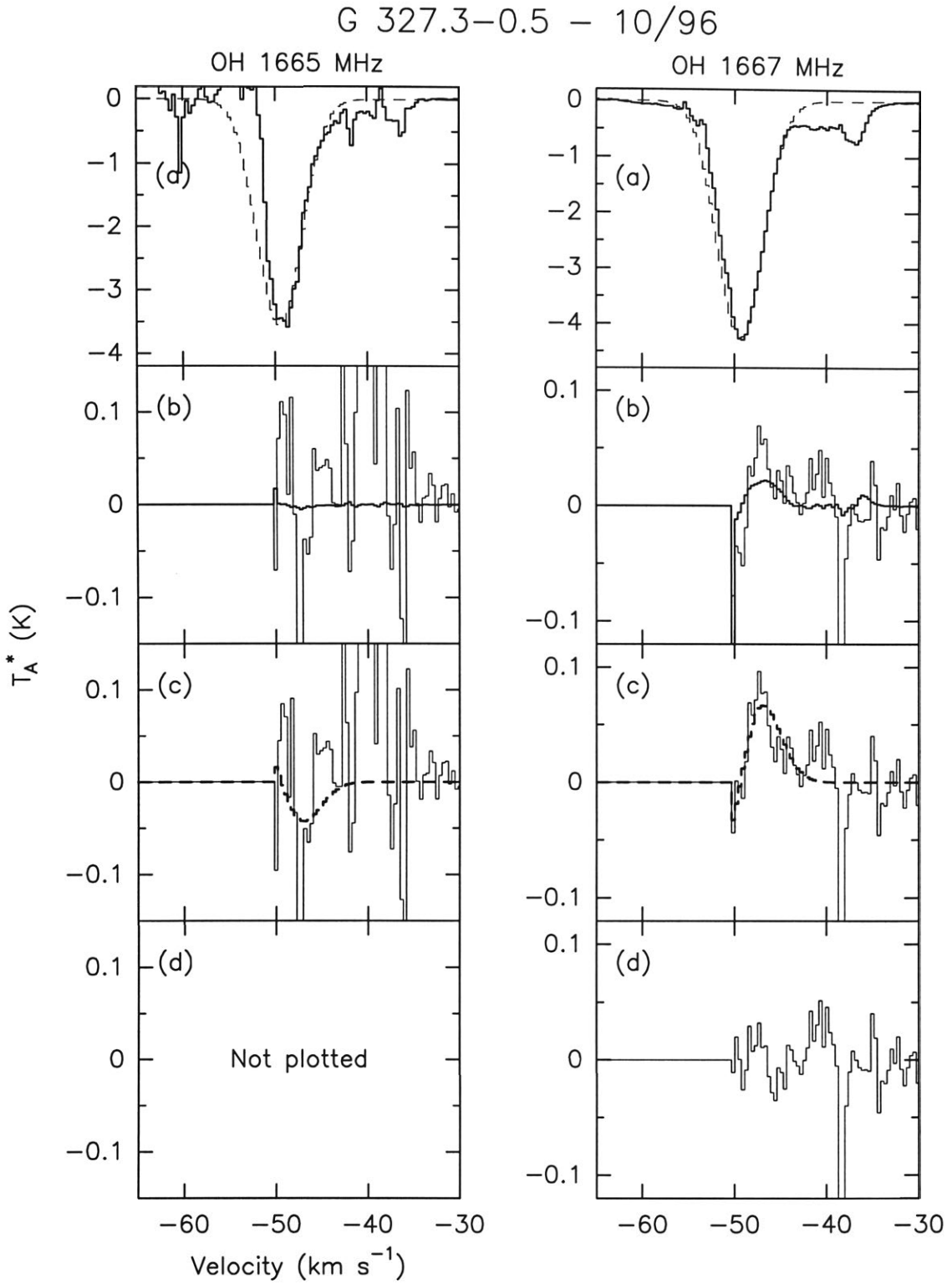

Figure 2.32.— Fitting the V spectra for G 327.3–0.5. Panel (a) shows the I spectra (solid) with the fitted Gaussian (dashed); panel (b) shows the fits of the derivative of I to V; panel (c) shows the fits of the derivative of the Gaussian to the gain-subtracted V spectra; panel (d) shows the residuals of the fits in (c). The fits are restricted to velocities greater than -50 km s^{-1}, as shown in the plots.

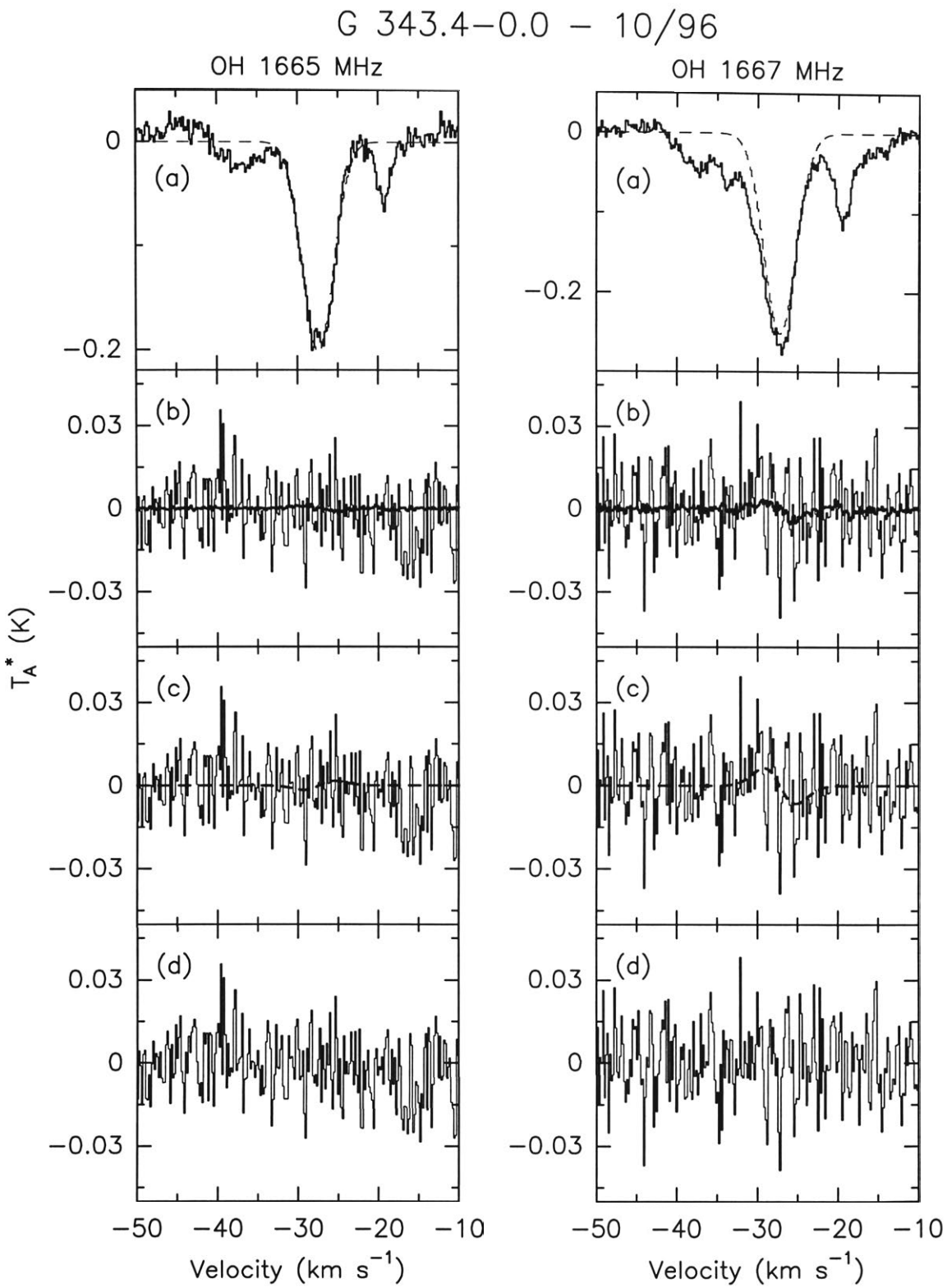

Figure 2.33.— Fitting the V spectra for the -27 km s^{-1} component of G 343.4–0.0. Panel (a) shows the I spectra (solid) with the fitted Gaussian (dashed); panel (b) shows the fits of the derivative of I to V; panel (c) shows the fits of the derivatives of the Gaussian to the gain-subtracted V spectra; panel (d) shows the residual of the fits in (c).

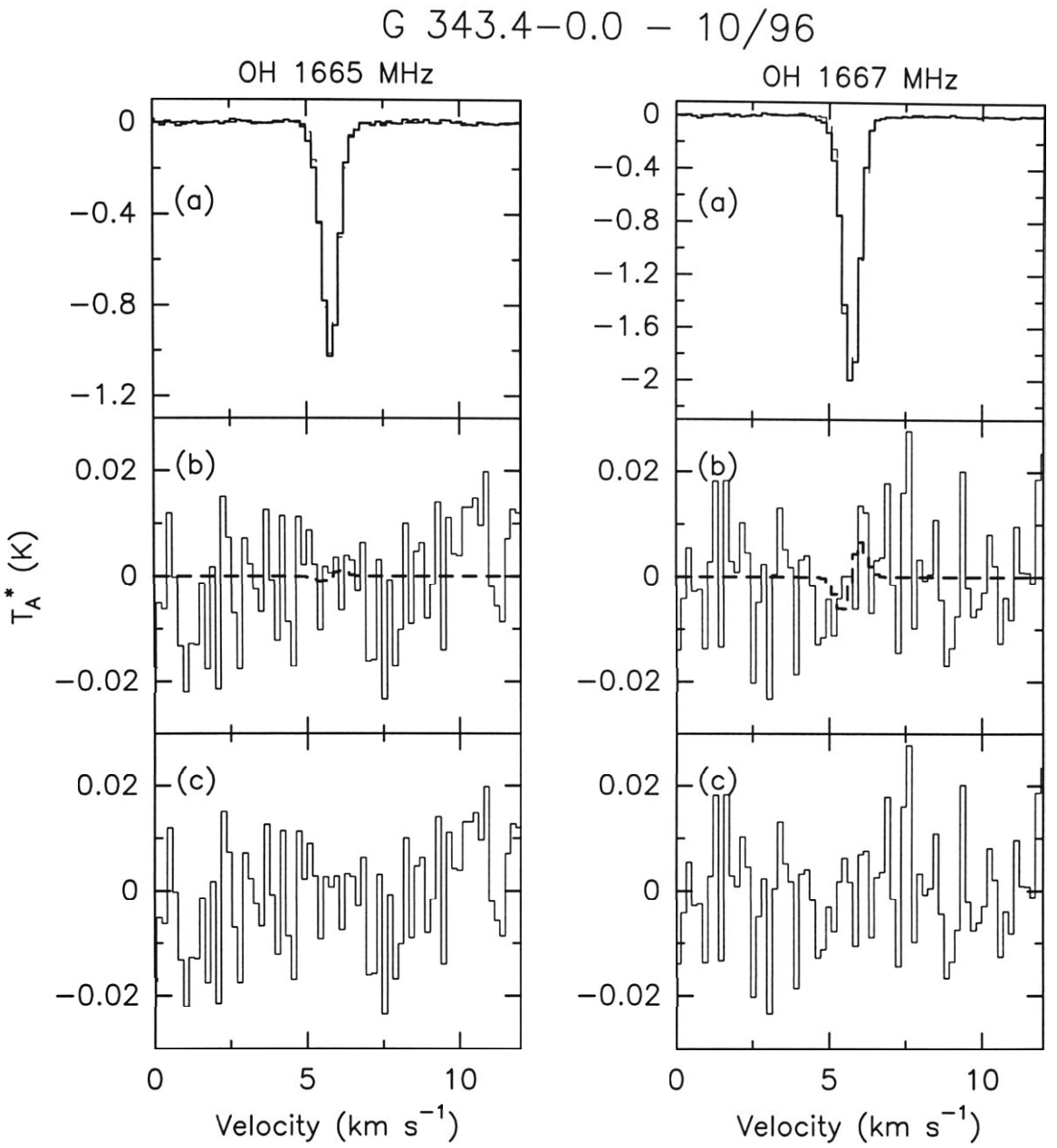

Figure 2.34.— Fitting the V spectra for the 6 km s^{-1} component of G 343.4–0.0. Panel (a) shows the I spectra (solid) with the Gaussian component (dashed); panel (b) shows the fits of the derivative of I to V; panel (c) shows the residuals of these fits.

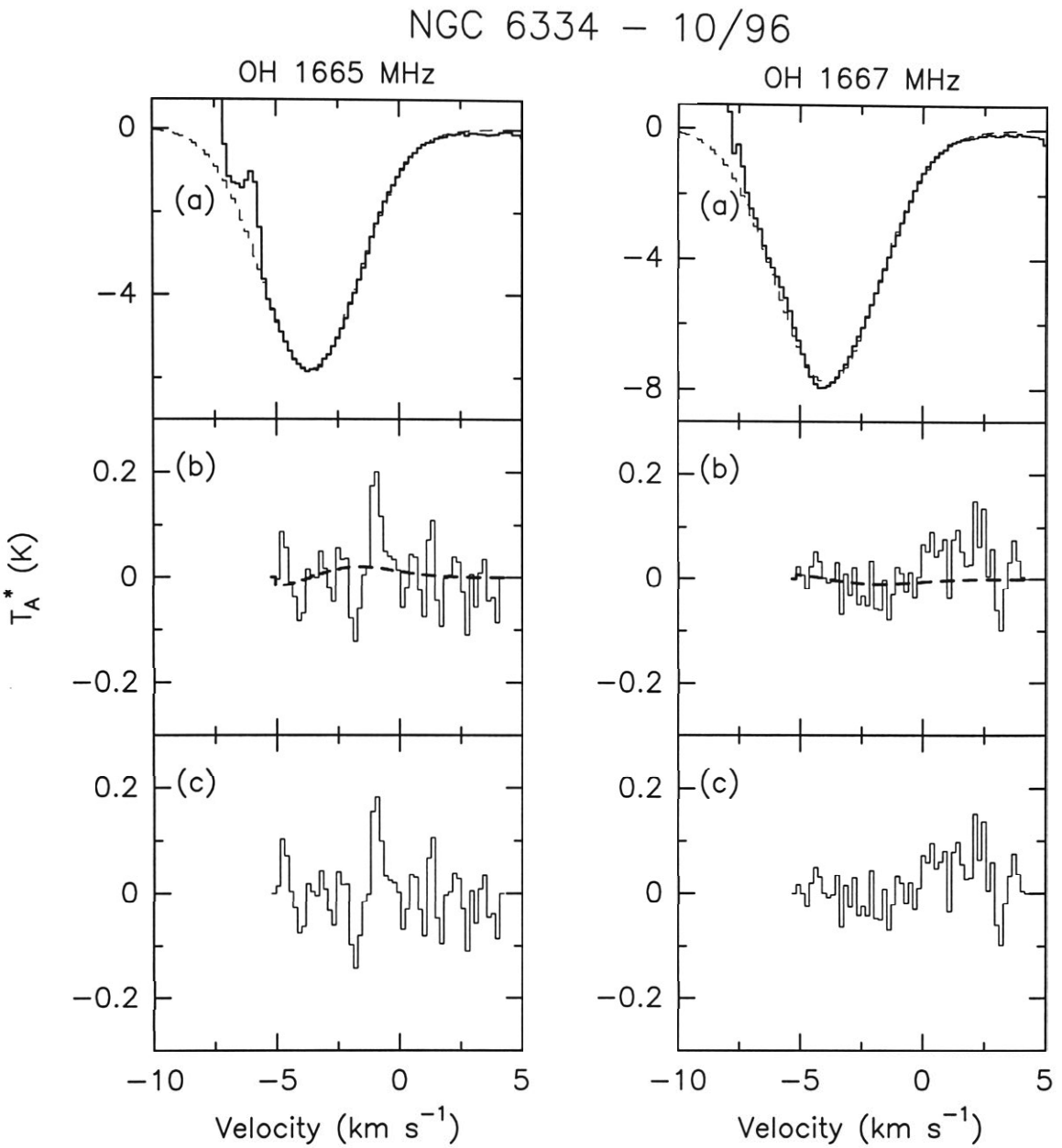

Figure 2.35.— Fitting the V spectra for the -3 km s^{-1} component of NGC 6334. Panel (a) shows the I spectra (solid) with the fitted Gaussian (dashed); panel (b) shows the fits of the derivative of I to V; panel (c) shows the residuals of the fits in (b). The fits are restricted to velocities greater than -5 km s^{-1}, as shown in the plots.

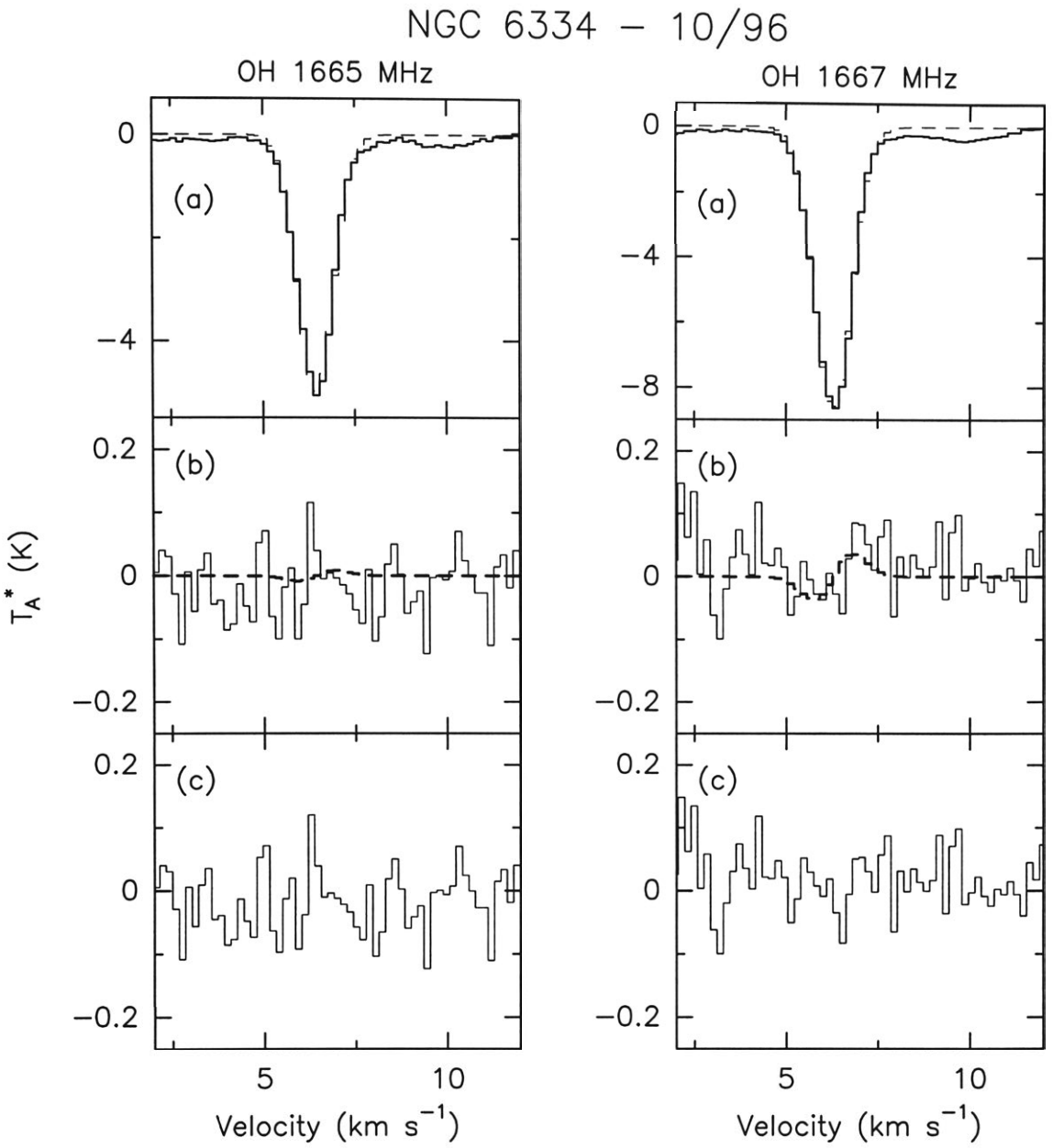

Figure 2.36.— Fitting the V spectra for the 6 km s^{-1} component of NGC 6334. Panel (a) shows the I spectra (solid) with the fitted Gaussian (dashed); panel (b) shows the fits of the derivative of I to V; panel (c) shows the residuals of the fits in (b).

for the -3 km s^{-1} component, which is from molecular gas directly associated with the H II region. The fits have been restricted in velocity due to the masers at the low velocity edge of the line. Panel (a) shows the Gaussian component (dashed line) overlayed on the I spectra, panel (b) the fits of the derivative of this Gaussian to the V spectra, and (c) the residuals of the fits in (b). Fig. 2.36 shows similar results for the 6 km s^{-1} component.

G 8.1+0.2: Fig. 2.37 shows that G 8.1+0.2 is reasonably well fitted by two Gaussian components, as shown in panel (a). There are masers on the high velocity edge of the absorption lines, and so the fits to the V spectra are restricted to the low velocity channels. Panel (b) shows the fits of the derivative of the raw I spectra to the V spectra. Panel (c) shows the fit of the derivatives of the two Gaussians to the gain-subtracted V spectra, with the derivatives and the gain terms being fitted simultaneously. In panel (d) we show the sum of the Gaussian derivatives fitted to the V spectra.

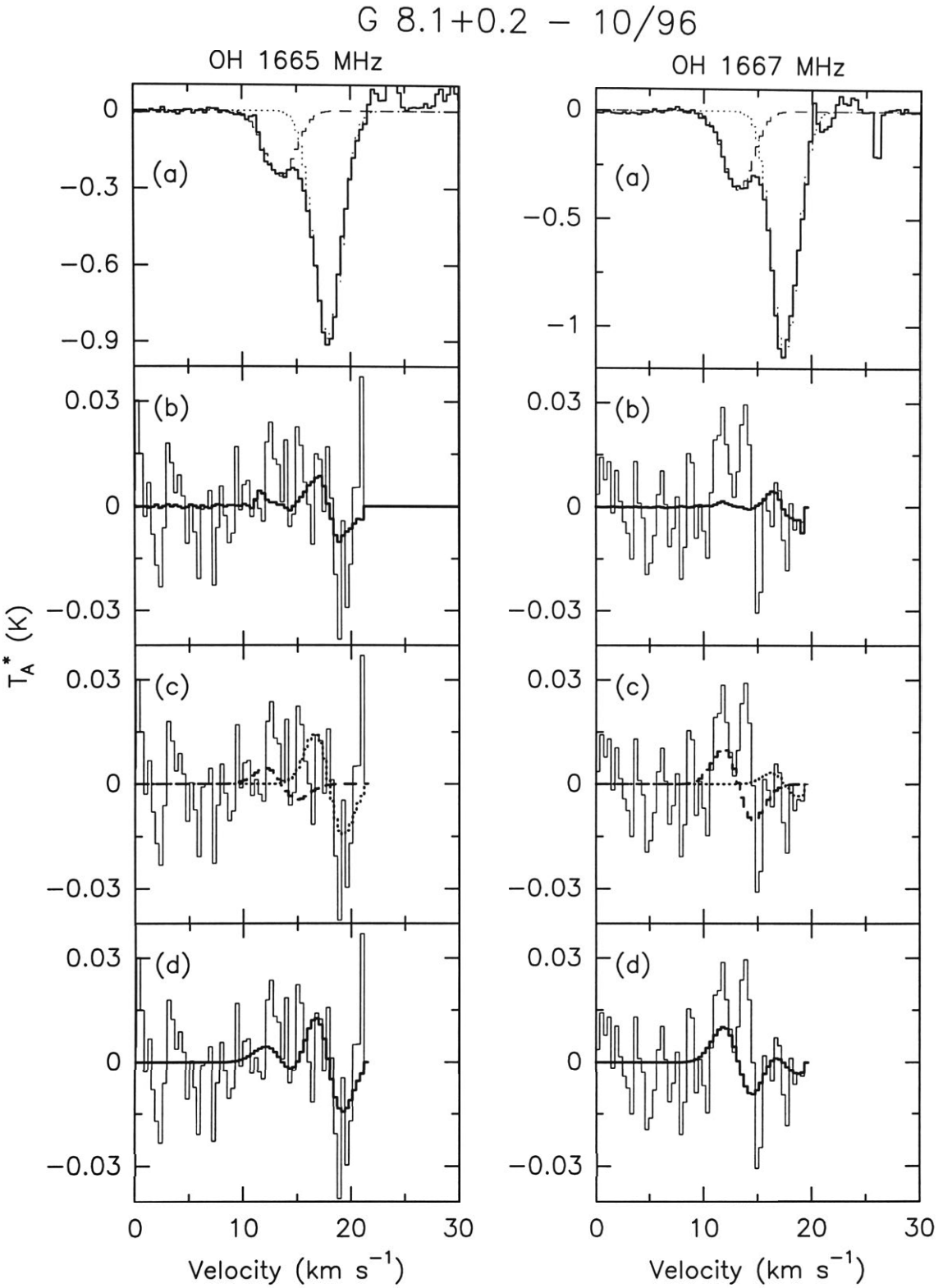

Figure 2.37.— Fitting the V spectra for G 8.1+0.2. Panel (a) shows the I spectra (solid) with the Gaussian subcomponents (dashed & dotted); panel (b) shows the fits of the derivative of I to V; panel (c) shows the individual fits of the derivatives of the Gaussian components to the gain-subtracted V spectra; panel (d) shows the sums of the derivatives of the Gaussian components overlayed on the V spectra.

2.5. Discussion

2.5.1. The magnetic field and virial equilibrium

To investigate whether magnetic fields are dynamically important in our molecular cloud sample we need to compare our measurements of magnetic field strengths against the hypotheses outlined in §2.1. In addition to the data on magnetic field strengths we require information about the molecular gas in which we have measured the Zeeman effect, in particular the cloud size R and the mean column density N.

For molecular clouds observed in OH emission (e.g., Chamaeleon I) the cloud properties may be determined directly by mapping the extent of OH emission. One potential problem with this approach is the large beam size, and therefore poor angular resolution, of single dish radiotelescopes at the OH ground state frequencies near 1.6 GHz, for example the Parkes telescope beam size is $13'$ at this frequency. Another is the uncertainty in determining the excitation temperature T_{ex} and the optical depth τ for the OH transitions, if the usual assumption of local thermodynamic equilibrium is not met (Crutcher 1977, 1979), which may result in estimates of the OH column density $N(\mathrm{OH})$ that are up to an order of magnitude different from their true values (as described in the appendix to this chapter).

For molecular clouds seen in absorption we cannot use the OH absorption map size to determine the true size of the region traced by OH. This is because the observed absorption map size is dependent on the angular size and strength of the background continuum source, and the size and column density of the foreground molecular cloud. From earlier studies we know that the ^{13}CO $J = 1 \rightarrow 0$ transition near 110 GHz traces similar gas densities [$n(\mathrm{H_2}) \sim 2 \times 10^3$ cm^{-3}] to the 1665 and 1667 MHz OH transitions in typical molecular clouds (e.g., Myers et al. 1978; Wouterloot & Habing 1985). Under special circumstances, such as within the photon-dominated region (PDR) associated with the H II region S106, OH may trace higher densities, e.g. 10^4 cm^{-3} (Roberts et al. 1995), and

the $C^{18}O$ $J = 1 \rightarrow 0$ transition near 109 GHz is then a better tracer of the gas sampled by the OH absorption.

All but one of the molecular clouds we observed for the Zeeman effect were observed in OH absorption against background H II regions (though not all of the clouds responsible for the absorption lines are directely associated with the H II region). Thus we are unable to use OH absorption observations to determine their size. It should be emphasised that the angular size of the background continuum source is not related to the linear size of the foreground absorbing clouds in which we measure the Zeeman effect, and we cannot use the angular size of the continuum region to determine the size of the molecular cloud.

Since we believe that the ^{13}CO $J = 1 \rightarrow 0$ transition traces similar gas densities to OH we have attempted to map all of our absorption line sources in this transition with the ATNF Mopra radiotelescope. A description of the observations and the resulting velocity channel maps are presented in Appendix 2A at the end of this chapter. Our aim was to map the intensity of the integrated spectral line down to the half-power contour level for each molecular cloud. We did not achieve this for all sources.

The results of our analysis are presented in Table 2.5. In this Table, column (1) lists the source name, columns (2) – (3) the velocity parameters of the component being studied, column (4) the assumed cloud size, typically the FWHM size of the ^{13}CO map, and column (5) the average column density of H_2 over the map. The next three columns list theoretically determined quantaties: column (6) lists the value of $N_{\mathcal{KG}}$ as determined from eqn (2.10), column (7) the value of $B_{\mathcal{MG}}$ as determined from eqn (2.9), and column (8) the value of $B_{\mathcal{MKG}}$ from eqn (2.8). Column (9) lists the magnetic field strength (or 3σ upper limit) as determined observationally from our Zeeman analysis of the Gaussian components. In some cases we compare our results to the magnetic field strength determined from the whole line profile, B_w, rather than from the Gaussian subcomponents B_G, as explained below when each source is discussed.

We now briefly discuss how the physical properties presented in Table 2.5

Table 2.5. Comparison of Observed Magnetic Field Strengths with Virial Values

Source	V_{lsr} ($km\,s^{-1}$)	ΔV ($km\,s^{-1}$)	R (pc)	N (10^{21} cm^{-2})	$N_{\mathcal{KG}}$ (10^{21} cm^{-2})	$B_{\mathcal{MG}}$ (μG)	$B_{\mathcal{MKG}}$ (μG)	$\mid B_G \mid$ or $3\sigma_G$ (μG)
RCW 38	1.4	2.3	1.5	4.0	14.0	10	17	38
RCW 57	−22.6	6.5	3.6	40.0	30.0	50	50	203
Cham I	4.4	1.0	1.3	8.0	3.0	20	4	9
G 343.4–0.0	5.7	0.7	0.5	2.0	4.0	4	4	9
RCW 57	−26.1	3.4	4.0	15.0	10.0	25	13	12
NGC 6334	6.3	1.2	—	2.0	—	4	—	12
G 326.7+0.6	−21.6	2.0	4.3	2.0	3.3	5	4	15[a]
NGC 6334	−3.8	4.9	7.0	10.0	20.0	23	16	33
G 8.1+0.2	17.5	3.0	—	9.0	—	22	—	45
Carina	−25.4	5.8	3.3	6.0	40.0	15	45	51[a]
G 326.7+0.6	−1.9	2.0	0.8	1.0	20.0	3	22	63
G 326.7+0.6	−44.8	6.5	4.7	23.0	32.0	40	40	69
G 343.4–0.0	−27.4	4.7	2.0	10.0	50.0	25	61	96[a]
G 327.3–0.5	−49.0	5.4	4.3	30.0	24.0	80	30	105
G 8.1+0.2	13.3	3.3	—	34.0	—	81	—	153

[a]Results from fitting the entire line profile quoted, so $3\sigma_w$ used.

were determined for each source.

RCW 38: In RCW38, identifying spatially the molecular gas component in which we have detected the Zeeman effect is difficult, since the ^{13}CO emission line profiles, like that of the OH absorption lines profile, are non-Gaussian and most likely consist of a superposition of profiles arising from different gas clumps along the line-of-sight (but associated with RCW 38). The spatial resolution of the ^{13}CO observations is $\sim 1'$, and the sum of the ^{13}CO profiles over the spatial region covered by the $13'$ Parkes radiotelescope beam is almost identical to the OH absorption profile. This agreement is in accord with our assumption that ^{13}CO and OH trace similar gas densities. The channel maps presented in Fig. 2A.1 span the velocity range $V \pm \Delta V/2$ (i.e., 0.2 to 2.6 $km\,s^{-1}$) where V is the line centre velocity and ΔV is the FWHM of the inferred Zeeman component. From this figure we see that, of the 3 peaks located within the central 50% contour (heavy line), the western-most component has the properties most like those expected of the molecular gas responsible for the Zeeman effect, in that it peaks near the velocity of the Zeeman component at 1.4 $km\,s^{-1}$, and fades away toward the extreme channels of the map. We thus tentatively identify this feature as the gas clump in which we have detected the Zeeman effect. The column density of ^{13}CO is then estimated by integrating the line profiles over

0.2 to 2.6 $\mathrm{km\,s^{-1}}$ for those spectra spatially located within the 50% contour *of this molecular gas component.* Our assumptions may thus (i) underestimate R, but R cannot be more than about twice the value we determine, as shown by the channel maps, and (ii) overestimate N, since we assume that all the emission at the western-most peak in the velocity range 0.2 to 2.6 $\mathrm{km\,s^{-1}}$ is due only to the molecular cloud responsible for the Zeeman effect.

Chamaeleon: We have not mapped Chamaeleon in ^{13}CO. Chamaeleon has been mapped in OH with the Parkes radio telescope by Toriseva et al. (1985). However, as mentioned above, the large beam-size of these observations makes it difficult to determine the cloud size. Therefore, we prefer to use the near-infrared extinction mapping from the DENIS survey (Cambresy et al. 1997). From this study we are able to determine the column density and map size in a very direct manner.

Carina: We have not mapped the Carina Molecular Cloud in ^{13}CO, so we have used the results from the PhD study of Brooks, who has kindly allowed us access to her ^{12}CO and ^{13}CO data which were also collected with the Mopra telescope. We estimate the map size from the ^{12}CO map present in Brooks, Whiteoak & Storey (1998), which provides us with an upper limit to R since ^{12}CO traces lower density gas of $< 10^3$ $\mathrm{cm^{-3}}$, and we estimate the mean column density from ^{13}CO observations of a few positions located within the Parkes OH beam. A distance of 2.5 kpc is assumed. Note that we use the value of $3\sigma_w$ from the entire line profile in Table 2.5.

RCW 57: From the ^{13}CO channel maps presented in Fig. 2A.2 we infer that the NE clump corresponds to the -26.1 $\mathrm{km\,s^{-1}}$ OH absorption component, while the SW clump corresponds to the -22.6 $\mathrm{km\,s^{-1}}$ OH absortion component. The clumps are spatially separated, which implies that high-resolution OH Zeeman observations with the Australia Telescope Compact Array (ATCA) may reveal whether our tentative detection of the Zeeman effect in the -22.6 $\mathrm{km\,s^{-1}}$ component is real. We use the accepted kinematic distance to the H II region of 3.6 kpc in the analysis.

G 326.7+0.6: The ^{13}CO channel maps for the velocity range spanned by the four separate OH absorption components are presented in Figs. 2A.3 – 2A.6. For only three of the molecular clouds do we have sufficient ^{13}CO data to determine N and R with any confidence. For the molecular cloud near -44 km s^{-1} we have an almost complete map and the determination of R is straightforward. The OH line profile for the molecular gas near -22 km s^{-1} has been modelled as a superposition of two Gaussian components, but for the ^{13}CO analysis we treat them as one component and use the value of $3\sigma_w$ in Table 2.5. We estimate from Fig. 2A.4 that we have mapped approximately half of the cloud associated with the -22 km s^{-1} OH component, and determine the cloud size accordingly. The kinematic distance for this component is estimated at 1.5 kpc. We ignore the cloud near -13 km s^{-1} since we have insufficient information to determine any of its properties. For the cloud near -2 km s^{-1} we are able to estimate R and N from the integrated map (not shown), which is just the sum of the channel maps shown in Fig 2A.6. The local CO distance (Schwartz et al. 1988) is estimated to be 150 pc, but an inspection of the UK Schmidt survey plates reveal very little extinction in this region, and therefore we asign a greater distance of 500 pc to the cloud near -2 km s^{-1} (e.g., Bok 1977).

G 327.3–0.5: The channel maps are shown in Fig 2A.7, and the determination of R and N is straightforward. The kinematic distance of 3.3 kpc is assumed.

G 343.4–0.0: The maps for the ^{13}CO emission associated with the OH absorption near -27 km s^{-1} show two distinct clouds, with similar sizes and column densities (Fig 2A.8). We assume that we are seeing the brighter, northern component in the OH absorption profile. If the OH absorption profile is due to both the clouds seen in ^{13}CO, then our value for R is underestimated by about a factor two. However, this would not change the conclusions drawn from the results in Table 2.5. The distance is assumed to be the near kinematic distance of 2.8 kpc. The ^{13}CO emission associated with the 6 km s^{-1} component is very widespread (Fig 2A.9). We assume that we have mapped about half the cloud, but this could be an underestimate. Using the local CO analysis of Schwartz

et al. (1988) the distance is estimated to be 750 pc.

NGC 6334: We have not mapped the ^{13}CO associated with the well studied NGC 6334 region. NGC 6334 has previously been mapped in ^{13}CO by Dickel et al. (1977) with a 70″ beam. From their maps we are able to estimate R for the molecular gas associated with the -3 km s^{-1} OH absorption component, the component associated with the H II region. We have a limited number of our own ^{13}CO observations, enough to estimate N for both velocity components. The distance to the H II region is taken to be 1.7 kpc. We are unable to estimate R for the local gas component near 6 km s^{-1}.

G 8.1+0.2: Observations of this source are virtually non-existent, so we use our OH observations to determine N, as described in the appendix. Since the continuum is weak we assume $T_{ex} \sim 5$ K, and a filling factor of 0.5. No estimation of R is possible. Further observations of this source are required, such as ^{13}CO $J = 1 \rightarrow 0$ observations, as the values determined from the OH observations are very uncertain.

We examine below each hypothesis outlined in §2.1 below. Since the predictions of our simple model are accurate only to within a factor two, we compare our theoretical expectations for the field strength with twice the observed line-of-sight field strength, $2B_{los}$.

(a) Clouds are supported primarily by the mean magnetic field.

For the hypothesis that our simple cloud is supported primarily by the mean magnetic field not to be true requires $B_{\mathcal{MG}} > 2B_{los}$ (or $6\sigma_G$). Since most of our values for B_{los} are upper limits we do not use the result $2B_{los} > B_{\mathcal{MG}}$ as a confirmation of our hypothesis. In Table 2.5 we see that our data shows no strong evidence against the hypothesis that the clouds are supported primarily by the mean magnetic field. There are two cases which may not be in accord with this hypothesis. For Cham I we find that $B_{\mathcal{MG}} \simeq 20$ μG while $2B_{los}$ ($\equiv 2B_G$) $\simeq 18$ μG. For the -26.1 km s^{-1} component of RCW 57, $B_{\mathcal{MG}} \simeq 25$ μG, while $2B_{los}$ $\simeq 24$ μG. For these two sources we thus find $B_{\mathcal{MG}} \simeq 2B_{los}$. Considering the assumptions we made in our simple models and the methods used to determine

the cloud properties, these results are consistent with our hypothesis.

(b) Clouds are supported primarily by the turbulent motions associated with MHD waves.

If molecular clouds are supported primarily by the turbulent motions associated with MHD waves then we expect equipartition between the kinetic, gravitational and magnetic energy densities, and if $B_{\mathcal{MKG}} > 2B_{los}$ then this cannot be true. A comparison of these values in Table 2.5 indicates that in most cases this hypothesis could be valid. Considering the assumptions made in our model in §2.1, the data for all the sources we observed are consistent with molecular clouds being supported against free-fall collapse by the MHD waves.

(c) Clouds are supported primarily by turbulent motions unrelated to the magnetic field.

To examine the hypothesis that magnetic fields are not dominant in molecular cloud support, we compare the observed mean column density N (probably accurate to a factor 2) with our model values of $N_{\mathcal{KG}}$. If $N > N_{\mathcal{KG}}$ then there is evidence that the primary cloud support is due to non-magnetic turbulent motions. In just less than half of our sources (five) we find $N_{\mathcal{KG}} > 2N$, which strongly suggests that this hypothesis cannot hold for those sources. Thus, for about half the sources, we can state that significant support cannot be provided by non-magnetic turbulent motions *if* the clouds are in virial balance on the large scale.

Following Crutcher et al. (1993) we can estimate the number of detections we would expect for the two hypotheses $B = B_{\mathcal{MKG}}$ and $B = B_{\mathcal{MG}}$. For a measurement of the Zeeman effect with sensitivity σ and a detection requirement of $B\cos\theta > 3\sigma$, then for a random orientation of σ the probability of detecting a field strength of B is $P = 1 - 3\sigma/B$. For the case $3\sigma > B$, $P = 0$. The sum of the individual probabilities for each observation is just the predicted number of Zeeman detections for the sample. For $B = B_{\mathcal{MKG}}$ the predicted number of detections is 1.2, while for $B = B_{\mathcal{MG}}$ the prediction is for 0.55 detections. Both hypotheses therefore indicate we would obtain only one detection of the Zeeman

effect in our sample, which is consistent with the actual number of detections of one or two.

In summary, though most of our magnetic field strength measurements are upper limits, these results do not argue against magnetic fields being dynamically important in the large scale support of molecular clouds against free-fall collapse, and in about half the sources studied it can be argued that our results indicate they must be important. In some cases, e.g., Chamaeleon, it is possible that they are not important, and that non-magnetic turbulent motions are sufficient to provide the bulk large scale support against gravity. The question then is, what is the mechanism which provides this turbulence, which is supersonic (from comparison of the thermal sound speed and the observed line-widths), but from the inferred molecular cloud lifetimes cannot be highly dissipative, or at least must be replenished on relatively short timescales (e.g., Shu, Adams & Lizano 1987).

2.5.2. Supersonic linewidths in molecular clouds - MHD waves?

Arons & Max (1975) first suggested that the observed line widths in molecular clouds, much larger than those expected from thermal broadening, could be the result of hydromagnetic wave motions within the cloud. Since our observations probe both the mean magnetic field, through the Zeeman effect, and the turbulent motions within the cloud, through the non-thermal part of the line widths, we are able to examine whether our observations are consistent with their hypothesis (see also Zweibel & Josafatsson 1983; Shu et al. 1987; Myers & Goodman 1988a,b; McKee et al. 1993; Zweibel & McKee 1995). Since we are dealing with directly observable quantities, a comparison of the line widths and magnetic field strengths in order to investigate the possible existence of hydromagnetic waves is likely to lead to more meaningful results than the comparison of B and $B_{\mathcal{MKG}}$ as was undertaken in the previous section.

We assume that perturbations of the magnetic field have strength δB and

act perpendicular to the direction of the mean magnetic field B_o, so that only shear Alfvénic waves are considered. The velocity fluctuations associated with these perturbation have amplitude

$$\delta v \approx v_A \frac{\delta B}{B_o} \tag{2.18}$$

where v_A is the Alfvén speed, and is given by

$$v_A = \frac{B}{(4\pi\rho)^{1/2}} \quad . \tag{2.19}$$

We also assume the perturbations are sub-Alfvénic, i.e., $\delta v \leq v_A$, so $\delta B \leq B_o$ and shocks do not persist (Arons & Max 1975).

Since the magnetic field is orientated at some angle θ to the line-of-sight, we measure $B_{los} = B_o \cos\theta$ from the Zeeman effect, and the wave motions along the line-of-sight at a particular frequency have velocity

$$u = \delta v \sin\theta \cos\phi$$

for a particular phase ϕ of the wave train. We assume that we sample the full range of ϕ (i.e., 0 – 2π) within the beam, and so we measure

$$<u^2>= \frac{1}{2}\delta v^2 \sin^2\theta$$

and eqn. (2.18) implies

$$<u^2>= \frac{\delta B^2 \sin^2\theta}{8\pi\rho} \quad .$$

If we assume the observed line widths are hydromagnetic in origin, then the amplitude of the perturbations are directly related to them, and for the typically large line widths we observe,

$$\Delta v \approx \Delta v_{NT} = u(8\ln 2)^{1/2} = \delta B \sin\theta \left(\frac{\ln 2}{\pi\rho}\right)^{1/2}$$

hence

$$\frac{\delta B}{B_o} \approx \frac{1}{\tan\theta}\frac{\Delta v}{B_{los}}\left(\frac{\pi\rho}{\ln 2}\right)^{1/2} \tag{2.20}$$

where Δv and B_{los} are the observable quantities, and Δv_{NT} is the non-thermal line width. For typical values we can rewrite eqn (2.20) as

$$\frac{\delta B}{B_o} \approx \frac{1.3}{\tan\theta}\left(\frac{\Delta v}{\text{km s}^{-1}}\right)\left(\frac{B_{los}}{10\ \mu\text{G}}\right)^{-1}\left(\frac{n}{10^3\ \text{cm}^{-3}}\right)^{1/2} \quad . \tag{2.21}$$

Table 2.6. Determination of $\delta B/B_o$

Source	V_{lsr} ($km\,s^{-1}$)	δV ($km\,s^{-1}$)	$\mid B_G \mid$ or $3\sigma_G$ (μG)	$\delta B/B_o$		
				$\theta = 15°$	$\theta = 45°$	$\theta = 75°$
Orion B	10.0	1.2	24	2.4	0.7	0.2
RCW 38	1.4	2.3	38	2.9	0.8	0.2
RCW 57	−22.6	6.5	203	1.6	0.4	0.1
Cham I	4.4	1.0	9	5.4	1.4	0.4
G 343.4–0.0	5.7	0.7	9	3.8	1.0	0.3
RCW 57	−26.1	3.4	12	13.7	3.7	1.0
NGC 6334	6.3	1.2	12	4.8	1.3	0.3
G 326.7+0.6	−21.6	1.7	15	5.5	1.5	0.4
NGC 6334	−3.8	4.9	33	7.2	1.9	0.5
G 8.1+0.2	17.5	3.0	45	3.2	0.9	0.2
G 326.7+0.6	−20.8	2.5	54	2.2	0.6	0.2
G 326.7+0.6	−1.9	2.0	63	1.5	0.4	0.1
G 326.7+0.6	−44.8	6.5	69	4.6	1.2	0.3
G 326.7+0.6	−13.3	2.0	81	1.2	0.3	0.1
Carina	−24.9	4.0	90	2.2	0.6	0.2
G 327.3–0.5	−49.0	5.4	105	2.5	0.7	0.2
Carina	−26.2	6.8	126	2.6	0.7	0.2
G 343.4–0.0	−27.4	4.7	153	1.5	0.4	0.1
G 8.1+0.2	13.3	3.3	153	1.0	0.3	0.1

For our observations to be consistent with a wave-like model requires that $\delta B/B_o < 1$. The results are given in Table 2.6. It is immediately obvious from this Table that the majority of the observations are consistent with $\delta B/B_o < 1$, for some angle θ to the line-of-sight. While this does not necessarily imply that the observed line-widths are due to hydromagnetic waves, it clearly does not contradict this idea.

2.6. Conclusions

We observed the OH ground state transitions at 1665 and 1667 MHz toward nine southern galactic sources in an attempt to detect the Zeeman effect and hence measure the magentic field strength. The Zeeman effect was definitely detected in one cloud associated with RCW 38, with a magnetic field strength of 38 ± 2 μG, and possibly in one cloud associated with RCW 57, for which we measure -203 ± 25 μG.

By comparison of observational data on the magnetic field strength B (or sensitive upper limits, $3\sigma_B$), line width Δv, column density N, and cloud size R, with a simple model of a spherical molecular cloud without surface pressure terms, we find no evidence to contradict the following hypotheses:
(a) Clouds are supported primarily by the mean magnetic field.
(b) Clouds are supported primarily by the turbulent motions associated with MHD waves.

However, almost all of our magnetic field strength measurements are upper limits, and so we are unable to conclusively prove or disprove either hypothesis.

A comparison of the observed column density with that expected if the non-magnetic, non-thermal motions are sufficient to support the cloud against gravitational collapse suggests that in about half the clouds observed these non-magnetic motions are insufficient to support the cloud, and another means of large scale support is required.

A more direct test of hypothesis *(b)* was performed by comparing the ob-

served line widths, assuming they arise from hydromagnetic waves, with the observed magnetic field strength. This comparison shows that the observations are consistent with the line widths being due to hydromagnetic wave motions, but again this is not a definitive proof.

As we have seen, detecting the Zeeman effect in molecular clouds is extremely challenging from an observational perspective, and the upper limits we determined, while not contradicting the idea that magnetic fields play a key role in large scale support of molecular clouds, are tantalizingly close to the theoretical values obtained by assuming that they are important in cloud support. A considerable investment of time was required to obtain these measurements, and to bring the magnetic field strength upper limits down to values significantly below the theoretical values predicted by our simple model would require an even greater investment of time. Our aim was to increase significantly the number of magnetic field strength detections. We did not achieve this aim. Since most of the bright OH sources in both hemispheres have now been observed for the Zeeman effect there is probably little progress to be made in further large scale single dish OH Zeeman studies.

It is possible our low detection rate is due to tangling of field lines and/or large scale averaging out of the line-of-sight field strength due to changes in field direction within the telescope beam. Interferometric OH Zeeman studies undertaken to sample the small scale field structure do find significant small scale variations in the field direction, such as line-of-sight reversals. However, these observations come with their own set of problems, such as determining exactly where the OH is excited. The OH may be excited in foreground clouds associated or unassociated with the background H II region, with densities of order 10^3 cm^{-3}, or the region near PDRs where molecules reform, with densities of 10^4 cm^{-3} or higher. See e.g., Roberts et al. 1995; Brogan et al. 1998.

Another avenue for further progress in single dish Zeeman studies is the possibility of using higher frequency transitions, such as CN near 113 GHz and CCS near 11 and 22 GHz, which are thought to trace higher densities ($n(H_2)$ $\gtrsim 10^5$ cm^{-3}) and therefore may probe larger field strengths, since the field is

thought to scale as n^{κ}, where $n \equiv n(H_2)$ is the volume density and κ lies between $^1/_3$ and $^1/_2$ (Troland 1990; Crutcher 1994). However, higher frequencies mean lower sensitivity to the Zeeman effect, as discussed in this chapter, and the performance of receivers and the atmosphere at these frequencies makes these observations very challenging.

REFERENCES

Arons, J., & Max, C. E., 1975, ApJ, 196, L77

Batchelor, R. A., McCulloch, M. G., & Whiteoak, J. B., 1981, MNRAS, 194, 911

Bitran, M., Alvarez, H., Bronfman, L., May, J., & Thaddeus, P., 1997, A&AS, 125, 99

Bok, B. J., 1977, PASP, 89, 597

Brand, J., van der Bij, M. D. P., de Vries, C. P., Israel, F. P., de Graauw, T., van de Stadt, H., Wouterloot, J. G. A., Leene, A., & Habing, H., J., 1984, A&A, 139, 181

Brand, J., & Blitz, J., 1993, A&A, 275, 67

Brogan, C., Troland, T. H., Roberts, D. A., & Crutcher, R. M., 1998, submitted to ApJ

Bronfman, L., Alvarez, H., Cohen, R. S., & Thaddeus, P., 1989, ApJS, 71, 481

Brooks, K. J., 1995, Honours Thesis, Univ. Wollongong (Australia)

Brooks, K. J., Whiteoak, J. B., & Storey, J. W. V., 1998, Publ. Astron. Soc. Aust., in press

Cambrésy, L., Epchtein, N., Copet, E., de Batz, B., Kimeswenger, S., Le Bertre, T., Rouan, D., & Tiphène, D., 1997, A&A, 324, L5

Caselli, P., & Myers, P. C., 1995, ApJ, 446, 665

Caswell, J. L., & Robinson, B. J., 1974, Aust. J. Phys., 27, 597

Caswell, J. L., Haynes, R. F., & Goss, W. M., 1980, Aust. J. Phys., 33, 639

Caswell, J. L., & Haynes, R. F., 1983a, Aust. J. Phys., 36, 361

Caswell, J. L., & Haynes, R. F., 1983b, Aust. J. Phys., 36, 417

Caswell, J. L., & Haynes, R. F., 1987, Aust. J. Phys., 40, 215

Caswell, J. L., & Haynes, R. F., 1987, A&A, 171, 261

Chan, S. J., Henning, Th., & Schreyer, K., 1996, A&AS, 115, 285

Crutcher, R. M., 1977, ApJ, 216, 308

Crutcher, R. M., 1979, ApJ, 234, 881

Crutcher, R. M., 1994, in ASP Conf. Ser. 65, Clouds, Cores, and Low Mass Stars, ed. D. P. Clemens & R Barvainis (San Fransisco: ASP), 87

Crutcher, R. M., & Kazès, I., 1983, A&A, 125, L23 (CK83)

Crutcher, R. M., Kazès, I., & Troland, T. H., 1987, A&A, 181, 119

Crutcher, R. M., Troland, T. H., Goodman, A. A., Heiles, C., Kazès, I., & Myers, P. C., 1993, ApJ, 407, 175

Crutcher, R. M., Roberts, D. A., Troland, T. H., & Goss, W. M., 1998, ApJ, in press

Dame, T., Elmegreen, B., Cohen, R., & Thaddeus, P., 1986, ApJ, 305, 892

de Graauw, T., Lidholm, S., Fitton, B., Beckman, J., Israel, F. P., Nieuwenhuijzen, H., Vermue, J., 1981, A&A, 102, 257

Dickel, H. R., & Wall, J. V., 1974, A&A, 31, 5

Dickel, H. R., Dickel, J. R., & Wilson, W. J., 1977, ApJ, 217, 56

Elitzur, M., 1992, Astronomical Masers (Dordrecht: Kluwer)

Frogel, J. A., & Persson, S. E., 1974, ApJ, 192, 351

Garden, R. P., Hayashi, M., Gatley, I., Hasegawa, T., & Kaifu, N. 1991, ApJ, 374, 540

Gardner, F. F., & Whiteoak, J. B., 1978, MNRAS, 183, 711

Goodman, A. A., 1989, PhD. Thesis, Harvard Univ.

Goodman, A. A., & Heiles, C., 1994, ApJ, 424, 208

Goss, W. M., 1968, ApJS, 15, 131

Goss, W. M., Manchester, R. N., & Robinson, B. J., 1970, Aust. J. Phys., 23, 559

Grabelsky, D. A., Cohen, R. S., Bronfman, L., & Thaddues, P., 1988, ApJ, 331, 181

Hartley, M., Manchester, R. N., Smith, R. M., Tritton, S. B., & Goss, W. M. 1986, A&AS, 63, 27

Heiles, C., 1988, ApJ, 324, 321

Heiles, C., & Stevens, M., 1986, ApJ, 301, 331

Heiles, C., Goodman, A. A., McKee, C. F., & Zweibel, E. G., 1993, in Protostars and Planets III, ed. E. H. Levy & J. I. Lunine (Tucson: Univ. Arizona Press), 279

Ho, P. T. P., Moran. J. M., & Rodríguez, L. F. 1982, ApJ, 262, 619

Kazès, I., & Crutcher, R. M., 1986, A&A, 164, 328

Kazès, I., Troland, T. H., Crutcher, R. M., & Heiles, C., 1988, ApJ, 335, 263

Kramer, K. E., 1998, PhD Thesis, Boston Univ.

Kutner, M. L., & Ulich, B. L., 1981, ApJ, 250, 341

Larson, R. B., 1981, MNRAS, 194, 809

Manchester, R. N., Robinson, B. J., & Goss, W. M., 1970, Aust. J. Phys., 23, 751

Massi, F., Brand, J., & Felli, M., 1997, A&A, 320, 972

Megeath, S. T., Cox, P., Bronfman, L., Roelfsema, P. R., 1996, A&A, 305, 296

McGregor, P. J., Harrison, T. E., Hough, J. H., & Bailey, J. A., 1994, MNRAS, 267, 755

McKee, C. F., Zweibel, E. Goodman, A. A., & Heiles, C., 1993, in Protostars and Planets III, ed. E. H. Levy & J. I. Lunine (Tucson: Univ. Arizona Press), 327

Moorey, G. G., Sinclair, M. W., & Payne, J. M., 1997, in IAU Symp. 170, CO: Twenty-Five Years of Millimeter-Wave Spectroscopy, eds. W. B. Latter, S. J. E., Radford, P. R. Jewell, J. G. Magnum, & J. Bally (Dordrecht: Kluwer), 441

Myers, P. C., 1983, ApJ, 270, 105

Myers, P. C., 1995, in Molecular Clouds and Star Formation, ed. C. Yuan & J. You (Singapore; World Scientific), 47

Myers, P. C., Ho, P. T. P., Schneps, M. H., Chin, G., Pankonin, V., & Winnberg, A., 1978, ApJ, 220, 864

Myers, P. C., & Goodman, A. A., 1988a, ApJ, 326, L27

Myers, P. C., & Goodman, A. A., 1988b, ApJ, 329, 392

Myers, P. C., & Goodman, A. A., 1991, ApJ, 373, 509

Neckel, T., 1978, A&A, 69, 51

Peng, R. S., & Whiteoak, J. B., 1992, MNRAS, 254, 301

Persi, P., Roth, M., Tapia, M., Ferrari-Toniolo, M., & Marenzi, A. R., 1994, A&A, 282, 474

Radford, H. E., 1961, Phys. Rev., 122, 114

Reid, M. J., & Silverstein, E. M., 1990, ApJ, 361, 483

Roberts, D. A., Crutcher, R. M., & Troland, T. H., 1995, ApJ, 442, 208

Robinson, B. J., Goss, W. M., & Manchester, R. N., 1970, Aust. J. Phys., 23, 363

Robinson, B. J., Caswell, J. L., & Goss, W. M., 1971, Astrophys. Lett., 9, 5

Rohlfs, K., & Wilson, T. L., 1996, Tools of Radio Astronomy (Berlin: Springer-Verlag)

Sault, R. J., Killeen, N. E. B., Zmuidzinas, J., & Loushin, R., 1990, ApJS, 74, 437

Schwartz, P. R., Gee, G., & Huang, Y. -L., 1988, ApJ, 327, 350

Schwartz, R. D., 1991, in Loss Mass Star Formation in Southern Molecular Clouds, ESO Scientific Report 11, ed. B. Reipurth (Garching: ESO), 93

Shu, F. H., Adams, F. C., & Lizano, S., 1987, ARA&A, 25, 23

Tapia, M., Roth, M., Marraco, H., & Ruiz, M. T., 1988, MNRAS, 232, 661

Toriseva, M., Höglund, B., & Mattila, K., 1985, Rev. Mexicana Astron. Af., 10, 135

Townes, C. H., & Schawlow, A. L., 1975, Molecular Spectroscopy (New York: Dover)

Troland, T. H., 1990, in Galactic and Intergalactic Magnetic Fields, ed. R. Beck, P. P. Kronberg, & R. Wielebinski (Dordrecht: Kluwer), 293

Troland, T. H., Crutcher, R. M., & Kazès, I., 1986, ApJ, 304, L57

Troland, T. H., & Heiles, C., 1982, ApJ, 252, 179

Turner, B. E., 1979, A&AS, 37, 1

Turner, B. E., & Heiles, C., 1971, ApJ, 170, 453

Whiteoak, J. B., & Gardner, F. F., 1974, A&A, 37, 389

Whiteoak, J. B., & Gardner, F. F., 1978, MNRAS, 185, 33P

Whiteoak, J. B., Otrupcek, R. E., & Rennie, C. J., 1982, Publ. Astron. Soc. Aust., 4, 434

Whiteoak, J. B., & Otrupcek, R. E., 1984, Proc. Astron. Soc. Aust. 5, 552

Whiteoak, J. B., Gardner, F. F., Manefield, G. A., Hoglund, B., & Johansson, L. E. B., 1985, Publ. Astron. Soc. Aust., 6, 6

Wouterloot, J. G. A., & Habing, H. J., 1985, A&AS, 60, 43

Zeeman, P., 1895, ApJ, 5, 332

Zweibel, E. G., & McKee, C. F., 1995, ApJ, 439, 779

Zweibel, E. G., & Josafatsson, K., 1983, ApJ, 270, 511

2A. ^{13}CO J = 1 → 0 Mapping of Clouds Observed for the Zeeman Effect

In order to determine the size R and average column density N for the clouds in our Zeeman survey, we have attempted to map them in the ^{13}CO $J = 1 \rightarrow 0$ transition with the ATNF Mopra telescope (Moorey, Sinclair & Payne, 1997). OH and ^{13}CO are believed to trace similar gas densities of $\sim 2 \times 10^3$ cm^{-3} (e.g., Myers et al. 1978; Heiles et al. 1993), but the typical beam size for ^{13}CO observations is $\sim 1'$, compared with $\sim 10'$ for single dish OH observations. Thus ^{13}CO is the preferred tracer of the densities we are probing with our Zeeman observations as discussed in more detail in §2.5.1. In addition, aside from the poor spatial resolution of the OH observations, we are generally observing OH in absorption, which makes the determination of R improbable.

We now present the usual analysis for OH data and outline the uncertainties involved in its use.

The equation of radiative transfer may be expressed as (e.g. Ho, Moran, & Rodríguez 1982)

$$T_{mb} = f[J(T_{ex}) - J(T_C)][1 - \exp(-\tau)] \ , \qquad (2A.1)$$

where T_{mb} is the main-beam brightness temperature, τ is the optical depth of the cloud in the molecular transition, f is the filling factor, T_{ex} is the excitation temperature of the transition, T_C is the combined background temperature (the cosmic background temperature T_{bg} plus any contribution from a background continuum source, T_S), and

$$J(T) = \frac{h\nu}{k} \frac{1}{\exp(h\nu/kT) - 1} \ .$$

At the frequencies of the OH ground state transitions near 1.6 GHz $J(T) \equiv T$ for the temperatures observed in molecular clouds ($T \lesssim 100$ K), and so

$$T_{mb} = f[T_{ex} - T_C][1 - \exp(-\tau)] \ . \qquad (2A.2)$$

The observed antenna temperature T_A^* is proportional to T_{mb}, with a proportionality constant η_{mb} (the main beam efficiency) which is the same for both the

1665 and 1667 MHz OH transitions. Therefore the ratio of observed antenna temperatures is

$$\frac{T_A^*(1667)}{T_A^*(1665)} = \frac{T_{ex}(1667) - T_C}{T_{ex}(1665) - T_C} \frac{1 - \exp(-\tau_{1667})}{1 - \exp(-\tau_{1665})} \quad . \tag{2A.3}$$

If the transitions are in LTE then $T_{ex}(1665) = T_{ex}(1667)$ and $\tau_{1665} = 0.552\tau_{1667}$ and eqn. (2A.3) simplifies to

$$\frac{T_A^*(1667)}{T_A^*(1665)} = \frac{1 - \exp(-\tau_{1667})}{1 - \exp(-0.552\tau_{1667})} \quad , \tag{2A.4}$$

which may be solved for τ_{1667} and hence $T_{ex}(1667)$. With this knowledge it is possible to determine the column density of OH, $N(\mathrm{OH})$, which is given by (Goss 1968; Turner & Heiles 1971)

$$N(\mathrm{OH}) = \frac{8\pi \mathrm{k}\nu}{\mathrm{hc^2 A}} T_{ex} \frac{\sum \mathrm{g_i}}{\mathrm{g_u}} \int \tau \mathrm{d}\nu \quad , \tag{2A.5}$$

where ν is the frequency of the transition and A is its Einstein A coefficient, g_i is the statistical weight for level i and g_u is the statistical weight for the upper state of the transition. Thus

$$\begin{aligned} N(\mathrm{OH}) &= 4.25 \times 10^{16} \left(\frac{T_{ex}(1667)}{\mathrm{K}}\right) \tau_{1667} \left(\frac{\Delta\nu}{\mathrm{MHz}}\right) \mathrm{cm}^{-2} \quad . \\ &= 2.25 \times 10^{14} \left(\frac{T_{ex}(1667)}{\mathrm{K}}\right) \tau_{1667} \left(\frac{\Delta v}{\mathrm{km\,s^{-1}}}\right) \mathrm{cm}^{-2} \quad . \end{aligned} \tag{2A.6}$$

Although we could use the OH observations to infer the column density N, there are pitfalls with this analysis (e.g., Crutcher 1977, 1979). The most important is the often used assumption of a common excitation temperature for the 1665 and 1667 transitions due to the assumption of LTE, which can result in determinations of the optical depths and hence column densities which are an order of magnitude too high. In addition, the conversion from $N(\mathrm{OH})$ to $N(\mathrm{H_2})$ is not well known.

The optical depth of OH could be found, in principle, directly for sources observed in absorption against a background source of antenna temperature T_S, from the equation of radiative transfer in the Rayleigh-Jeans approximation

$$\tau = -\ln\left[1 - \frac{T_{mb}}{f(T_{ex} - T_S - T_{bg})}\right] \tag{2A.7}$$

where T_{bg} is the cosmic background temperature. However, our poor knowledge of T_{ex} and f (due to the large beam sizes – see e.g., §12.4.1 of Rohlfs & Wilson 1996) for most sources makes this equation difficult to use in practice.

We thus use ^{13}CO observations to determine the properties of the gas which we are sampling with the Zeeman effect. The total column density N of a linear, rigid rotor, molecule such as CO can be derived from the optical depth, τ, and excitation temperature, T_{ex}, of a rotational transition at frequency ν, using the expression (e.g. Garden et al. 1991)

$$N = \frac{3h}{8\pi^3\mu^2} \frac{k(T_{ex} + hB/3k)}{(J+1)hB} \frac{\exp(E_J/kT_{ex})}{1-\exp(-h\nu/kT_{ex})} \int \tau d\nu \quad , \tag{2A.8}$$

where μ is the permanent dipole moment and J is the rotational quantum number of the lower state. This expression assumes that all energy levels are populated according to LTE at the temperature T_{ex}.

The total column density of ^{13}CO can be determined from ^{13}CO $J = 1 \rightarrow 0$ observations by assuming the emission is optically thin. This assumption is shown to be true in most cases for the clouds in our sample by a comparison of the ^{12}CO $J = 1 \rightarrow 0$ and ^{13}CO $J = 1 \rightarrow 0$ intensities (e.g., the CO survey of the Hartley et al. (1986) Southern Dark Clouds by Otrupcek et al. (in preparation), using the Mopra radiotelescope). The total column density is then given by

$$N(^{13}\mathrm{CO}) = 2.42 \times 10^{14} F(T_{ex}) \int T_{mb}(^{13}\mathrm{CO}) dv \tag{2A.9}$$

where

$$F(T_{ex}) = \frac{T_{ex} + 0.88}{1-\exp(-5.29/T_{ex})} \frac{1}{J(T_{ex}) - J(T_{bg})}$$

with $\int T_{mb}(^{13}\mathrm{CO}) dv$ expressed in K km s^{-1}, and N in cm^{-2}. For $T_{ex} \sim 10$ K, $F(T_{ex}) \sim 4$, and increases to ~ 8 for $T_{ex} \sim 35$ K, which is the typical range of values for T_{ex} for the clouds we are observing (e.g., Myers et al. 1978). Thus assuming $F(T_{ex}) = 6$ will allow the determination of N to within a factor 2, ignoring the uncertainties in the other variables. The average column density $N(\mathrm{H_2})$ may then be found by a suitable choice of the abundance ratio of ^{13}CO to $\mathrm{H_2}$, which we take to be $[\mathrm{H_2}/^{13}\mathrm{CO}] = 5 \times 10^5$ (e.g., Rohlfs & Wilson 1996).

2A.1. Observations

The observations of ^{13}CO $J = 1 \rightarrow 0$ were undertaken in April 1997 with the 22 m ATNF Mopra radiotelescope. At the ^{13}CO $J = 1 \rightarrow 0$ frequency of 110201.37 MHz only the inner 15 m of the surface is illuminated, providing an effective beam size of 45″.

The receiver was a dual linear polarization SIS receiver with a total system temperature measured to be $\sim$ 150 K in good weather. The 16384 channel autocorrelator was configured for two IFs, providing a velocity resolution of 0.17 $\mathrm{km\,s^{-1}}$ over a velocity range of $\sim$ 220 $\mathrm{km\,s^{-1}}$ (1024 spectral channels with a 64 MHz bandwidth) at the ^{13}CO $J = 1 \rightarrow 0$ frequency. One IF was centred on the ^{13}CO $J = 1 \rightarrow 0$ frequency, the second being centred on the SiO $\nu = 1$, $J = 2 \rightarrow 1$ transition at 86243.44 MHz for regular pointing checks using SiO masers listed in the SEST (Swedish-European Submillimetre Telescope) Handbook.

The mapping was performed on a 1′ grid in position switching mode, with an on-source integration time of 4 minutes per position. As the weather conditions were stable we were able to use reference sharing, using the same off-position spectrum for multiple on-source positions for each map to allow for the removal of the instumental spectrum and variations of the system response with frequency across the bandwidth. Removal of first-order baselines was sufficient in most cases to correct for any system effects not removed by the reference observation.

The spectra were calibrated offline for atmospheric attenuation and the variation of telescope beam efficiency with elevation, and the intensity scaled to the T_A^* scale of SEST by observations of Orion ($\alpha_{1950} = 05^{\mathrm{h}}32^{\mathrm{m}}47\overset{\mathrm{s}}{.}0$, $\delta_{1950} = -05°24'23''$) in the ^{13}CO $J = 1 \rightarrow 0$ transition, assuming $T_A^*(\mathrm{Orion}) = 13$ K (Appendix C of the SEST Handbook, V2.1). The conversion to T_{mb} is given by $T_{mb} = T_A^*/\eta_{mb}^{\mathrm{SEST}}$ where $\eta_{mb}^{\mathrm{SEST}} = 0.7$ near 110 GHz.

In general we attempted to map down to at least the 50% level of the peak emission in each source. The individual spectra were then converted to CLASS

format, and spectral cubes were formed for each source, to allow for interactive map examination with `aipsview`, part of the forthcoming AIPS++ package.

2A.2. Results

The data are presented here as channel maps, and are shown in Figs 2A.1 – 2A.9. The contours are 30, 50, 70, and 90% of the peak emission *over the velocity range plotted in each panel*, with the heavy contour marking the 50% contour. The individual sources are discussed in §2.5.1. In the analysis of column densities we have assumed $T_{ex}(^{13}\mathrm{CO}) = 20$ K, so $F(T_{ex}) \sim 6$. Distance estimates for the individual sources are discussed in the text, and are generally extracted from the literature, or the kinematic distance has been determined from the OH velocity and the rotation curve of Brand & Blitz (1993).

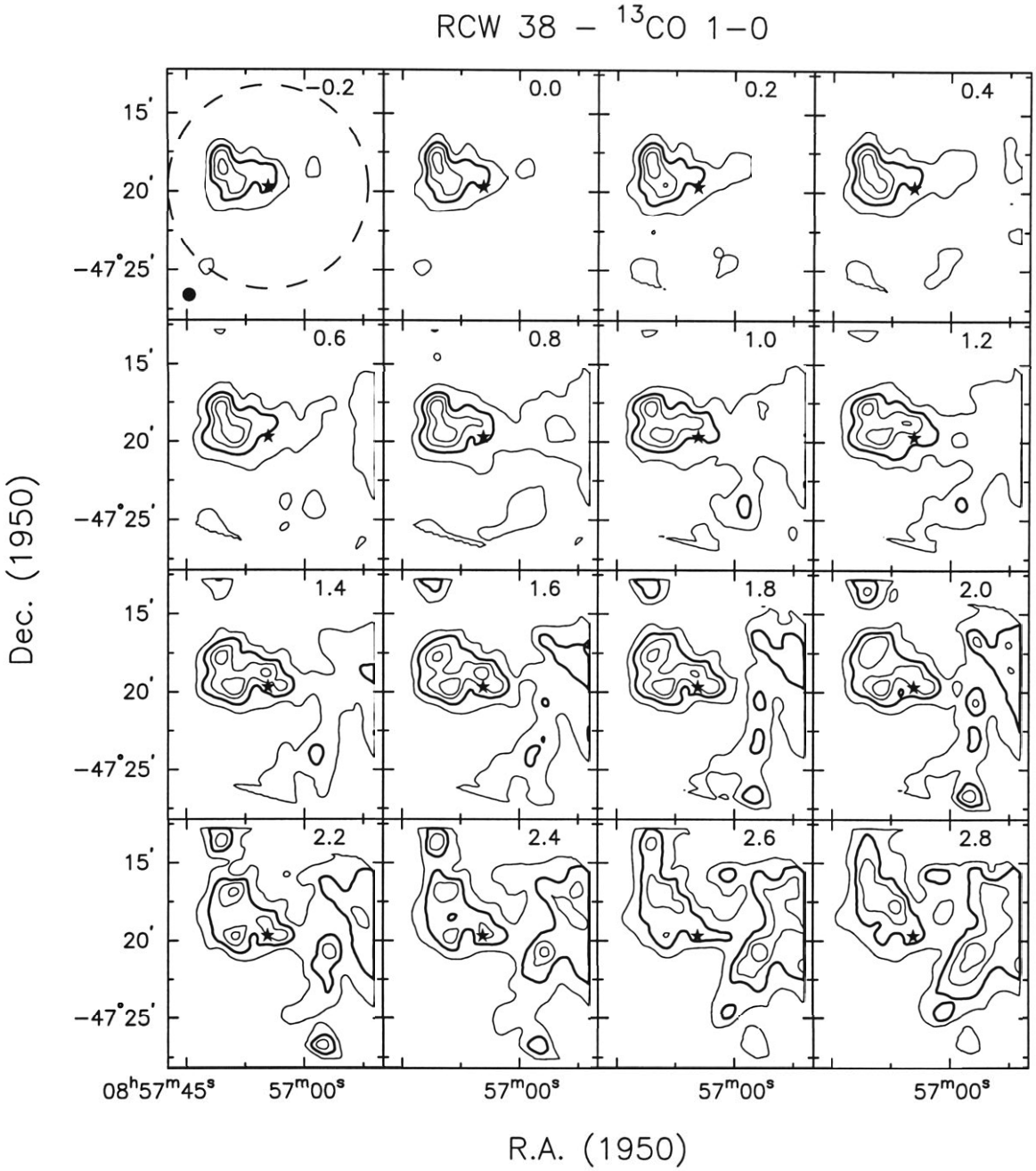

Figure 2A.1.— ^{13}CO $J = 1 \rightarrow 0$ channel maps for RCW 38. The velocity for each panel is indicated in the upper right. The Mopra beam size is shown in the lower left of the first panel as a filled circle, and the Parkes OH beam size is indicated by the dashed circle, which is centred on the position observed for the Zeeman effect (indicated with a star). Contours are 30, 50, 70, and 90% of the peak emission for the velocity range shown. The heavy contour is the 50% contour.

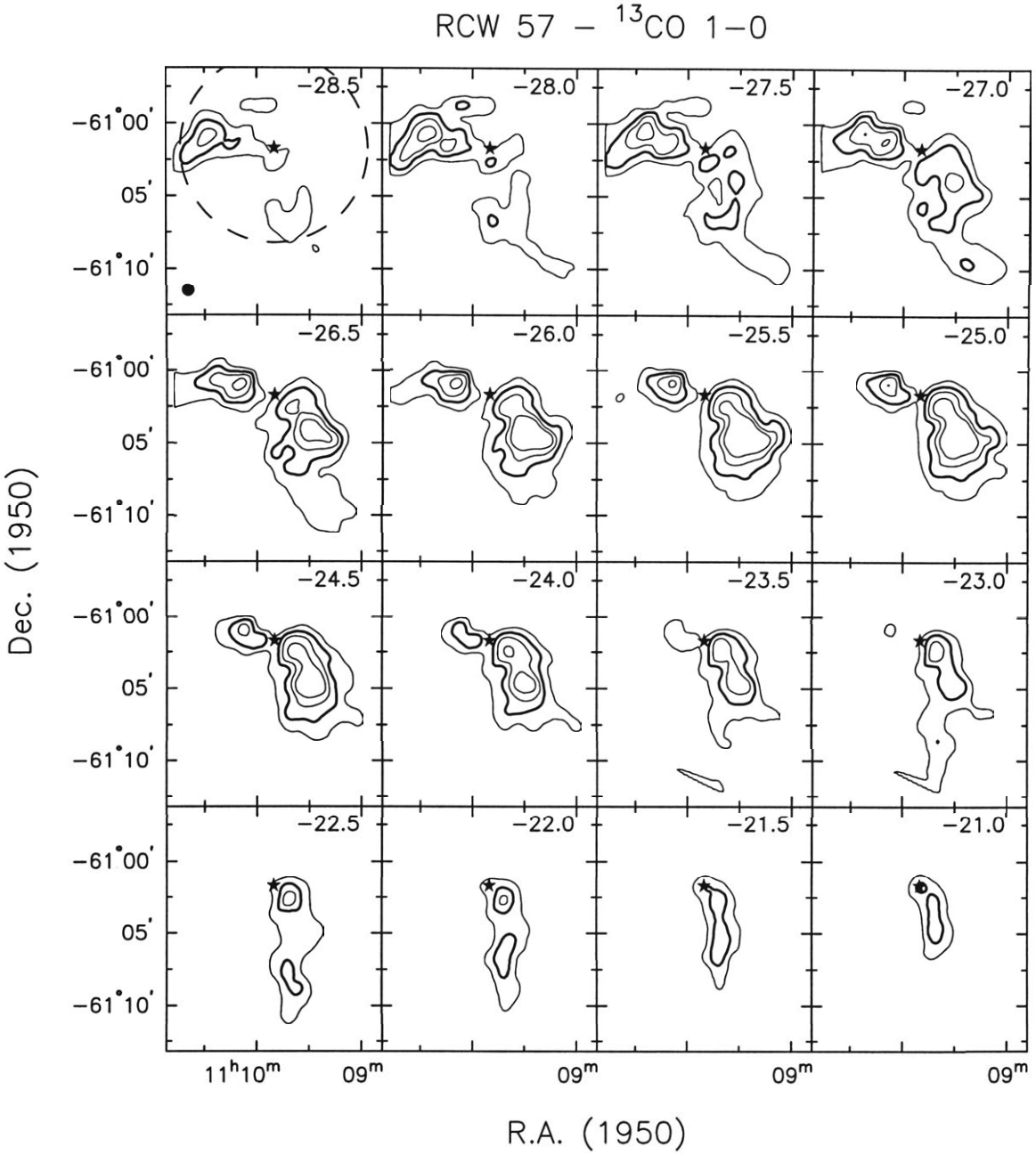

Figure 2A.2.— ^{13}CO $J = 1 \rightarrow 0$ channel maps for RCW 57. The velocity for each panel is indicated in the upper right. The Mopra beam size is shown in the lower left of the first panel as a filled circle, and the Parkes OH beam size is indicated by the dashed circle, which is centred on the position observed for the Zeeman effect (indicated with a star). Contours are 30, 50, 70, and 90% of the peak emission for the velocity range shown. The heavy contour is the 50% contour.

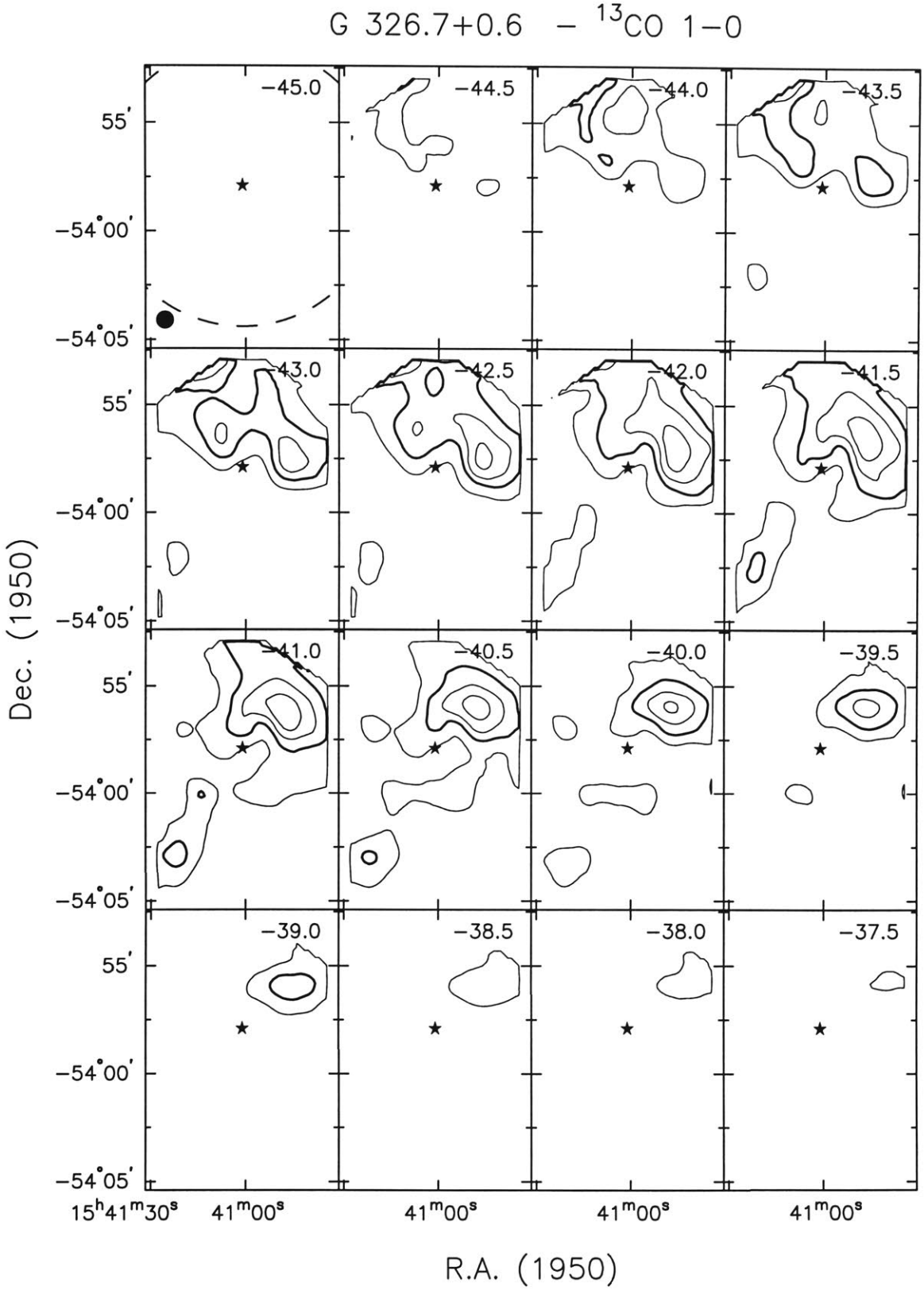

Figure 2A.3.— ^{13}CO $J = 1 \rightarrow 0$ channel maps corresponding to the OH -44 km s^{-1} component of G 326.7+0.6. The velocity for each panel is indicated in the upper right. The Mopra beam size is shown in the lower left of the first panel as a filled circle, and the Parkes OH beam size is indicated by the dashed circle, which is centred on the position observed for the Zeeman effect (indicated with a star). Contours are 30, 50, 70, and 90% of the peak emission for the velocity range shown. The heavy contour is the 50% contour.

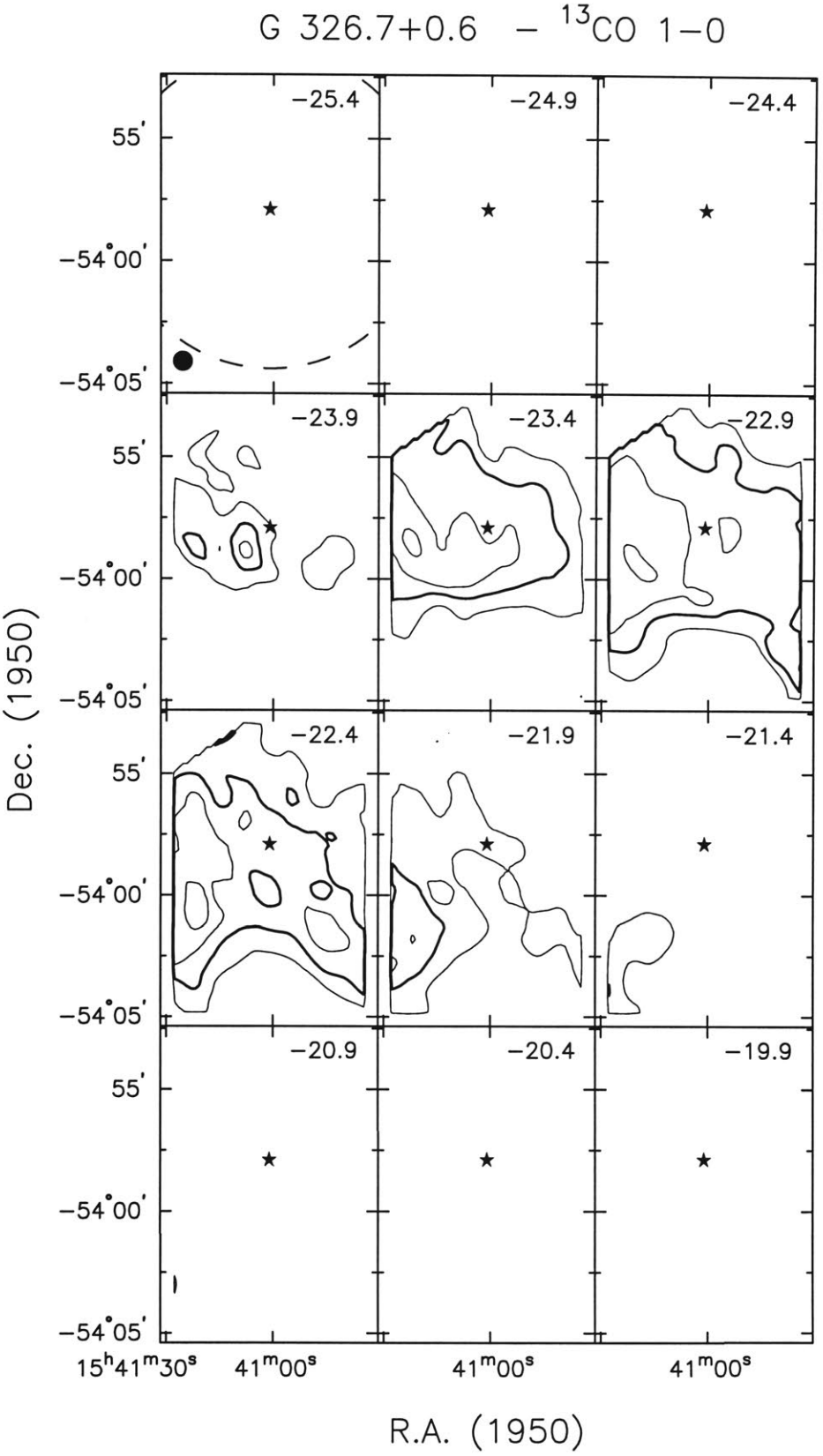

Figure 2A.4.— ^{13}CO $J = 1 \rightarrow 0$ channel maps corresponding to the OH -22 km s^{-1} component of G 326.7+0.6. The velocity for each panel is indicated in the upper right. The Mopra beam size is shown in the lower left of the first panel as a filled circle, and the Parkes OH beam size is indicated by the dashed circle, which is centred on the position observed for the Zeeman effect (indicated with a star). Contours are 30, 50, 70, and 90% of the peak emission for the velocity range shown. The heavy contour is the 50% contour.

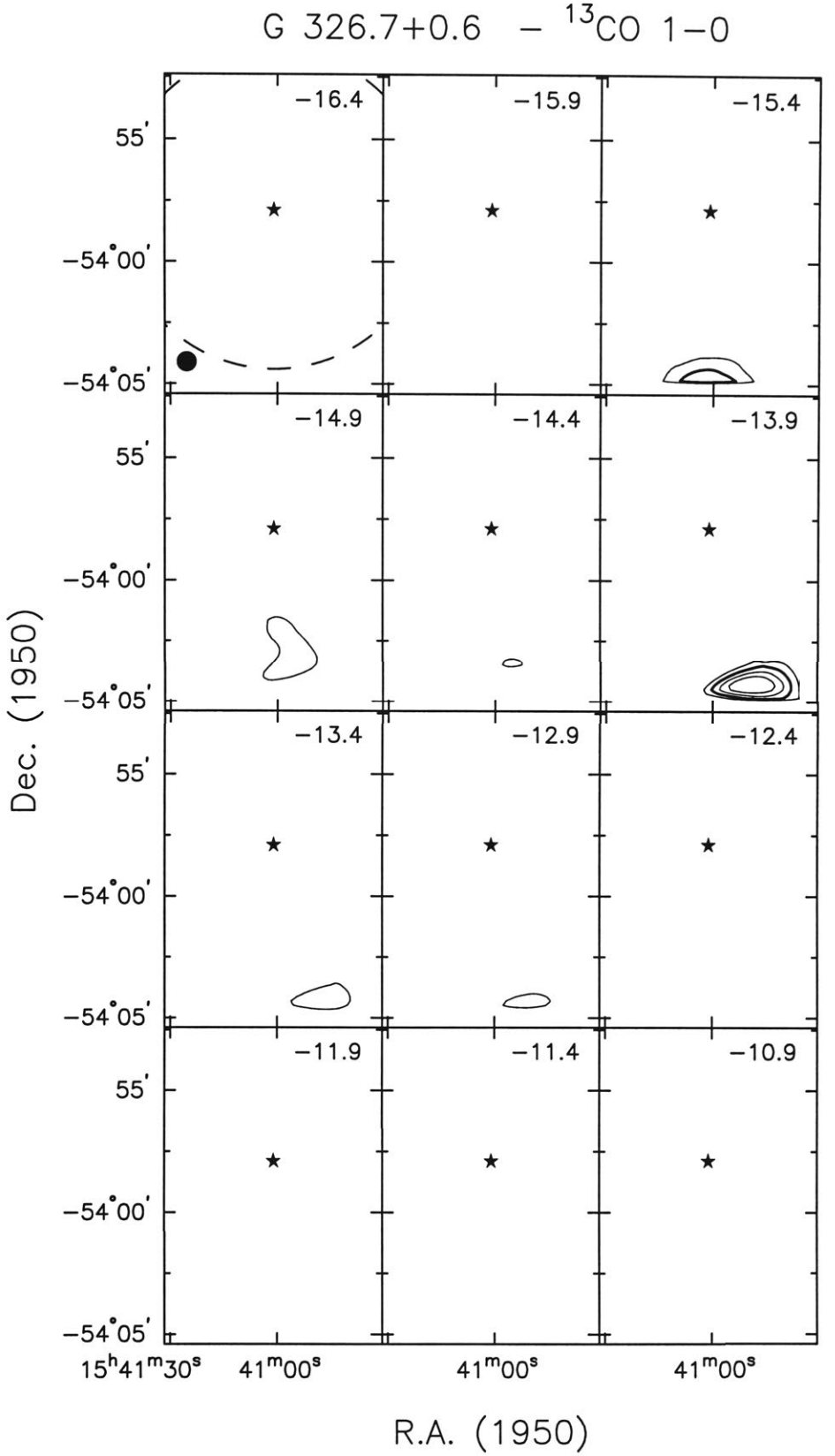

Figure 2A.5.— ^{13}CO $J = 1 \rightarrow 0$ channel maps corresponding to the OH -13 km s^{-1} component of G 326.7+0.6. The velocity for each panel is indicated in the upper right. The Mopra beam size is shown in the lower left of the first panel as a filled circle, and the Parkes OH beam size is indicated by the dashed circle, which is centred on the position observed for the Zeeman effect (indicated with a star). Contours are 30, 50, 70, and 90% of the peak emission for the velocity range shown. The heavy contour is the 50% contour.

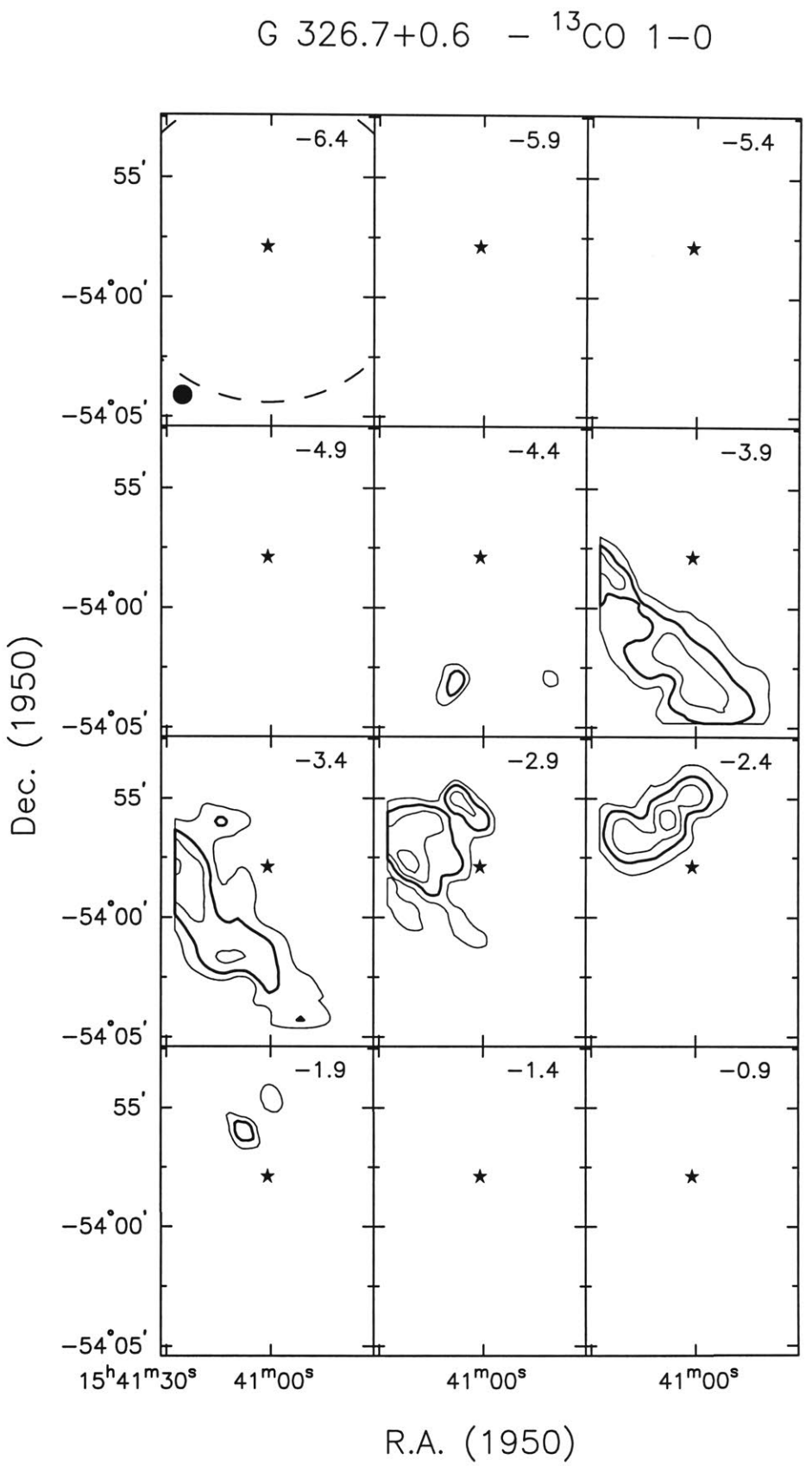

Figure 2A.6.— ^{13}CO $J = 1 \rightarrow 0$ channel maps corresponding to the OH -2 km s^{-1} component of G 326.7+0.6. The velocity for each panel is indicated in the upper right. The Mopra beam size is shown in the lower left of the first panel as a filled circle, and the Parkes OH beam size is indicated by the dashed circle, which is centred on the position observed for the Zeeman effect (indicated with a star). Contours are 30, 50, 70, and 90% of the peak emission for the velocity range shown. The heavy contour is the 50% contour.

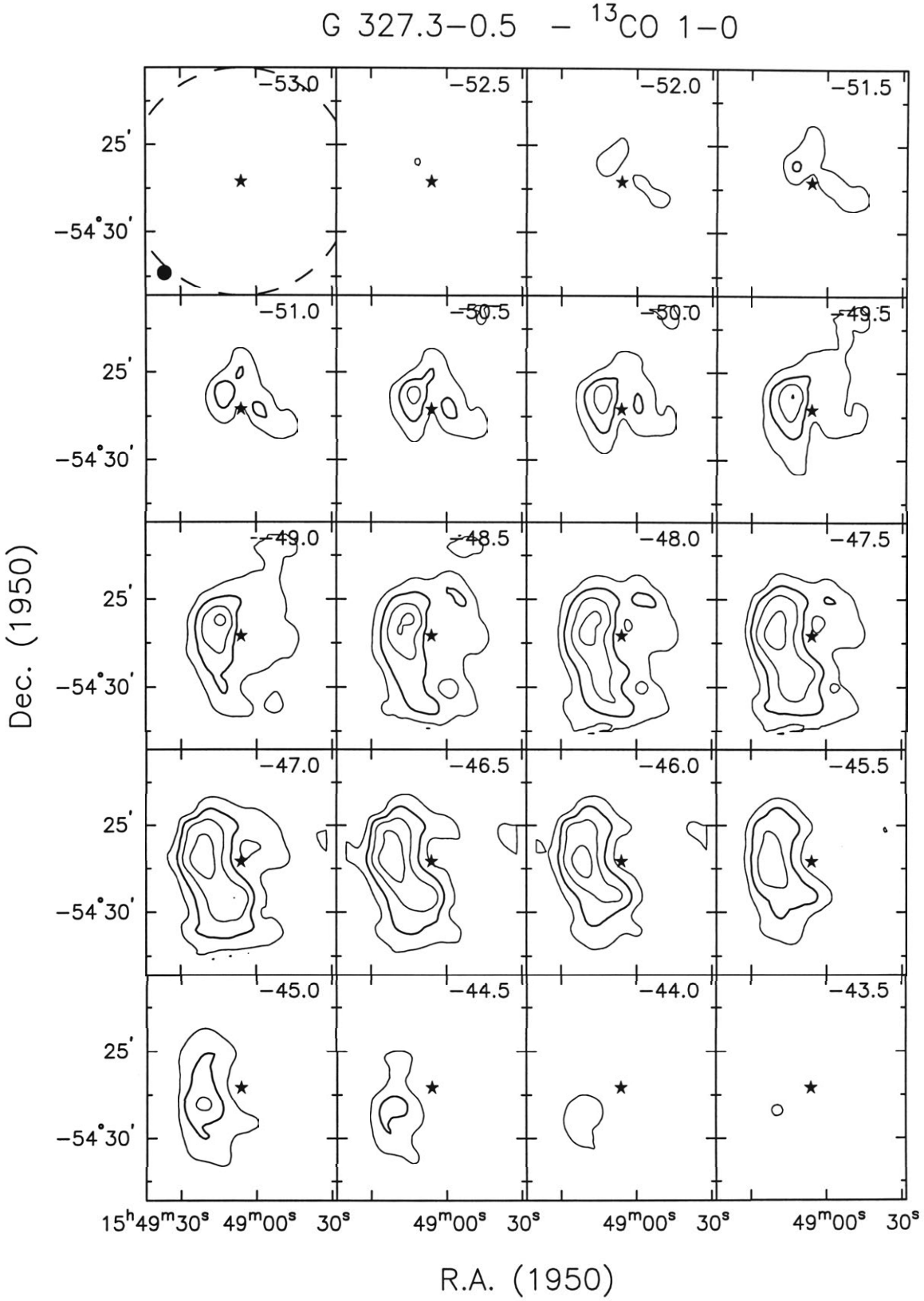

Figure 2A.7.— ^{13}CO $J = 1 \rightarrow 0$ channel maps for G 327.3–0.5. The velocity for each panel is indicated in the upper right. The Mopra beam size is shown in the lower left of the first panel as a filled circle, and the Parkes OH beam size is indicated by the dashed circle, which is centred on the position observed for the Zeeman effect (indicated with a star). Contours are 30, 50, 70, and 90% of the peak emission for the velocity range shown. The heavy contour is the 50% contour.

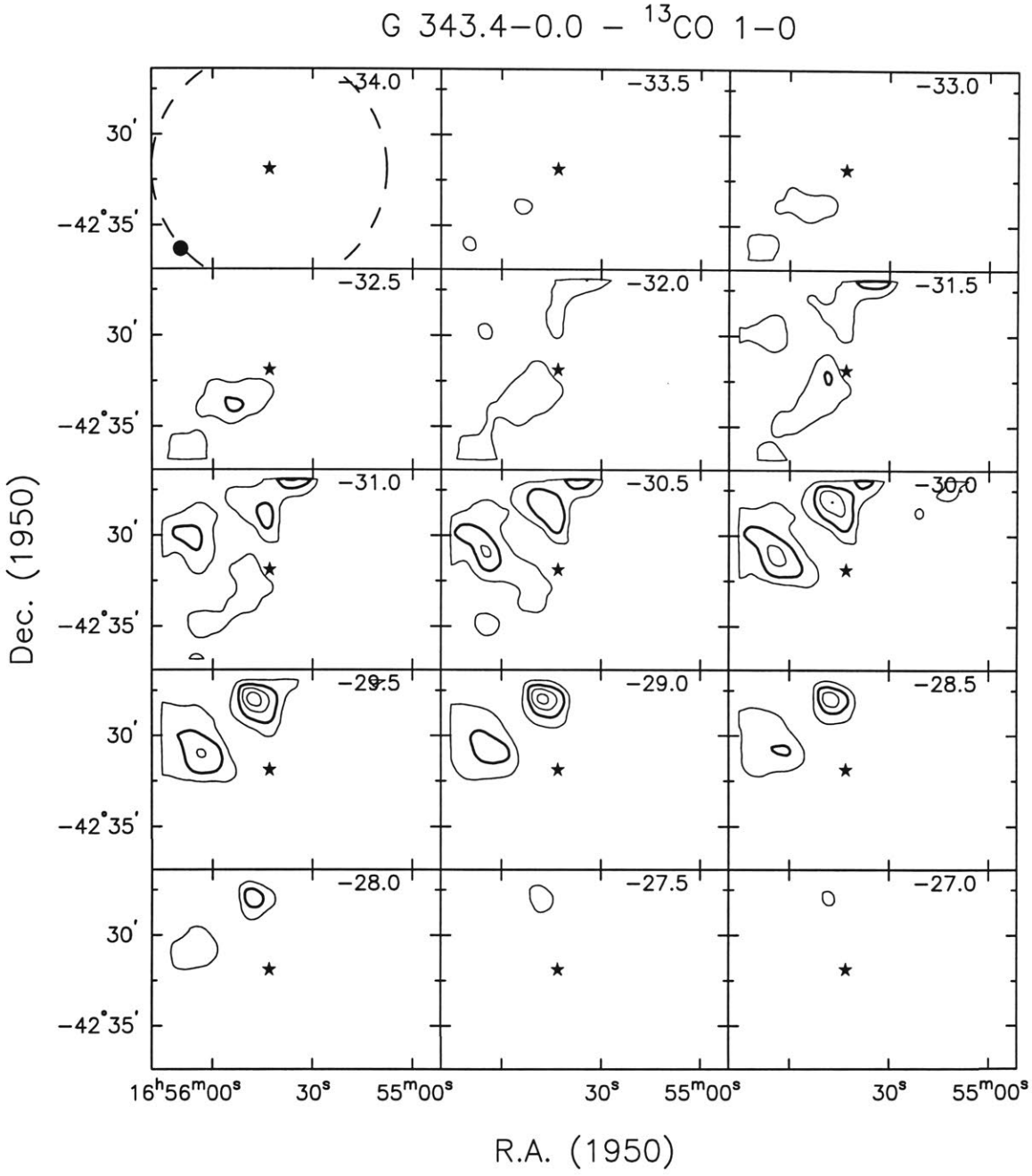

Figure 2A.8.— ^{13}CO $J = 1 \rightarrow 0$ channel maps corresponding to the OH -27 km s^{-1} component of G 343.4–0.0. The velocity for each panel is indicated in the upper right. The Mopra beam size is shown in the lower left of the first panel as a filled circle, and the Parkes OH beam size is indicated by the dashed circle, which is centred on the position observed for the Zeeman effect (indicated with a star). Contours are 30, 50, 70, and 90% of the peak emission for the velocity range shown. The heavy contour is the 50% contour.

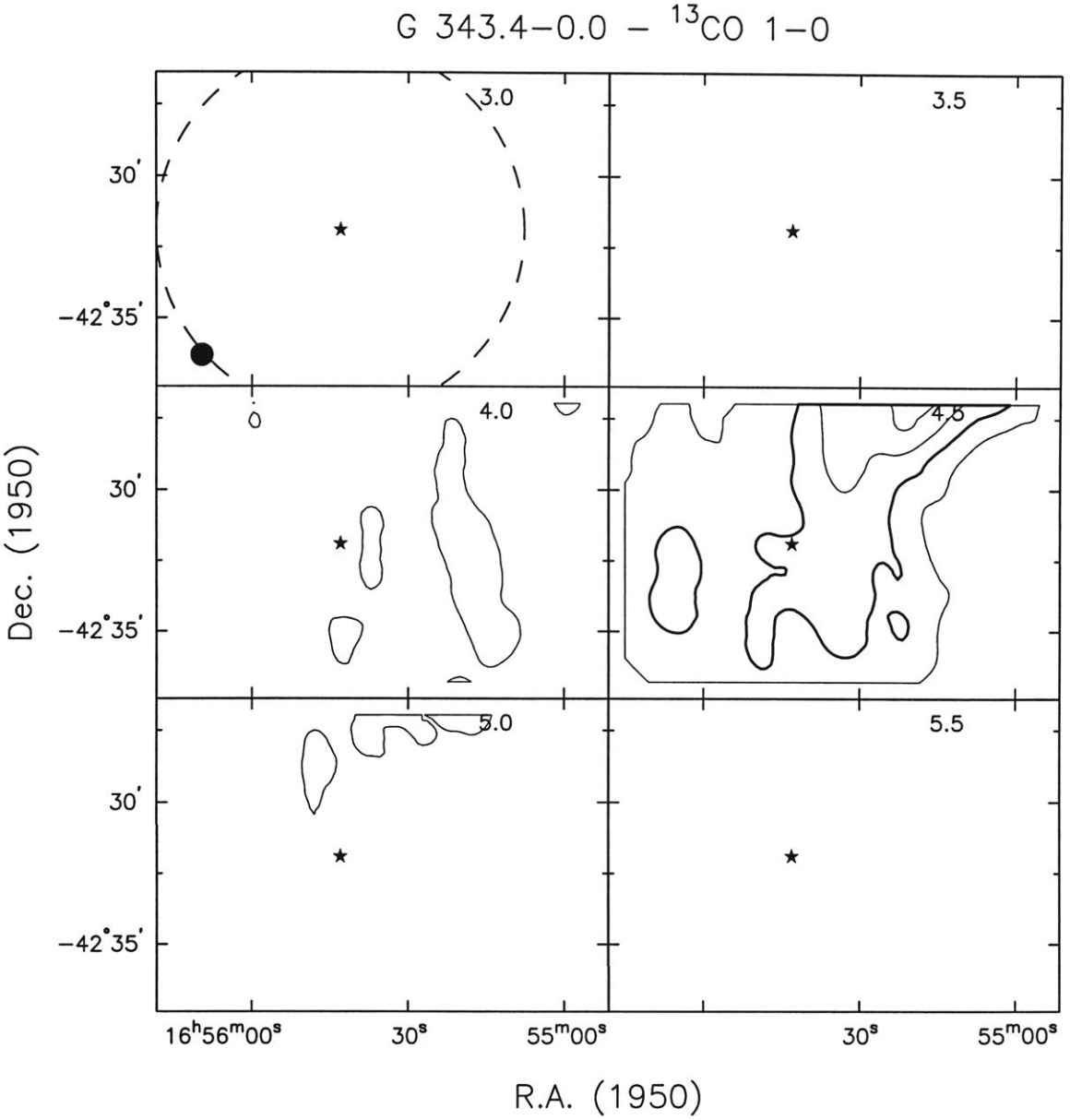

Figure 2A.9.— ^{13}CO $J = 1 \rightarrow 0$ channel maps corresponding to the OH 6 km s^{-1} component of G 343.4–0.0. The velocity for each panel is indicated in the upper right. The Mopra beam size is shown in the lower left of the first panel as a filled circle, and the Parkes OH beam size is indicated by the dashed circle, which is centred on the position observed for the Zeeman effect (indicated with a star). Contours are 30, 50, 70, and 90% of the peak emission for the velocity range shown. The heavy contour is the 50% contour.

Chapter 3

Discovery of a highly collimated molecular outflow in the southern Bok globule BHR 71[1]

[1]Bourke, T. L., Garay, G., Lehtinen, K. K., Köhnenkamp, I., Launhardt, R., Nyman, L-Å., May, J., Robinson, G., & Hyland, A. R., 1997, ApJ, 476, 781-800

ABSTRACT

We report observations of the southern Bok globule BHR 71 in the $J = 1 \rightarrow 0$ and $J = 2 \rightarrow 1$ lines of ^{12}CO, the $J = 1 \rightarrow 0$ lines of ^{13}CO and C^{18}O, and $(J,K) = (1,1)$ and (2,2) inversion lines of NH_3 made with angular resolution of $\sim 20''$ to $\sim 9'$. We also report 1.3 mm continuum observations made with SEST with $\sim 20''$ resolution. The low angular resolution molecular observations indicate that the globule has a diameter of ~ 0.5 pc, a kinetic temperature of 11 K, a total mass of $\sim 40\ M_\odot$, and an average molecular density of $\sim 9 \times 10^3$ cm^{-3}. The high angular resolution observations reveal the presence, near the center of the globule, of a highly collimated bipolar outflow with lobes extending by ~ 0.3 pc in opposite directions from a strong 1.3 millimeter continuum source. The morphology and velocity structure of the flow is found to be well described by a biconical outflow that is inclined from the line of sight at an angle of $\sim 84°$, has a semi-opening angle of 15°, and in which the gas moves outwards with an approximate constant radial velocity (with respect to the cone apex) of ~ 28 km s^{-1}. The outflow appears to be driven by a very young stellar object with $L_{bol} \sim 9\ L_\odot$, whose characteristics at infrared and millimeter wavelengths are similar to those of the so-called Class 0 sources.

3.1. Introduction

Bok & Reilly (1947) first suggested that small (angular sizes of a few arc minutes) dark clouds, now known as Bok globules, might be gravitationally unstable and hence potential sites for the formation of low mass stars. This hypothesis has proven to be correct by a wealth of infrared and submillimeter observations which show that the presence of heavily obscured low-mass embedded sources in Bok globules is quite common (e.g. Yun & Clemens 1990, 1994, 1995; Launhardt & Henning 1994). Further, there is increasing observational evidence that as they are being formed, low mass stars undergo periods of copious mass loss. This ubiquitous phenomenon is observationally manifested by the presence of Herbig-Haro objects (see review by Reipurth 1991), optical jets (see review by Mundt 1988), and highly supersonic molecular outflows (see reviews of Bachiller & Gómez-González 1992; Fukui et al. 1993; Bachiller 1996; and references therein). In most cases the spatial structure of the ejected gas is bipolar. The nature of this phenomenon is however still poorly understood.

In recent years a new class of outflows has been identified: the highly collimated outflows of which L1448 (Bachiller et al. 1990; Bachiller, Martín-Pintado, & Planesas 1991) is the prototype. The discovery of these highly collimated outflows has had a strong influence on the theoretical study of bipolar outflows, and has resulted in a series of new models in which the driving source is a highly collimated, mostly atomic jet (e.g. Masson & Chernin 1993; Raga & Cabrit 1993). There is general agreement that the highly collimated outflows represent the earliest stage in outflow evolution, and that understanding their nature will provide new insights into the mechanism at work driving all bipolar outflows.

An equally important discovery is that of a new class of young stellar objects (YSOs), which may very well be the true low-mass protostars, i.e. the bulk of their final stellar matter has not yet been assembled. Dubbed "Class 0" sources (André, Ward-Thompson, & Barsony 1993; hereafter AWB) in the spirit of the Lada (1991) classification scheme, these sources are characterised as having a strong submillimeter luminosity compared to their bolometric luminosity, a nar-

row spectral energy distribution (SED) which is well represented by a blackbody of temperature 15 – 30 K, show no emission at wavelengths below 10 μm, and have indirect evidence for a central YSO, for example a highly collimated outflow (Barsony 1994; André 1995). In addition, submillimeter observations show that they possess large amounts of circumstellar dust, typically a factor 10 greater than Class I sources (e.g. Bontemps et al. 1996). Simple arguments indicate that these sources have ages of a few $\times$ 10^4 years, and all the various evolutionary diagrams that have been proposed for YSOs point to the Class 0 sources as being very young (e.g. AWB; Myers & Ladd 1993; Bontemps et al. 1996). However, the expected number of Class 0 YSOs at any given time is expected to be low, due to the short lifetime of this evolutionary stage (Barsony 1994), and this has been borne out observationally (e.g. AWB). Thus, identifying and studying new Class 0 sources is important for the development of star formation theories.

Due to their simple geometry and environment, isolated globules are among the best suited objects for a detailed study of the process of formation of individual stars. The dark cloud BHR 71 [Bourke, Hyland & Robinson 1995a; a.k.a. Sa136 (Sandqvist 1977), DC 297.7–2.8 (Hartley et al. 1986)] is an excellent example of an isolated opaque Bok globule. It is located near the southern Coalsack, and has an angular size at optical wavelengths of $8' \times 3'$ (Hartley et al. 1986). It appears in the H_2CO survey of southern dark clouds by Goss et al. (1980), the ^{12}CO survey of the Carina Arm by Grabelsky et al. (1987) and the NH_3 survey of southern hemisphere globules by Bourke et al. (1995b). Bourke et al. (1995b) mapped the dense ammonia core in BHR 71, and from their observations derived a core mass of $\sim 3\ M_\odot$ (corrected from Bourke et al. for the new distance estimate of 200 pc – see Seidensticker & Schmidt-Kaler 1989) and a kinetic temperature of 13 K. Maps of the IRAS emission toward this object, made using the coadded images from the IRAS Sky Survey Atlas, show the presence of two infrared sources projected toward the globule. One of them, IRAS 11590–6452, is projected near the center of the globule and is heavily obscured, suggesting that a low mass star has been formed, or is in the process of formation, in the innermost region of BHR 71.

Near-infrared observations of BHR 71 by Bourke et al. (1993; see also Bourke 1994) shows that bipolar-like nebulosity is visible either side of IRAS 11590–6452, suggesting that a molecular outflow may be present in BHR 71. In this Chapter we present observations of BHR 71 in lines of ^{12}CO, ^{13}CO, C^{18}O and NH_3, and continuum observations at 1.3 mm, with angular resolutions ranging from 20″ to 9′. We report the discovery of a highly collimated bipolar molecular outflow in BHR 71, centered on IRAS 11590–6452. We also report the detection of a strong 1.3 mm continuum source, which is coincident with IRAS 11590–6452. We find that this source corresponds to a cold object ($T_{dust} \sim 35$ K), with a core-envelope structure and a total luminosity of $L_{bol} \sim 9\ L_{\odot}$. The observed and derived characteristics suggest that the driving source of the outflow is a very young stellar object, possibly a new example of a Class 0 protostar.

3.2. Observations

The observations were made using the 1.2 m Millimeter Wave Radiotelescope at the Cerro Tololo Interamerican Observatory (CTIO), Chile, the 15 m Swedish–ESO Submillimetre Telescope (SEST) located on La Silla, Chile, and the Parkes 64 m radio telescope in Australia. The basic observing parameters are summarized in Table 3.1.

3.2.1. CTIO radiotelescope

The observations with the CTIO radiotelescope of the emission in the ^{12}CO $J = 1 \rightarrow 0$ ($\nu = 115271.201$ MHz) and ^{13}CO $J = 1 \rightarrow 0$ ($\nu = 110201.370$ MHz) lines from BHR 71 were undertaken during May – June 1994 and May 1995, respectively. At the observed frequencies the half-power beam width of the telescope was $\sim 8\farcm8$. The receiver was a liquid nitrogen-cooled Schottky receiver (see Bronfman et al. 1988 for a description). The spectrometer consisted of a 256 channel filter bank, each channel being 100 kHz wide. This provided velocity resolutions of 0.26 and 0.27 km s^{-1} at the frequencies of the ^{12}CO $J = 1 \rightarrow 0$ and

Table 3.1. Summary of Observational Parameters

Observation	Frequency (GHz)	Beam (FWHM)	Spacing	Positions observed	Δv ($km\,s^{-1}$)	rms noise (K)
			CTIO radiotelescope			
^{12}CO $J = 1 \rightarrow 0$	115.271	8.'8	3.'75	100	0.26	0.20
^{13}CO $J = 1 \rightarrow 0$	110.201	8.'8	3.'75	50	0.27	0.13
			SEST radiotelescope			
^{12}CO $J = 1 \rightarrow 0$	115.271	45″	60″	50	0.112	0.20
			20″	177		0.50
^{13}CO $J = 1 \rightarrow 0$	110.201	47″	60″	34	0.117	0.08
			90″	50		0.25
$C^{18}O$ $J = 1 \rightarrow 0$	109.782	47″	40″	93	0.118	0.10
^{12}CO $J = 2 \rightarrow 1$	230.538	23″	20″	36	0.056	0.50
1.3 mm continuum	236 ($\Delta\nu = 50$)	23″	...	7 maps	...	...
			Parkes radiotelescope			
NH_3 $(J,K) = (1,1)$	23.694	84″	60″	30	0.12/0.05	0.03
NH_3 $(J,K) = (2,2)$	23.722	84″	60″	5	0.12/0.05	0.03

^{13}CO $J = 1 \rightarrow 0$ lines, respectively.

In the ^{12}CO $J = 1 \rightarrow 0$ line we mapped, with an angular spacing of 3.'75, a region $\sim 40'$ in diameter. In each of the 100 positions observed we integrated until the rms noise per channel was reduced to 0.20 K in main-beam temperature (antenna temperature corrected for main-beam efficiency; $\eta_{mb} = 0.82$). Typically, this was achieved after integrating for about 12 minutes per position. In the ^{13}CO $J = 1 \rightarrow 0$ line we mapped, with an angular spacing of 3.'75, a region $\sim 30'$ in diameter. In each of the 50 positions observed we integrated for 20 minutes, reaching typically an rms noise per channel in main-beam temperature of 0.13 K.

3.2.2. Swedish–ESO Submillimetre Telescope

^{12}CO and ^{13}CO observations

The observations of ^{12}CO $J = 1 \rightarrow 0$ and ^{13}CO $J = 1 \rightarrow 0$ line emission using SEST were undertaken during April 1994, April 1995, September 1995 and October 1995. In the 3 mm range the telescope was equipped with dual-polarization Schottky mixer receivers (April 1994 and April 1995) or SIS receivers (September – October 1995). The telescope beamsize at the observed frequencies was $\sim$ 45″ (FWHM) and the main beam efficiency was 0.70. Most of the observations were performed in frequency-switched mode. Higher signal-to-noise observations were performed in position-switched mode, with the reference position located at $\alpha_{1950} = 11^{\rm h}53^{\rm m}44.^{\rm s}7$ and $\delta_{1950} = -65°13'58''$.

In the ^{12}CO $J = 1 \rightarrow 0$ transition we observed 177 positions within a $\sim$ $200'' \times 480''$ region with 20″ spacing in frequency-switched mode. The system temperatures varied between 350 and 900 K, depending on weather conditions and observing session (in September and October 1995 the new SIS receiver was used, which resulted in significantly lower system temperatures), and the resulting rms noise in antenna temperature was between 0.2 and 0.9 K for an integration time of 50 seconds. In position-switched mode a region of $6' \times 10'$ in

size was mapped with 60″ spacing (50 positions). The system temperatures were in the range 530 – 590 K. The integration time on source at each position was 2 minutes, resulting in an rms noise of typically 0.2 K in antenna temperature. For all the ^{12}CO observations the backend used was a high resolution acousto-optical spectrometer with 1000 channels and a velocity coverage of ~ 112 km s^{-1} for frequency-switched observations, and 2000 channels with a velocity coverage of ~ 225 km s^{-1} for position-switched observations. The resolution in both cases was 0.112 km s^{-1}.

In the ^{13}CO $J = 1 \rightarrow 0$ transition we observed 34 positions with 60″ spacing in position-switched mode, and 50 positions with 90″ spacing over a 9′ × 9′ region in frequency-switched mode. The 1000 channels provided a velocity resolution of 0.118 km s^{-1} and a velocity coverage of ~ 117 km s^{-1}. The system temperatures were ~ 220 K for the position-switched observations, and ~ 350 K for the frequency-switched observations. The integration time on source at each position was 3 minutes (position-switched) or 1 minute (frequency-switched), resulting in an rms noise in a single spectral line channel of typically 0.08 K or 0.25 K in antenna temperature, respectively.

Observations of ^{12}CO $J = 2 \rightarrow 1$ ($\nu = 230538.000$ MHz) were undertaken in April 1994 and April 1995 with 20″ spacing about the center of the globule and at the CO peaks in the outflow lobes, simultaneously with the $J = 1 \rightarrow 0$ observations. System temperatures varied between 600 – 750 K. Observations were frequency-switched, and the 1000 channels of the spectrometer provided a velocity coverage of 56 km s^{-1} with a velocity resolution of 0.056 km s^{-1}. Integration times were the same as for the $J = 1 \rightarrow 0$ observations, 50 seconds, resulting in an rms noise of ~ 0.5 K. The effective beamsize at 1 mm is ~ 23″ (FWHM), and the main beam efficiency is 0.60.

C^{18}O observations

Observations of C^{18}O $J = 1 \rightarrow 0$ ($\nu = 109782.160$ MHz) were undertaken in April 1994. We observed 93 positions in frequency-switched mode within a 6′.7

$\times$ 6.'7 region with 40″ spacing. The 1000 channels of the spectrometer provided a velocity coverage of $\sim$ 118 km s^{-1} with a velocity resolution of 0.118 km s^{-1}. System temperatures were $\sim$ 330 K and the on-source integration time was 2 minutes per position, resulting in an rms noise in antenna temperature of $\sim$ 0.1 K.

Continuum observations

The continuum observations were carried out during November 1995 using the SEST single channel bolometer operating at 1.3 mm. The bolometer has a center frequency of 236 GHz and a bandwidth of $\sim$ 50 GHz. It consists of a Germanium element inside a ^{3}He cryostat cooled to about 0.3 K. A similar bolometer is described by Kreysa (1990). At 1.3 mm the telescope has an effective beamwidth of 23″ (FWHM). Beam-switching was done with a focal-plane chopper having a horizontal beam throw of 70″. Seven maps were obtained by scanning in azimuth at a rate of 8″ per second, with adjacent scans separated by 8″ in elevation (about a third of the beamwidth). Pointing was done on a nearby quasar and found to be repeatable to within $\pm$ 3″. The atmospheric transmission was measured by skydips every two hours. Focus measurements were done more frequently after sunrise and sunset. The zenith opacities varied during the observing run (two nights) and were in the range $0.13 < \tau < 0.28$. Uranus was used as the calibrator source and was assumed to have a brightness temperature of 96 K at 236 GHz. The flux calibration is believed to be accurate to 20%, the uncertainty being caused mainly by the limited accuracy of the adopted calibrator temperature. The raw data were corrected for atmospheric attenuation and transformed into NOD2 format (Haslam 1974) using SEST software. Final data reduction was done with the software package MAP (written by R. Zylka, MPIfR Bonn) which uses the NOD2 and GAG libraries. The double beam maps were restored into single-beam maps using an improved algorithm of Emerson, Klein, & Haslam (1979), shifted, averaged (weighted by their rms noise, resulting in a final map with an rms noise level of $\sim$ 35 mJy/beam) and transformed from an azimuth-elevation system into the equatorial coordinate system.

3.2.3. Parkes radio telescope

Ammonia observations of BHR 71 have previously been reported by Bourke et al. (1995b), and full details of the observational techniques can be found there. Observations of BHR 71 were undertaken at the Parkes radio telescope in the $(J,K) = (1,1)$ and (2,2) transitions of NH_3 at 23.694495 and 23.722633 GHz respectively, during November 1991 and February 1994. In November 1991 the old Parkes 1024-channel digital correlator was split into 2 sections of 512 channels, providing a velocity resolution of 0.12 $\mathrm{km\,s^{-1}}$. The globule was mapped in the (1,1) line at 30 positions with 60″ spacing about the Hartley et al. (1986) position ($\alpha_{1950} = 11^{\mathrm{h}}59^{\mathrm{m}}10^{\mathrm{s}}$, $\delta_{1950} = -64°52'24''$), and both transitions were also observed at the IRAS PSC position ($\alpha_{1950} = 11^{\mathrm{h}}59^{\mathrm{m}}03\overset{\mathrm{s}}{.}1$, $\delta_{1950} = -64°52'11''$). In February 1994 the new Parkes 16384-channel digital correlator was split into 2 sections of 2048 channels, providing a resolution of 0.05 $\mathrm{km\,s^{-1}}$. Mapping was performed in the (1,1) line with 30″ spacing centered on the IRAS position in a 13 point cross, and 5 positions were simultaneously observed in the (2,2) transition. Absolute calibration of the 1994 observations are uncertain, so the (1,1) mapping results from this session are not used. However, since the (1,1) and (2,2) observations were undertaken simultaneously absolute calibration is not important for the derivations of properties using these transitions. The beamwidth at these frequencies was $\sim 84''$.

3.3. Results

3.3.1. Globule characteristics

Optical images of BHR 71, in blue and far-red light, are shown in Figure 3.1. The image on the left is from the UK Schmidt IIIaJ survey plate and was obtained from the Digital Sky Survey (DSS)[2], while the image on the right is an I band

[2]The Digitized Sky Survey was produced at the Space Telescope Science Institute under U.S. Government grant NAG W-2166. The UK Schmidt Telescope was operated by the Royal

Figure 3.1.— *Next Page*

Optical images of the Bok globule BHR 71. *Left panel*, the UK Schmidt IIIaJ image, taken from the Digital Sky Survey (DSS). The FOV is $\sim 35'$ on a side. The lack of stars toward the center clearly defines the globule. *Right panel*, I band image taken with a 1024 $\times$ 1024 pixel TEK CCD on the 1 m telescope at Siding Spring Observatory. The FOV is $\sim 9'$ on a side. The opacity of the globule is evident in this image, as well as a conical shaped nebulosity protruding from near its center.

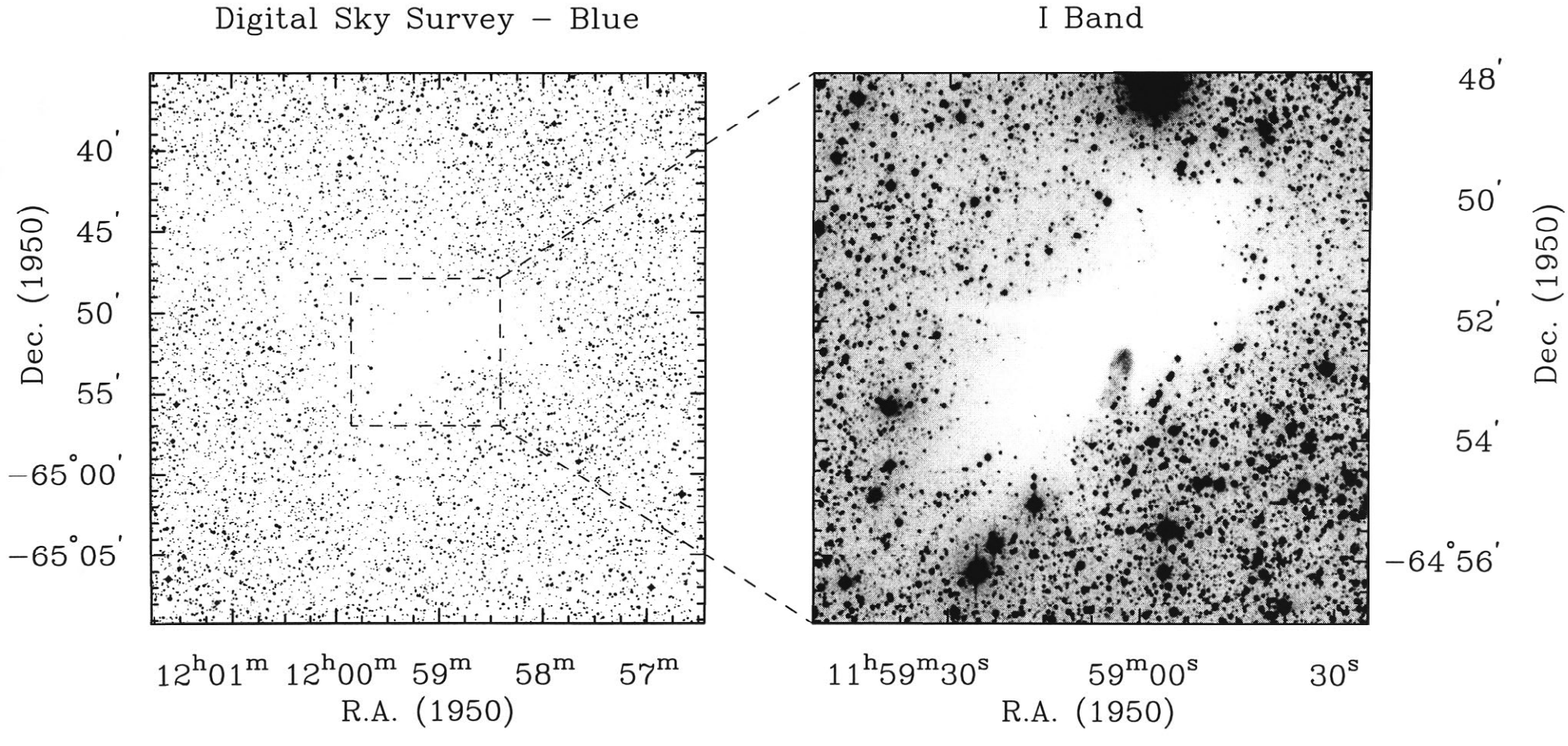
Digital Sky Survey – Blue
I Band
Dec. (1950)
40'
45'
50'
55'
−65°00'
−65°05'
12h01m
12h00m
59m
58m
57m
R.A. (1950)
48'
50'
52'
54'
−64°56'
Dec. (1950)
11h59m30s
59m00s
30s
R.A. (1950)

image taken in January 1993 with a 1024 × 1024 pixel TEK CCD on the 1 m telescope of the Mt Stromlo and Siding Spring Observatories, located at Siding Spring, Australia. The coordinate system of both images was determined by comparison with stars from the Hubble Space Telescope Guide Star Catalog. In the DSS image, the Bok globule nature of the cloud is clearly evident – it is well isolated and very opaque. In the I band image, the central region of the globule is still very opaque, despite the large number of background stars present. Nebulosity is also visible in the I band image, hinting at its active star-forming state. In fact, stars may be seen through the nebulosity, suggesting that a hole or cavity has been created there. From its association (positional and velocity) with the Coalsack, Bourke et al. (1995b) estimated the distance to BHR 71 at 175 pc, based on the work of Rodgers (1960). However, more recent determinations of the distance to the Coalsack (Seidensticker & Schmidt-Kaler 1989) place it nearer to 200 pc. We adopt a value of 200 pc as the distance to BHR 71. Conversion between angular and linear size is thus $1' \sim 0.06$ pc, or $1\farcm7 \sim 0.1$ pc.

^{12}CO and ^{13}CO

Maps of the velocity integrated ^{12}CO and ^{13}CO emission from BHR 71 overlayed on the DSS image are shown in Figure 3.2. The range of velocity integration is from -6 to -3 km s^{-1} for both molecules. The ^{12}CO $J = 1 \rightarrow 0$ emission arises from roughly a circular region, with observed major and minor axis of $14\farcm5$ and $14\farcm2$ (full width at half power), respectively. The deconvolved sizes, computed by assuming that the observed size is the quadrature sum of the true cloud size and the telescope beam ($8\farcm8$), both assumed to have Gaussian shapes, are $11\farcm5$ and $11\farcm1$ (0.68×0.65 pc). The emission in the ^{13}CO $J = 1 \rightarrow 0$ line

---

Observatory Edinburgh with funding from the UK Science and Engineering Research Council (later the UK Particle Physics and Astronomy Research Council), until 1988 June, and thereafter by the Anglo-Australian Observatory. The blue plates of the southern Sky Atlas and its Equatorial Extension (together known as the SERC-J), as well as the Equatorial Red (ER), and the Second Epoch [red] Survey (SES) were all taken with the UK Schmidt.

Figure 3.2.— *Next Page*

Integrated CO maps of BHR 71 (CTIO). *Left panel*, ^{12}CO $J = 1 \rightarrow 0$ emission integrated over the velocity range $-6 < v_{lsr} < -3$ km s^{-1}, overlayed on the I band image. The contour levels are 20, 35, 50, 65, 80 and 95% of the peak $\int T_{mb} dv$ of 10.0 K km s^{-1}. *Right panel*, ^{13}CO $J = 1 \rightarrow 0$ emission integrated over the same velocity range as the ^{12}CO emission. The contour levels are 20, 35, 50, 65, 80 and 95% of the peak $\int T_{mb} dv$ of 2.8 K km s^{-1}.

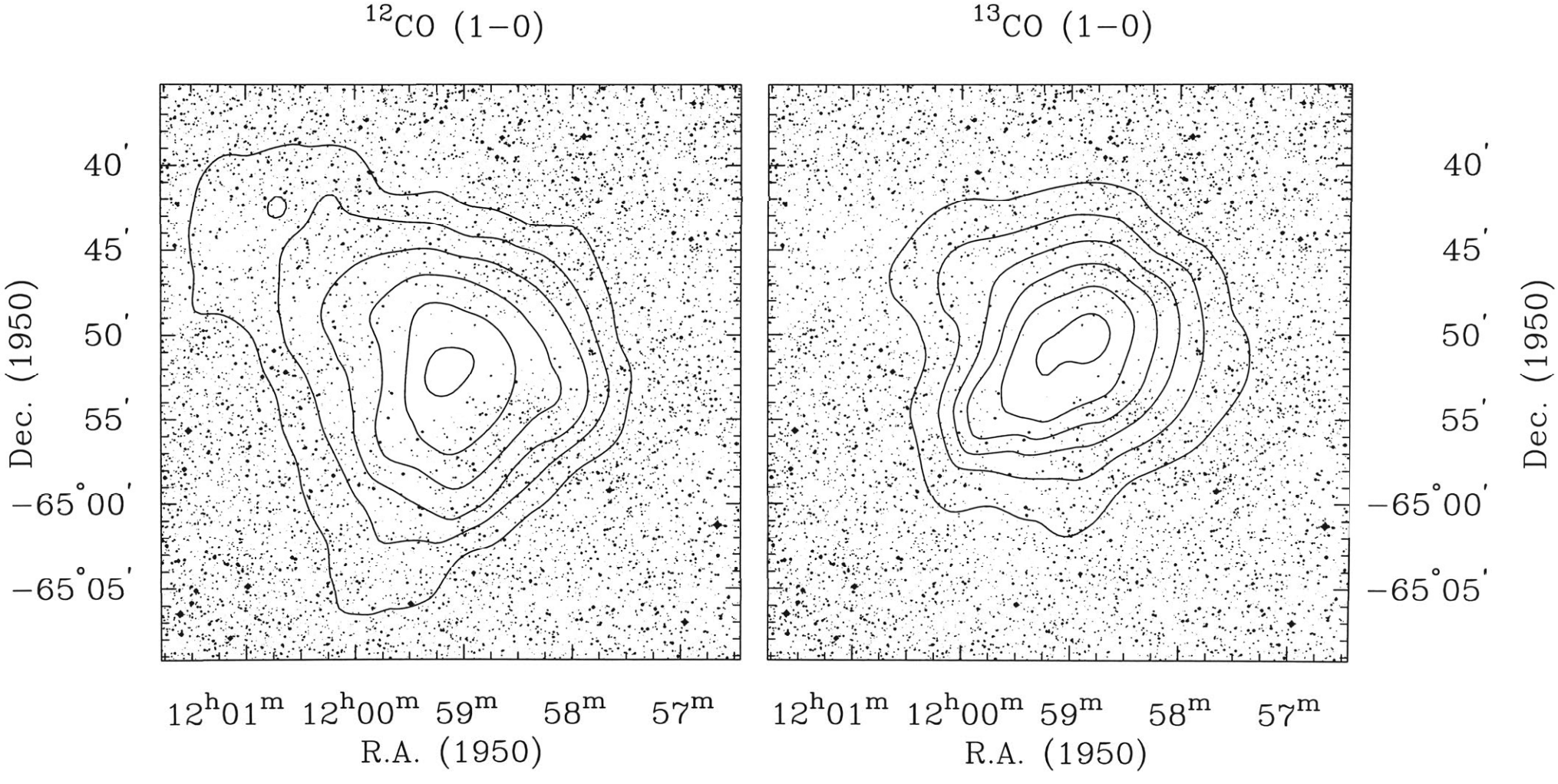
^{12}CO (1−0)
^{13}CO (1−0)
40′
45′
50′
55′
−65°00′
−65°05′
Dec. (1950)
12^{h}01^m 12^{h}00^m 59^m 58^m 57^m
R.A. (1950)

is elongated in a direction with position angle (PA) of $\sim 125°$, having observed major and minor axes of 14.′2 and 11.′2, respectively. The deconvolved major and minor axes for ^{13}CO are 11.′1 and 6.′9, respectively (0.65 × 0.40 pc). Unlike the well studied Bok globule B335, the molecular emission is well centered on the region of greatest visual extinction (Frerking, Langer, & Wilson 1987). The slight extension to the northeast traces a low visual extinction region seen more clearly on the original Schmidt plate. From the profiles of the ^{12}CO $J = 1 \rightarrow 0$ and ^{13}CO $J = 1 \rightarrow 0$ emission integrated over the source, we determined line center velocities of –4.26 and –4.35 km s^{-1}, and line widths of 1.09 ± 0.01 and 0.80 ± 0.02 km s^{-1}, respectively.

C^{18}O and NH$_3$

In Figure 3.3 we show integrated C^{18}O and NH$_3$ maps overlayed on the I band image. The range of velocity integration is the same as for Figure 3.2. Both maps show a relatively elongated core with position angles of $\sim 126°$ and $\sim 117°$ respectively. The deconvolved map sizes (FWHM) are 5.′3 × 2.′5 for C^{18}O and 3.′5 × 2.′1 for NH$_3$, which imply linear sizes of 0.31 pc × 0.15 pc and 0.20 pc × 0.12 pc respectively. As discussed by Myers (1995), a molecular cloud does not have a unique size, its dimension and appearance in a particular map being a strong function of the tracer used to observe it. The ammonia observations most likely trace the denser gas within the globule core, while C^{18}O is tracing the cloud column density. The C^{18}O contours match very well the extinction in the I band image, but indicate some non-uniformities in column density which are discussed in §3.5.1. The ammonia contours show a relatively symmetric dense core, with a slight elongation to the northwest. However, the beam size used (84″) does not allow a detailed study of the density structure. From the sum of all C^{18}O spectra across the source we determine V_{lsr} = –4.63 km s^{-1} and ΔV (FWHM) = 0.82 ± 0.01 km s^{-1}. For NH$_3$ we determine V_{lsr} = –4.45 km s^{-1} and ΔV = 0.69 ± 0.03 km s^{-1} (using the higher spectral resolution observations and fitting the ammonia hyperfine structure). We will assume a cloud velocity of $\sim$ –4.5 km s^{-1} for future discussion.

Figure 3.3.— *Next Page*

Integrated emission in the lines of $C^{18}O$ $J = 1 \rightarrow 0$ (SEST) and NH_3 (J,K) = (1,1) (Parkes). *Left panel*, $C^{18}O$ map, integrated over the velocity range $-6 < v_{lsr} < -3$ km s^{-1}, overlayed on the I band image. The contour levels are 20, 35, 50, 65, 80 and 95% of the peak $\int T_{mb} dv$ of 2.4 K km s^{-1}. *Right panel*, NH_3 (J,K) = (1,1) emission integrated over the same velocity range as the $C^{18}O$ emission. The contour levels are 20, 35, 50, 65, 80 and 95% of the peak $\int T_{mb} dv$ of 3.8 K km s^{-1}.

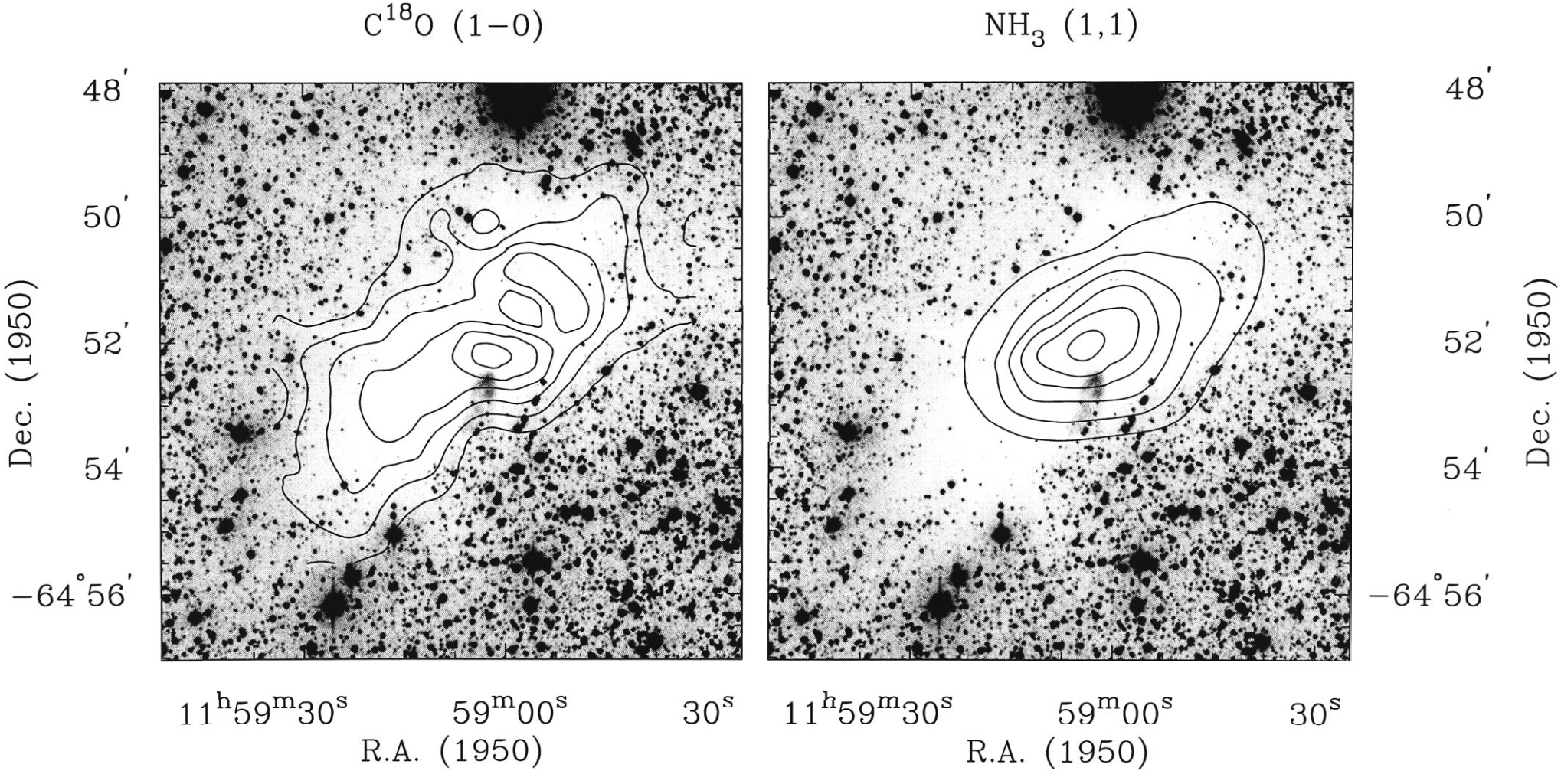
C18O (1−0)
NH3 (1,1)
48'
50'
52'
54'
−64°56'
Dec. (1950)
11h59m30s
59m00s
30s
R.A. (1950)

3.3.2. Molecular outflow

Morphology

Figure 3.4 shows the ^{12}CO $J = 1 \rightarrow 0$ spectra across a $6' \times 10'$ region of BHR 71, mapped with SEST in position-switched mode. Strikingly seen in this figure is the presence toward the northwest of strong emission at velocities redshifted with respect to the systemic dark cloud velocity of ~ -4.5 km s^{-1}, and toward the southeast the presence of strong emission at blueshifted velocities. The emission in the redshifted wing is seen in the LSR velocity range from about -3 to 7 km s^{-1}, and the emission in the blueshifted wing is seen in the range from about -14 to -6 km s^{-1}.

Figure 3.5 shows the emission in the ^{12}CO $J = 1 \rightarrow 0$ line wings integrated over the velocity range $-14 < v_{lsr} < -6$ km s^{-1} (left panel) and $-3 < v_{lsr} < 7$ km s^{-1} (right panel). Clearly distinguished are two lobes symmetrically placed about the 1.3 mm continuum source (marked with a star – see §3.3.3). The bulk of the emission from the southwest lobe arises at velocities that are blueshifted with respect to the ambient cloud velocity, while the bulk of the emission from the northwest lobe arises from velocities that are redshifted. Consequently, we will refer to the southeast lobe as the *blue lobe* and to the northwest lobe as the *red lobe*. The angular size in the direction of the flow of the southeast and northwest lobes are $\sim 5\farcm3$ and $\sim 5\farcm0$, respectively, which at a distance of 200 pc translate into linear sizes of 0.31 and 0.29 pc, respectively. From the observed major and minor axes of the lobes we estimate that the semi-opening angle of the outflow is approximately $15° \pm 5°$. The collimation factor is high, with a length-to-width ratio of at least 5 in the lobes, as determined from the half-power contour. The axial alignment of the peaks in the lobes, and the peak in the mm continuum (§3.3.3 and Fig. 3.13), is very high, suggesting that the ambient medium is relatively homogeneous and/or the outflow source is not precessing significantly. The position angle of the outflow is $\sim 165°$ and is not aligned with either of the globule axes.

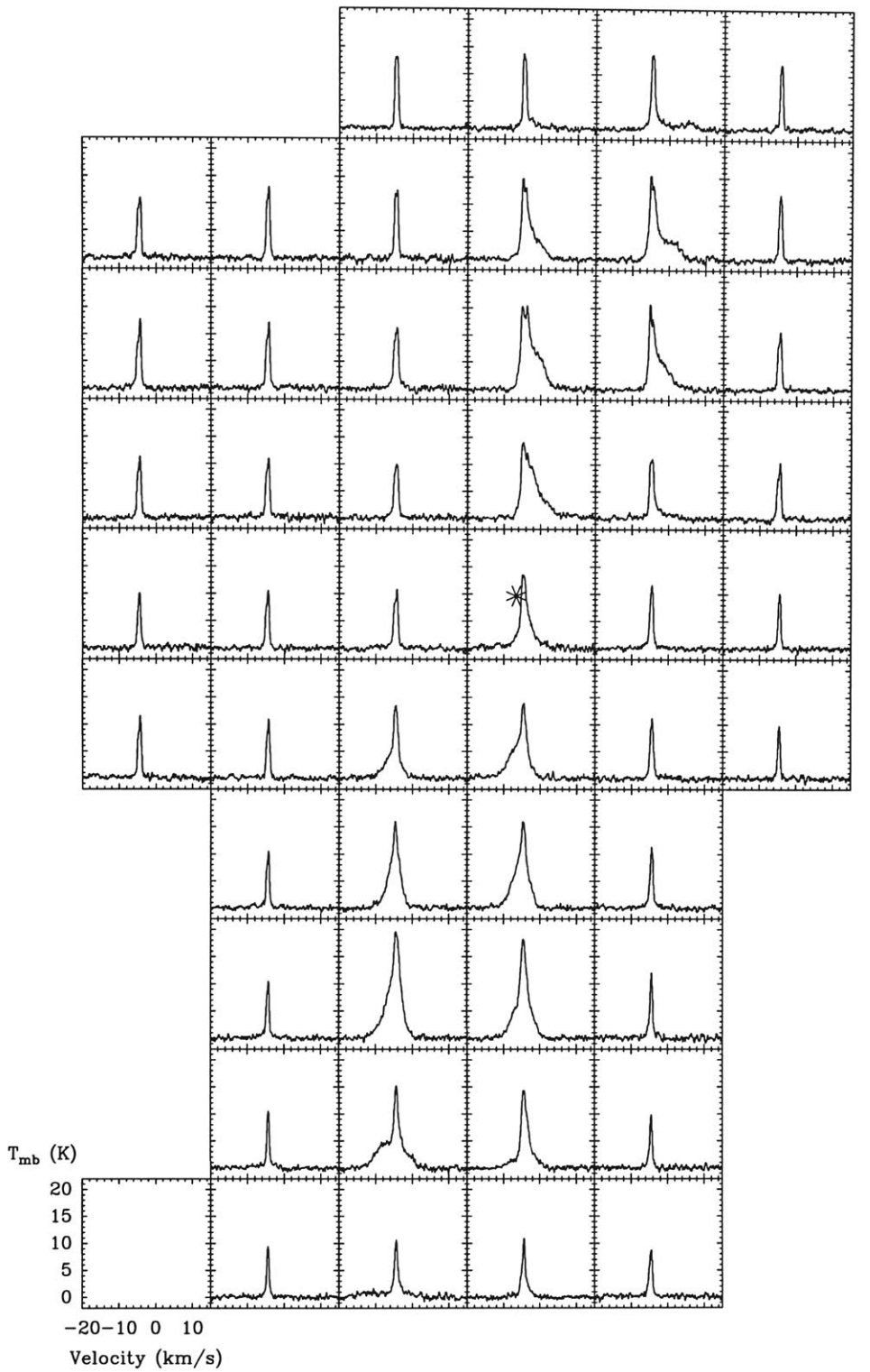

Figure 3.4.— ^{12}CO $J = 1 \rightarrow 0$ spectra over the $6'$ by $10'$ region mapped with position-switching at SEST. The asterisk marks the position of the mm continuum source. The angular separation between panels is $60''$. The scale is given in the panel in the lower left.

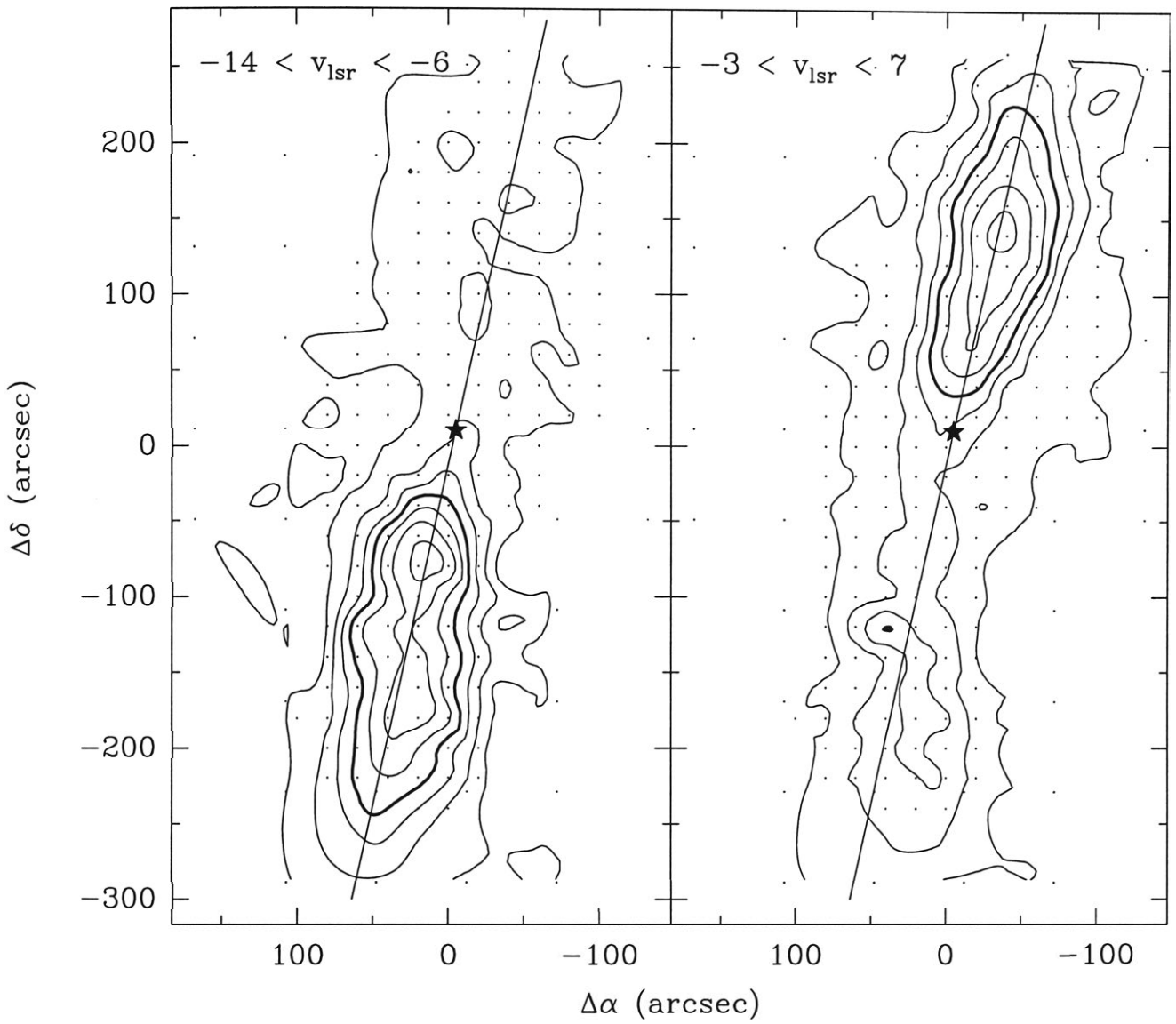

Figure 3.5.— *Left panel*, ^{12}CO $J = 1 \rightarrow 0$ emission integrated over the velocity range $-14 < v_{lsr} < -6$ km s^{-1}, which is blue shifted with respect to the ambient velocity of -4.5 km s^{-1}. *Right panel*, ^{12}CO $J = 1 \rightarrow 0$ emission integrated over the velocity range $-3 < v_{lsr} < 7$ km s^{-1}, which is red shifted with respect to the ambient velocity. Contours are 5, 20, 35, 50, 65, 80, 95% of the peak $\int T_{mb} dv$ of 36.1 K km s^{-1} in the blue lobe and 44.2 K km s^{-1} in the red lobe. The heavier contour marks the 50% level in each panel. The observed positions are indicated.

Velocity structure

In order to investigate the spatial distribution of the outflowing gas as a function of velocity, we have divided the line wing emission into three pairs of velocity intervals: designated as the high, intermediate and low velocity intervals, respectively. Each velocity pair is symmetric with respect to the ambient cloud velocity of -4.5 km s^{-1}. The range of velocity integration for the high velocity pair are from -13.2 to -10.8 km s^{-1} for the blueshifted component and from 1.8 to 4.2 km s^{-1} for the redshifted component; for the intermediate velocity pair the ranges are from -10.8 to -8.4 km s^{-1} and from -0.6 to 1.8 km s^{-1} for the blueshifted and redshifted components, respectively; finally, for the low velocity pair the ranges are from -8.4 to -6.0 km s^{-1} and -3.0 to -0.6 km s^{-1} for the blueshifted and redshifted components, respectively. In Figure 3.6 we present maps of the velocity integrated emission in the six velocity intervals defined above, and over the velocity range of the ambient gas emission (middle panel; $-6 < v_{lsr} < -3$ km s^{-1}). It is clear from this figure that in both the high and intermediate velocity intervals, the blueshifted and redshifted emission arises from two distinct spatially displaced lobes which are symmetric with respect to the flow center. On the other hand, the emission in the low-velocity interval shows superimposed blueshifted and redshifted lobes. These kinematical characteristics can also be appreciated in Figure 3.7, which shows a position-velocity diagram along the major axis of the outflow. Figure 3.4 also shows this quite clearly in the high signal-to-noise position-switched observations. In the low velocity range blueshifted and redshifted emission is observed toward each of the lobes. The observed ^{12}CO emission pattern is in very good agreement with that expected if the flow is viewed nearly perpendicular to its symmetry axis, in which case the flow morphology appears as two spatially distinct high velocity components with superposed blueshifted and redshifted emission (Cabrit & Bertout 1986).

Figure 3.6 also shows that the spatial extent of the ^{12}CO emission in the three velocity intervals is nearly the same, the lobe sizes showing little dependence on the velocity range. This behaviour can neither be explained by a model of an explosive flow which is freely expanding, since in this case the flow should

Figure 3.6.— *Next Page*

^{12}CO $J = 1 \rightarrow 0$ integrated over the high, intermediate, and low velocity channel ranges as described in the text. The velocity range of each panel is indicated. Note that the velocity width is 3.0 km s^{-1} for the central panel, which is the velocity range of the ambient gas (indicated with a heavier border), and 2.4 km s^{-1} for the other panels. Contours are 10 to 30 K km s^{-1} (interval 2 K km s^{-1}) for the central panel, and 1 to 15 K km s^{-1} (interval 1 K km s^{-1}) for the other panels. The star marks the position of the mm source and the diagonal line marks the radial axis of the outflow. At the lower velocity intervals (relative to the ambient velocity of -4.5 km s^{-1}), blue shifted and red shifted emission is seen toward both lobes. At higher velocities the outflow becomes more collimated (extreme panels).

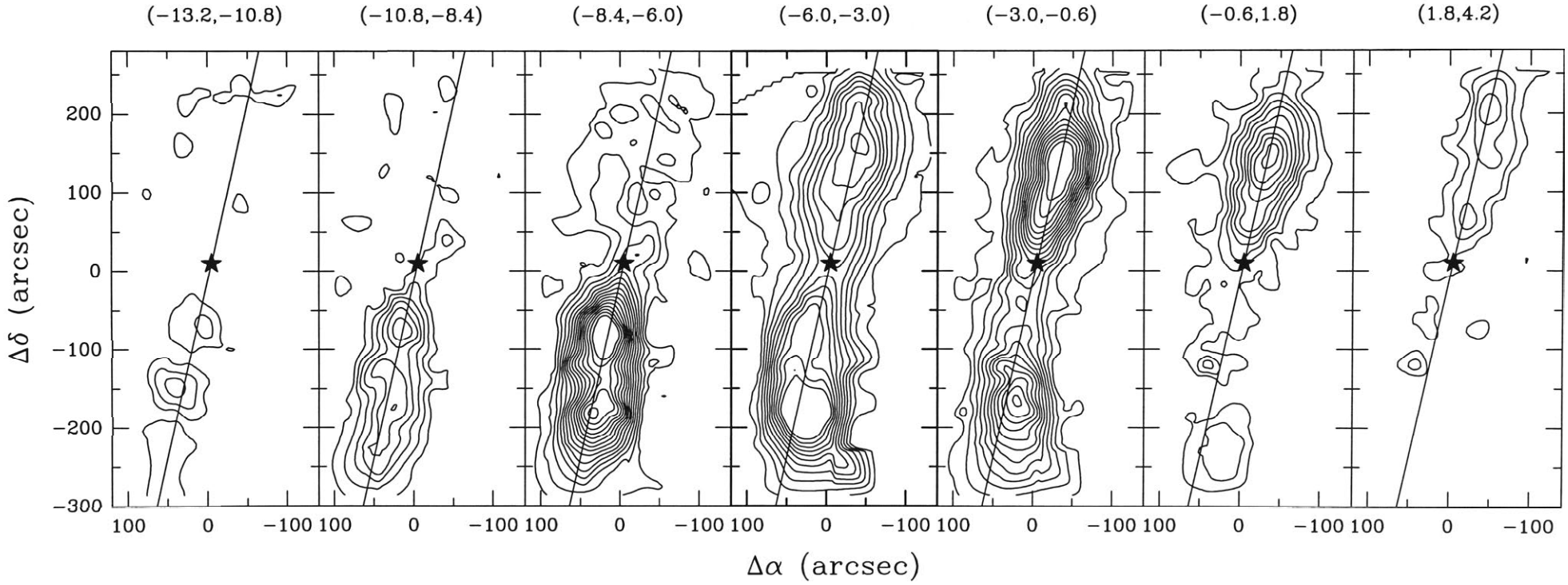
(−13.2,−10.8)
(−10.8,−8.4)
(−8.4,−6.0)
(−6.0,−3.0)
(−3.0,−0.6)
(−0.6,1.8)
(1.8,4.2)
Δδ (arcsec)
200
100
0
−100
−200
−300
100
0
−100
Δα (arcsec)

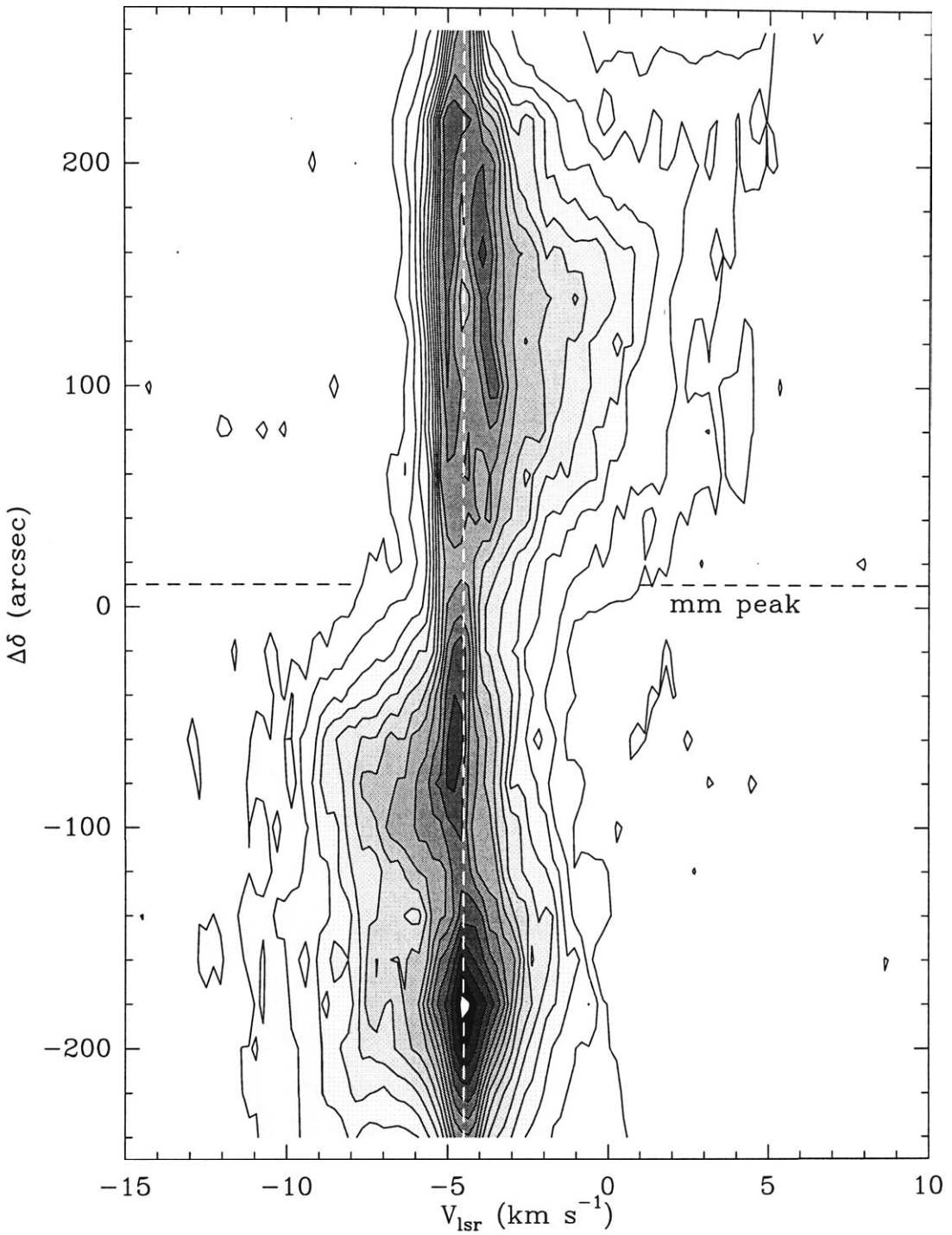

Figure 3.7.— Position-velocity diagram of ^{12}CO $J = 1 \rightarrow 0$ along the major axis of the outflow. Contour levels are 1.4 to 23.8 K by 1.4 K in T_{mb}. The systemic velocity (vertical dashed line) and position of the mm peak are as indicated.

be more extended in the high velocity range, nor by a decelerated but steady flow in which case the lobes should be more extended in the low velocity range (Snell et al. 1984). The independence of lobe size with wing velocity points rather to a model of a steady flow with constant outflow velocity (Cabrit & Bertout 1986; Cabrit, Goldsmith, & Snell 1988). Further, the channel maps in Figure 3.6 also show that there is a systematic increase in flow collimation with increasing flow velocity.

Heating of the ambient gas by the outflow

Figure 3.6 shows that the integrated emission in the velocity range of the ambient cloud (middle panel; $-6 < v_{lsr} < -3$ km s^{-1}) is significantly greater in the outflow lobes than at the position of the embedded mm source. Not only is the integrated intensity greater, but the peak CO intensity in both the $J = 1 \rightarrow 0$ and $J = 2 \rightarrow 1$ transitions is greater toward the outflow lobes (see also Fig. 3.4). This can be appreciated in Figure 3.8 which shows spectra at 4 positions along the outflow axis, one in the red lobe, two in the blue, and at the position of the mm source. This is an unusual result, seen previously in only a few outflows from low mass sources (e.g. L1157 – Umemoto et al. 1992; RNO43 – Bence, Richer, & Padman 1996), and indicates that the excitation temperature of the ambient gas toward the outflow lobes is greater than at the position of the embedded source. The excitation temperature can be estimated from the $J = 2 \rightarrow 1 / J = 1 \rightarrow 0$ line intensity ratios (Levreault 1988). To compute these, the $J = 2 \rightarrow 1$ data, taken with a smaller beam, have been convolved with nearby spectra to approximate the beam size of the $J = 1 \rightarrow 0$ data. We find $J = 2 \rightarrow 1 / J = 1 \rightarrow 0$ ratios of ~ 0.85 at the central position and ~ 0.95 in the lobes. If the lines are optically thick (as suggested by the ^{12}CO $J = 1 \rightarrow 0 / ^{13}$CO $J = 1 \rightarrow 0$ ratios), then these ratios imply excitation temperatures of < 15 K at the embedded source position and > 30 K in the lobes. A similar temperature enhancement was observed by Umemoto et al. (1992) in the outflow from the very red low-mass source IRAS 20386+6751 in L1157. They confirmed the temperature enhancement with observations of ammonia, which indicated kinetic temperatures in excess of 30 K

in the outflow lobes (see also Bachiller, Martín-Pintado, & Fuente 1993). If the ambient gas were heated solely by stellar radiation, we would expect the CO maxima to occur at the position of the embedded source (position "mm"). The fact that the peaks occur toward the outflow lobes suggests that the ambient gas there is heated by interactions with the outflow. This heating most likely results from shocks associated with the jet driving the outflow, as discussed later in §3.5.1. Our ammonia observations, undertaken before the discovery of the outflow, do not cover the regions of the lobe peaks, so the magnitude of the temperature enhancement in BHR 71 remains to be determined. Observations of the (1,1) and (2,2) lines at the offset position $(\Delta\alpha', \Delta\delta') = (0,-1)$ (within the I band nebulosity) shows only a hint of a slight enhancement in kinetic temperature. However, the signal-to-noise in the (2,2) spectrum is low, and so any broadening of the (2,2) line at this position would not be seen in our data.

3.3.3. The Embedded source

Figure 3.9 shows a map of the 1.3 mm continuum emission from the central region of BHR 71, revealing a strong compact source with a peak position at $\alpha_{1950} = 11^{\rm h}59^{\rm m}2\overset{\rm s}{.}3$, $\delta_{1950} = -64°52'01''$ (uncertainties in this position are estimated at $1\sigma = 5''$). For comparison, the major and minor axes of the error ellipse of IRAS 11590–6452 are shown (see below). Figure 3.10 shows a comparison of annular averages centered on the position of peak emission of the mm source with similar averages for Uranus (angular size $3\overset{''}{.}5$) (upper), and a decomposition of the profile into 2 Gaussian components (lower). It is clear from Figures 3.9 and 3.10 that the source as a whole is extended. However, the lower panel of Figure 3.10 shows that the source profile is well fitted by 2 Gaussians, a narrow "central" component, and a broad "extended" component, which is also seen in the three best individual maps of the seven made ($\tau < 0.2$), and so is not a result of poor alignment of the individual maps. Similar two component continuum structures are observed toward other very young low mass protostars, e.g. L1448-mm (Guilloteau et al. 1992; Bachiller et al. 1995a) and B335 (Chandler et al. 1990). The central component is unresolved, and the upper limit to

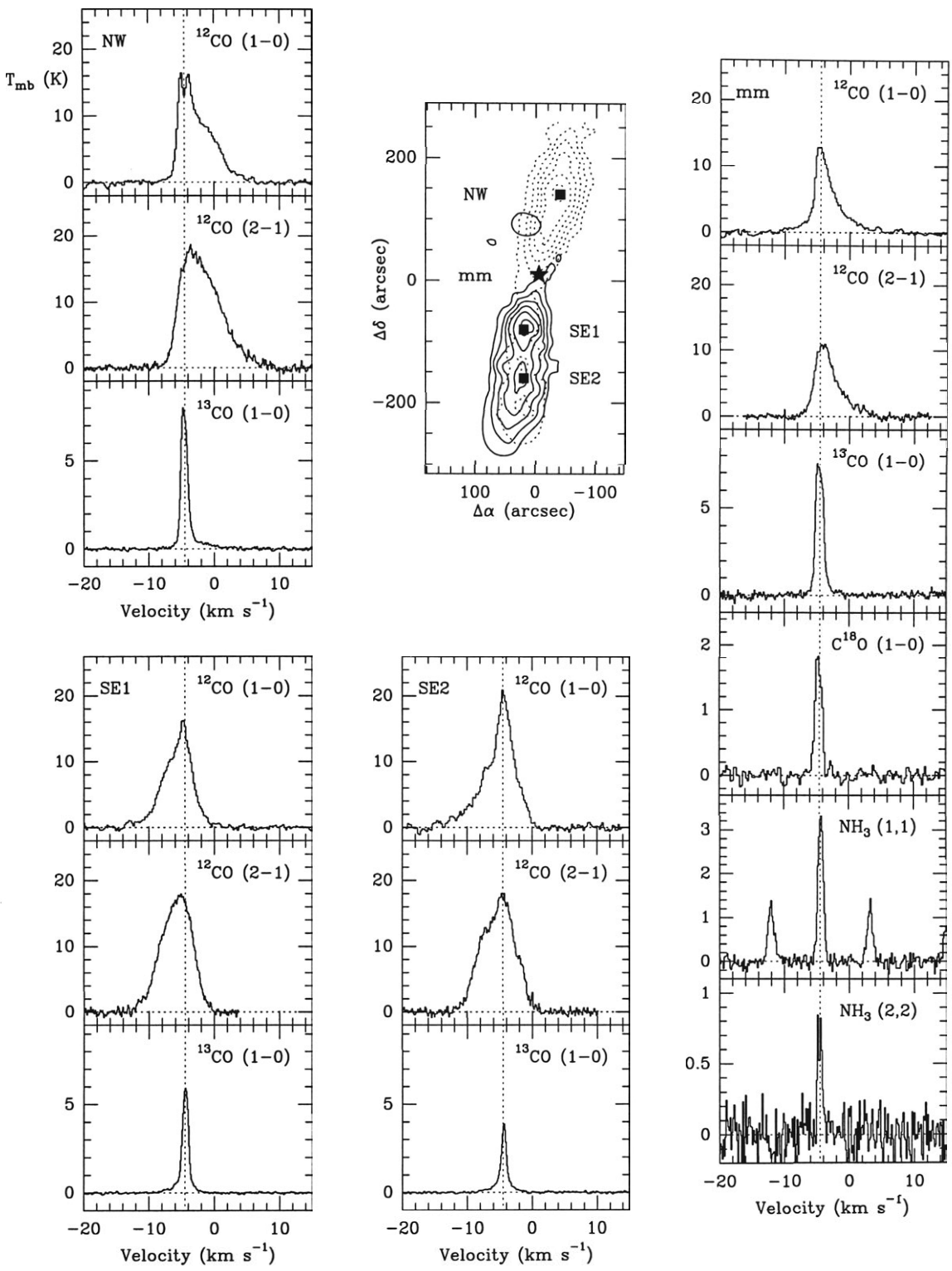

Figure 3.8.— Spectra of ^{12}CO $J = 1 \rightarrow 0$ and $J = 2 \rightarrow 1$, ^{13}CO $J = 1 \rightarrow 0$, C^{18}O $J = 1 \rightarrow 0$, and NH_3 $(J,K) = (1,1)$ and $(2,2)$, toward select positions in the BHR 71 outflow. Filled squares mark the positions in the outflow map for which we show spectra, with their labels. The star marks the position of the mm continuum peak, for which we also show spectra. The systemic velocity of -4.5 km s^{-1} is indicated for each spectrum.

Figure 3.9.— *Next Page*

1.3 mm continuum emission overlayed on the I band image. *Left panel*, full field of view for the I band image, showing the relation of the mm emission to the globule. The emission is very well centered on the globule. Contour levels are 5, 20, 35, 50, 65, 80, 95% of the peak flux of 2 Jy/beam. *Right panel*, enlargement of the region indicated on the left panel. The mm continuum is well aligned with the projected apex of the conical reflection nebula. The solid contour is the 50% level, and the cross marks the position and error ellipse of IRAS 11590–6452 as given in the PSC (see text). The beam size is indicated in the lower left of the panel.

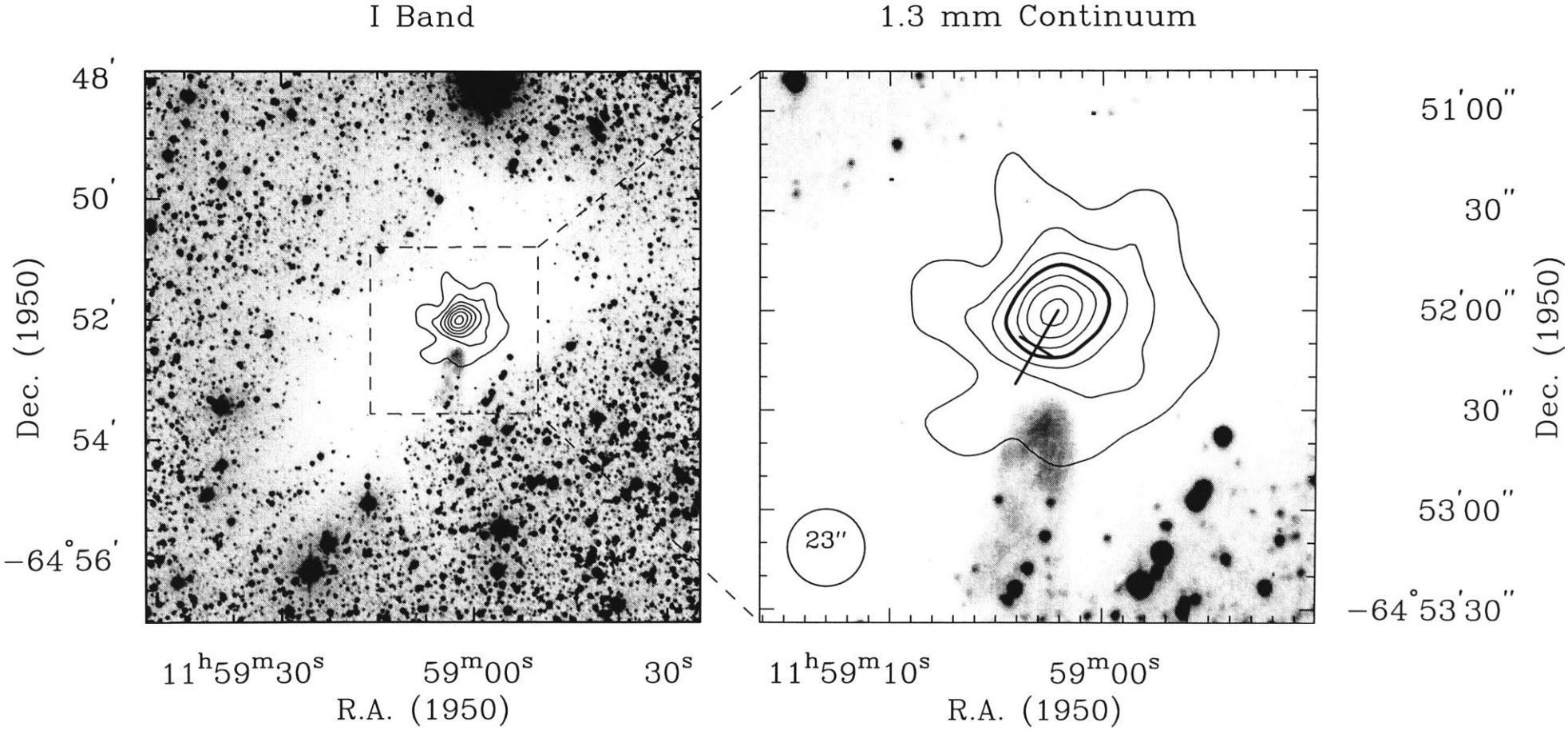
I Band
1.3 mm Continuum
48′
50′
52′
54′
Dec. (1950)
−64°56′
11h59m30s
59m00s
30s
R.A. (1950)
23″
51′00″
30″
52′00″
30″
53′00″
−64°53′30″
Dec. (1950)
11h59m10s
59m00s
R.A. (1950)

its deconvolved FWHM is 7″ (1400 AU). The deconvolved size of the extended component is $\sim$ 40″ (7600 AU). The peak flux is measured at 2.0 Jy/beam, and from the continuum map we estimate that the integrated flux in the central component is $\sim$ 1.7 Jy and in the extended component 2.6 Jy.

Maps of the IRAS emission at 12, 25, 60, and 100 μm from a region of equal size to the I band image (Fig. 3.1) are presented in Figure 3.11. These maps, made from the coadded images of the Infrared Sky Survey Atlas (ISSA), have been processed with the Maximum Correlation Method (MCM) algorithm (Aumann, Fowler, & Melnyk, 1990) at IPAC, and show that there are two infrared sources projected toward the globule: (i) a northern object, IRAS 11589–6447, bright at 12 μm and below the detection limits at the longest wavelength; and (ii) a southern object, IRAS 11590–6452, bright at 100 μm and below the detection limits at the shortest wavelength. The peak position of the southern object at 100 μm is $\alpha_{1950} = 11^{\rm h}59^{\rm m}03\overset{\rm s}{.}1$, $\delta_{1950} = -64°52'07''$, while that of the northern object at 12 μm is $\alpha_{1950} = 11^{\rm h}58^{\rm m}58\overset{\rm s}{.}3$, $\delta_{1950} = -64°48'03''$. In Table 3.2 we give the flux densities of these objects in the IRAS bands taken from the Point Source Catalog. The position of IRAS 11590–6452 is coincident, within the errors, with the position of the 1.3 mm continuum source detected with SEST, and thus is likely to be associated with the source driving the molecular outflow. IRAS 11589–6447 appears in the IRAS catalogue of low resolution spectra (LRS) between 7.7 and 22.6 μm (Olnon et al. 1986). It shows a prominent 10 μm emission band, and has been classified as belonging to the LRS class "29", possible a star with an O-rich envelope. te Lintel Hekkert et al. (1991) searched for 1612 MHz OH emission toward this source as part of a large survey of candidate OH/IR stars, selected on the basis of their IRAS colours. They did not detect any emission. IRAS 11589–6447 can be identified in the I band image as the extremely bright star to the north of the globule.

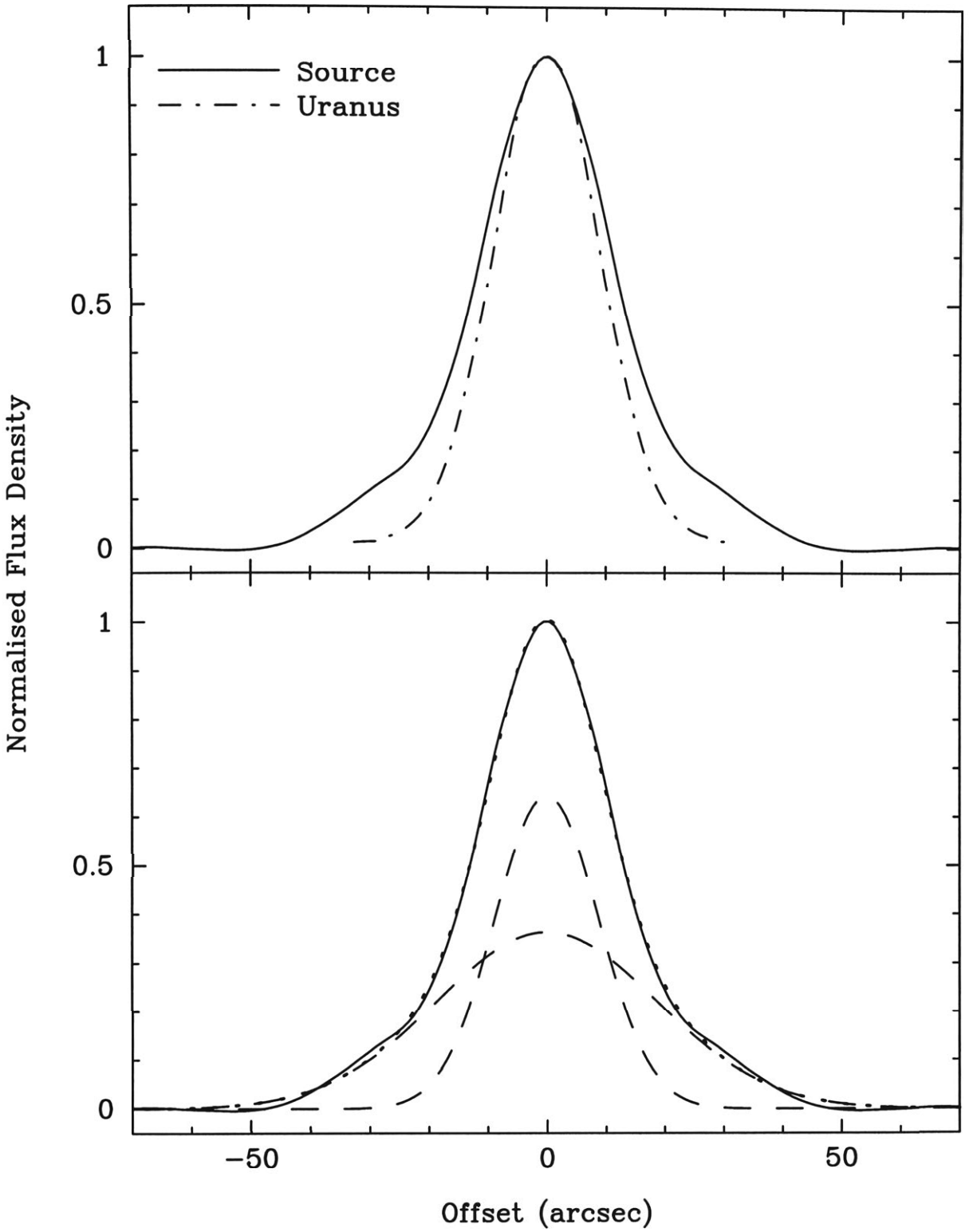

Figure 3.10.— *Upper panel*, normalised profiles of the annularly averaged flux of the mm emission from the continuum source (solid line) and Uranus (broken line). The offsets for the continuum source are relative to the peak position. *Lower panel*, the normalised profile of the annularly averaged flux of the mm emission deconvolved into 2 Gaussian components, as indicated. The composite of the 2 Gaussians is shown as the dotted line. The FWHM of the beam is 23″.

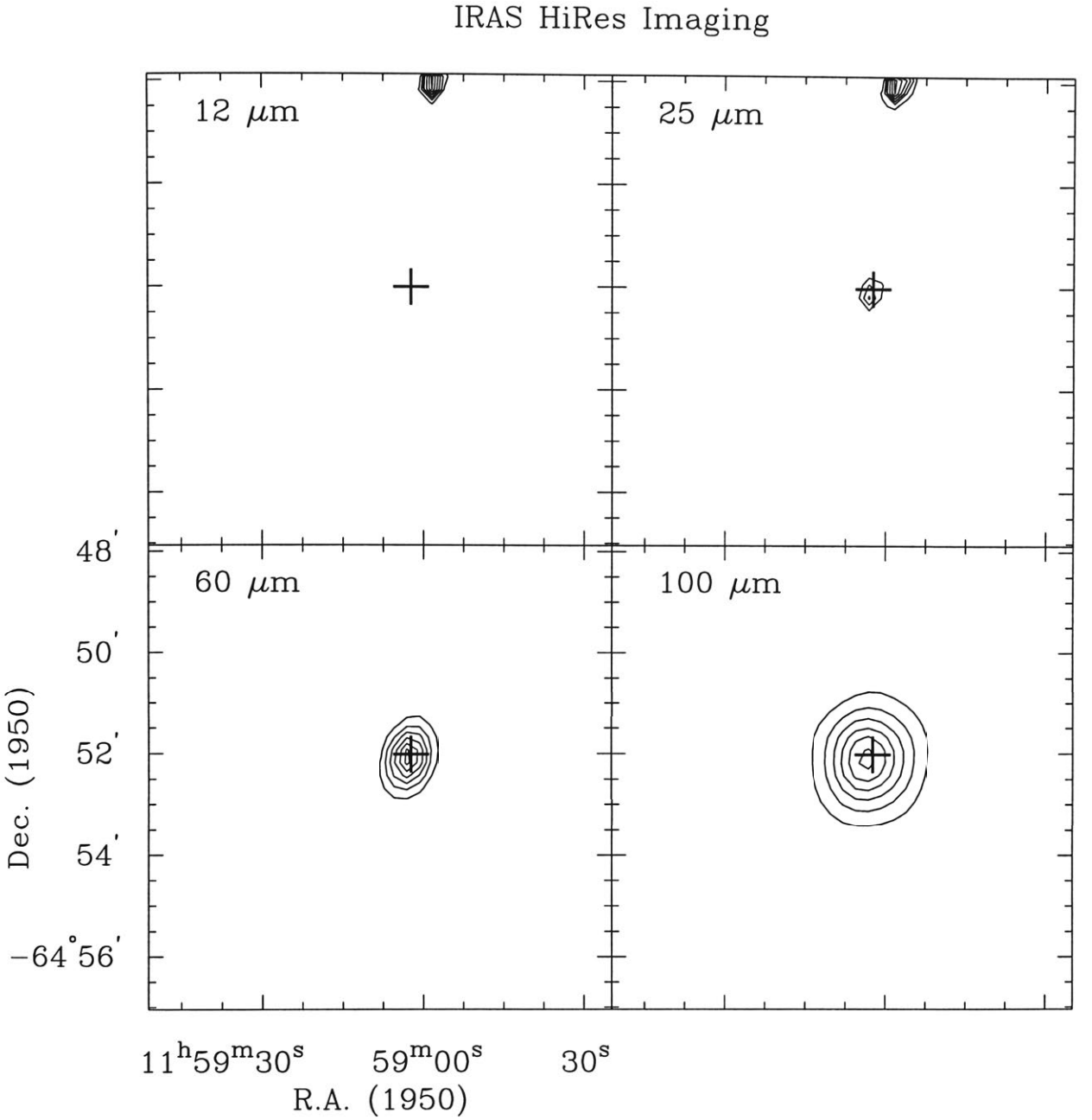

Figure 3.11.— Contour maps of the IRAS emission toward BHR 71. These coadded maps have been processed by IPAC using the MCM algorithm with 20 iterations. Final beam sizes are estimated at $\sim 70'' \times 38''$ for the 12 μm, $\sim 45'' \times 30''$ for 25 μm, $\sim 70'' \times 45''$ for 60 μm, and $\sim 105'' \times 85''$ for 100μm. Levels are 20, 35, 50, 65, 80, 95% of the peak in each map (1.2 Jy/ster – 12 μm; 0.53 Jy/ster – 25 μm; 1.1 Jy/ster – 60 μm; 0.80 Jy/ster – 100 μm). The peak position of the mm source is marked with a cross. The image size is the same as that of the I band image (Fig. 3.1).

Table 3.2. Flux Densities

Source	$S_{12\mu m}$	$S_{25\mu m}$	$S_{60\mu m}$	$S_{100\mu m}$	$S_{1300\mu m}$
			(Jy)		
IRAS 11590–6452	0.25L	6.53	77.38	192.90	1.7
IRAS 11589–6447	22.02	13.07	2.67	15.41L	...

Note. — L indicates upper limit only.

3.4. Analysis

3.4.1. Physical properties of the globule

^{12}CO and ^{13}CO

The determination of the physical characteristics of the BHR 71 globule is based on the observations of the ^{12}CO $J = 1 \rightarrow 0$ and ^{13}CO $J = 1 \rightarrow 0$ lines at CTIO, and are described in detail in the appendix. At the peak position we measured a main beam brightness temperature in the ^{12}CO $J = 1 \rightarrow 0$ line of 8.0 K. Assuming that this emission is optically thick and that it completely fills the beam, we find that the excitation temperature of the ^{12}CO $J = 1 \rightarrow 0$ transition is $\sim$ 11 K. For comparison, Bourke et al. (1995b) derived a rotational temperature between the (1,1) and (2,2) inversion transitions of NH_3 of 12 K.

In Table 3.3 we present observed and derived properties of ^{12}CO and ^{13}CO at nine positions within the globule, separated by about one beamwidth. The optical depth in the ^{12}CO $J = 1 \rightarrow 0$ and ^{13}CO $J = 1 \rightarrow 0$ lines is derived from their ratio of observed brightness temperatures [see eqs. (3A.2) & (3A.3)]. We find that ^{12}CO is optically thick across the entire mapped region, with $\tau_{12} \sim$ 40 near the globule center. For ^{13}CO we determine $\tau_{13} \sim 0.4$ near the center, with only small variations across the mapped region. In columns 9 and 11 of

Table 3.3. ^{12}CO and ^{13}CO observed and derived globule parameters

Offset		Observed						Derived		
		^{12}CO			^{13}CO					
Δl (′)	Δb (′)	T_a^* (K)	V_{lsr} (km s^{-1})	ΔV (km s^{-1})	T_a^* (K)	V_{lsr} (km s^{-1})	ΔV (km s^{-1})	τ_{13}	$\tau_{13}\Delta V$ (km s^{-1})	$N(^{13}\mathrm{CO})$ (10^{15} cm^{-2})
−7.50	−7.50	1.95±0.18	−4.39±0.03	0.71±0.07	0.58±0.11	−4.26±0.06	0.72±0.13	0.35	0.26	1.93
0.00	−7.50	4.35±0.24	−4.34±0.02	1.06±0.06	1.24±0.10	−4.30±0.03	0.72±0.06	0.33	0.24	1.82
7.50	−7.50	2.52±0.20	−4.10±0.03	0.86±0.06	0.59±0.11	−4.10±0.05	0.60±0.14	0.27	0.16	1.20
−7.50	0.00	3.79±0.19	−4.42±0.02	0.93±0.04	1.27±0.10	−4.38±0.03	0.77±0.07	0.40	0.31	2.33
0.00	0.00	6.55±0.22	−4.42±0.01	1.09±0.03	2.42±0.09	−4.42±0.01	0.82±0.03	0.46	0.38	2.84
7.50	0.00	2.48±0.20	−4.23±0.03	1.24±0.08	0.59±0.09	−4.34±0.05	0.74±0.10	0.27	0.20	1.49
−7.50	7.50	0.75±0.20	−4.29±0.09	0.82±0.17	0.36±0.11	−4.33±0.07	0.47±0.18	0.66	0.31	2.35
0.00	7.50	2.44±0.18	−4.14±0.03	1.05±0.06	0.41±0.11	−4.30±0.10	0.97±0.19	0.19	0.18	1.35
7.50	7.50	2.69±0.19	−4.01±0.03	1.11±0.06	0.27±0.10	−4.07±0.12	0.82±0.24	0.11	0.09	0.66

Note.—Offsets, in galactic co-ordinates, are relative to $l = 297.^{\circ}75$, $b = -2.^{\circ}75$, near the center of the globule.

Table 3.3 we list, respectively, the ^{13}CO opacity and column density at a number of positions within the globule. The column density, as derived from equation (3A.5) was found to be $N(^{13}\mathrm{CO}) \sim 2.8 \times 10^{15}$ cm^{-2} near the globule center, dropping to $\sim 1 \times 10^{15}$ cm^{-2} at the edges of the map.

The total mass of molecular clouds can be estimated in at least two ways, as given by equation (3A.6) for the "LTE" mass and equation (3A.7) for the "CO" mass. For BHR 71 we find $\iint \tau_{13} dv d\Omega = 106$ km s^{-1} arcmin^2, which assuming an [$H_2/^{13}$CO] ratio of 7×10^5 (Frerking, Langer, & Wilson 1982), implies an LTE mass of $\sim 41\ M_\odot$. Alternatively, we find $\iint T_{mb}(^{12}\mathrm{CO}) dv d\Omega = 2.3 \times 10^3$ K km s^{-1} arcmin^2, implying it has a total molecular (CO) mass of $\sim 39\ M_\odot$.

The average density can be computed from the cloud mass once a cloud geometry is adopted. Assuming that the globule has a spherical morphology, with a diameter equal to the geometric mean of the half power diameters derived from the deconvolved major and minor axes (as determined from the ^{13}CO observations), and that it is at a distance of 200 pc, implying a cloud radius of 0.25 pc, we find that the globule has an average density of 9×10^3 cm^{-3}.

C^{18}O and NH$_3$

We use the observations of C^{18}O $J = 1 \rightarrow 0$ and NH$_3$ $(J,K) = (1,1)$ and $(2,2)$ to determine the physical characteristics of the dense core. Since the opacity of ^{13}CO $J = 1 \rightarrow 0$ transition is moderate ($\tau < 0.5$) we can safely assume the C^{18}O $J = 1 \rightarrow 0$ transition is optically thin. The column density of C^{18}O is then given by equation (3A.8). At the peak of the C^{18}O map we find $N(\mathrm{C}^{18}\mathrm{O}) = 2.0 \times 10^{15}$ cm^{-2}, which implies $N(\mathrm{H_2}) \sim 1.2 \times 10^{22}$ cm^{-2} assuming an [H_2/C^{18}O] ratio of 5.9×10^6 (Rohlfs & Wilson 1996). The total mass traced by C^{18}O may then be found using equation (3A.9). For BHR 71 we determine $\iint T_{mb} dv d\Omega = 28.2$ K km s^{-1} arcmin^2, which implies a mass of $\sim 12\ M_\odot$.

Analysis techniques of the NH$_3$ observations are given in Bourke et al. (1995b). Briefly, the hyperfine components of the (1,1) inversion transition are modelled to derive the optical depth and excitation temperature at the observed

position. The optical depth of the (1,1) line and the ratio of antenna temperatures of the (2,2) and (1,1) transitions may then be used to determine the rotational temperature, and hence the kinetic temperature and volume density. For BHR 71, Bourke et al. (1995b) derive a kinetic temperature at the globule center of 13 K, a mean density for the core of 2.4×10^4 cm^{-3}, and a core mass within the FWHM contour of $\sim 3\ M_\odot$ (corrected for the new distance assumption of 200 pc). From more recent ammonia observations, we find that the kinetic temperature at the offset positions ($\Delta\alpha = \pm 1'$, $\Delta\delta = \pm 1'$) relative to the IRAS PSC position shows little variation, with only slight evidence that the temperature drops to 11 K east and west of the center, and increases slightly to the south.

Table 3.4. Globule parameters

Molecule	V_{lsr} (km s^{-1})	ΔV (km s^{-1})	Diameter[a] (pc)	$<N>$[b] (cm^{-2})	$n(H_2)$ (cm^{-3})	Mass ($M_\odot$)
^{12}CO	–4.26	1.09	0.66	3.0×10^{17}	4×10^3	39
^{13}CO	–4.35	0.80	0.51	2.8×10^{15}	9×10^3	41
C^{18}O	–4.63	0.82	0.22	2.0×10^{15}	2×10^4	12
NH_3	–4.45	0.69	0.15	9.2×10^{14}	2×10^4	3

[a]Geometric mean of major and minor axes.

[b]Beam averaged column density.

A summary of the observed and derived parameters of the BHR 71 globule are given in Table 3.4.

3.4.2. Molecular outflow

Outflow inclination

The dynamics of molecular outflows can, in principle, be elucidated from a comparison of the observed spatial and velocity structure of the flows with synthetic maps. For instance, it should be possible to discern whether the flow is steady or explosive and whether the flow moves with constant velocity or is being accelerated (e.g. Snell et al. 1984). In this spirit, Cabrit & Bertout (1986, 1990) have computed the ^{12}CO line formation in accelerated and constant velocity bipolar outflows, for different values of view angle and flow opening angle. From the observed spatial and kinematical characteristics (e.g. profiles, position-velocity diagrams, etc.), Cabrit & Bertout found that, for biconical outflows with power law velocity fields of the form

$$\vec{v}(r) = v_o \left(\frac{r_o}{r}\right)^{\alpha} \hat{r} \quad , \tag{3.1}$$

where r is the radial distance from the apex of the flow, four cases can be distinguished, which depend on the inclination of the outflow axis to the line of sight, and the outflow opening angle. These cases are discussed in detail by Cabrit & Bertout.

The observed properties of the outflowing gas from BHR 71 strongly suggest that this molecular outflow is oriented nearly perpendicular to the line of sight and is flowing with a velocity that is nearly independent of the radial distance from the apex. In what follows we assume that the BHR 71 outflow can be modelled by a biconical flow with constant radial velocity [i.e. $\alpha = 0$ in eqn. (3.1)] and derive the values of the model parameters imposed by the observations. First, from the ratio of the observed maximum blueshifted and redshifted velocities within a single lobe, it is possible to estimate the inclination angle, i, of the flow (Cabrit et al. 1988). Using the maximum observed blueshifted and redshifted velocities toward the blue lobe, of ~ 8 and ~ 4 km s^{-1}, respectively, and assuming a semi-opening angle of $15° \pm 5°$, we derive $i = 85° \pm 5°$. Similarly, using the maximum observed redshifted and blueshifted velocities toward the red lobe,

of $\sim$ 10 and $\sim$ 3 km s^{-1} respectively, we find that $i = 82° \pm 5°$. Hereafter, we will adopt an inclination angle for the BHR 71 outflow of 84°. The outflow is thus orientated very close to the plane of the sky. The flow velocity can then be estimated as $V_m/cos(i-\theta_{max})$, where V_m is the maximum observed flow velocity. Using the observed value of V_m of $\sim$ 10 km s^{-1} and the derived value for $i-\theta_{max}$ of $\sim$ 69°, we derive a flow velocity of $\sim$ 28 km s^{-1}. Single bipolar outflows with spatial and kinematical characteristics similar to those of the BHR 71 outflow have been observed toward B335 and RNO43 (Cabrit et al. 1988).

Energetics

The mass in the lobes can be estimated from the ^{12}CO observations assuming the emission is optically thin, as described in detail in §3A.2. The main source of error in determing the mass in the outflow arises from the adoption of the velocity boundary between the wing and the ambient line. Further sources of error in this approach are the uncertainties in [$H_2/^{12}$CO], in the excitation temperature, and the possibility that the ^{12}CO $J = 1 \rightarrow 0$ wing emission might be moderately optically thick at low flow velocities. A general discussion of source of errors in the computation of flow mass have been given by Margulis & Lada (1985) and Cabrit & Bertout (1990).

For the BHR 71 outflow, we will adopt as the velocity boundary of the blue and red wing emission the values of -6 and -3 km s^{-1}, respectively. The lobe emission is integrated over the velocity range $-14 < v_{\rm lsr} < -6$ km s^{-1} in the southeast lobe, and $-3 < v_{\rm lsr} < 7$ km s^{-1} in the northwest lobe (Fig. 3.5). From the ^{12}CO $J = 1 \rightarrow 0$ and $J = 2 \rightarrow 1$ observations, we determine that $T_{ex} = 11$ K in the southeast and $T_{ex} = 13$ K in the northwest lobe, determined in the manner described in Levreault (1988). Using these temperatures and the observed emission in the velocity ranges given above we estimated masses of 0.06 $M_\odot$ and 0.14 $M_\odot$ for the southeast and northwest lobes, respectively. However, as discussed in the previous section, each lobe exhibits emission at both blueshifted and redshifted velocities with respect to the ambient cloud velocity, implying that these masses correspond to a strict lower limit to the total flow mass. In

the southeast lobe, the redshifted emission is clearly seen in the integrated velocity map (Fig. 3.5). The mass arising from redshifted emission in the southeast lobe is estimated to be 0.03 $M_{\odot}$, so the total mass in the southeast lobe is $\sim$ 0.09 $M_{\odot}$. In the northwest lobe, the blueshifted emission is also present, and the mass arising from blueshifted emission in the northwest lobe is $\sim$ 0.08 $M_{\odot}$, resulting in a total mass for the northwest lobe of $\sim$ 0.22 $M_{\odot}$.

The mass of the low velocity flow hidden in the ambient cloud range of velocities within the southeast and northwest lobes was estimated, using the method of Margulis & Lada [(1985; see also equation (3A.16)], to be 0.04 and 0.10 $M_{\odot}$, respectively. The total mass within each lobe was also estimated by simultaneously fitting a broad Gaussian profile (the outflow gas) and a narrow Gaussian profile (the ambient cloud) to the integrated line profiles, obtaining similar masses to the ones quoted above.

From the observations of the ^{12}CO $J = 1 \rightarrow 0$ and ^{13}CO $J = 1 \rightarrow 0$ lines in selected positions of the outflow it is possible to estimate the opacities of the flowing gas and therefore to assess whether or not our assumption that the ^{12}CO $J = 1 \rightarrow 0$ wing emission is optically thin is correct. The average ^{12}CO $J = 1 \rightarrow 0$ opacities in the line wing at different flow positions, computed from equation (3A.2) using the observed velocity integrated wing emission (columns 3 and 4 of Table 3.5) and assuming T_{ex} = 11 K (blue lobe) and 13 K (red lobe), and a = 89, are listed in column 5 of Table 3.5. Typically, the average ^{12}CO $J = 1 \rightarrow 0$ opacities of the blueshifted gas toward the southeast lobe are $\sim$ 2, while the opacities of the redshifted gas toward the northwest lobe are $\sim$ 3, implying that the flowing gas is moderately optically thick. To correct for this effect, we multiply the mass determined from the optically thin assumption by the factor $\tau_w/(1 - e^{-\tau_w})$, where τ_w is the average ^{12}CO $J = 1 \rightarrow 0$ optical depth in the line wing. We find that the opacity corrected masses within the blue and red lobes (M_{lobe}) are $\sim$ 0.23 and $\sim$ 0.69 $M_{\odot}$, respectively. The opacity corrected masses for the low velocity material hidden in the ambient line emission (M_{hidden}) are 0.09 and 0.30 $M_{\odot}$, respectively. Adding the lobe masses to the low velocity masses, we obtained masses of $\sim$ 0.3 and 1.0 $M_{\odot}$ for the southeast and northwest

Table 3.5. Opacity of Line Wing Emission

Offset position		$\int T_a(^{12}\mathrm{CO})dv$	$\int T_a(^{13}\mathrm{CO})dv$	τ_{12}
$\Delta\alpha$ (′)	$\Delta\delta$ (′)	(K km s^{-1})	(K km s^{-1})	
		Southeast lobe (Blue)		
−1.0	−5.0	13.1	0.20	0.8
−1.0	−4.0	13.8	0.29	1.6
−1.0	−3.0	8.1	0.46	5.5
−2.0	−4.0	9.2	0.11	0.2
−2.0	−3.0	12.3	0.48	3.7
−2.0	−2.0	15.0	0.47	2.8
		Northwest lobe (Red)		
−2.0	0.0	21.0	0.73	3.2
−2.0	1.0	19.9	0.87	4.2
−2.0	2.0	10.4	0.46	4.3
−3.0	1.0	13.0	0.29	1.8
−3.0	2.0	13.8	0.33	2.0

Note. — Offset positions are relative to $\alpha_{1950} = 11^{\mathrm{h}}59^{\mathrm{m}}01^{\mathrm{s}}.18$, $\delta_{1950} = -64°52'00''$.

lobes, respectively.

From the flow masses it is possible to estimate the momentum P and the kinetic energy E_k in the flow, as well as the mechanical luminosity L_m. A thorough discussion regarding the evaluation of these parameters has been given by Margulis & Lada (1985), Lada (1985) and Cabrit & Bertout (1990), and the relevant equations are given in the appendix [eqs. (3A.17) and (3A.18)]. Since for the BHR 71 outflow the radial velocity is approximately constant at 28 $\mathrm{km\,s^{-1}}$ (§3.4.2), we will assume $V_{char} = V_o$ for equation (3A.18), and the parameters determined in this manner are upper limits (Cabrit & Bertout 1990). In Table 3.6 we give the parameters of the blue and red lobes of the BHR 71 flow calculated using both methods. The dynamical time scale of the outflow, τ_d, is found from R/V_o, and is estimated at $\sim 10^4$ yrs. The geometric mean values for the outflow parameters are $\overline{P} \sim 11\ M_\odot\ \mathrm{km\,s^{-1}}$, $\overline{E_k} \sim 60\ M_\odot\ \mathrm{km^2\ s^{-2}}$, and $\overline{L_m} \sim 0.5\ L_\odot$.

3.4.3. The energy source of the outflow

The total far-infrared (IRAS) luminosity of IRAS 11590–6452 is found to be $L_{IRAS} \sim 8\ L_\odot$ (e.g. Casoli et al. 1986; Parker 1991), assuming a distance of 200 pc. Figure 3.12 shows the spectral energy distribution (SED) of IRAS 11590–6452 from 12 μm to 1.3 mm, typical of a very young embedded object. According to Lada's (1991) SED classification of low mass young stellar objects, IRAS 11590–6452 would correspond to an "extreme class I" object, which are characterized by being very weak in the near-infrared ($\lambda \leq 25\mu$m) and emitting most of their luminosity at far-infrared and millimeter wavelengths. The emission at the longer wavelengths ($\lambda > 25\mu$m) can be explained as dust thermal emission arising from a circumstellar shell, and is well fitted by a modified blackbody function of the form

$$B_\nu(T_d)\,[1 - \exp(-\tau_\nu)]\,\Omega_s \quad , \tag{3.2}$$

where τ_ν is the dust optical depth, $B_\nu(T_d)$ is the Planck function at the dust temperature T_d, and Ω_s is the solid angle subtended by the dust emitting region.

Table 3.6. Outflow Parameters

Lobe	M_{lobe}	M_{hidden}	M_{total}	P^{min}	P^{max}	E_k^{min}	E_k^{max}	L_m^{min}	L_m^{max}	t_d
	($M_\odot$)			($M_\odot$ km s^{-1})		($M_\odot$ km^2 s^{-2})		($L_\odot$)		(yr)
SE	0.23	0.09	0.32	0.7	9.0	1.5	125	0.004	1.9	10700
NW	0.69	0.32	1.01	2.5	28.3	5.9	396	0.021	6.4	10200
Total	0.92	0.41	1.33	3.2	37.3	7.4	521	0.025	8.3	...

NOTE.—P^{min}, E_k^{min}, L_m^{min} are determined using M_{lobe}; P^{max}, E_k^{max}, L_m^{max} are determined using M_{total}.

The opacity is assumed to vary with frequency as ν^{β}, i.e. $\tau_{\nu} = (\nu/\nu_o)^{\beta}$, where ν_o is the frequency at which the optical depth is unity. Due to the limited number of spectral points, we have set the value of β equal to 1.5, consistent with previous values found for very red sources driving highly collimated outflows ($1 < \beta < 2$; AWB; André 1995). We also estimated the dust temperature *a priori* at 35 K since the good detection at 60 μm suggests that it will be greater than 30 K. The fit is shown in Figure 3.12. The fact that the 25 μm emission is not fit by our simple modelling can easily be explained if there exists small grains which are transiently heated to high temperatures, or by emission from within a disk region, or both. The angular size derived for the compact component from the modified blackbody fit to the spectrum is 3.″5 (700 AU), assuming a Gaussian flux distribution. However, more detections at the longest wavelengths are required in order to better constrain the fit.

From the fit to the SED we find that the wavelength at which the opacity is unity is ~ 350 μm, implying that the thermal dust emission at 1.3 mm is optically thin ($\tau_{1.3mm} \sim 0.14$). Thus, the observed flux density at 1.3 mm allows us to estimate the mass of the dense circumstellar material around the driving source of the outflow. Using $T_d = 35$ K and $S_{1.3mm} = 1.7$ Jy in equation (3A.20) implies a circumstellar mass M_{cm} of 1.0 $M_{\odot}$ for the unresolved central component. For the extended component, taking $S_{1.3mm} = 2.6$ Jy, we obtain a mass of 1.4 $M_{\odot}$ (assuming a temperature of 35 K). The total circumstellar mass is therefore $M_{cm} \sim 2.4$ $M_{\odot}$. If the extended component is cooler that 35 K then our mass estimate for this component is a lower limit, e.g. for a temperature of 20 K the mass in the extended component would be 2.8 $M_{\odot}$. The bolometric luminosity has been estimated in the manner described in Chen et al. (1995), and we find $L_{bol} \sim 8$ $L_{\odot}$, the same result as for L_{IRAS}. Integrating under the fitted curve in Figure 3.12 implies $L_{bol} \sim 9$ $L_{\odot}$.

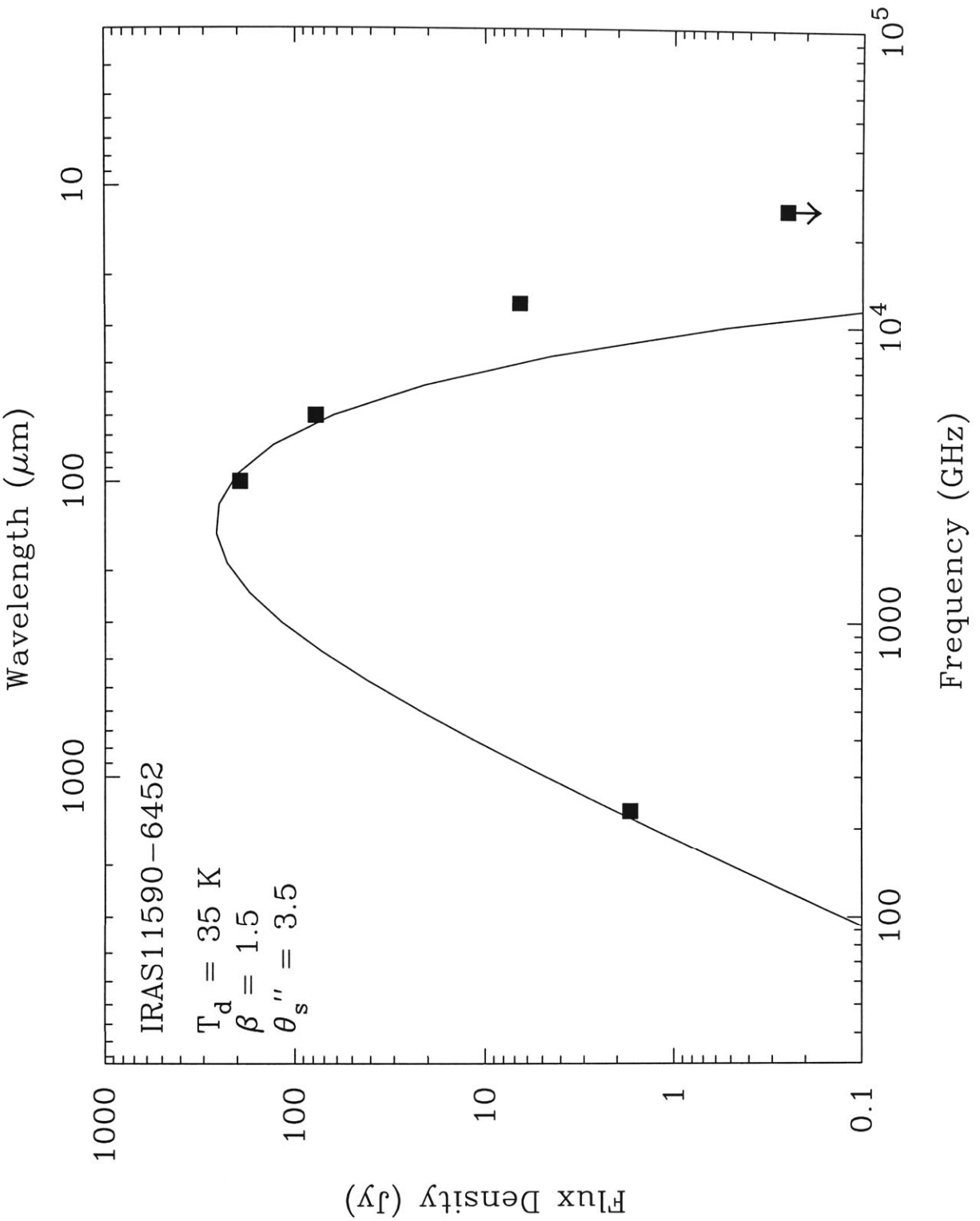

Figure 3.12.— Spectral energy distribution of IRAS 11590–6452. The solid curve is a fit to the spectrum wth a modified blackbody function of the form $B_\nu(T_d)\left[1-\exp(-(\nu/\nu_o)^\beta)\right]$. The parameters used in the fit are indicated on the figure.

3.5. Discussion

3.5.1. Shocks in a very young outflow

Figure 3.13 presents an overview of the outflow system in BHR 71, with the blue contours representing the blue lobe of the outflow, red contours the red lobe (see Fig. 3.5), and the black contours representing the 1.3 mm continuum emission (Fig. 3.9). Figure 3.13 shows that the outflow is highly collimated, and that the lobes are cylindrical in shape – the outflow angle does not stay constant, but becomes narrower as the radial distance from the flow center increases. This implies that we are probably witnessing a very young jet driven outflow in action (e.g. Masson & Chernin 1993; Raga & Cabrit 1993), where the outflow results from the prompt entrainment of material in the wake of a bow shock created by the jet as it plows through the ambient molecular material. The youth of the outflow is also inferred from the young dynamical age of $\sim 10^4$ yrs, and the high degree of collimation of the outflow lobes, particularly the increase in collimation at higher velocities (Bachiller & Gómez-González 1992).

The increase in CO emission, and hence gas kinetic temperature, at the ambient cloud velocity in the direction of the outflow lobes indicates that the outflow is heating the ambient gas in some way. The L1157 outflow, which exhibits similar CO behaviour to BHR 71, shows strong evidence for shock excitation in the lines of SiO, CH_3OH, H_2, and NH_3 (3,3), suggesting that the enhancement seen in BHR 71 is a result of shock heating of the ambient gas by bow-shocks at the head of the jet driving the outflow, and supporting the view that the outflow is jet driven (Umemoto et al. 1992; Mikami et al. 1992; Bachiller et al. 1993, 1995b; Davis & Eislöffel 1995; Tafalla & Bachiller 1995; Zhang et al. 1995; Gueth, Guilloteau, & Bachiller 1996). The enhancement of SiO and CH_3OH is thought to be the result of grain destruction caused by the passage of shocks through the ambient medium (Bachiller & Gómez-González 1992), and is believed to be an indicator of outflow evolution, with only the youngest outflows i.e. those that have not yet cleared away the ambient material, showing enhancements in these molecules. We have extensive observations

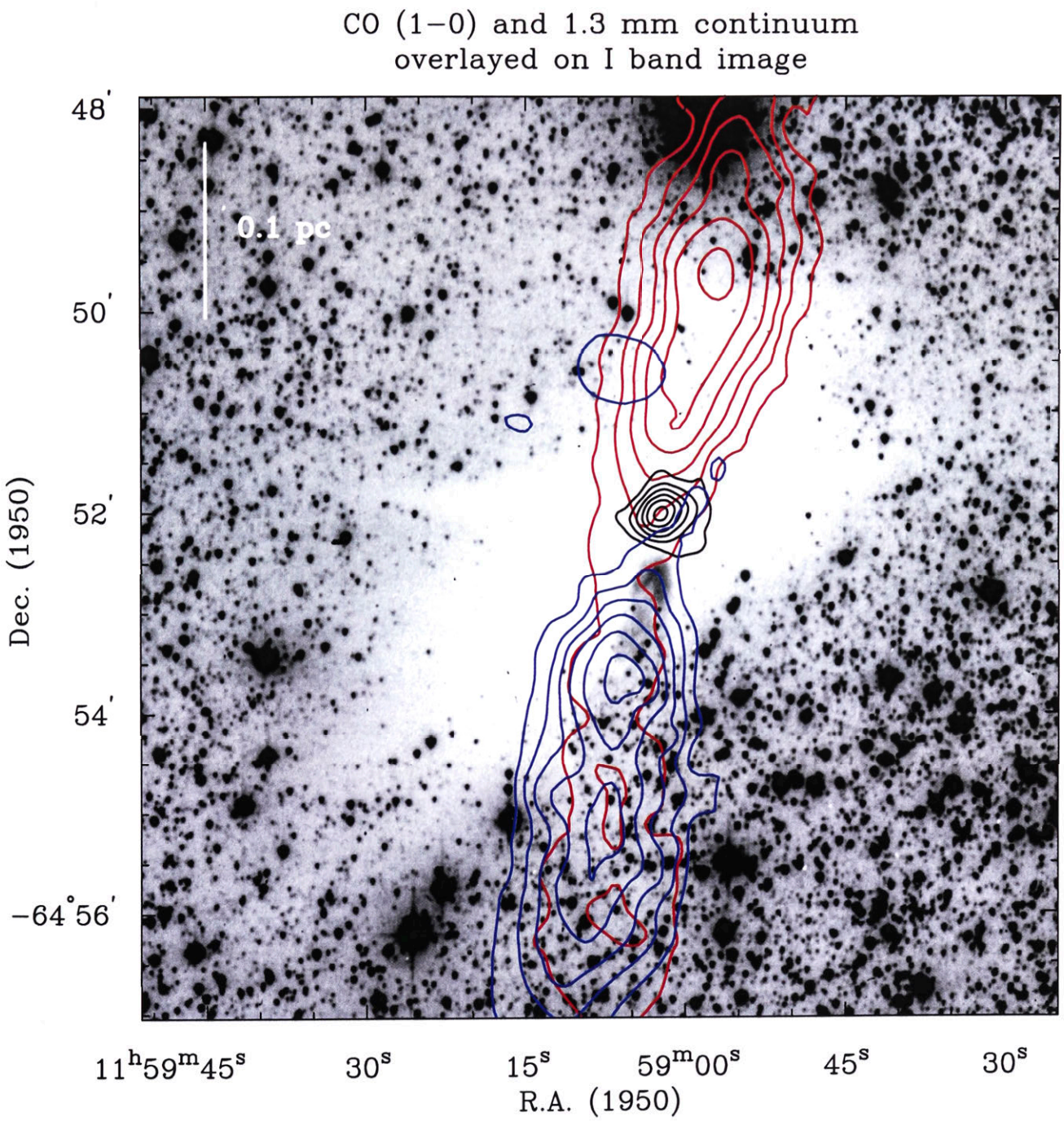

Figure 3.13.— An overview of the IRAS 11590–6452/BHR 71 outflow system. The blue contours represent the blue outflow lobe, the red contours the red outflow lobe, and the black contours the 1.3 mm continuum emission. The linear size scale is indicated in the upper left.

of SiO and CH_3OH toward the outflow in BHR 71 which, like L1157, show strong intensity increases and line wings in the outflow, but little or no emission at the position of the embedded source (see next Chapter).

Further evidence for bow shocks come from observations of molecular hydrogen emission in the near-infrared (NIR), which show a close spatial correlation between NIR bow shock structures and limb-brightened cavity structures with the integrated CO lobe emission in the flow (e.g. Bachiller et al. 1995a; Bally, Lada, & Lane 1993; Davis & Eislöffel 1995). In Figure 3.13 we see that the first peak of CO emission in the blue lobe coincides with the termination of the nebulosity seen in the I band image. Observations in the NIR (Bourke 1994; Bourke et al. in preparation; see Fig 3.14) shows extensive molecular hydrogen emission is associated with both the blue and red lobes of the outflow, and that an arc-like structure coincides with the first blue peak. Similar structures have been observed in other highly collimated outflows (Davis & Eislöffel 1995), adding further support to the view that shocks are playing a major role in the BHR 71 outflow.

3.5.2. Globule disruption by the outflow

One remarkable feature of the outflow is the extent to which it can be traced outside of the optical boundary of the globule, as defined by the I band extinction. This feature is evident even when comparing the outflow to the image taken in blue light (Fig. 3.1). A similar phenomena is seen in B335 (Cabrit et al. 1988 and Frerking et al. 1987). The spatial coincidence between the nebulosity and the blue lobe suggests that the outflow may be breaking through the front side of the globule, or at least has carved out a cavity along the outflow axis, with the nebulosity resulting from light scattered into the line of sight by the cavity walls. The stars that may be seen along the line of sight to the nebulosity are most probably background stars, rendered visible due to the decrease in extinction caused by the evacuation of material by the outflow. The fact that the nebulosity is narrow compared to the outflow lobes may add further support to the

Figure 3.14.— *Next Page*

Overlay of the integrated ^{12}CO $J = 1 \rightarrow 0$ contours from the spectra shown in Fig 3.4 on the H_2 2.122 μm image (not continuum subtracted). The image is a mosaic taken with the infrared array camrea IRIS on the AAT. The solid contours represent the blue-shifted outflow and are integrated over the velocity range -9.1 to -5.5 km s^{-1} while the dashed contours represent the red-shifted outflow and are integrated over the velocity range -3.1 to 0.5 km s^{-1} (see next Chapter). Contours are 35, 45, 55, 65, 75, 85, and 95% of the peak $\int T_{mb} dv$ of 22.4 K km s^{-1} for the blue-lobe and 24.4 K km s^{-1} for the red-lobe. The star marks the position of the mm-IRAS source and the offsets are relative to it.

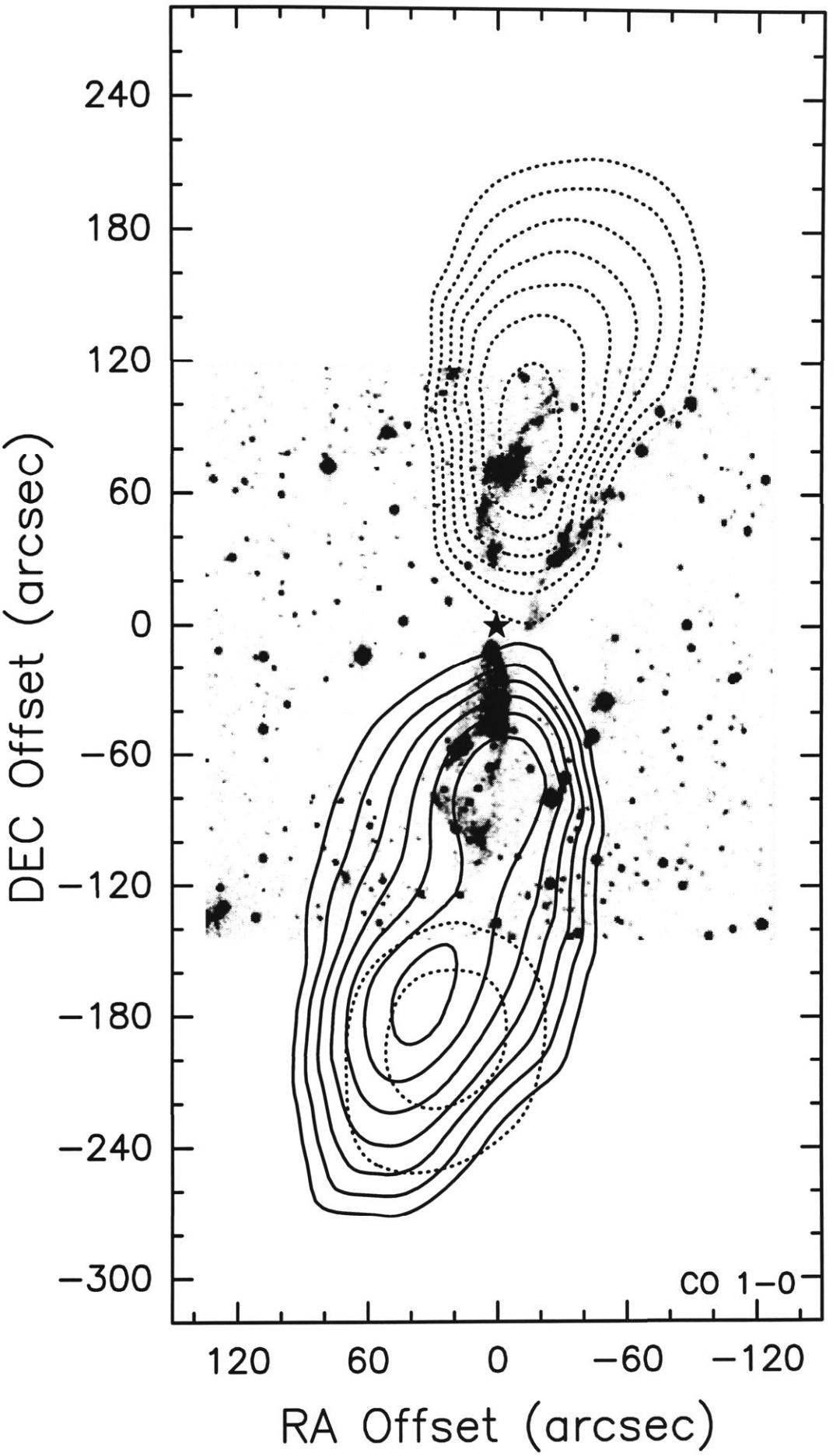
240
180
120
60
0
−60
−120
−180
−240
−300
DEC Offset (arcsec)
120
60
0
−60
−120
RA Offset (arcsec)
CO 1−0

idea that the outflow is jet driven, and the cavity has resulted from the passage of bow shocks along the jet which have cleared away the ambient material. The contours of $C^{18}O$ (Fig. 3.3) provide further evidence that an evacuation is taking place, and that the globule is being disrupted by the outflow. Along the outflow axis toward the blue lobe we see that the $C^{18}O$ contours take a sharp dip toward the globule center, indicating a decrease in column density along the line of sight to the blue lobe. Toward the red lobe the nesting of the $C^{18}O$ contours to higher column density is disrupted, suggesting that the gas in this region has also been disturbed by the outflow.

3.5.3. Comparison with the B335 outflow

Cabrit et al. (1988) have investigated the properties of the outflow in the well studied Bok globule B335 in a similar manner to this Chapter. In Table 3.7 we list the derived properties of the two globules for comparison. Data for B335 are taken from Cabrit et al. (1988; outflow), Frerking et al. (1987; ambient CO), Menten et al. (1984; ambient NH_3), and Benson & Myers (1989; ambient NH_3). In calculating their upper limits, Cabrit et al. did not attempt to correct for the outflow mass hidden in the ambient line core. For Table 3.7 we have recalculated our upper limits using M_{lobe} as the outflow mass (Table 3.6), rather than M_{total} which was used in Table 3.6, to be consistent with Cabrit et al. In this table we introduce quantities used by Cabrit et al. the momentum, or outflow, efficiency ($Fc/L_{bol} \equiv P/t_d \times c/L_{bol}$), and the energy efficiency (L_m/L_{bol}). We give only "upper" limit estimates for t_d from Cabrit et al. and have redetermined Fc/L_{bol} appropriately. We also estimate the mass traced by ammonia for B335 based on the studies of Menten et al. (1984) and Benson & Myers (1989), using the method of Bourke et al. (1995b).

Though the globules have similar masses regardless of the tracer used, the properties of the outflows and central sources are significantly different. The embedded source in B335 has a luminosity of 3 $L_\odot$ and a circumstellar mass of 0.8 $M_\odot$, while the values for the embedded source in BHR 71 are greater by a

Table 3.7. Comparison of properties: B335 & BHR 71

Property	B335		BHR 71		BHR 71/B335
	min	max	min	max	
D (pc)	250		200		...
$M(NH_3)$ ($M_\odot$)	2		3		1.5
$M(C^{18}O)$ ($M_\odot$)	11		12		1
$M(CO)$ ($M_\odot$)	36		40		1
L_{bol} ($L_\odot$)	3		9		3
M_{cm} ($M_\odot$)	0.8		2.4		3
M_{lobe} ($M_\odot$)	0.2		0.9		5
P ($M_\odot$ km s^{-1})	0.4	2.2	3.2	25.8	10
E_k ($M_\odot$ km^2 s^{-2})	0.4	10.1	7.4	360	26
L_m ($L_\odot$)	1.7(–4)	1.8(–2)	2.5(–2)	5.7	220
t_d (yr)	9.3(4)		1.0(4)		0.1
V_{char} (km s^{-1})	10		28		3
Fc/L_{bol}	70	390	1800	14000	31
L_m/L_{bol}	5.6(–5)	5.9(–3)	2.8(–3)	0.6	70

Note. — The ratio is the geometric mean of two ratios when a min and max value are quoted. Values in parentheses are powers of 10.

factor of 3 on both counts. In BHR 71 we are dealing with a more massive and luminous source. The outflow properties are also significantly different. Though both globules have highly collimated outflows, it appears that the outflow in BHR 71 is younger, more energetic, and the central source is more efficient at transferring momentum and energy to its outflow. In fact, all the parameters relating to the dynamics of the outflow, i.e. momentum, kinetic energy, mechanical luminosity, momentum efficiency (Fc/L_{bol}) and energy efficiency (L_m/L_{bol}), are *at least an order of magnitude greater in the BHR 71 outflow.* However, the spectral characteristics of both outflow sources suggest that the outflows are driven by very young "Class 0" sources (see below).

Thus, while the globules B335 and BHR 71 are similar, the YSO/outflow system in BHR 71 seems to be a scaled up version of the system in B335 in many aspects, i.e. it is more energetic and driven by a more powerful source, but at the same time it is younger.

3.5.4. The nature of the driving source

In §3.4.3 we estimated that the total circumstellar mass around IRAS 11590–6452 is $\sim 2.4\ M_{\odot}$. Whether the bulk of this mass is in the form of a disk, an infalling envelope, or a combination of the two, is not clear. Cabrit & André (1991) found that low luminosity ($L_{bol} < 100\ L_{\odot}$) deeply embedded YSO's with well developed molecular outflows have considerably stronger millimeter fluxes than those without flows. The location of the BHR 71 outflow in the normalized 1.3 mm flux density versus bolometric luminosity diagram (see Cabrit & André's Fig. 1) is as expected for a molecular flow with a massive circumstellar disk. Cabrit & André proposed that the dichotomy between outflow and non-outflow sources is due to the presence of massive circumstellar disk structures around molecular outflow sources, suggesting a connection between circumstellar disk mass and the driving engine of protostellar outflows.

AWB have proposed a new class of protostellar objects, based primarily on their submillimeter observations of a number of young protostars. This new

class, the so-called Class 0 sources, are defined as having (1) indirect evidence for the existence of a central YSO (e.g. a molecular outflow), and (2) an SED well characterised by a single modified blackbody with a temperature of $\sim 15 - 30$ K, which implies a high value of L_{submm}/L_{bol}, where L_{submm} is the luminosity a wavelengths longer than 350 μm (AWB; André 1995). Property (1) insures that the sources are not pre-protostellar, while (2) distinguishes them from Class I sources, which are more evolved (André 1995). AWB proposed that Class 0 sources be defined as those objects which have $L_{submm}/L_{bol} > 5 \times 10^{-3}$, which in turn implies $M_{cm}/M_* > 1$, where M_* is the mass of the protostellar object (based on assumptions about mass infall rates and circumstellar dust temperatures). This number is meant to indicate that sources with this property "have yet to accrete the bulk of their final stellar mass" (André 1995). For IRAS 11590–6452, we find that $L_{submm}/L_{bol} \sim 2 \times 10^{-2}$. The dust temperature we have used of 35 K is greater than the range defined in (2), but is similar to values found for other Class 0 candidates, e.g. L1448-mm (Bachiller et al. 1995a).

In a similar vein, André (1995) and Bontemps et al. (1996) have argued that a plot of circumstellar mass against bolometric luminosity (essentially integrated 1.3 mm flux against L_{bol}) can be used as an evolutionary indicator. While Reipurth et al. (1993) have shown that there is a correlation between these two properties for Class I sources, the Class 0 sources have circumstellar masses an order of magnitude greater. The location of IRAS 11590–6452 in such a plot not only indicates that it may have a massive circumstellar disk (if Cabrit & André 1991 are correct), but that it is similar to the Class 0 sources in possessing a relatively large circumstellar mass. Bontemps et al. (1996) have also argued that the outflow properties of Class 0 sources are significantly different from the properties of outflows from Class I sources. When they plot outflow momentum flux against L_{bol} they find a good correlation for Class I sources, but outflows from Class 0 sources have a much larger momentum flux. They find that Class I sources have a momentum efficiency ("outflow efficiency") of ~ 100 on average, while Class 0 sources have an average value an order of magnitude greater. For the BHR 71 outflow, we estimate an outflow efficiency of ~ 5500.

Myers & Ladd (1993) have attempted to classify YSOs on the basis of their "bolometric temperature", T_{bol}, which they define as the temperature of a blackbody having the same mean frequency as the observed source SED, the mean frequency being the ratio of the first and zeroth moments of the spectrum. For main sequence stars, $T_{bol} \equiv T_{eff}$, while for embedded protostellar objects, for which no measure of T_{eff} is possible, and which have spectra much broader that a blackbody, T_{bol} is very low, typically < 100 K (Chen et al. 1995). Previous determinations of T_{bol} for a large number of sources (Myers & Ladd 1993; Chen et al. 1995) show a clear trend for the youngest sources to have the lowest values of T_{bol} (see Fig. 6 of Chen et al. 1995), and how the use of a log-log diagram of L_{bol} versus T_{bol} (the "BLT" diagram) can distinguish sources of different "classes" in the scheme of Lada (1991). These studies required that in order to calculate T_{bol} the source must have been detected at six or more frequencies. For IRAS 11590–6452, detections at only four frequencies have been made. However, these detections bound the frequency at which the peak emission occurs (Fig. 3.12), and allows us to to estimate that $T_{bol} \sim 56$ K with some confidence. Placing IRAS 11590–6452 on Figure 6 of Chen et al. indicates that it is a Class 0 protostellar source (André 1995).

The high obscuration, cold dust temperature, low bolometric temperature, and significant amount of circumstellar material around IRAS 11590–6452, the central source of BHR 71, are characteristic of Class 0 young stellar objects (e.g. André 1995, and references therein). These objects are thought to be still building up their mass from a surrounding infalling envelope, and therefore are at the earliest known stage of evolution of protostars. There are presently about 30 known objects within this class (Bachiller 1996), several of which were discovered because they are associated with highly collimated outflows. We suggest that at the center of BHR 71 lies a very young protostar which is still accreting matter.

3.6. Summary & Conclusions

We have observed the southern Bok globule BHR 71 in the $J = 1 \rightarrow 0$ and $J = 2 \rightarrow 1$ transitions of ^{12}CO, the $J = 1 \rightarrow 0$ transition of ^{13}CO and C^{18}O, in the $(J,K) = (1,1)$ and (2,2) inversion transitions of ammonia, and in the continuum at 1.3 mm, with angular resolutions ranging from 20″ to 9′. The main results and conclusions presented in this Chapter are summarized as follows.

1) The observations of the $J = 1 \rightarrow 0$ ^{12}CO and ^{13}CO lines with low angular resolution (FWHM 8.′8) indicate that the emission arises from roughly a circular region of size $\sim$ 0.5 pc. From these observations we derive that the molecular gas has a kinetic temperature of 11 K, an average molecular density of $\sim 9 \times 10^3$ cm^{-3}, and a total mass of $\sim$ 40 $M_\odot$.

2) C^{18}O emission arises from an elongated structure of size $\sim$ 0.3 $\times$ 0.15 pc and mass 12 $M_\odot$, which is spatially correlated with the I band extinction. The C^{18}O, which traces column density, appears to have been disrupted by the passage of the outflow. The ammonia observations, which sample denser gas, also show an elongated structure, of size $\sim$ 0.2 $\times$ 0.1 pc. From these observations we derive that the central region of the globule has a density 2 $\times$ 10^4 cm^{-3} and a kinetic temperature of 13 K. The mass of the dense core traced by ammonia is 3 $M_\odot$.

3) The observations of the $J = 1 \rightarrow 0$ ^{12}CO line emission with high angular resolution (FWHM 45″) reveal the presence, toward the center of the globule, of a highly collimated bipolar outflow with lobes extending by $\sim$ 0.3 pc in opposite directions. The bulk of the emission from the southwest lobe arises at velocities that are blueshifted (velocity range from about -14 to -6 km s^{-1}) with respect to the ambient cloud velocity, while the bulk of the emission from the northwest lobe arises from velocities that are redshifted (velocity range from about -3 to 7 km s^{-1}). In addition, both blueshifted and redshifted emission at low outflow velocities ($1.2 < |v - v_o| < 3.6$ km s^{-1}, where v_o is the ambient cloud velocity) is detected toward each of the lobes. The observed morphology and velocity structure of the flow is well accounted for with a simple model of a biconical

outflow with a semi-opening angle of 15°, in which the gas moves outwards with a constant radial velocity (with respect to the cone apex) of $\sim$ 28 km s^{-1} and that is viewed nearly perpendicular to its symmetry axis. The inclination of the outflow axis from the line of sight is found to be $\sim$ 84°.

4) We find that the excitation temperature of the outflowing gas is 11 K in the southeast lobe and 13 K in the northwest lobe. The total flow masses within each lobe, taking into account the mass in the velocity range of the ambient cloud and optical depth effects of the flowing gas, are 0.3 $M_{\odot}$ and 1.0 $M_{\odot}$ for the southeast and northwest lobes, respectively. The mechanical luminosity of the molecular outflow is $\sim$ 0.5 $L_{\odot}$ and its dynamical age is $\sim$ 10^4 years.

5) The 1.3 mm continuum observations reveals a strong compact source at the origin of the outflow, which is coincident with the source IRAS 11590–6452, surrounded by an extended component. The total luminosity is $L_{bol} \sim 9\ L_{\odot}$. The spectral energy distribution of this object, likely to be associated with the source driving the molecular outflow, is similar to those of circumstellar structures surrounding very young embedded protostellar objects or Class 0 sources in the classification scheme of André et al. (1993). The emission at the longer wavelengths ($\lambda > 25\mu$m) can be simply explained as dust thermal emission arising from an extended cold circumstellar structure with a dust temperature of $\sim$ 35 K (assuming a dust opacity power law dependence with frequency of $\sim$ 1.5). We find that the circumstellar mass associated with IRAS 11590–6452 is $\sim$ 2.4 $M_{\odot}$.

We conclude that the BHR 71 outflow is a new example of the class of highly collimated molecular outflows which appear to be driven by very young protostellar objects with extremely cold spectral signatures, thought to play a crucial role in the formation of standard bipolar flows. In the next Chapter we present the results of our observations of CS, SiO, HCO^+, and CH_3OH emission from the outflow, which show abundance enhancements similar to those seen toward other highly collimated outflows, in particular the L1157 outflow.

REFERENCES

André, P. 1995, Ap&SS, 224, 29

André, P., Ward-Thompson, D., & Barsony, M. 1993, ApJ, 406, 122 (AWB)

Aumann, H. H., Fowler, J. W., & Melnyk, M. 1990, AJ, 99, 1681

Bachiller, R. 1996, ARA&A, 34, 111

Bachiller, R., Cernicharo, J., Martín-Pintado, J., Tafalla, M., & Lazareff, B. 1990, A&A, 231, 174

Bachiller, R., & Gómez-González, J. 1992, Astron. Astrophys. Rev., 3, 257

Bachiller, R., Guilloteau, S., Dutrey, A., Planesas, P., & Martín-Pintado, J. 1995a, A&A, 299, 857

Bachiller, R., Liechti, S., Walmsley, C. M., & Colomer, F. 1995b, A&A, 295, L51

Bachiller, R., Martín-Pintado, J., & Fuente, A. 1993, ApJ, 417, L45

Bachiller, R., Martín-Pintado, J., & Planesas, P. 1991, A&A, 251, 639

Barsony, M. 1994, in Clouds, Cores, and Low Mass Stars, ed. D. P. Clemens, R. Barvainis (Provo: Astronomical Society of the Pacific), 197

Bally, J., Lada, C. J., & Lane, A. P. 1993, ApJ, 418, 322

Bence, S. J., Richer, J. S., & Padman, R. 1996, MNRAS, 279, 866

Benson, P. J., & Myers, P. C. 1989, ApJS, 71, 89

Bok, B. J., & Reilly, E. F. 1947, ApJ, 105, 255

Bontemps, S., André, P., Terebey, S., & Cabrit, S. 1996, A&A, 311, 858

Bourke, T. L. 1994, MSc thesis, Univ. of New South Wales

Bourke, T. L., Hyland, A. R., & Robinson, G. 1995a, MNRAS, 276, 1052

Bourke, T. L., Hyland, A. R., Robinson, G., & James, S. D. 1993, Proc. Astron. Soc. Australia, 10, 236

Bourke, T. L., Hyland, A. R., Robinson, G., James, S. D., & Wright, C. M. 1995b, MNRAS, 276, 1067

Bronfman, L., Cohen, R. S., Alvarez, H., May, J., & Thaddeus, P. 1988, ApJ, 324, 248

Cabrit, S., & André, P. 1991, ApJ, 379, L25

Cabrit, S., & Bertout, C. 1986, ApJ, 307, 313

Cabrit, S., & Bertout, C. 1990, ApJ, 348, 530

Cabrit, S., Goldsmith, P. F., & Snell, R. L. 1988, ApJ, 334, 196

Casoli, F., Dupraz, C., Gerin, M., Combes, F., & Boulanger, F. 1986, A&A, 169, 281

Chandler, C. J., Gear, W. K., Sandell, G., Hayashi, S., Duncan, W. D., Griffen, M. J., & Hazell, A. S. 1990, MNRAS, 243, 330

Chen, H., Myers, P. C., Ladd, E. F., & Wood, D. O. S. 1995, ApJ, 445, 377

Chini, R., Krügel, E., & Wargau, W. 1987, A&A, 181, 378

Combes, F. 1991, ARA&A, 29, 195

Davis, C. J., & Eislöffel, J. 1995, A&A, 300, 851

Emerson, D. T., Klein, U., & Haslam, C. G. T. 1979, A&A, 76, 92

Frerking, M. A., Langer, W. D., & Wilson, R. W. 1982, ApJ, 262, 590

Frerking, M. A., Langer, W. D., & Wilson, R. W. 1987, ApJ, 313, 320

Fukui, Y., Iwata, T., Mizuno, A., Bally, J., & Lane, A. P. 1993, in Protostars & Planets III, ed. E. H. Levy & J. I. Lunine (Tucson: Univ. Arizona Press), 603

Garden, R. P., Hayashi, M., Gatley, I., Hasegawa, T., & Kaifu, N. 1991, ApJ, 374, 540

Gordon, M. A. 1995, A&A, 301 853

Goss, W. M., Manchester, R. N., Brooks, J. W., Sinclair, M. W., Manefield, G. A., & Danzinger, I. J. 1980, MNRAS. 191, 533

Grabelsky, D. A., Cohen, R. S., Bronfman, L., Thaddeus, P. & May, J. 1987, ApJ, 315, 122

Gueth, F., Guilloteau, S., & Bachiller, R. 1996, A&A, 307, 891

Guilloteau, S., Bachiller, R., Fuente, A., & Lucas, R. 1992, A&A, 265, L49

Haslam, C. G. T. 1974, A&AS, 15, 333

Hartley, M., Manchester, R. N., Smith, R. M., Tritton, S. B., & Goss, W. M. 1986, A&AS, 63, 27

Ho, P. T. P., Moran. J. M., & Rodríguez, L. F. 1982, ApJ, 262, 619

Kreysa, E. 1990, in From Ground-Based to Space-Borne Sub-mm Astronomy (Proc. 29th Liège Int. Astr. Colloq.), ed. B. Kaldeich (Noordwijk: ESA) 265

Lada, C. J. 1985, ARA&A, 23, 267

Lada, C. J. 1991, in The Physics of Star Formation and Early Stellar Evolution, ed. C. J. Lada & N. D. Kylafis (Dordrecht: Kluwer), 329

Lang, K. R. 1980 Astrophysical Formulae (Berlin: Springer-Verlag)

Launhardt, R., & Henning, Th. 1994, in Clouds, Cores, and Low Mass Stars, ed. D. P. Clemens, R. Barvainis (Provo: Astronomical Society of the Pacific), 224

Levreault, R. M. 1988, ApJS, 67, 283

te Lintel Hekkert, P., Caswell, J. L., Habing, H. J., Haynes, R. F., & Norris, R. P. 1991, A&AS, 90, 327

Margulis, M., & Lada, C. J. 1985, ApJ, 299, 925

Masson, C. R., & Chernin, L. M. 1993, ApJ, 414, 230

Menten, K. M., Walmsley, C. M., Krügel, E., & Ungerechts, H. 1984, A&A, 137, 108

Mikami, H., Umemoto, T., Yamamoto, S., & Saito, S. 1992, ApJ, 392, L87

Myers, P. C. 1995, in Molecular Clouds and Star Formation, ed. C. Yuan, J. You (Singapore: World Scientific), 47

Myers, P. C., & Ladd, E. F. 1993, ApJ, 413, L47

Mundt, R. 1988, in Formation and Evolution of Low Mass Stars, ed. A. K. Dupree & M. T. V. T. Lago (Dordrecht: Kluwer), 257

Olnon, F. M., Raimond, E., Neugebauer, G., van Duinen, R. J., & Habing, H. J. 1986, A&AS, 65, 607

Ossenkopf, V., & Henning, Th. 1994 A&A, 291, 943

Parker, N. D. 1991, MNRAS, 251, 63

Raga, A. C., & Cabrit, S. 1993, A&A, 278, 267

Reipurth, B. 1991, in The Physics of Star Formation and Early Stellar Evolution, ed. C. J. Lada & N. D. Kylafis (Dordrecht: Kluwer), 497

Reipurth, B., Chini, R., Krügel, E., Kreysa, E., Sievers, A. 1993, A&A, 273, 221

Rodgers, A. W. 1960, MNRAS, 120, 163

Rohlfs K., & Wilson T. L. 1996, Tools of Radio Astronomy, 2nd. Ed. (Berlin: Springer-Verlag)

Sandqvist, A. 1977, A&A, 57, 467

Seidensticker, K. J., & Schmidt-Kaler, Th. 1989, A&A, 225, 192

Snell, R. L., Scoville, N. Z., Sanders, D. B., & Erickson, N. R. 1984, ApJ, 284, 176

Tafalla, M., & Bachiller, R. 1995, ApJ, 443, L37

Umemoto, T., Iwata, T., Fukui, Y., Mikami, H., Yamamoto, S., Kameya, O., & Hirano, N. 1992, ApJ, 392, L83

Yun, J. L., & Clemens, D. P. 1990, ApJ, 365, L73

Yun, J. L., & Clemens, D. P. 1994, AJ, 108, 612

Yun, J. L., & Clemens, D. P. 1995, AJ, 109, 742

Zhang, Q., Ho, P. T. P., Wright, M. C. H., & Wilner, D. J. 1995, ApJ, 451, L71

3A. Derivation of Important Equations

In this appendix we summarize the equations that have been used to derive the physical properties of the BHR 71 globule and its molecular outflow.

3A.1. Derivation of globule properties

^{12}CO and ^{13}CO

The main beam brightness temperature of the line emission from a molecular cloud is given by (e.g. Ho, Moran, & Rodríguez 1982)

$$T_{mb} = f[J(T_{ex}) - J(T_{bg})][1 - \exp(-\tau)] \quad , \tag{3A.1}$$

where τ is the optical depth of the cloud in the molecular transition, f is the filling factor, T_{ex} is the excitation temperature of the transition, T_{bg} is the background temperature, and

$$J(T) = \frac{h\nu}{k} \frac{1}{\exp(h\nu/kT) - 1} \quad .$$

The optical depth in the ^{12}CO $J = 1 \rightarrow 0$ and ^{13}CO $J = 1 \rightarrow 0$ lines can be derived from their ratio of observed brightness temperatures as follows. Using equation (3A.1) for both lines, we find

$$\frac{1 - \exp(-\tau_{12}/r)}{1 - \exp(-\tau_{12})} = \frac{[J_{12}(T_{ex}) - J_{12}(T_{bg})]}{[J_{13}(T_{ex}) - J_{13}(T_{bg})]} \frac{T_{mb}(^{13}\mathrm{CO})}{T_{mb}(^{12}\mathrm{CO})}, \tag{3A.2}$$

where r is the τ_{12}/τ_{13} optical depth ratio, given by

$$r = a \frac{1 - \exp(-h\nu_{12}/kT_{ex})}{1 - \exp(-h\nu_{13}/kT_{ex})} \frac{(kT_{ex}/hB_{13} + 1/3)}{(kT_{ex}/hB_{12} + 1/3)} \quad , \tag{3A.3}$$

where a is the [^{12}CO/^{13}CO] isotopic abundance ratio, and B is the rotational constant of the molecule. Subscripts 12 and 13 refers to the ^{12}CO and ^{13}CO isotopes, respectively. If the excitation temperature is known, these two relations, which are independent of the filling factor, allows the optical depths to be determined. We avoided making the usual approximation that $\tau_{12} \gg 1$, and solved equation (3A.2) using an interpolation procedure, assuming a [^{12}CO/^{13}CO] abundance ratio of 89 (Lang 1980).

The total column density N of a linear, rigid rotor, molecule can be derived from the optical depth, τ, and excitation temperature, T_{ex}, of a rotational transition at frequency ν, using the expression (e.g. Garden et al. 1991)

$$N = \frac{3h}{8\pi^3\mu^2}\frac{k(T_{ex}+hB/3k)}{(J+1)hB}\frac{\exp(E_J/kT_{ex})}{1-\exp(-h\nu/kT_{ex})}\int \tau dv \quad , \tag{3A.4}$$

where μ is the permanent dipole moment and J is the rotational quantum number of the lower state. This expression assumes that all energy levels are populated according to local thermodynamic equilibrium (LTE) at the temperature T_{ex}. In particular the total column density of the ^{13}CO molecule is given, in terms of the opacity and excitation temperature of the $J = 1 \rightarrow 0$ transition, by

$$N(^{13}\mathrm{CO}) = 2.42 \times 10^{14}\frac{T_{ex}+0.88}{1-\exp(-5.29/T_{ex})}\int \tau_{13} dv \quad . \tag{3A.5}$$

where v is measured in $\mathrm{km\,s^{-1}}$.

The total mass of molecular clouds can be estimated in at least two ways. The first, and most straightforward method, is through observations of an optically thin molecule, which allows a direct estimate of the mass in the observed molecular species, from which the total mass may be inferred assuming an appropriate abundance ratio. The mass computed in this way is usually called the LTE mass, since typically only one transition is measured and an extrapolation to the total column density is done assuming a local thermodynamic equilibrium (LTE) population. Integrating equation (3A.5) over the solid angle subtended by the source, we find

$$\begin{aligned}\left(\frac{M_{LTE}}{M_\odot}\right) &= 0.312\left(\frac{\mu_m}{2.72m_H}\right)\left(\frac{[\mathrm{H_2}/^{13}\mathrm{CO}]}{7\times10^5}\right)\left(\frac{D}{\mathrm{kpc}}\right)^2 \\ &\quad \times\frac{T_{ex}+0.88}{1-\exp(-5.29/T_{ex})}\iint \tau_{13} dv d\Omega \ , \end{aligned} \tag{3A.6}$$

where μ_m is the mean molecular mass per $\mathrm{H_2}$ molecule, m_H is the mass of a hydrogen atom, D is the source distance, v is in $\mathrm{km\,s^{-1}}$, and Ω is in $\mathrm{arcmin^2}$. When ^{13}CO $J = 1 \rightarrow 0$ and ^{12}CO $J = 1 \rightarrow 0$ data are available, the integral on the right hand side can be directly computed from the opacity of the ^{13}CO line [derived from eqs. (3A.2) & (3A.3)] and the observed line width at each position across the molecular cloud.

A second method, commonly used when isotopic lines measurements are not available, is to assume that the H_2 column density, $N(H_2)$, is proportional to the observed velocity integrated ^{12}CO emission, $\int T_{mb}(^{12}CO)dv$,

$$N(H_2) = X \int T_{mb}(^{12}CO)dv \quad .$$

Integrating this expression over the solid angle subtended by the cloud, and assuming $X = 2.3 \times 10^{20}$ cm^{-2}/(K km s^{-1}) (e.g. Rohlfs & Wilson 1996; see Combes 1991 for a discussion), we find that the molecular mass, usually referred as the CO mass, is given by

$$\left(\frac{M_{CO}}{M_\odot}\right) = 0.425 \left(\frac{X}{2.3 \times 10^{20}}\right) \left(\frac{\mu_m}{2.72 m_H}\right) \left(\frac{D}{\mathrm{kpc}}\right)^2 \iint T_{mb}(^{12}CO)\, dv d\Omega \quad , \tag{3A.7}$$

where v is in km s^{-1}, and Ω is in arcmin^2.

$C^{18}O$

In the optically thin limit the column density of $C^{18}O$ is given by

$$N(C^{18}O) = 2.42 \times 10^{14} \frac{T_{ex} + 0.88}{1 - \exp(-5.27/T_{ex})} \frac{1}{J(T_{ex}) - J(T_{bg})} \int T_{mb}(C^{18}O)dv \quad . \tag{3A.8}$$

The total mass traced by $C^{18}O$ may then be found using equation (3A.6) modified for optically thin $C^{18}O$

$$\left(\frac{M_{LTE}}{M_\odot}\right) = 2.58 \left(\frac{\mu_m}{2.72 m_H}\right) \left(\frac{[H_2/C^{18}O]}{5.9 \times 10^6}\right) \left(\frac{D}{\mathrm{kpc}}\right)^2 \frac{T_{ex} + 0.88}{1 - \exp(-5.27/T_{ex})} \times \frac{1}{J(T_{ex}) - J(T_{bg})} \iint T_{mb}(C^{18}O)dv d\Omega \quad . \tag{3A.9}$$

3A.2. Derivation of molecular outflow properties

The mass in the lobes of a molecular outflow can be estimated from ^{12}CO observations assuming that the ^{12}CO $J = 1 \rightarrow 0$ flow emission is optically thin. Assuming that the energy levels of ^{12}CO are populated according to local thermodynamic equilibrium, the total ^{12}CO column density at each observed position

within each lobe is given by equation (3A.4). In the optically thin limit

$$N(^{12}\mathrm{CO}) = F(T_{ex}) \int T_B(v) dv \quad , \tag{3A.10}$$

where

$$F(T_{ex}) \equiv 2.31 \times 10^{14} \frac{T_{ex} + 0.92}{1 - \exp(-5.53/T_{ex})} \frac{1}{J(T_{ex}) - J(T_{bg})} \quad ,$$

and v is measured in $\mathrm{km\,s^{-1}}$. The mass at each observed position (α, δ) is given by

$$M(\alpha, \delta) = [\mathrm{H_2}/^{12}\mathrm{CO}]\ \mu_m\ A(\alpha, \delta)\ N(^{12}\mathrm{CO}) \quad , \tag{3A.11}$$

where $A(\alpha, \delta)$ is the size of the emitting area at the observed position. For our frequency-switched observations, the emitting area is taken to be a box of dimension equal to the spatial resolution of the observations, i.e. $20''$. The mass at each position within the flow travelling at a particular velocity v with respect to the ambient cloud is then given by

$$M(v, \alpha, \delta) = [\mathrm{H_2}/^{12}\mathrm{CO}]\ \mu_m\ A(\alpha, \delta)\ F(T_{ex})\ T_B(v, \alpha, \delta) \Delta v \quad , \tag{3A.12}$$

where Δv is the velocity resolution of the observations. The total mass is then simply (Margulis & Lada 1985)

$$\begin{aligned} M &= \iiint M(v, \alpha, \delta) dv d\alpha d\delta \\ &= [\mathrm{H_2}/^{12}\mathrm{CO}]\ \mu_m\ A(\alpha, \delta)\ F(T_{ex})\ \Delta v \iiint T_B(v, \alpha, \delta)\ dv d\alpha d\delta \end{aligned} \tag{3A.13}$$

In practical terms one first performs the spatial integral by summing all the spectra in the region of interest, obtaining

$$M(v) = [\mathrm{H_2}/^{12}\mathrm{CO}]\ \mu_m\ A(\alpha, \delta)\ F(T_{ex})\ \Delta v \sum_{\Omega} T_B(v) \quad , \tag{3A.14}$$

and then summing over the velocity

$$M = \int M(v) dv = \sum_{v} M(v) \quad . \tag{3A.15}$$

To estimate the contribution to the flow mass from the low velocity material emitting in the same velocity range as the ambient cloud gas we follow the

prescription of Margulis & Lada (1985), approximating the integrated brightness emission in this velocity range as

$$\int_{lobe}\int_{v_b}^{v_r} T_{mb}\,dv\,d\Omega = \int_{lobe}\left(\frac{T^b+T^r}{2}\right)(v_r - v_b)\,d\Omega \quad , \tag{3A.16}$$

where T^b, v_b and T^r, v_r are the brightness temperature and velocity at the blue and red velocity boundaries, respectively.

The momentum P, kinetic energy, E_k, and the mechanical luminosity L_m of the flow may be determined as described by Margulis & Lada (1985), Lada (1985) and Cabrit & Bertout (1990). In the lower limits, these parameters are determined by performing the following integrals in a similar manner to equation (3A.13)

$$\begin{aligned} P &= \iiint M(v,\alpha,\delta)v\;dvd\alpha d\delta \\ E_k &= \frac{1}{2}\iiint M(v,\alpha,\delta)v^2\;dvd\alpha d\delta \\ L_m &= \frac{1}{2R}\iiint M(v,\alpha,\delta)v^3\;dvd\alpha d\delta \quad , \end{aligned} \tag{3A.17}$$

where R is the length of the outflow lobe. These equations assume no correction for flow inclination, and so are strict lower limits. Another method is to assume that all the mass is flowing at a velocity characteristic of the entire flow, V_{char}. The flow parameters are then determined by

$$\begin{aligned} P &= M\;V_{char} \\ E_k &= \frac{1}{2}M\;V_{char}^2 \\ L_m &= \frac{1}{2R}M\;V_{char}^3 \quad , \end{aligned} \tag{3A.18}$$

where M is the total mass of the lobe. If the maximum observed flow velocity is used as the characteristic velocity then the values found from equation (3A.18) are upper limits.

3A.3. Derivation of circumstellar mass

In general, for an isothermal dust source the total mass of circumstellar matter, M_{cm}, is given in terms of the observed flux density, S_ν, at an optically thin

frequency, ν, by (e.g. Chini, Krugel, & Wargau 1987)

$$M_{cm} = \frac{S_\nu D^2}{R_{dg}\kappa_\nu B_\nu(T_d)} \quad , \tag{3A.19}$$

where κ_ν is the mass absorption coefficient of dust, R_{dg} is the dust-to-gas mass ratio (assuming 10% He), and $B_\nu(T_d)$ is the Planck function at the dust temperature T_d. In particular for observations at 1.3 mm we can write

$$\left(\frac{M_{cm}}{M_\odot}\right) = 37 \left(\frac{S_{1.3mm}}{\mathrm{Jy}}\right) \left(\frac{D}{\mathrm{kpc}}\right)^2 \left(\frac{0.007}{R_{dg}}\right) \left(\frac{1\ \mathrm{cm^2\ g^{-1}}}{\kappa_{1.3mm}}\right) [\exp(11.04/T_d) - 1] \quad . \tag{3A.20}$$

The main source of uncertainty in the conversion of the observed flux density into gas mass is the $R_{dg}\kappa_\nu$ factor, or total mass opacity, which is a poorly known quantity (e.g. Gordon 1995). For dense and cold protostellar cores, Ossenkopf & Henning (1994) derive a dust opacity at 1.3 mm of $\kappa_{1.3mm} \sim 1\ \mathrm{cm^2\ g^{-1}}$.

Chapter 4

Molecular abundance enhancements in the highly collimated bipolar outflow BHR 71[1]

[1]Garay, G., Köhnenkamp, I., Bourke, T. L., Rodríguez, L. F., & Lehtinen, K. K., accepted by ApJ. To appear December 1998

ABSTRACT

We report observations of the $J = 3 \rightarrow 2$ and $J = 2 \rightarrow 1$ transitions of SiO and CS, the $J_k = 3_k \rightarrow 2_k$ and $J_k = 2_k \rightarrow 1_k$ transitions of CH_3OH, and the $J = 1 \rightarrow 0$ transition of HCO^+, made with SEST, toward the highly collimated bipolar outflow BHR 71. Broad wing emission was detected toward the outflow lobes in all the observed molecular lines. The shape of the profiles are strikingly different from molecule to molecule. For CS and HCO^+ the emission from the outflowing gas appears as a weak broad feature superposed upon a strong narrow emission from the quiescent ambient gas. For CH_3OH the intensity of the broad emission feature is considerably stronger than that of the narrow component, while for SiO the broad feature completely dominates the emission spectra.

The spatial distribution of the integrated wing emission is considerably extended, and broadly similar in all the observed molecular transitions, showing well separated blue and red shifted lobes with FWHM angular sizes of $2\farcm4 \times 1\farcm3$ and $2\farcm4 \times 1\farcm4$, respectively. We find that the abundance of methanol and silicon monoxide in the outflow lobes is enhanced with respect to that of the ambient cloud by factors of up to $\sim$ 40 and 350, respectively. The large enhancements of methanol and silicon monoxide in the outflow lobes are most likely due to the release from grains of ice mantles and Si-bearing species via shocks produced by the interaction between the outflow and dense ambient gas. On the other hand, we find that the abundance of HCO^+ in the outflowing gas is smaller than that in the ambient gas by roughly a factor of 20, a decrease consistent with theoretical predictions of shock models.

4.1. Introduction

BHR 71 (Bourke et al. 1995a,b) or Sandqvist 136 (Sandqvist 1977) is a well isolated Bok globule, located at a distance of $\sim$ 200 pc from the Sun, which harbors a highly collimated bipolar outflow near its center (Bourke et al. 1997 – hereafter Chapter 3; see Fig. 4.1 and the previous Chapter). The CO outflow is found to be well described as a biconical flow, with a semi-opening angle of 15° and inclined from the line of sight by an angle of $\sim$ 84°, in which the gas moves outwards with a constant radial velocity (with respect to the cone apex) of $\sim$ 28 $\mathrm{km\,s^{-1}}$. The outflow appears to be driven by a very young stellar object, with a total luminosity of $\sim 9 L_{\odot}$, possibly still undergoing accretion of matter. Its characteristics at infrared and millimeter wavelengths are similar to those of the Class 0 objects (André 1995).

The class of highly collimated outflows are thought to be driven by jets that accelerate the ambient gas through the propagation of shocks (e.g., Raga & Cabrit 1993). The interaction of high velocity jets from young stars with the surrounding ambient gas generates strong shock waves which are expected to produce a significant transformation of the physical properties of the molecular surroundings as well as of its chemical composition (see review by Bachiller 1996). Although there has been a substantial amount of work on the physical characteristics of outflows, very little is known about their chemical composition. Very few multi-line mapping studies of molecular outflows have been performed so far (Blake et al. 1995, Bachiller & Pérez Gutiérrez 1997). Basic questions such as (1) how is the chemistry of the swept-up ambient molecular material affected by the winds from young stellar objects, and (2) do molecular abundances serve as sensitive probes of the evolutionary stage of bipolar outflows (e.g., van Dishoeck & Blake 1995) have not yet been answered. The lobes of the BHR 71 outflow extend by $\sim 4'$ in the plane of the sky, hence this is an ideal source for a detailed study, using single-dish instruments, of the physical and chemical characteristics across highly collimated, low velocity shocks. In this Chapter we report on extensive molecular observations, made with the SEST, of the BHR 71 outflow in rotational transitions of silicon monoxide (SiO), methanol (CH_3OH),

carbon monosulfide (CS), and formyl ion (HCO^+).

4.2. Observations

The observations were carried out using the 15 m Swedish-ESO Submillimetre Telescope (SEST) located on La Silla, Chile, during 1995 September and October. The molecules, transitions, and frequencies observed and the instrumental parameters are summarized in Table 4.1. We used SiS receivers to simultaneously observe the 2 and 3 mm lines of silicon monoxide, methanol, and carbon monosulfide. Single-sideband receiver temperatures were typically 120 K for both receivers. As backend we used high resolution acousto-optical spectrometers providing a channel separation of 43 kHz and a total bandwidth of 43 MHz. This resulted in spectral resolutions of 0.13 and 0.09 $\mathrm{km\,s^{-1}}$ and total velocity coverages of 133 and 89 $\mathrm{km\,s^{-1}}$ at the 96.7 and 145.1 GHz frequencies of the CH_3OH lines, respectively. Within the available bandwidths, three rotational lines of CH_3OH could be observed at 2 mm ($J_k = 3_0 \rightarrow 2_0$ A^+, $J_k = 3_{-1} \rightarrow 2_{-1}$ E, and $J_k = 3_0 \rightarrow 2_0$ E lines) and four rotational lines at 3 mm ($J_k = 2_1 \rightarrow 1_1$ E, $J_k = 2_0 \rightarrow 1_0$ E, $J_k = 2_0 \rightarrow 1_0$ A^+, and $J_k = 2_{-1} \rightarrow 1_{-1}$ E lines). The antenna half-power beamwidth and main beam efficiency of the telescope at the different observed frequencies are given in Table 4.1.

During the 1995 September observing session we mapped the molecular emission within a region of $\sim 5' \times 10'$, with $1'$ spacings, in each of the above transitions. The observations were performed in the position switched mode, with the reference position located at $\alpha_{1950} = 11^h53^m44\overset{s}{.}7$, $\delta_{1950} = -65°13'58''$. The integration times on source were typically 3 minutes per position. The resulting rms noise in antenna temperature are given in column 7 of Table 4.1. During the 1995 October observing run we undertook deeper observations toward the SE1 and NW CO peaks in the outflow lobes (Chapter 3) and toward the center of the globule. The goal was to obtain sensitive data in order to perform rotational diagram analysis. The observed positions are at offsets from the IRAS source position ($\alpha_{1950} = 11^h59^m03\overset{s}{.}1$, $\delta_{1950} = -64°52'11''$) of $(40'', -100''$; SE1

Figure 4.1.— *Next Page*

Contour map of velocity integrated CO $J = 1 \rightarrow 0$ line wing emission from the BHR 71 bipolar outflow, superimposed on a V-band image of the globule taken from the Digitized Sky Survey. Solid contours correspond to the emission integrated in the velocity range from –14 to –6 $\mathrm{km\,s^{-1}}$ (blueshifted wing) and short-dashed contours to the integrated emision in the velocity range from –3 to 7 $\mathrm{km\,s^{-1}}$ (redshifted wing). Contours are 20, 35, 50, 65, 80, and 95% of the peak $\int T_A^* dv$ of 25.8 K $\mathrm{km\,s^{-1}}$ in the blue lobe, and 31.7 K $\mathrm{km\,s^{-1}}$ in the red lobe. Long-dashed contours represent ^{13}CO $J = 1 \rightarrow 0$ emission integrated between –6 and –3 $\mathrm{km\,s^{-1}}$. Contours for ^{13}CO are 20, 35, 50, 65, 80, and 95% of the peak of $\int T_{\mathrm{mb}} dv$ of 2.8 K $\mathrm{km\,s^{-1}}$. The star marks the position of the mm-IRAS source 11590–6452 (Chapter 3). The ^{12}CO data is from SEST and the ^{13}CO data from the CTIO radio telescope (Chapter 3).

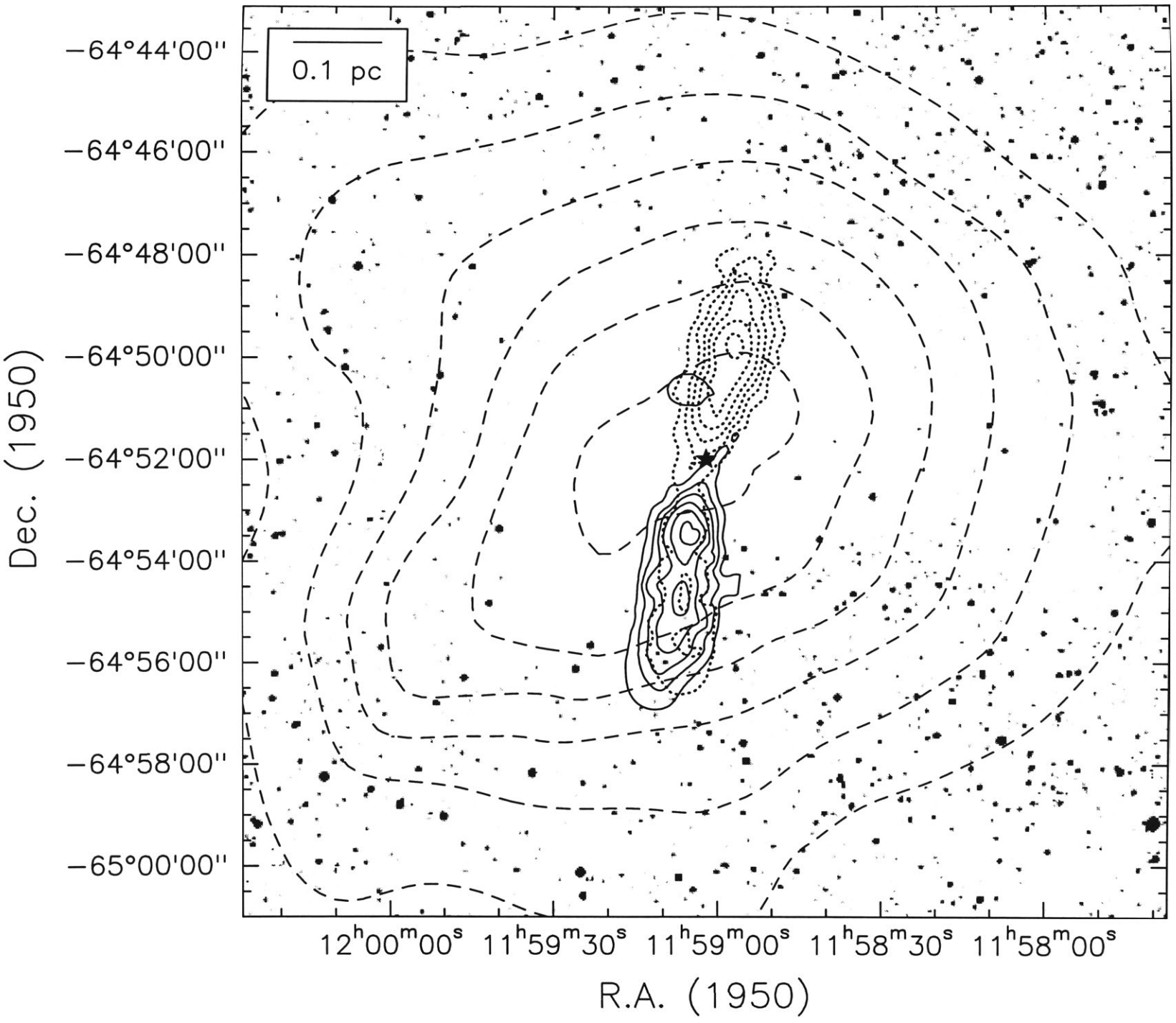
0.1 pc
−64°44'00"
−64°46'00"
−64°48'00"
−64°50'00"
−64°52'00"
−64°54'00"
−64°56'00"
−64°58'00"
−65°00'00"
Dec. (1950)
12h00m00s
11h59m30s
11h59m00s
11h58m30s
11h58m00s
R.A. (1950)

Table 4.1. Summary of Observational Parameters

Molecule	Transition	Frequency (MHz)	Beam Size (FWHM ″)	η	Δv (km s^{-1})	rms Noise[1] (K)
CH_3OH	$J_k = 2_0 \rightarrow 1_0$ A$^+$	96741.42	52	0.73	0.133	0.06
	$J_k = 3_0 \rightarrow 2_0$ A$^+$	145103.23	34	0.66	0.089	0.10
SiO	$J = 2 \rightarrow 1$	86846.998	57	0.75	0.149	0.03
	$J = 3 \rightarrow 2$	130268.702	40	0.68	0.099	0.04
CS	$J = 2 \rightarrow 1$	97980.968	52	0.73	0.132	0.04
	$J = 3 \rightarrow 2$	146969.049	34	0.66	0.088	0.06
	$J = 5 \rightarrow 4$	244935.606	22	0.45	0.053	0.09
HCO^+	$J = 1 \rightarrow 0$	89188.518	56	0.75	0.145	0.08
$H^{13}CO^+$	$J = 1 \rightarrow 0$	86754.294	57	0.75	0.149	0.03

[1] 1σ rms noise in antenna temperature.

peak), $(-40'', 140''$; NW peak) and $(0'', 0'')$. We made five-point cross maps about each of these three positions, with $15''$ spacings, in the $J = 3 \rightarrow 2$ and $J = 2 \rightarrow 1$ lines of SiO and CS, and the $J_k = 3_k \rightarrow 2_k$ and $J_k = 2_k \rightarrow 1_k$ lines of CH_3OH. The integration time per position ranged between 4 to 8 minutes. The observations were performed in dual beam-switching mode, with a beam separation of $11'47''$ in azimuth.

In addition, we supplement the above with observations of the $H^{13}CO^+$ $J = 1 \rightarrow 0$ and CS $J = 5 \rightarrow 4$ lines at the IRAS position which were undertaken in 1994 April. Details are given in Table 4.1.

4.3. Results

The spectra of the emission in the seven observed molecular transitions, across the $5' \times 10'$ region mapped with SEST with $1'$ spacing, are shown in Figure 4.2. Also shown for comparison are the spectra of the ^{12}CO $J = 1 \rightarrow 0$ emission, taken from Chapter 3). Offsets are from the reference position at $\alpha_{1950} = 11^h59^m01^s.18$, $\delta_{1950} = -64°52'00''$ which itself is offset by $(\Delta\alpha, \Delta\delta) =$

(7″, 1″) from the position of the mm source as given in Chapter 3. Two emission components, originating from physically and chemically different environments, can be distinguished from this figure. A narrow line emission, at a velocity of -4.45 km s^{-1}, arising from the quiescent gas of the BHR 71 globule, and a broad line emission which arises from the bipolar outflowing gas (cf. Chapter 3). The line wing emission was detected in all the observed molecular transitions. The shape of the profiles are, however, different from molecule to molecule depending on the relative intensities between the narrow and broad components. Particularly striking are the cases of methanol and silicon monoxide molecules, for which the emission from the broad component is much stronger than that from the narrow component. The broad emission is detected at redshifted velocities with respect to the systemic ambient cloud velocity toward the northwest region of the map (the red lobe) and at blueshifted velocities toward the southeast region (the blue lobe).

To illustrate in more detail the differences between the line profiles we show in Figure 4.3 the spectra of the line emission averaged across the blue lobe, the red lobe, and the central core region. Emission in the lines of SiO is detected only from the lobes, no (or very weak) emission being detected at the core of the globule at the level of 0.06 K. The CH_3OH profiles show strong emission from the wing component and weak emission at the velocities of the ambient cloud. The vertical bars shown in the spectra of methanol indicate the expected positions of the three rotational transitions, within the displayed velocity range, for a rest velocity of -4.45 km s^{-1}. On the other hand, the CS and HCO^+ profiles show a mixture of strong emission from the quiescent ambient cloud and relatively weaker wing emission at the position of the lobes. Figure 4.3 also shows that the average emission from the red lobe is brighter than that from the blue lobe, by roughly a factor of 2, and that toward the red lobe the wing emission in the SiO lines is considerable broader than in the CH_3OH lines. As discussed in the previous Chapter the blue lobe appears to be breaking through the near side of the globule, resulting in a well defined cavity being visible at optical wavelengths (Fig. 3.13 in the previous Chapter). It is therefore likely that the amount of

Figure 4.2.— *Next Page*

Observed spectra of several molecules across the central $5' \times 10'$ of the BHR 71 globule. The grid spacing is $1'$. The asterix marks the position of the mm-IRAS source 11590–6452 (Chapter 3). In each box the velocity scale ranges from -19 to 19 $\mathrm{km\,s^{-1}}$. The antenna temperature scale is from -0.2 to 0.6 K for SiO; -0.3 to 2.2 K for CH_3OH; -0.2 to 1.0 K for CS; -0.3 to 3.0 K for HCO^+; and -1.0 to 10.0 K for CO. Offsets are relative to $\alpha_{1950} = 11^{\mathrm{h}}59^{\mathrm{m}}01\overset{\mathrm{s}}{.}18$, $\delta_{1950} = -64°52'00''$.

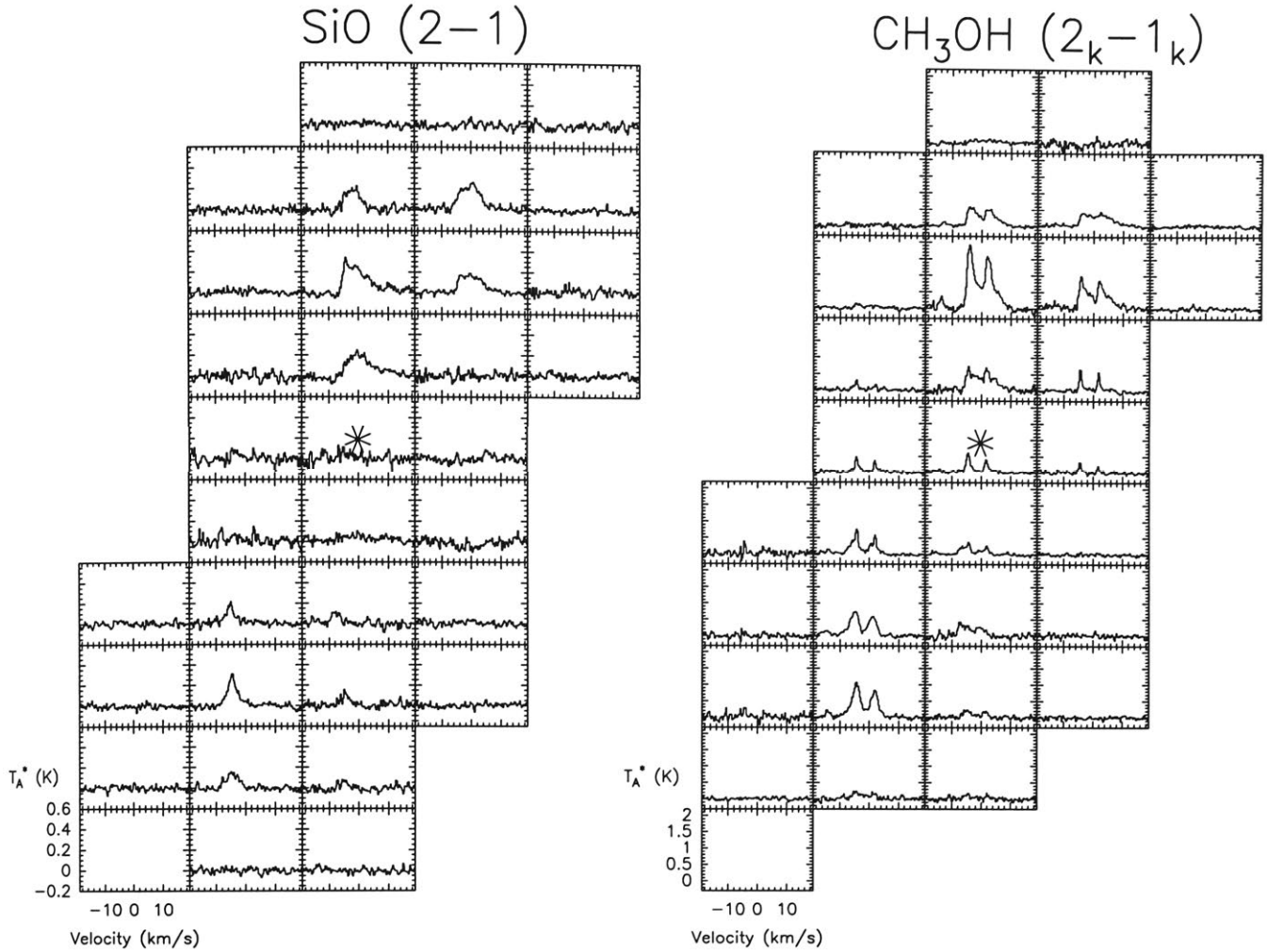
SiO (2−1)
CH3OH (2k−1k)
TA* (K)
0.6
0.4
0.2
0
−0.2
2
1.5
1
0.5
0
−10 0 10
Velocity (km/s)

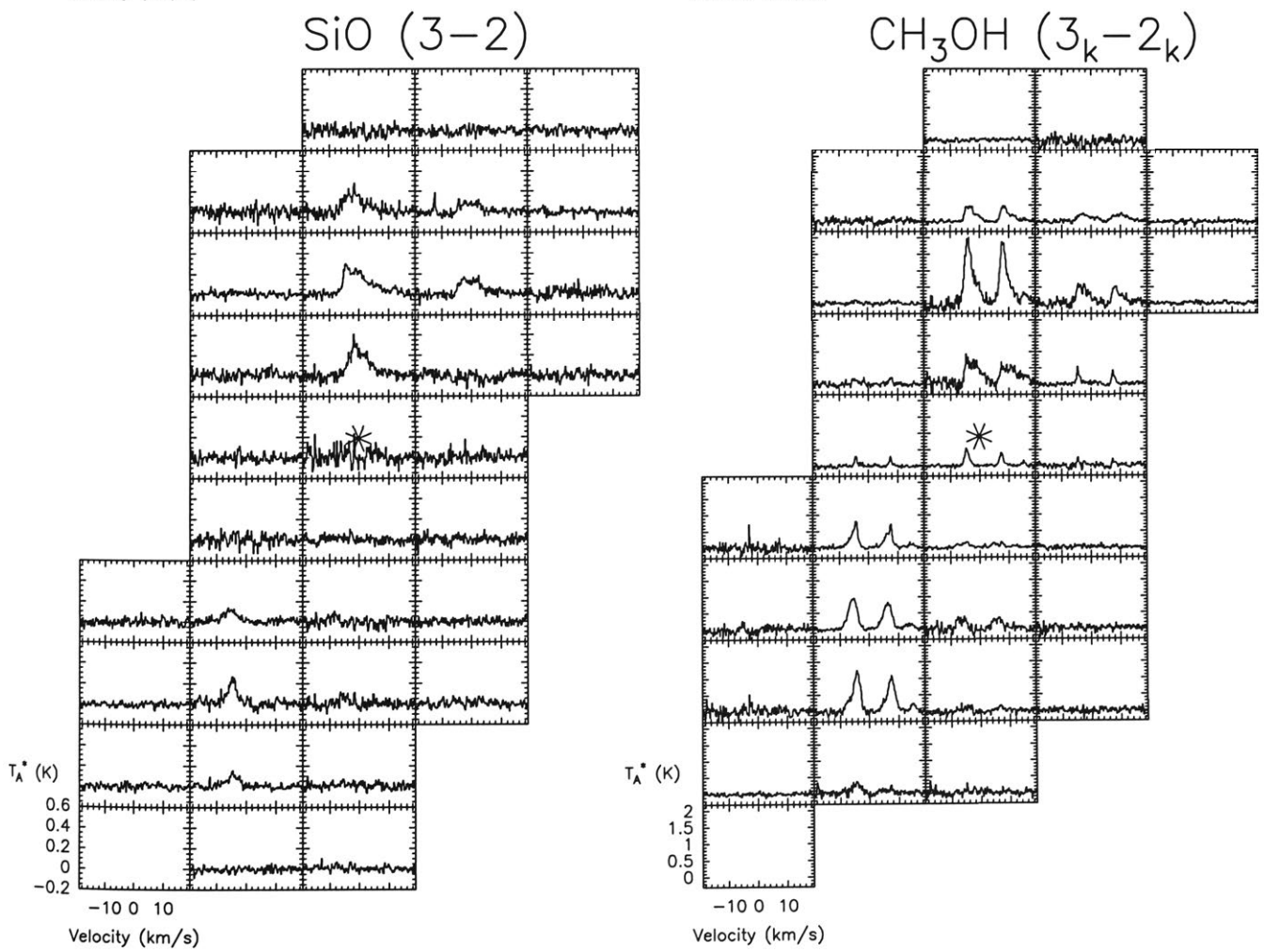
SiO (3−2)
CH3OH (3k−2k)
TA* (K)
0.6
0.4
0.2
0
−0.2
2
1.5
1
0.5
0
−10 0 10
Velocity (km/s)

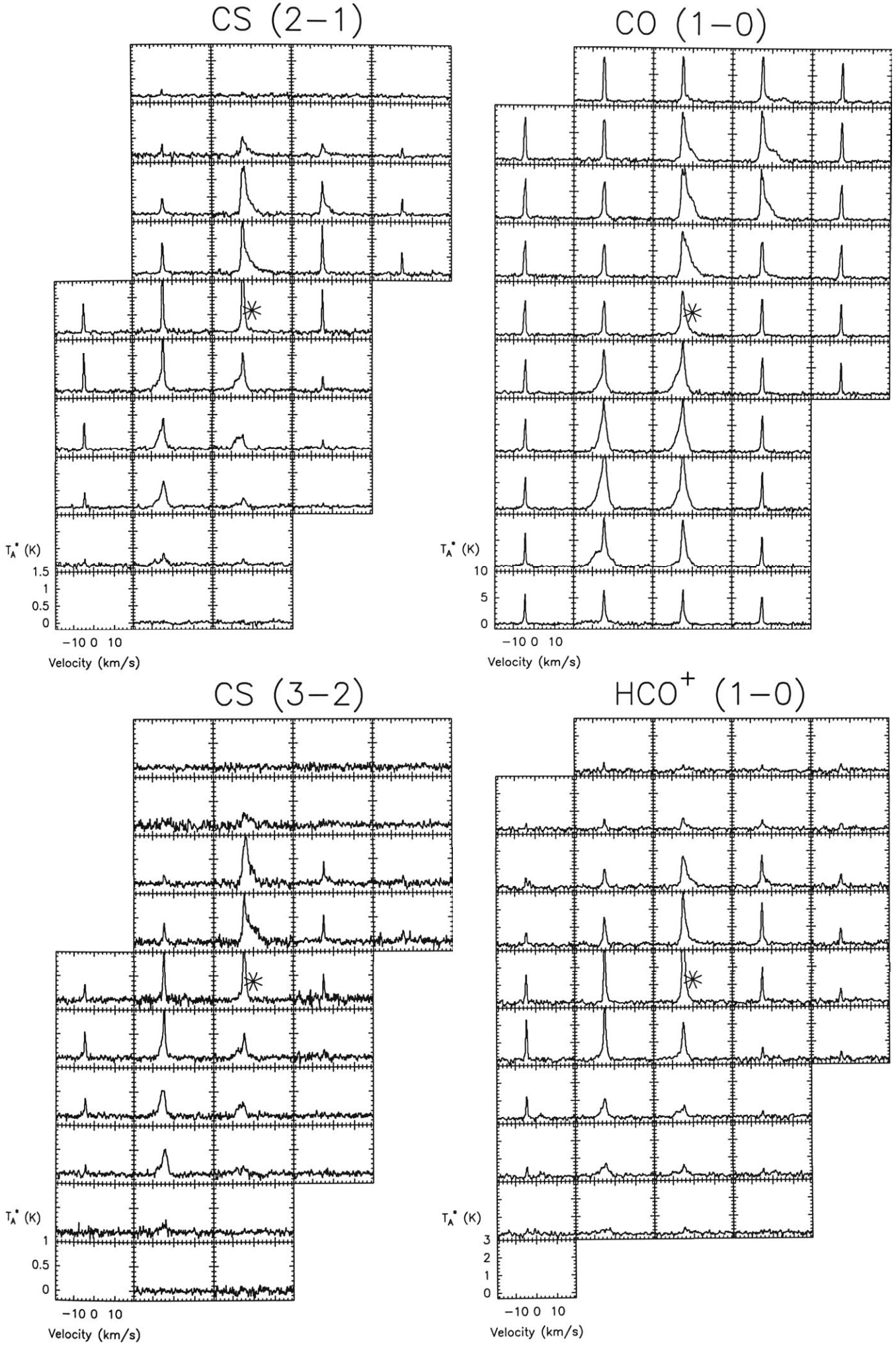
CS (2−1)
CO (1−0)
CS (3−2)
HCO+ (1−0)
T*A (K)
1.5
1
0.5
0
10
5
3
2
−10 0 10
Velocity (km/s)

ambient material interacting with the outflow in the blue lobe is significantly less than in the red lobe, resulting in weaker emission being observed toward the blue lobe.

Maps of the velocity integrated emission in the ranges of the blue wing (-9.1 to -5.5 km s^{-1}; continuous line) and red wing (-3.1 to 0.5 km s^{-1}; dashed line) are shown in Figure 4.4. The star marks the position of the mm continuum source. Also shown, for comparison, is a map of the ^{12}CO $J = 1 \rightarrow 0$ emission in the same velocity range. The spatial distribution of the integrated wing emission is broadly similar in all the observed molecular transitions, showing well separated blue and red shifted lobes aligned in a direction with a position angle of $\sim$ 168°. From the maps of the SiO, CH_3OH, and CS emission we measure FWHM angular sizes of $2\farcm4 \times 1\farcm3$ for the red lobe and $2\farcm4 \times 1\farcm4$ for the blue lobe. The peaks of the molecular emission are offset by $\sim 2'$ ($\sim$ 0.1 pc) from the central mm-source. While the integrated wing emission morphology is notably similar in the 2 and 3 mm transitions of a given molecule, there are some differences in the spatial distribution of different molecular species. Compared to methanol and CS, the SiO lobes appear to extend further away from the driving source, exhibiting spatial extensions similar to those of the CO lobes. While some of the differences in the position of the peak emission seen in Fig. 4.4 can be ascribed to our spatial undersampling, this circumstance cannot explain the differences in spatial extent which appear to be intrinsic to the data. With the present observations is not possible to discern whether the emission from the lobes arises from either a uniform distribution of high velocity gas or from small cloudlets. The low values of the observed main beam brightness temperature suggest, however, that clumpiness is important.

The spectra of the emission in the lines of methanol, silicon monoxide and carbon monosulfide toward the SE1, NW and core positions obtained from the pointed, higher signal-to-noise (S/N) observations are shown in Figure 4.5. In these deep integrations weak SiO emission from the core position, barely evident in the shorter integrations shown in Figure 4.3, is clearly seen. The shape of the methanol lines toward the SE1 and NW peaks are distinctly different.

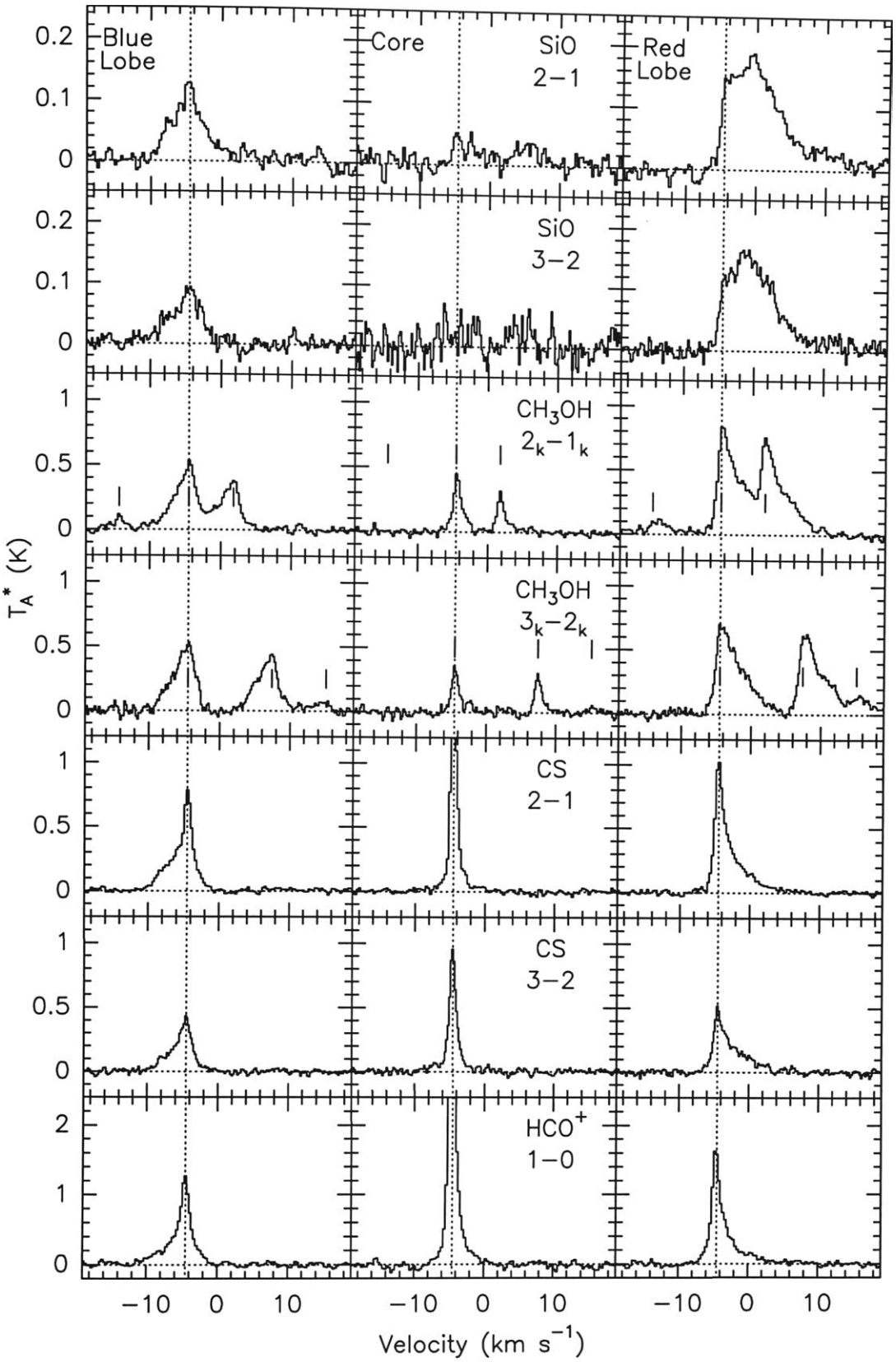

Figure 4.3.— Spectra of the spatially integrated line emission from the blue (left column) and red (right column) lobes of the BHR 71 outflow and from the "core" region (centered on IRAS 11590–6452; middle column). The observed transitions are labeled in the upper right corner of the spectra shown in the middle column. The vertical dashed line indicates the systemic velocity of the globule of 4.5 $\mathrm{km\,s^{-1}}$. The vertical ticks on the CH_3OH spectra indicate the different CH_3OH transitions observed.

Figure 4.4.— *Next Page*

Contour maps of velocity integrated line wing emission from the BHR 71 bipolar outflow. Continuous contours correspond to the emission integrated in the velocity range from -9.1 to -5.5 km s^{-1} (blueshifted wing) and dashed contours to the integrated emission in the velocity range from -3.1 to 0.5 km s^{-1} (redshifted wing). Contours are 35, 45, 55, 65, 75, 85, and 95% of the peak $\int T_A^* dv$ in each lobe. The peaks are 0.37 K km s^{-1} for the blue lobe and 0.88 K km s^{-1} for the red lobe of the SiO $J = 2 \rightarrow 1$ map; 0.32 (blue) and 1.01 (red) K km s^{-1} for the SiO $J = 3 \rightarrow 2$ map; 1.22 and 2.83 K km s^{-1} for the CH_3OH $J_k = 2_0 \rightarrow 1_0$ map; 1.78 and 2.81 K km s^{-1} for the CH_3OH $J_k = 3_0 \rightarrow 2_0$ map; 1.19 and 1.85 K km s^{-1} for the CS $J = 2 \rightarrow 1$ map; 0.85 and 1.47 K km s^{-1} for the CS $J = 3 \rightarrow 2$ map; 15.71 and 17.08 K km s^{-1} for the CO $J = 1 \rightarrow 0$ map; and 1.48 and 2.14 K km s^{-1} for the HCO^+ map. The star indicates the position of the mm–IRAS source 11590–6452. The beam FWHM for each transition is indicated in the upper left of each map by the shaded circle. Offsets are relative to $\alpha_{1950} = 11^h59^m01\overset{s}{.}18$, $\delta_{1950} = -64°52'00''$.

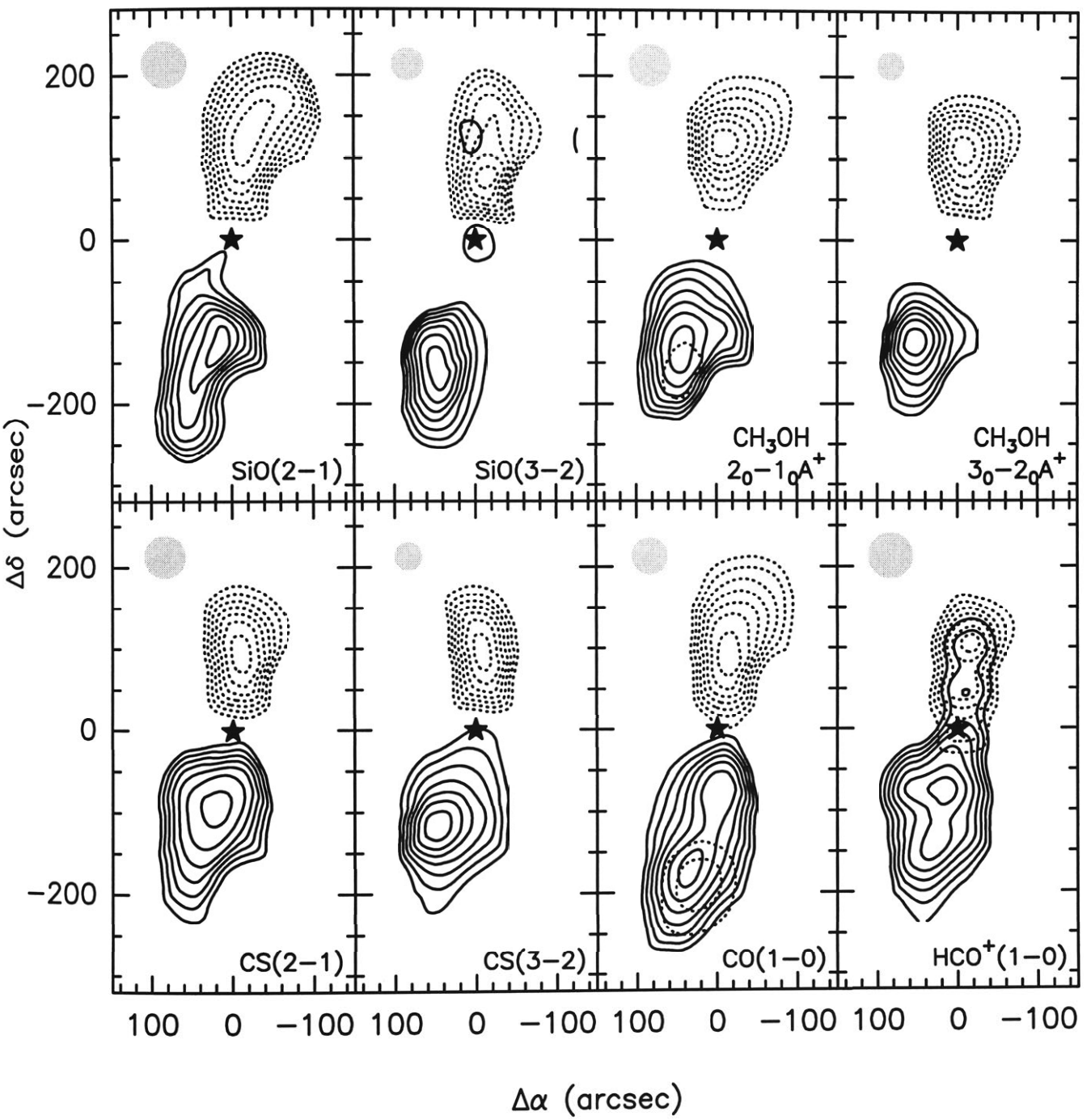
200
0
−200
Δδ (arcsec)
SiO(2−1)
SiO(3−2)
CH3OH
2₀−1₀A+
CH3OH
3₀−2₀A+
CS(2−1)
CS(3−2)
CO(1−0)
HCO+(1−0)
100 0 −100 100 0 −100 100 0 −100 100 0 −100
Δα (arcsec)

While the profile of the emission in each individual line of methanol from the SE1 peak can be well fitted by a single Gaussian component, those toward the NW peak are clearly non Gaussian, their shapes being better reproduced by a blend of emission from a narrow component and a broader redshifted component. In Table 4.2 we summarize the results of Gaussian profiles fit to the emission from the SE1 peak (one Gaussian component per line), NW peak (two Gaussian components per line), and core position (one Gaussian component per line). The line center velocities given in this Table and below are relative to the ambient cloud velocity of -4.45 km s^{-1}. The average line center velocity of the six methanol lines observed toward the SE1 peak is -1.3 km s^{-1} and the average line width is 3.7 km s^{-1}. The two Gaussian components fitting the NW emission have average line center velocities of 0.3 and 3.0 km s^{-1} and line widths of 2.0 and 3.8 km s^{-1}. Hereafter we will refer to these components as the low (LV) and intermediate (IV) velocity components. Even though its center velocity is close to the ambient gas velocity, it is unlikely that LV emission from the NW peak arises from the quiescent ambient gas (see §4.5.1). Toward the core position we detected relatively strong emission at $\sim$ 28.1 km s^{-1} from the $J_k = 3_{12} \rightarrow 2_{21}$ rotational line of C_3H_2 (Vrtilek, Gottlieb, & Thaddeus 1987). Emission from this transition is not detected toward the lobes of the outflow, suggesting that this line might be a good probe for studies of the kinematics and physical conditions of the molecular gas surrounding the central energy source.

The peak intensity, center velocities, line widths, and integrated emission of SiO, obtained from Gaussian fits to the profiles shown in Figure 4.5, are given in Table 4.3. As noted before, due to the higher sensitivity, SiO emission is detected toward the core position. The line center velocity is, however, displaced by $\sim$ 1.5 km s^{-1} from the ambient cloud velocity, suggesting that the SiO emission seen toward the core does not arise solely from the quiescent ambient gas. The SiO line profiles observed toward the NW red peak exhibit, in addition to strong emission in the LV and IV ranges, weaker, more redshifted, emission up to radial velocites of $\sim$ 25 km s^{-1} from the ambient cloud radial velocity. We will refer to this feature as the high velocity (HV) component. From the inclination angle,

Table 4.2. CH_3OH Line Parameters

Transition	V_{rel}[1] ($km\,s^{-1}$)	Δv ($km\,s^{-1}$)	T_a^* (K)	$\int T_a^* dv$ (K $km\,s^{-1}$)	Comments[2]
		Red lobe: NW peak			
$J_k = 2_0 \rightarrow 1_0$ E	0.2	1.9	0.30	0.60	LV
	3.2	3.5	0.14	0.51	IV
$J_k = 2_0 \rightarrow 1_0$ A^+	0.4	2.1	1.96	4.41	LV
	3.1	3.2	0.87	2.95	IV
$J_k = 2_{-1} \rightarrow 1_{-1}$ E	0.3	1.9	1.28	2.59	LV
	2.5	4.8	0.71	3.64	IV
$J_k = 3_0 \rightarrow 2_0$ A^+	0.3	2.0	1.73	3.77	LV
	2.8	4.4	0.96	4.46	IV
$J_k = 3_{-1} \rightarrow 2_{-1}$ E	0.3	2.1	1.59	3.57	LV
	3.0	4.0	0.81	3.44	IV
$J_k = 3_0 \rightarrow 2_0$ E	0.2	2.2	0.45	1.03	LV
	3.2	2.9	0.15	0.47	IV
		Blue lobe: SE1 peak			
$J_k = 2_0 \rightarrow 1_0$ E	−1.4	3.4	0.12	0.43	LV&IV
$J_k = 2_0 \rightarrow 1_0$ A^+	−1.2	4.1	0.68	2.96	LV&IV
$J_k = 2_{-1} \rightarrow 1_{-1}$ E	−1.2	3.7	0.53	2.08	LV&IV
$J_k = 3_0 \rightarrow 2_0$ A^+	−1.4	3.7	0.83	3.26	LV&IV
$J_k = 3_{-1} \rightarrow 2_{-1}$ E	−1.3	3.6	0.71	2.69	LV&IV
$J_k = 3_0 \rightarrow 2_0$ E	−1.7	3.5	0.17	0.62	LV&IV
		Core: mm-source			
$J_k = 2_0 \rightarrow 1_0$ E	−0.2	1.0	0.078	0.084	
$J_k = 2_0 \rightarrow 1_0$ A^+	0.2	1.8	0.53	1.03	
$J_k = 2_{-1} \rightarrow 1_{-1}$ E	0.2	1.9	0.37	0.76	
$J_k = 3_0 \rightarrow 2_0$ A^+	0.2	1.8	0.53	0.99	
$J_k = 3_{-1} \rightarrow 2_{-1}$ E	0.2	2.0	0.44	0.97	
$J_k = 3_0 \rightarrow 2_0$ E	−0.2	2.1	0.083	0.19	

[1]Velocity relative to the ambient cloud velocity of $-4.45\ km\,s^{-1}$.

[2]LV indicates low velocity component, IV indicates intermediate velocity component (see text).

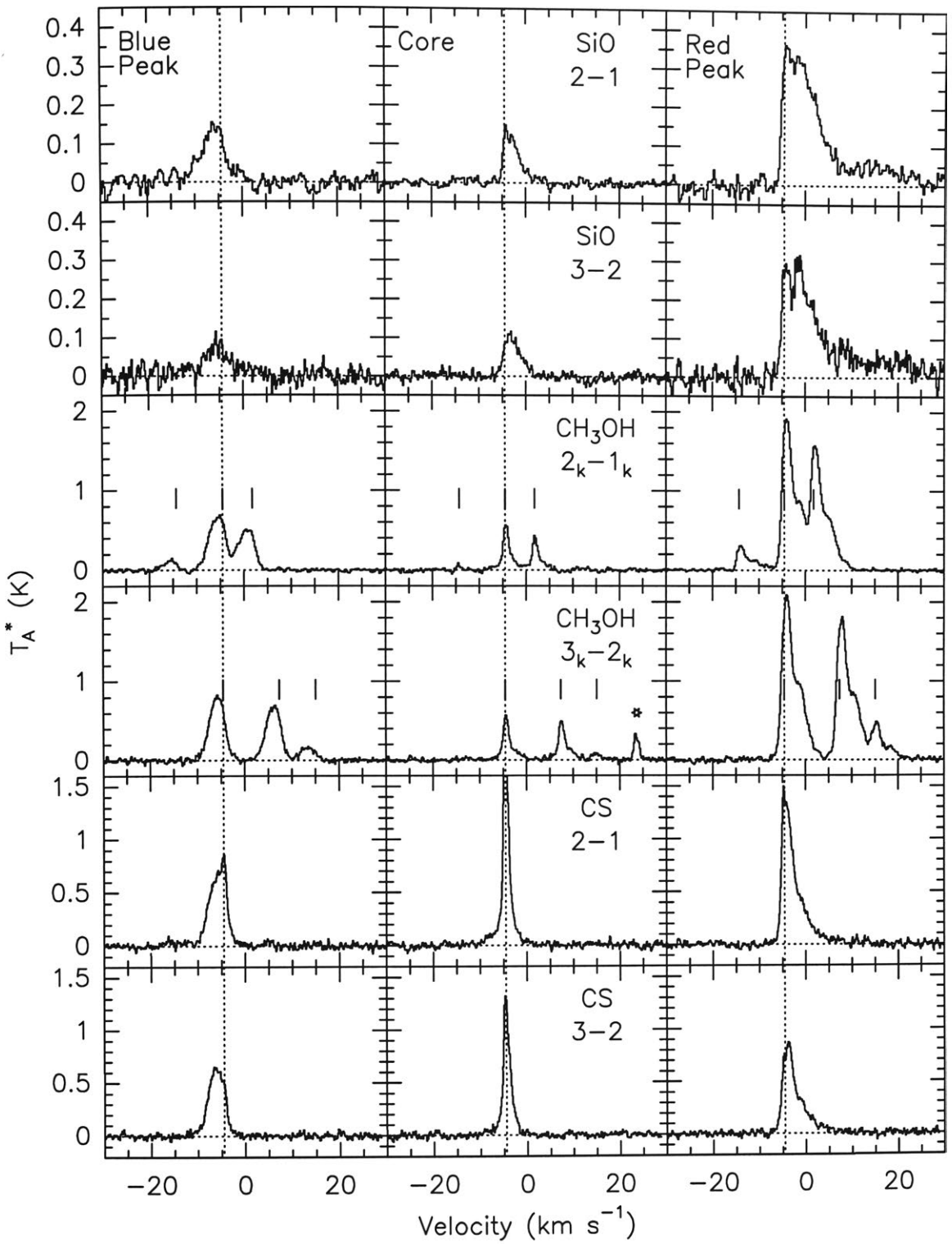

Figure 4.5.— Spectra of the line emission observed toward the SE1 peak (offset 20″, –80″ from the mm–IRAS source) of the blue lobe (left column); toward the mm source (the "core" position, middle column); and toward the NW peak (offset –40″, 140″) of the red lobe (right column), as defined in the previous Chapter. Transitions are labeled in the upper right corner of the spectra shown in the middle column. The velocity scale is from -29 to 29 km s^{-1}. The vertical dashed line indicates the systemic velocity of the globule of 4.5 km s^{-1}. The vertical ticks on the CH_3OH spectra indicate the different CH_3OH transitions observed, and the star in the CH_3OH $J_k = 3_k \rightarrow 2_k$ panel indicates the $J_k = 3_{12} \rightarrow 2_{21}$ transition of C_3H_2.

i, and the semi-opening angle, θ, of a biconical outflow, it is possible to derive the actual flow velocity from the maximum observed radial velocity (Cabrit & Bertout 1990). Using $i = 84°$ and $\theta = 15°$ (Chapter 3), we find that the HV gas has a flow velocity of ~ 70 km s^{-1}. However, the semi-opening angle was determined using the observed LV and IV emission. It is generally found that the gas moving at the highest velocities is more collimated than the slower moving gas in molecular outflows (e.g., Bachiller et al. 1990; Chapter 3), and so the value of 70 km s^{-1} for the HV component is most likely only a lower limit to the true velocity. Emission from the HV component is not evident in the other molecular species observed here, nor toward the SE1 peak of the blue lobe, although it is seen in deep CO observations toward the NE peak (Bourke, unpublished). As shown in Table 4.3, three Gaussian components were required to fit the SiO profiles observed at the NW peak position of the red lobe. Even though the solutions are formally correct, and giving similar line center velocities and line widths for both SiO transitions, the assumption of Gaussian profiles for the wing emission is arguable and therefore these results should be taken only as illustrative.

4.4. Analysis

4.4.1. Column densities and rotational temperatures

In order to derive the rotational temperature, T_{rot}, and the total column density, N_T, of methanol we used a rotational diagram analysis (see e.g., Linke, Frerking & Thaddeus 1978; Blake et al. 1987), with the assumptions of optically thin conditions and local thermodynamical equilibrium (LTE), which relates the integrated line intensity, rotational temperature, and column density via

$$\frac{3k \int T_{mb} dv}{8\pi^3 \mu^2 \nu S} = \frac{N_u}{g_u} = \frac{N_T}{Q(T_{rot})} \exp\left(-\frac{E_u}{kT_{rot}}\right) \quad , \tag{4.1}$$

where μ, ν, and S are the transition dipole moment, frequency, and line strength of the transition, respectively, $\int T_{mb} dv$ is the velocity integrated main beam brightness, obtained directly from the observations, E_u is the upper state energy,

Table 4.3. SiO LINE PARAMETERS

Transition	V_{rel}[1] ($km\,s^{-1}$)	Δv ($km\,s^{-1}$)	T_a^* (K)	$\int T_a^* dv$ (K $km\,s^{-1}$)	Comments[2]
		Red lobe: NW peak			
$J = 2 \rightarrow 1$	0.4	2.0	0.23	0.48	LV
	3.8	6.6	0.30	2.08	IV
	16.6	23.8	0.061	1.54	HV
$J = 3 \rightarrow 2$	0.3	2.1	0.20	0.46	LV
	3.8	5.6	0.24	1.44	IV
	15.1	20.5	0.051	1.11	HV
		Blue lobe: SE1 peak			
$J = 2 \rightarrow 1$	−1.6	5.9	0.14	0.87	LV&IV
$J = 3 \rightarrow 2$	−1.0	5.0	0.071	0.37	LV&IV
		Core: mm-source			
$J = 2 \rightarrow 1$	1.3	3.5	0.13	0.48	
$J = 3 \rightarrow 2$	1.6	4.1	0.10	0.45	

[1]Velocity relative to the ambient cloud velocity of $-4.45\ km\,s^{-1}$.

[2]LV indicates low velocity component, IV indicates intermediate velocity component, HV indicates high velocity component (see text).

and $Q(T_{rot})$ is the rotational partition function. In Table 4.4 we summarize the rotational temperatures and column densities of CH_3OH derived toward selected positions of the red and blue lobes of the outflow. For the blue lobe we integrated the emission in the LSR velocity range from -9.3 to -5.3 km s^{-1}, while for the red lobe we integrated the emission in the LSR velocity range from -3.7 to 0.3 km s^{-1}. These ranges have been chosen such that there is no overlap between the emission in the different components of the methanol lines nor a possible contribution from the ambient cloud gas. They mainly span the intermediate velocity range of the outflowing gas. As a mode of illustration we show in Figure 4.6 the rotational diagrams corresponding to the CH_3OH emission from the SE1 and NW peaks of the blue and red lobes. Toward these positions we detected emission in seven rotational lines of CH_3OH. The rotational temperature and N_T/Q ratio of methanol derived from a linear least squares fit to these data are shown in the lower left corner. The rotational temperatures of the outflowing gas at the different positions are broadly similar, with an average value of 7 K and a dispersion of 1 K. A similar analysis was performed for the CS and SiO molecules for which we detected emission in two rotational lines. The results are summarized in Table 4.4. We find that there is no significant differences among the rotational temperatures derived using different molecular species.

The rotational diagram analysis cannot be applied to the outflow CO emission because the lines are optically thick (Chapter 3). However, the excitation temperature of CO can be estimated from the observed main beam brightness temperature when the line emission is optically thick and the filling factor of the emission is unity. At the NW peak position of the red lobe we find an average main beam ^{12}CO $J = 2 \rightarrow 1$ brightness temperature, in the range of velocities between -3 to -2 km s^{-1}, of 17 K. At the SE1 and SE2 peak positions of the blue lobe we measure average main beam ^{12}CO $J = 2 \rightarrow 1$ brightness temperatures, in the range of velocities between -7 to -6 km s^{-1}, of $\sim$ 13 K. We will adopt these values as the excitation temperatures of the outflowing CO gas in the red and blue lobes of BHR 71, respectively. We used the ^{12}CO $J = 2 \rightarrow 1$

Table 4.4. Derived Parameters of Outflowing Gas

Offset[a] position	Lobe	CH_3OH			SiO			CS			HCO^+	CO	
		T_R (K)	N_T/Q (cm^{-2})	N_T (cm^{-2})	T_R (K)	N_T/Q (cm^{-2})	N_T (cm^{-2})	T_R (K)	N_T/Q (cm^{-2})	N_T (cm^{-2})	N_T (cm^{-2})	T_R (K)	N_T (cm^{-2})
(1,−3)	Blue	6	8.7×10^{12}	2.0×10^{14}	9	9.8×10^{10}	6.6×10^{11}	6	9.9×10^{11}	5.9×10^{12}	8.7×10^{11}	13	9.2×10^{16}
(1,−2)	Blue	9	6.1×10^{12}	1.4×10^{14}	9	8.1×10^{10}	5.4×10^{11}	8	8.4×10^{11}	5.0×10^{12}	9.7×10^{11}	13	2.5×10^{17}
SE1	Blue	7	1.0×10^{13}	2.3×10^{14}	6	2.6×10^{11}	1.8×10^{12}	10	1.2×10^{12}	6.9×10^{12}	...	...	...
(0,2)	Red	6	2.2×10^{13}	5.0×10^{14}	8	2.9×10^{11}	2.0×10^{12}	7	1.9×10^{12}	1.1×10^{13}	1.9×10^{12}	17	3.5×10^{17}
(−1,2)	Red	6	1.6×10^{13}	3.6×10^{14}	6	2.4×10^{11}	1.6×10^{12}	6	1.8×10^{12}	1.1×10^{13}	8.3×10^{11}	17	1.8×10^{17}
NW	Red	6	3.2×10^{13}	7.2×10^{14}	7	4.6×10^{11}	3.1×10^{12}	7	2.2×10^{12}	1.3×10^{13}	...	...	...

[a]Offsets are relative to R.A.(1950) = $11^h59^m20^s.0$, Dec.(1950) = $-64°51'00''$

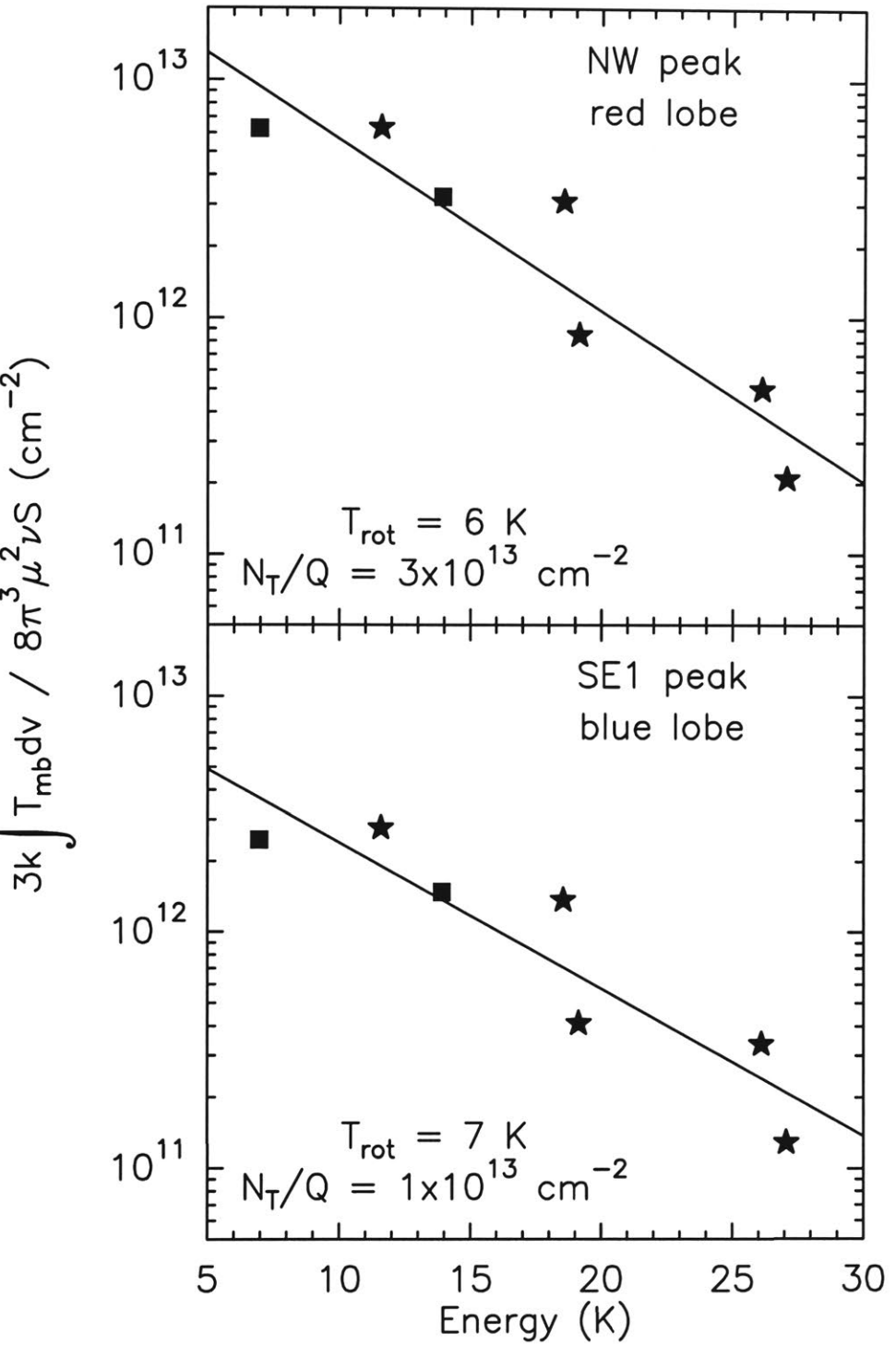

Figure 4.6.— Rotational diagrams for the methanol transitions observed toward the red and blue lobes of BHR 71. The lines correspond to least squares linear fits to the observed data. The derived values of the rotational temperature and total column density are given in the lower left corner.

data because they were collected using a smaller beam than the ^{12}CO $J = 1 \rightarrow 0$ data, thus minimizing a possible correction for a filling factor different from 1, and because the optical depth of the emission in the ^{12}CO $J = 2 \rightarrow 1$ line is larger than that in the ^{12}CO $J = 1 \rightarrow 0$ line.

4.4.2. Densities

To determine the density in the outflow we used the CS $J = 2 \rightarrow 1$ and $J = 3 \rightarrow 2$ observations and a spherically symmetric LVG statistical equilibrium code (see e.g., Snell et al. 1984; Mundy et al. 1986) which includes radiation trapping due to optical depth effects. Inputs of the code are the column density, determined in our case from the rotational diagram analysis, and the kinetic temperature of the gas. Since a direct estimate of the last is not available, we ran the model for kinetic temperatures of 15, 25, 50 and 100 K. The LVG analysis shows that the $J = 3 \rightarrow 2$ to $J = 2 \rightarrow 1$ intensity ratio is relatively insensitive to the kinetic temperature in this range, and that the gas density that produces the best fit to the observations, assuming the outflow CS emission is optically thin, is $n(H_2) \sim 10^5$ cm^{-3}.

A determination of the density of the ambient gas using the same procedure as above is probably not reliable, due to the possibility that the CS line may be optically thick. To avoid this problem we made use of the observation of the $J = 5 \rightarrow 4$ line at the (0,0) position, for which we have a 3σ detection. By using three CS transitions optical depth effects are accounted for by the LVG analysis. We assume that the ambient gas temperature of the BHR 71 globule is $\sim 10 - 15$ K, as derived by Bourke et al. (1995b) from observations of ammonia lines. The intensities and line widths of the three CS transitions are solved for simultaneously to give the column density and density, obtaining $N(CS) \sim 2 \times 10^{13}$ cm^{-2} and $n(H_2) \sim 3 \times 10^5$ cm^{-3} for temperatures in the adopted range. For comparison, Bourke et al. (1995b) estimate $n(H_2) \sim 3 \times 10^4$ cm^{-3} from ammonia observations with a much larger beam. Observations of C^{34}S are required to more accurately determine the density of the ambient gas.

4.4.3. Temperatures

As discusssed in §4.4.1, we find that the rotational temperature of the methanol emission from the outflowing gas in BHR 71 is typically $\sim$ 7 K. Whether this temperature provides an estimate of the kinetic temperature of the outflowing gas is arguable due to the possibility that the methanol populations may be sub-thermally excited (Bachiller et al. 1995; Avery & Chiao 1996). For the L1157 outflow Bachiller et al. (1995) found that the rotational temperature of methanol is $\sim$ 12 K, while Tafalla & Bachiller (1995) determined, from ammonia observations, that the kinetic temperature of the outflowing gas is $\sim$ 100 K, indicating that the methanol populations in the outflowing gas of L1157 are extremely sub-thermal. To assess whether a similar situation exists in the BHR 71 outflow we undertook a methanol excitation analysis using the same statistical equilibrium LVG code as Bachiller et al. (1995). We include levels up to J = 12 and K = 3, with the maximum number of levels set to 100. For the calculations we assume $N/\Delta v = 1 \times 10^{14}$ cm^{-2} (km s^{-1})$^{-1}$ in the outflow, which is consistent with our data, and ran the model for a density of 10^5 cm^{-3} and kinetic temperatures of 12, 50 and 100 K. Our aim here is not to determine precisely the kinetic temperature, which is not feasible considering the limited number of data points and the complexities of the methanol molecule, but to estimate the range of kinetic temperatures which are consistent with our data. In particular, when the methanol is sub-thermally excited model rotational diagrams including a large number of transitions show that excitation temperatures of the individual k-ladders are larger than between the k-ladders (Bachiller et al. 1995), with the result that the derived $T_{\rm rot}$ is very dependent on the transitions included in the analysis. From the analysis we find that our methanol observations are consistent with $T_{\rm K} \sim$ 50 – 100 K in the outflow, suggesting that the methanol is highly sub-thermally excited.

4.4.4. Molecular abundances

The chemical composition of a gas cloud is usually characterized by the fractional abundance of molecules relative to molecular hydrogen, the main constituent of the interstellar gas. The abundance of H_2 in the lobes of the BHR 71 outflow is not known, and difficult to estimate. Therefore, in the following discussion we will consider fractional abundances relative to the CO abundance which can be directly derived from our observations. We note that the $[CO]/[H_2]$ abundance ratio seems to be rather insensitive to difference in physical conditions and chemistry in different molecular environments, having values in the range from 7×10^{-5} to 1×10^{-4}, a variation of only $\sim 40\%$ (van Dishoeck et al. 1993). This variation could be explained by observations which indicate that up to 40% of the CO in dense clouds may be depleted onto grains (e.g., Whittet et al. 1989; Chiar et al. 1995). Some of this CO may be liberated in outflows by shocks, and so any comparison with CO that assumes a constant CO abundance may overestimate the relative abundance of other molecules. However, shock models predict that the abundance of CO remains relatively constant through the shock, whether J- or C-type (Iglesias & Silk 1978; Bergin, Melnick, & Neufeld 1998), and so this may not be a problem, though these models do not appear to consider the possibility of direct desorption of CO from grains.

The abundance of molecular species X relative to CO, [X]/[CO], in the outflowing gas of the BHR 71 lobes are given in Table 4.5. They were computed as the ratio of the molecular column density of species X, obtained from the rotational analysis (see Table 4.4), and the column density of CO molecules in the corresponding velocity range. The latter was computed from the ratio of the observed emission in the ^{12}CO and ^{13}CO lines assuming a $^{12}CO/^{13}CO$ ratio of 89 and an excitation temperature of 13 K for the blue lobe and 17 K for the red lobe (see the previous Chapter for a description of the method). Since for the BHR 71 cloud the ambient gas and shocked gas are well distinguished, both spatially and kinematically, the derived abundances of the outflowing gas are not affected by the emission of the quiescent gas. We find that the $[CH_3OH]/[CO]$ and [SiO]/[CO] abundances toward the lobes are typically $\sim 1 \times 10^{-3}$ and $\sim 6 \times$

10^{-6}, respectively. The column densities of HCO^+ in the outflow were estimated from the observed emission in the $J = 1 \rightarrow 0$ line, assuming it is optically thin, and using the same excitation temperatures as for CO.

Table 4.5. Molecular Abundances Relative to CO

Feature	Offset position[a]	[CH_3OH/CO]	[SiO/CO]	[CS/CO]	[HCO^+/CO]
		BHR 71 outflow			
Blue lobe	(1,−3)	2×10^{-3}	7×10^{-6}	6×10^{-5}	9×10^{-6}
Blue lobe	(1,−2)	6×10^{-4}	2×10^{-6}	2×10^{-5}	4×10^{-6}
Red lobe	(0 , 2)	1×10^{-3}	6×10^{-6}	3×10^{-5}	5×10^{-6}
Red lobe	(−1,2)	2×10^{-3}	9×10^{-6}	6×10^{-5}	5×10^{-6}
		BHR 71 ambient			
Core	(0 , 0)	5×10^{-5}	...	8×10^{-6}	9×10^{-5}
		Dark clouds			
TMC-1		3×10^{-5}	$< 3 \times 10^{-8}$	1×10^{-4}	8×10^{-5}
L134N		4×10^{-5}	$< 5 \times 10^{-8}$	9×10^{-6}	1×10^{-4}

[a]Offsets are in arc minutes relative to $\alpha_{1950} = 11^h59^m01^s.18$, $\delta_{1950} = -64°52'00''$

To quantitatively assess the chemical changes of the ambient medium due to the outflow phenomena requires a knowledge of the chemical abundances of the quiescent ambient gas. Since molecular observations of the BHR 71 globule away from the outflow system are not available, we will adopt, where appropriate, as ambient gas abundances those determined from our observations at the core position. The derived relative abundance of molecules in the ambient gas are presented in Table 4.5. The CO column density was determined, as described above, using the observations of the CO ($J = 1 \rightarrow 0$) and ^{13}CO ($J = 1 \rightarrow 0$) line emission assuming an excitation temperature of 11 K (Chapter 3). This method was also used to derive the HCO^+ column density from observations of the HCO^+ ($J = 1 \rightarrow 0$) and $H^{13}CO^+$ ($J = 1 \rightarrow 0$) line emission. We find that the emission in the $J = 1 \rightarrow 0$ line of both CO and HCO^+ is optically thick. For CS and CH_3OH we used the rotational diagram method described

in §4.4.1, with the caveat that the CS $J = 2 \rightarrow 1$ lines may be optically thick, in which case the CS column density would be underestimated. However, the result is in good agreement with the value obtained from the LVG analysis of §4.4.2. As a check we computed the relative abundance of CS at the (2′, –2′) offset position, which is away from the influence of the outflow and embedded source, and for which we have the ^{13}CO observations needed to determine the CO column densities. We find that the relative abundance of CS in this position is the same, within the errors, as the one derived toward the core. Also to assess a possible contribution to the CH_3OH core emission from the outflow, and/or a circumstellar disk, we computed the CO and CH_3OH column densities at the (1′, 0′) offset position, obtaining the same CH_3OH relative abundance. Since it may be argued that the emission observed toward the core position may not serve as a good probe of the chemical state of the ambient medium, we also show in Table 4.5 the relative abundances derived toward two starless low mass dark clouds, the TMC-1 ridge and L134N (see van Dishoeck et al. 1993, and references therein). The abundances derived toward the core of BHR 71 are almost identical to those measured for L134N. Finally, we note that the BHR 71 ambient gas SiO abundance cannot be estimated from the observations at the core position since in this case the emission most likely originates from gas associated with the outflow process. In fact, SiO emission from quiescent gas is usually not detected. In particular, for TMC-1 and L134N only upper limits exist in the abundance of SiO. In the following discussion we adopt as fiducial value of the [SiO/CO] abundance ratio in the quiescent ambient gas a value of 4 $\times$ 10^{-8}, corresponding to the geometrical mean of the upper limits determined for the TMC-1 ridge and L134N cloud.

Table 4.6 gives the abundance enhancement factor of gas phase molecular species in the BHR 71 outflow with respect to the ambient gas values in BHR 71. At the peak position of the red lobe the [CH_3OH]/[CO] and [SiO]/[CO] abundance ratios are enhanced with respect to that of the quiescent ambient gas in dark globules by factors of $\sim$ 40 and $\geq$ 350, respectively. On the other hand, the abundances of HCO^+ at the peak of the lobes are smaller than that in the

ambient gas by a factor of ~20.

Table 4.6. ABUNDANCE ENHANCEMENT

Molecule	Blue lobe		Red lobe	
	(1,−3)	(1,−2)	(0,2)	(−1,2)
CH_3OH	40	10	30	40
SiO	290	90	220	350
CS	8	3	4	8
HCO^+	0.10	0.04	0.06	0.06

4.5. Discussion

The data presented in the previous section clearly illustrate that the chemistry of the molecular gas near the core of the globule has been substantially modified as a result of the interaction between the outflow and the ambient medium. The spectacular abundance enhancement in the lobes with respect to that of the ambient medium may be interpreted to indicate that shocks play an essential role in the production of these molecules (Bachiller 1996; Schilke et al. 1997; Caselli, Hartquist & Havnes 1997). Shocks can raise the gas temperature and drive many chemical reactions which are inefficient at ambient cloud temperatures. They can also partially destroy dust grains leading to the injection of several absorbed atoms and molecules from the grain surface into the gas phase. In the following discussion we first compare the spatial distribution and line profile shape of the SiO emission from BHR 71 with those observed toward other outflows, which should provide clues about the type of shocks that give rise to the abundance enhancement in BHR 71. Then we discuss possible explanations for the enhancement or depletion in the abundance of each of the observed molecular species.

4.5.1. Comparison with other outflows

Strong abundance enhancement in SiO and/or CH_3OH have been detected in a number of other outflows, such as L1448 (Bachiller, Martín-Pintado & Fuente 1991), IRAS 03282+3025 (Bachiller et al. 1994), and L1157 (Mikami et al. 1992; Bachiller et al. 1995; Zhang et al. 1995; Avery & Chiao 1996). The first two sources are representative of the class of bipolar outflows associated with supersonic jets. The L1448 CO outflow is characterized by the presence of an extremely high velocity (EHV) outflow, at a velocity of $\sim$ 65 $\mathrm{km\,s^{-1}}$ with respect to the ambient cloud velocity, and a more standard high velocity (SHV) outflow at a velocity of $\sim$ 15 $\mathrm{km\,s^{-1}}$. In this source the SiO emission is associated with high-velocity molecular bullets (Bachiller et al. 1991), probably tracing shocks produced by a central jet. The SiO line profiles observed toward the central region of L1448 exhibit two strong emission features blueshifted and redshifted from the ambient cloud velocity by about the velocity of the EHV flow. The blueshifted (redshifted) feature shows a steep decrease in intensity toward the blue (red) and a slower decline toward the ambient cloud velocity. Away from this position the SiO spectra show two velocity components of weaker emission associated with the EHV and the SHV outflows. In the case of IRAS 03282+3025, which also consists of a well collimated jet of fast gas (at velocities of $\sim$ 57 $\mathrm{km\,s^{-1}}$) and a more extended, slower (at velocities of $\sim$ 17 $\mathrm{km\,s^{-1}}$) standard outflow component, the SiO emission is only detected at the end of the EHV blue lobe of the CO outflow (Bachiller et al. 1994), where possibly there is a maximum interaction of the outflow with the ambient gas. In the L1157 outflow the SiO emission toward the red CO lobe is located at the end of the lobe (Zhang et al. 1997), while toward the blue CO lobe is more widespread and appears as successive clumps which are intepreted as indicating the positions of bow shocks in the flow (Zhang et al. 1995). The SiO line profile observed toward the blue lobe show a steep increase from the ambient cloud velocity toward the peak radial velocity and a gradual decrease toward the more blueshifted velocities. This line asymmetry is opposite to that exhibited by the blueshifted emission from the bullets of the L1448 flow.

The spatial distribution and spectral line shape of the SiO emission from the BHR 71 flow are similar to those of the L1157 outflow, and markedly different from those of the other two sources, possible reflecting differences in the physical conditions of the ambient gas, driving source, and mechanism of shock excitation. The SiO line profile observed at the NW position of the BHR 71 red lobe, showing a broad redshifted feature with a peak at a radial velocity close to the ambient cloud velocity, a gradual decrease in intensity from the peak toward more redshifted velocities, and a rapid decline toward the ambient cloud velocity, is very similar in shape (besides the reversal in velocity) to the line profile observed at the peak of the blue lobe of the L1157 outflow. These profiles, if produced by shocks, suggest that a small fraction of the molecular gas is accelerated to shock velocities while the majority remain close to the ambient cloud velocity. For a shock moving with speed V_s, an observer that is at rest with respect to the pre-shock gas will see broad lines with a significant contribution from velocities considerably lower than V_s for a C-type shock and relatively narrow lines at velocities of $\sim \pm V_s$ for a J-type shock (cf., Hollenbach 1997). The overall shape of the SiO line profiles in BHR 71 hints then for the presence of C-type shocks. Regarding the spatial distribution, the large extent of the SiO emission in BHR 71, comparable in size to that of the CO, is similar to that seen toward the blue lobe of the L1157 outflow, and notably different from the L1448 and IRAS 03282+3025 outflows in which the SiO is enhanced along the axes of the molecular outflow and/or at their ends. The latter distribution is characteristic of outflows associated with supersonic jets in which the molecular enhancement is expected to be narrowly confined to the immediate vicinity of the bow shock generated by the fast jet as it entrains ambient molecular material.

The widespread distribution of SiO emission in the lobes of BHR 71, similar in extent to the CO emission which is thought to comprise mostly of swept up ambient gas, suggests that the chemical enhancement in this source takes place in a shell-like structure produced by the dynamical interaction between the ambient cloud and an underlying wide-angled wind or wind driven shell. The observed shape of the line profile of the SiO emission gives further support

to the hypothesis that the SiO emission arises from quiescent material that have been accelerated by the passage of a shock driven by the wind, producing a shell-like outflow, rather than from fast bullets ejected by the YSO and moving in the ambient cloud. The BHR 71 outflow would then be an example of the class of outflows driven by a less collimated wide-angle wind, with the molecular enhancement ocurring in a large shocked shell, surrounding the wind bubble, formed as the wind ablates material from dense clumps in the surroundings. Toward the blue-shifted lobe of BHR 71 there is a large cavity carved out by the outflow on the near-side of the globule (Fig. 3.13 of the previous Chapter). The amount of material available in this region for processing by the shocks has probably diminished, though clearly still sufficient to kinetically excite the rotational transitions of many molecular species. Figure 4.1 shows that while the blue lobe may be protruding out of the densest part of the globule (as shown by the optical image), there is still a large amount of moderately dense gas outside of the optical boundaries (as indicated by the ^{13}CO emission).

The existence of a supersonic jet toward BHR 71 might not be ruled out, however. In fact it has been suggested that most molecular outflow sources might have jet- and shell-like structures simultaneously, with one structure dominating over the other depending on the evolutionary stage (Padman, Bence & Richer 1997). High resolution imaging of both the L1448 and L1157 outflows show that close to the source the CO peaks in a shell-like structure, while the SiO remains essentially jet-like (Gueth, Guilloteau, & Bachiller 1996; Zhang et al. 1997). This feature may be the result of a wandering jet in L1157, but in L1448 it appears to be a result of prompt entrainment of material by the underlying jet (Bachiller et al. 1995). Some evidence for the presence of a jet in BHR 71 is provided by the high velocity (flow velocity of $\sim$ 70 km s^{-1}) component seen in SiO, which might be probing a more collimated component of the outflow. Molecular hydrogen observations in the near-infrared (NIR) at 2.12 μm show extensive emission along the axis of the BHR 71 outflow (Bourke 1994; Bourke et al. in preparation; see Fig 4.7), which may be the result of successive eruptive events from the vicinity of the YSO. Toward the northwest, the H_2 emission

traces a curved, elongated structure which could indicate a wandering jet with multiple bow-shocks along its length. However, toward the southeast the H_2 emission lies mainly outside the SiO blue lobe and seems to abruptly terminate at the inner edge of this lobe. The difference in the spatial distribution of SiO and H_2 could be attributed to multiple outflow episodes, with the shell-like outflow seen in SiO representing an older event than the jet-like H_2 events. In this view the SiO flow would then correspond to a coasting shell created during an earlier jet episode.

4.5.2. SiO enhancement

The high abundance of SiO molecules seen in BHR 71, and other molecular outflows, is most likely due to the injection into the gas phase by shocks of Si atoms and/or Si-bearing species. Once silicon is injected into the gas phase, chemical models based on ion-molecule reactions predict a large abundance of SiO molecules (Turner & Dalgarno 1977; Hartquist, Oppenheimer & Dalgarno 1980). Models of the chemistry in regions behind fast dissociative shocks predict a substantial enhancement in the abundance of SiO molecules (Neufeld & Dalgarno 1989). In particular, for shocks with velocities of 60 – 80 $\mathrm{km\,s^{-1}}$ propagating in a gas with pre-shock density of 10^4 $\mathrm{cm^{-3}}$ (about the average density of the BHR 71 globule) the predicted column densities of SiO molecules are $\sim 2-4\times10^{12}$ $\mathrm{cm^{-2}}$, similar to those derived in the lobes of the BHR 71 flow. A major drawback with the application of dissociative shock models to the BHR 71 flow is its moderate outflow velocity ($\sim$ 28 $\mathrm{km\,s^{-1}}$), since shock velocities less than $\sim$ 50 $\mathrm{km\,s^{-1}}$ are not fast enough to dissociate molecules. It is possible, however, that the weak HV emission seen in SiO, likely to be associated with high velocity jets, could be explained by this type of model.

C-type shocks appear to be the most promising to explain the bulk characteristics of the BHR 71 flow. In particular the synthesis of molecules from atoms and ions can be highly efficient behind non-dissociative C-type shocks. In fact, the detection of profuse SiO emission from other highly collimated bipolar

Figure 4.7.— *Next Page*

Overlay of the integrated SiO $J = 2 \rightarrow 1$ (*left*) and ^{12}CO $J = 1 \rightarrow 0$ (*right*) contours from Fig. 4.4 on the H_2 2.122 μm image (not continuum subtracted). The image is a mosaic taken with the infrared array camrea IRIS on the AAT. The solid contours represent the blue-shifted outflow and are integrated over the velocity range -9.1 to -5.5 km s^{-1} while the dashed contours represent the red-shifted outflow and are integrated over the velocity range -3.1 to 0.5 km s^{-1}. Contours are 35, 45, 55, 65, 75, 85, and 95% of the peak $\int T_A^* dv$ for each lobe. The peaks are 0.37 K km s^{-1} for the blue lobe and 0.88 K km s^{-1} for the red lobe of the SiO $J = 2 \rightarrow 1$ map, and 15.71 and 17.08 K km s^{-1} for the CO $J = 1 \rightarrow 0$ map. The star marks the position of the mm-IRAS source and the offsets are relative to it.

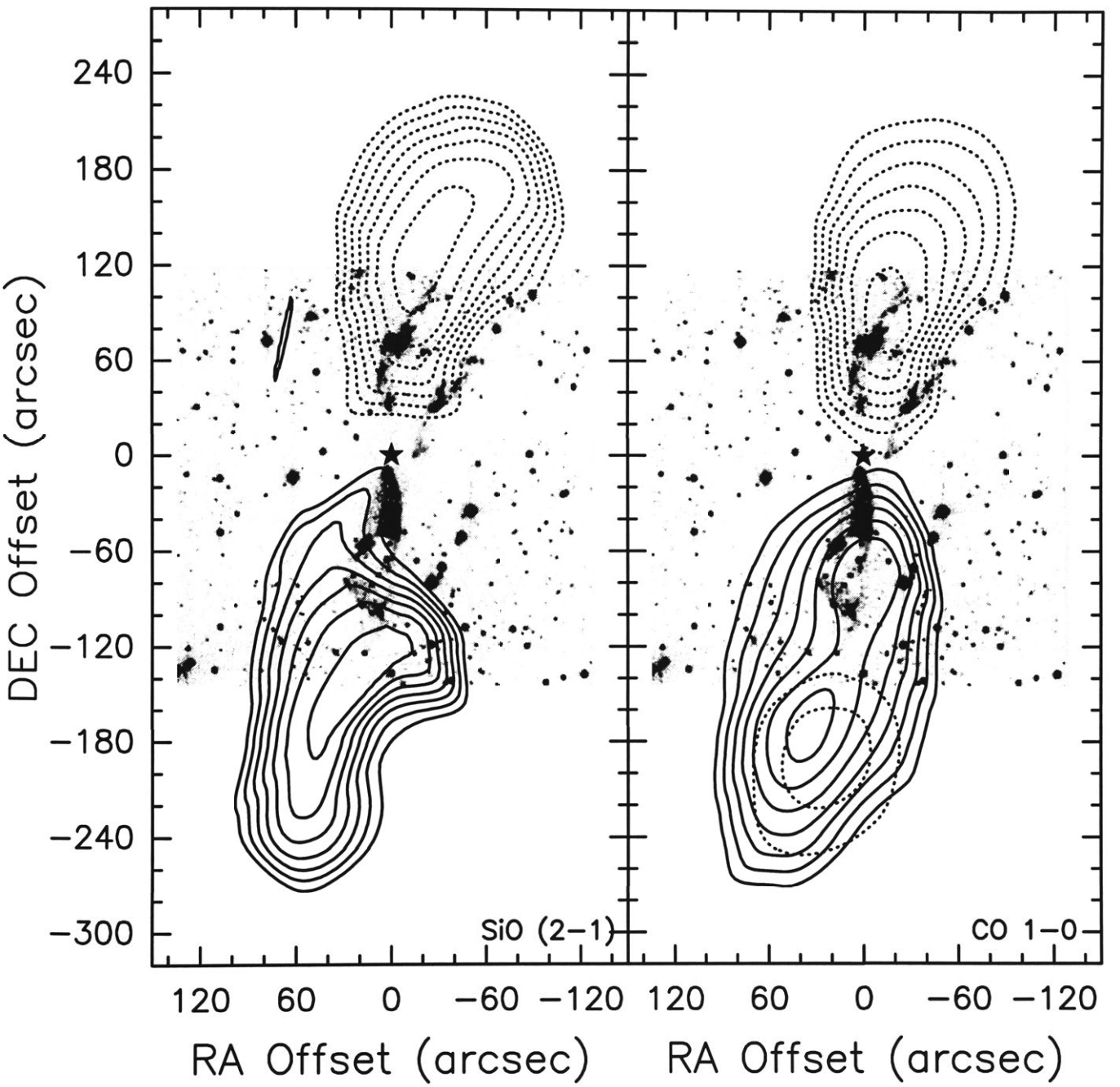
240
180
120
60
0
−60
−120
−180
−240
−300
DEC Offset (arcsec)
SiO (2−1)
CO 1−0
120
60
0
−60
−120
RA Offset (arcsec)
RA Offset (arcsec)

outflows with moderate outflow velocities (e.g., Bachiller et al. 1991; Mikami et al. 1992; Bachiller et al. 1995; Zhang et al. 1995), have triggered several theoretical works on the production of SiO behind C-type shocks. The main mechanism of injection of silicon is sputtering driven by neutral particle impact on charged grains (Draine 1995; Flower & Pineau des Forêts 1995; Schilke et al. 1997); although grain-grain collisions can be important for low velocity shocks ($25 \lesssim V_s \lesssim 35$ km s^{-1}) in dense regions ($n(H_2) > 5 \times 10^5$ cm^{-3}; Caselli et al. 1997). The sputtering of Si-bearing material can arise from either grain cores, namely refractory grains which are composed of silicates and graphites, or from grain mantles (Schilke et al. 1997). The release of Si-bearing material from grain cores requires higher impact energies than the release from mantles; substantial erosion of ice mantles can occur in C-shocks with velocities of ~ 25 km s^{-1}, while shock speeds of ~ 55 km s^{-1} are required in order to significantly erode the grain cores by He impacts. The inclusion of heavier species, such as CO and H_2O, can significantly lower the impact energies required for the erosion of grain cores, so that shock velocities as low as 25 km s^{-1} can cause substantial erosion of the grain cores (Schilke et al. 1997). Though the models are still preliminary, most are able to explain the column densities of SiO observed in the gas phase of molecular outflows. In particular, for the physical parameters typical of star forming regions Caselli et al. (1997) found that the gas phase SiO abundance behind C-shocks is larger than that in the quiescent gas by more than 3 orders of magnitude.

Another possible explanation for the widespread distribution of SiO in the BHR 71 outflow is the relative long lifetime of gas-phase SiO with respect to the outflow age (estimated at $\sim 10^4$ years in the previous Chapter). SiO is removed from the gas-phase via reactions with OH, and Herbst et al. (1989) have determined that the abundance of SiO is two orders of magnitude greater than SiO_2 (the product of SiO + OH), even after 3×10^5 yr, in regions applicable to the conditions in the BHR 71 region (their model 4), so that once formed, SiO is not quickly removed from the gas-phase. Pineau des Forêts et al. (1997) show that the abundance of SiO is still significant 10^4 years after the passage of

a shock, even taking into account re-accretion onto grains. So the widespread detection of SiO in the outflow may be an indication of its youth, suggested by its small dynamical lifetime (Chapter 3), and may indicate that heating of the lobes by shocks is sufficiently recent that there has not yet been time for radiative cooling to occur. Bachiller (1996) notes that SiO emission is generally only observed in the outflows from the youngest (Class 0) YSOs, consistent with the above scenario.

4.5.3. CH_3OH enhancement

We find that the $[CH_3OH]/[CO]$ abundance ratio of the outflowing gas in the lobes of BHR 71 is greater than that of the quiescent ambient gas by factors of $\sim$ 40. Similar enhancements in the abundance of methanol in other young bipolar outflows have been reported by Bachiller et al. (1995). These methanol abundances cannot be solely explained in terms of gas phase chemistry (Menten et al. 1988; Millar, Herbst & Charnley 1991). At the low temperature of molecular clouds, CH_3OH is thought to be depleted from the gas phase by condensation onto cold mantles of dust grains. The composition of the mantles depends on the physical conditions of the ambient medium. In particular, in an atomic hydrogen rich ambient medium such as that of molecular clouds, water and methanol are expected to be the two most abundant constituents of icy mantles surrounding silicate and carbonaceous grains (Tielens 1989). A natural explanation for the large increase of the abundance of CH_3OH in the gas phase would then be evaporation of ice mantles rich in CH_3OH molecules.

The interstellar processes by which molecular species are removed from the ices and returned to the gas phase are, however, still a matter of investigation. A potentially important result from laboratory measurements is that of Blake et al. (1991) who show that an amorphous H_2O:CH_3OH ice mixture when warmed to 120 K selectively injects methanol into the gas phase. In bipolar flows, the most likely source of heating is shocks, which can raise the temperature of the gas evaporating the icy organic mantles of the grains and returning this material to

the gas phase (Tielens & Allamandola 1987; Brown, Charnley, & Millar 1992). In the shock models of Schilke et al. (1997) ice mantles are completely destroyed in the shocks, their components being transfered to the gas phase. However, the details of how the methanol ice is liberated or how much is the abundance of methanol increased in the gas phase have yet to be quantitatively investigated. The similarities between the spatial distribution of the CH_3OH and SiO emission in the BHR 71 flow suggest that the process which leads to the evaporation of ice mantles also leads to the release of SiO and/or SiO_2 into the gas phase. In grain surfaces silicon is likely to be found in the form of SiO_2.

4.5.4. HCO^+ and CS abundances

Table 4.6 shows that the $[HCO^+]/[CO]$ abundance ratio of the outflowing gas in BHR 71 is smaller than in the quiescent ambient medium, or in other dark clouds, by typically a factor of 20 (cf., Guélin, Langer, & Wilson 1982; Baudry et al. 1981; Wootten et al. 1978; Swade 1989; Blake et al. 1995; Frerking, Langer, & Wilson 1987). Theoretical models of gas phase chemistry behind weak shocks propagating into dense gas predict that the abundance of molecules such as HCO^+, CN, and H_2CO should decrease with respect to the pre-shock abundances, while the abundances of molecules such as CO are unperturbed (Iglesias & Silk 1978; Mitchell 1987; Bergin et al. 1998). In particular, Inglesias & Silk (1978) find that for a 10 $km\,s^{-1}$ shock propagating into a cloud with a pre-shock density of 10^4 cm^{-3}, the abundance of HCO^+ should decrease by a factor of $\sim$ 20, while Bergin et al. (1998) find that for a 20 $km\,s^{-1}$ shock propagating into a cloud with a pre-shock density of 10^5 cm^{-3} and kinetic temperature of 30 K, the HCO^+ abundance should decreased by about a factor of 50. The low values of the $[HCO^+]/[CO]$ abundance ratio in the lobes of BHR 71 are consistent with the results predicted by shock models.

The [CS]/[CO] abundance ratios in the BHR 71 lobes are, on the other hand, similar to that of dark clouds, within the range of 10^{-5} – 10^{-4} (cf. Swade 1989; Fuller 1989; Irvine et al. 1987; Lemme et al. 1995), suggesting that the

abundance of the CS species is unperturbed or only slightly enhanced by the shock. In the few cases where the CS abundance in outflows from young stars has been estimated (e.g., Tafalla et al. 1997; Plambeck & Snell 1995; Takano 1986), an enhancement of a few is suggested, if any. A similar result is found for the shocked molecular cloud IC443 (e.g., Ziurys et al. 1989). This is in agreement with the few models that exist for the chemistry of CS in shocks (e.g., Pineau des Forêts et al. 1993; Leen & Graff 1988), which predict that the CS abundance remains essentially constant.

4.5.5. The low velocity emission

As mentioned earlier, in addition to the wing emission detected toward the lobes of BHR 71 in the lines of SiO and CH_3OH, we also detect emission at velocities comparable to the systemic velocity of the globule. In particular for silicon monoxide emission in the velocity range of the ambient cloud is clearly detected at the position of the lobes and barely visible toward the core. This can be appreciated in Figure 4.8 which shows velocity-position diagrams of the emission in the SiO lines along the symmetry axis of the outflow. The emission in the red lobe is roughly constant with velocity, with peaks at -4.1 and -0.8 km s^{-1}, while in the blue lobe the emission peaks at a velocity of -5.0 km s^{-1}, close to the ambient cloud velocity. This result might suggest that the low velocity emission originates in a stationary quiescent ambient gas that has not been disturbed by the passage of a shock. The enhancement of SiO and CH_3OH molecules would then be due to two different processes: (1) heating of grains within the ambient medium by a radiation field able to evaporate volatile grain mantles and trigger gas-phase reactions, and (2) direct shock processing of dust located within the shocked region. Possible sources of heating of the ambient gas are radiation fields from shocks (Wolfire & Königl 1991, 1993; Taylor & Williams 1996), X-rays emitted by the protostar (e.g., Sekimoto et al. 1997), and/or UV photons generated in the accretion disk surrounding the protostar (Spaans et al. 1995).

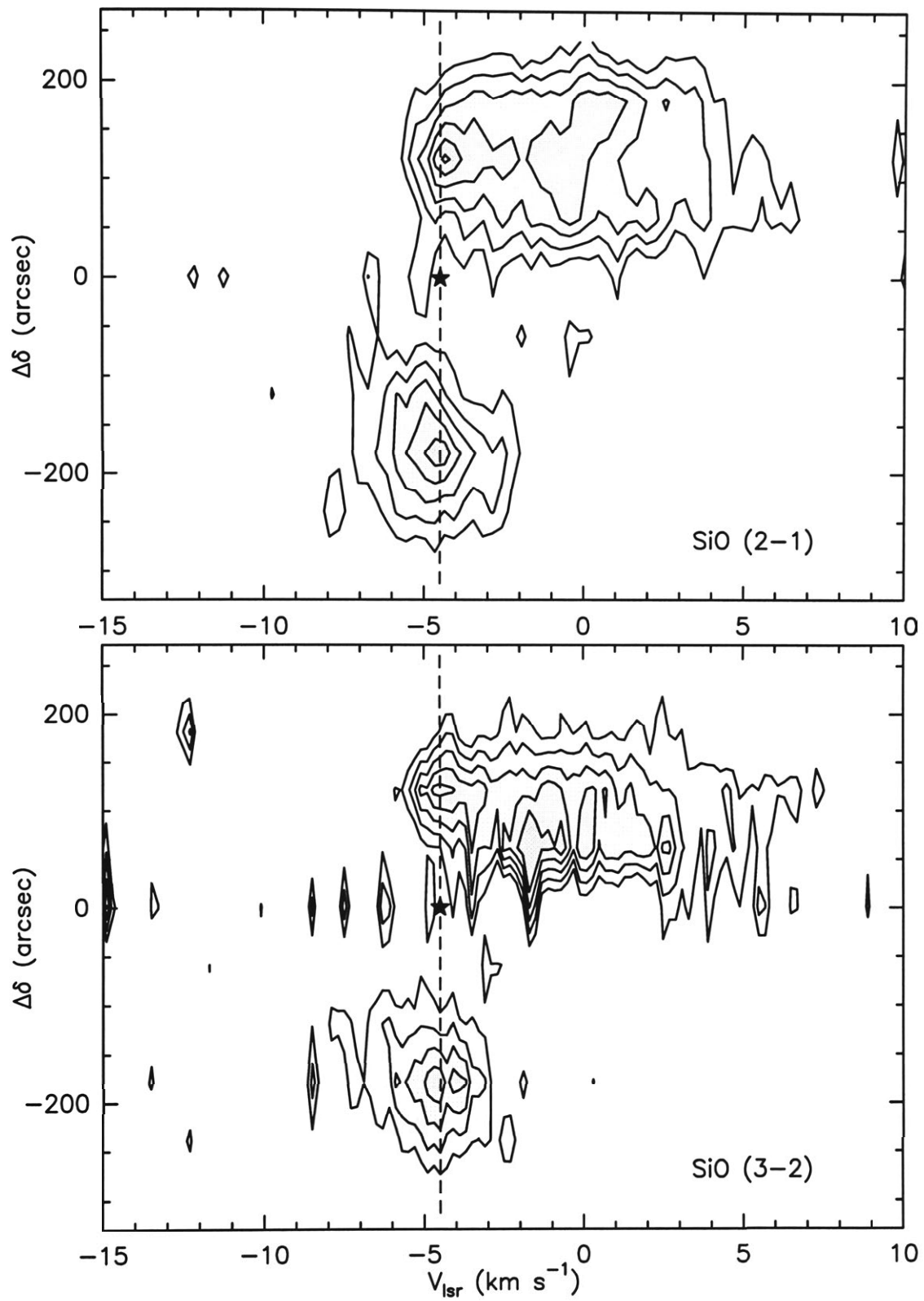

Figure 4.8.— Position-velocity diagram of the SiO emission along the symmetry axis of the outflow. *Upper*: SiO ($J = 2 \rightarrow 1$) – contour levels are 0.075 to 0.5 by 0.05 K in T_A^*. *Lower*: SiO ($J = 3 \rightarrow 2$) – contour levels are 0.075 to 0.3 by 0.05 K in T_A^*.

4.6. Summary

We have observed the highly collimated BHR 71 bipolar outflow in the $J = 3 \rightarrow 2$ and $J = 2 \rightarrow 1$ transitions of SiO and CS, the $J_k = 3_k \rightarrow 2_k$ and $J_k = 2_k \rightarrow 1_k$ transitions of CH_3OH, and the $J = 1 \rightarrow 0$ transition of HCO^+, using the SEST telescope. Broad wing emission was detected toward the outflow lobes in all the observed molecular transitions. The shape of the profiles are notably different from molecule to molecule depending on the relative intensities between a narrow line feature (arising from the ambient cloud in CS and HCO^+) and the broad component arising from the outflowing gas. Particularly striking are the cases of methanol and silicon monoxide molecules, for which the emission from the broad component is much stronger than that from the narrow component. Methanol lines exhibit the most intense wing emission suggesting that these lines are powerful signposts of the chemical impact of bipolar outflows on the surrounding ambient medium.

The spatial distribution of the integrated wing emission is broadly similar in all the observed molecular transitions, showing well separated blue and red shifted lobes. The extent of the lobes in the SiO and CH_3OH lines, of $\sim 0.14 \times 0.08$ pc, are similar to those of the CO lobes, perhaps indicating a common mechanisms for the excitation of these molecular lines. The SiO and CH_3OH profiles observed toward the red (blue) lobe are characterized by showing a broad wing emission with a maximum at a velocity close to the ambient cloud velocity, a gradual decrease in intensity from the peak velocity toward more redshifted (blueshifted) velocities, and a rapid decline in intensity toward the ambient cloud velocity. This spectral shape suggests that a small fraction of the molecular gas is accelerated to shock velocities while the majority remain close to the ambient cloud velocity, and is characteristic of standard C-type shocks (Hollenbach 1997). The line profile shape, together with the extended spatial distribution, of the SiO and CH_3OH emission suggest that C-shocks created by the interaction between the surrounding ambient medium and a wide-angle wind or wind driven shell, rather that a protostellar jet, play a major role in the production of these molecules toward the BHR 71 outflow. The intensity of the

emission in the red lobe is typically ~ 2 times stronger than that toward the blue lobe, and the line widths are broader, which is probable due to environmental effects, rather than intrinsic to the outflow mechanism.

We find that the abundance of methanol and silicon monoxide in the outflow lobes is enhanced with respect to that of typical dark clouds by factors of up to ~ 40 and 350, respectively, showing that these species are dramatically affected by the shocks. It appears that in the BHR 71 outflow the molecular enhancement takes place in a shell-like structure of swept up material driven by a wind, rather than by a protostellar jet. The associated shocks cause the evaporation of icy grain mantles resulting in the injection into the gas phase of large amount of ice mantle constituents, such as methanol. Further, the shock seems to be sufficiently powerful that refractory dust grains are partially destroyed, liberating into the gas phase a significant amount of Si atoms that are later converted to SiO by ion-molecule reactions and/or shock chemistry.

Our multiline molecular observations also reveal that the $[HCO^+]/[CO]$ abundance ratios of the outflowing gas in BHR 71 are smaller than in quiescent dark clouds by typically a factor of 20, which can be interpreted as a result of shock chemistry. The [CS]/[CO] abundance ratios are, on the other hand, similar to that of dark clouds, suggesting that the abundance of the CS species is unperturbed by the shock. Finally, we suggest that the SiO and CH_3OH emission detected toward the lobes might not only trace shocked outflowing gas but also quiescent ambient gas that has been heated by UV and X-ray radiation produced by either the shocks themselves, the protostar and/or the accretion disk.

REFERENCES

André, P. 1995, Ap&SS, 224, 29

Avery, L. W., & Chiao, M. 1996, ApJ, 463, 642

Bachiller, R. 1996, ARA&A, 34, 111

Bachiller, R., & Pérez Gutiérrez, M., 1997, in IAU Symp. 182, Herbig-Haro Flows and the Birth of Low Mass Stars, ed. B. Reipurth & C. Bertout (Dordrecht: Reidel), 153

Bachiller, R., Cernicharo, J., Martín-Pintado, J., Tafalla, M., & Lazareff, B. 1990, A&A, 231, 174

Bachiller, R., Martín-Pintado, J., & Fuente, A. 1991, A&A, 243, L21

Bachiller, R., Liechti, S., Walmsley, C. M., & Colomer, F. 1995, A&A, 295, L51

Bachiller, R., Tereby, S., Jarrett, T., Martín-Pintado, J., Beichman, C. A., & van Buren, D. 1994, ApJ, 437, 296

Baudry, A., Perault, M., De La Noe, J., Despois, D., & Cernicharo, J. 1981, A&A, 104, 101

Bergin, E. A., Melnick, G. J., & Neufeld, D. A. 1998, ApJ, in press

Blake, G. A., Sandell, G., van Dishoeck, E. F., Groesbeck, T. D., Mundy, L. G., & Aspin, C. 1995, ApJ, 441, 689

Blake, D., Allamandola, L., Sandford, S., Hudgings, D., & Freund, F. 1991, Science, 254, 548

Blake, G. A., Sutton, E. C., Masson, C. R., & Phillips, T. G. 1987, ApJ, 315, 621

Bourke, T. L., Garay, G., Lehtinen, K. K., Köhnenkamp, I., Launhardt, R., Nyman, L-Å, May, J., Robinson, G., & Hyland, A. R. 1997, ApJ, 476, 781 (Chapter 3)

Bourke, T. L. 1994, MSc thesis, Univ. New South Wales

Bourke, T. L., Hyland, A. R., & Robinson, G. 1995a, MNRAS, 276, 1052

Bourke, T. L., Hyland, A. R., Robinson, G., James, S. D., & Wright, C. M. 1995b, MNRAS, 276, 1067

Brown, P. D., Charnley, S. B., & Millar, T. J. 1992, in Chemistry and Spectroscopy of Interstellar Molecules, ed. N. Kaifu (Tokyo: Univ. Tokyo Press), 149

Cabrit, S., & Bertout, C. 1990, ApJ, 348, 530

Caselli, P., Hartquist, T. W., & Havnes, O. 1997, A&A, 322, 296

Chiar, J. E., Adamson, A. J., Kerr, T. H., & Whittet, D. C. B. 1995, ApJ, 455, 234

Draine, B. J. 1995, A&AS, 233, 111

Flower, D. R., & Pineau des Forêts, G. 1995, MNRAS, 275, 1049

Frerking, M. A., Langer, W. D., & Wilson, R. W. 1987, ApJ, 313, 320

Fuller, G. A. 1989, PhD Thesis, Univ. California Berkeley

Guélin, M., Langer, W. D., & Wilson, R. W. 1982, A&A, 107, 107

Gueth, F, Guilloteau, S., & Bachiller, R. 1996, A&A, 307, 891

Hartquist, T. W., Oppenheimer, M., & Dalgarno, A. 1980, ApJ, 236, 182

Herbst, E., Millar, T. J., Wlodek, S., & Bohme, D.K., 1989, A&A, 222, 205

Hollenbach, D. 1997, in IAU Symp. 182, Herbig-Haro Flows and the Birth of Low Mass Stars, ed. B. Reipurth & C. Bertout (Dordrecht: Reidel), 181

Iglesias, E. R. & Silk, J. 1978, ApJ, 226, 851

Irvine, W. M., Goldsmith, P. F., & Hjalmarson, A. 1987, in Interstellar Processes, ed. D. J. Hollenbach & H. A. Thronson (Dordrecht: Reidel), 561

Leen, T. M., & Graff, M. M. 1988, ApJ, 325, 411

Lemme, C., Walmsley, C. M., Wilson, T. L., & Muders, D. 1995, A&A, 302, 509

Linke, R. A., Frerking, M. A., & Thaddeus, P. 1978, ApJ, 234, L139

Menten, K. M., Walmsley, C. M., Henkel, C., & Wilson, T. L. 1988, A&A, 198, 253

Mikami, H., Umemoto, T., Yamamoto, S., & Saito, S. 1992, ApJ, 392, L87

Millar, T. J., Herbst, E., & Charnley, S. B. 1991, ApJ, 369, 147

Mitchell, G. F. 1987, in IAU Symp. 120, Astrochemistry, ed. M. S. Vardya & S. P. Tarafdar (Dordrecht: Reidel), 275

Mundy, L. G., Snell, R. L., Evans, N. J., Goldsmith, P. F., & Bally, J., 1986, ApJ, 306, 670

Neufeld, D. A., & Dalgarno, A. 1989 ApJ, 340, 869

Padman, R., Bence, S., & Richer, J. 1997, in IAU Symp. 182, Herbig-Haro Flows and the Birth of Low Mass Stars, ed. B. Reipurth & C. Bertout (Dordrecht: Reidel), 123

Peng, R. S., & Whiteoak, J. B. 1993 MNRAS, 260, 529

Pineau des Forêts, G., Flower, D. R., & Chièze, J. -P., 1997, in IAU Symp. 182, Herbig-Haro Flows and the Birth of Low Mass Stars, ed. B. Reipurth & C. Bertout (Dordrecht: Reidel), 200

Pineau des Forêts, G., Roueff, E., Schilke, P., & Flower, D. R. 1993, MNRAS, 262, 915

Plambeck, R. L., & Snell, R. L., 1995, ApJ, 446, 234

Raga, A. C., & Cabrit, S. 1993, A&A, 278, 267

Sandqvist, A. 1977, A&A, 57, 467

Sekimoto, Y., Tatematsu, K., Umemoto, T., Koyama, K., Tsuboi, Y., Hirano, N., & Yamamoto, S. 1997, ApJ, 489, L63

Snell, R. L., Mundy, L. G., Goldsmith P. F., Evans N. J., & Erikson, N. R., 1984, ApJ, 276, 625

Schilke, P., Walmsley, C.M., Pineau des Forêts, G., & Flower, D.R. 1997, A&A, 321, 293

Spaans, M., Hogerheijde, M.R., Mundy, L.G., & van Dishoeck, E. F. 1995, ApJ, 455, L167

Swade, D. L. 1989, ApJ, 345, 828

Takano, T. 1986, ApJ, 300, L85

Tafalla, M., Bachiller, R., Wright, C. H., & Welch, W. J. 1997, ApJ, 474, 329

Tafalla, M., & Bachiller, R. 1995, ApJ, 443, L37

Taylor, S. D., & Williams, D. A. 1996, MNRAS, 282, 1343

Tielens, A. G. G. M. 1989, in Interstellar Dust, ed. L. J. Allamandola & A. G. G. M. Tielens (Kluwer: Dordrecht), 239

Tielens, A. G. G. M., & Allamandola, L. J. 1987, in Physical Processes in Interstellar Clouds, ed. G. E. Morfill & M. Scholer (Dordrecht: Reidel), 333

Turner, J. L., & Dalgarno, A. 1977, ApJ, 213, 386

van Dishoeck, E. F., & Blake, G. A. 1995, Ap&SS, 224, 237

van Dishoeck, E. F., Blake, G. A., Draine, B. T., & Lunine, J. I. 1993, in Protostars and Planets III, ed. E. H. Levy & J. Lunine (Tucson: Univ. Arizona Press), 163

Vrtilek, J. M., Gottlieb, C. A., & Thaddeus, P. 1987, ApJ, 314, 716

Whittet, D. C. B., Adamson, A. J., Duley, W. W., Geballe, T. R., & McFadzean, A. D. 1989, MNRAS, 241, 707

Wolfire, M. G., & Königl, A. 1991, ApJ, 383, 205

Wolfire, M. G., & Königl, A. 1993, ApJ, 415, 204

Wootten, A., Evans, N. J., Snell, R., & Vanden Bout, P. 1978, ApJ, 225, L143

Zhang, Q., Ho, P. T. P., Wright, M. C. H., & Wilner, D. J. 1997, in IAU Symp. 182 Poster Proceedings, Low Mass Star Formation from Infall to Outflow, ed. F. Malbet & A. Castets (Observatiore de Grenoble)

Zhang, Q., Ho, P. T. P., Wright, M. C. H., & Wilner, D. J. 1995, ApJ, 451, L71

Ziurys, L. M., Snell, R. L., & Dickman, R. L. 1989, ApJ, 341, 857

Chapter 5

Summary and Future Directions

The main results and conclusions of this thesis are presented at the end of each chapter, and are not repeated here. In this Chapter we present a final summary, and outline (without detail) future directions for the research presented here.

5.1. Magnetic Field Measurements

In the first part of this thesis (Chapter 2) we reported on observations of the Zeeman effect in OH toward a selection of southern molecular clouds. Although the detection rate was very low, the upper limits on magnetic field strengths are consistent with the idea that magnetic fields are important in regulating star formation in molecular clouds, either through pressure support via the mean magnetic field, or turbulent support via MHD wave propagation, or a combination of the two. However, in many cases the 3σ upper limits are tantalisingly close to the critical values predicted by simple theoretical models if magnetic fields are to be important in molecular cloud physics. It would be ideal to be able to either lower significantly these upper limits, or detect the Zeeman effect towards the sources. Unfortunately the amount of observing time required to accomplish either aim is, in most cases, astronomically high given, the demands for time on modern telescopes. Another approach is to observe even more sources in the south, thus increasing the sample size. The drawback

there is that we have already observed all the sources where the detection of a field of order 30–50 μG is likely to be achievable in a reasonable amount of time (10–20 hours).

One program we are pursuing while the opportunity is available is a systematic program of Zeeman observations of northern molecular clouds which have not previously been observed for the Zeeman effect. This program is being undertaken at the Green Bank 140′ telescope, which has been successfully used previously for Zeeman work, and which will be decommissioned once the Green Bank Telescope (GBT) is operational. Northern OH Zeeman studies have been made with a variety of telescopes (Green Bank, Hat Creek, Nançay, Arecibo), so our aim is to observe, with only one telescope, group of objects chosen with a well defined selection criteria. By combining the results from Green Bank with the full Parkes sample (which we aim to extend by observing more sources) we will have sensitive Zeeman observations, using only two telescopes, of a well defined list of clouds. Even though we do not expect a high detection rate, sensitive upper limits are important for statistical studies, given the paucity of observations to date.

An important next step to the Zeeman work presented here is to observe both RCW 38 and RCW 57 with higher spatial resolution, to investigate the spatial structure of the magnetic field. This will then allow us to determine with more confidence in which component of the gas we are measuring the field, and thus allow a more accurate comparison of the cloud properties with the measured field strength. Such observations should be undertaken with the Australia Telescope Compact Array in the near future. If it is found that the field is being measured in gas associated with PDR regions of these two H II regions then a comparison of the Zeeman observations with mid-infrared polarimetry observations may be useful in investigating the three dimensional nature of the field.

5.2. The BHR 71 Outflow

The BHR 71 outflow (Chapters 3 and 4) is only the second outflow from a low-mass protostar to have been mapped in detail in SiO and CH_3OH. The other example is L1157. A comparison of the spatial structure of the SiO, CO and near-infrared hydrogen emission suggests that the L1157 outflow is jet driven. However, on small spatial scales both wind-driven (shell-like structures) and jet-driven phenomena are present. In BHR 71 it is difficult to decide with the present data which mechanism is dominant in driving the outflow, since signposts of both processes appear on the large scale. Further observations are required to either resolve this issue directly, or to provide the necessary data for detailed modelling. Good high spatial resolution maps in both ^{12}CO $J = 2 \rightarrow 1$ and SiO $J = 3 \rightarrow 2$ are required, to more accurately compare their spatial morphologies. CO is believed to be swept up ambient gas, while SiO is believed to be formed in-situ via C-shocks, so we might expect striking differences in their morphology, which is not evident in our poorly sampled maps.

It is also important to extend the near-infrared observations to cover the full extent of the molecular outflow, to look for bow-shock-like structures toward the head of the flow, and to compare the high resolution CO and SiO observations with the near-infrared observations along the length of the flow. If J-shocks are more important at the head of the flow, then observations of e.g., [FeII] may be important, though it is rarely observed toward outflows from low-mass protostars. In order to allow more detailed modelling of the shock structure then observations of the H_2 $v = 1 - 0$ S(1) line at 2.122 μm and the $v = 2 - 1$ S(1) line at 2.248 μm are required along the length of the outflow.

Since this outflow is one of the few to exhibit marked changes in the abundance of different molecular species, it is important to extend those observations to include a large number of species which may be similarly affected. Temporal modelling of shock propagation through molecular clouds, including full chemical networks, is just around the corner, and it is important that observations are available to confront these models as they evolve. By a combination of observa-

tion and theory (modelling) we may be able to identify different molecular species which allow us to date molecular outflows provided we have sufficient data on the initial conditions of the ambient cloud (e.g., density and temperature), and of the different molecular species within the outflow.

It is also important to study in more detail the few other outflows which exhibit the SiO abundance enhancements, since the two best studied cases, L1157 and BHR 71, show such different characteristics. Such a program is being undertaken by Garay and co-workers for sources visible from SEST.

Appendix A

Mid-infrared imaging and spectroscopy of the southern H II region RCW 38[1]

[1]Craig H. Smith, Tyler L. Bourke, Christopher M. Wright, Henrik W.W. Spoon, David K. Aitken, Garry Robinson, John W.V. Storey, Takuya Fujiyoshi, Patrick F. Roche, Thomas Lehmann, accepted by MNRAS in a slightly modified form.

ABSTRACT

We present mid-infrared images and an 8–13 μm spectrum of the southern H II region RCW 38. We determine the dust colour temperature from both our spectrum and images at 10 and 20 μm, and deduce the gas excitation from an image in the S IV fine structure line, as well as spectra of the Ar III, S IV and Ne II fine structure lines. Our observations are consistent with a complex of sources associated with the RCW 38 IRS1 region which represent knots of material in a shell, or ridge, surrounding a cavity of about 0.1 pc in radius, which is itself created by the stellar wind of the hot young source IRS2. The dust temperature does not peak closest to IRS2, but rather along the centre of the ridge, and is remarkably uniform over the extent of our image. From photoionisation models for the observed line ratios at IRS1 we deduce a stellar effective temperature and gas density of about 43 000–48 000 K and 10^4 cm^{-3} respectively. Whilst the star, or star cluster, IRS2 is ultimately responsible for the observed thermal and ionic emission, the relatively uniform dust temperature implies that the bulk of the dust heating in the region is provided by resonantly trapped Lyman α photons, rather than direct stellar photons. This then also implies that the dust is depleted with respect to the gas by a factor of at least 100 from its normal interstellar value. The small scale spatial variations in the continuum emission and temperature can be explained by changes in the gas–to–dust mass ratio. However, positional offsets between the peaks of S IV and dust emission may imply that the sulfur abundance is locally enhanced, possibly due to grain destruction via shocks.

A.1. Introduction

RCW 38 (Rodgers, Campbell & Whiteoak, 1960) is a luminous H II region ($\sim 7 \times 10^5$ $L_\odot$; Furniss, Jennings & Moorwood 1975) located in the region of the Vela Supernova remnant and the Gum nebula (Gum 1952, 1956). The reported distance to RCW 38 varies somewhat, but a reasonably consistent value is found amongst Radhakrishnan et al. (1972) of 1.5 kpc, Muzzio (1979) of 1.7 kpc, and Beck, Fisher & Smith (1991) of 1.7±0.9 kpc. We adopt a distance of 1.7 kpc for RCW 38.

Frogel & Persson (1974; hereafter FP74) produced a 10 μm map of the region with a spatial resolution of 14.″5 showing the warm dust emission to be spatially extended in a horse-shoe shape over a 1.8 × 1.8 arcmin^2 area. The peak of their map is labelled IRS1 but does not correspond with the bright 2.2 μm source IRS2 that dominates at near-infrared (NIR) wavelengths (FP74). FP74 found IRS1 to be extended on a scale of about 9″. Epchtein & Turon (1979) mapped a smaller (40 × 40 arcsec^2) region with a spatial resolution of 7″. They found the strong 10 μm peak IRS1 resolves into a number of more discrete sources, which they suggested may be due to local heating sources (i.e. a cluster of embedded young stars), or dust opacity variations.

A low resolution (warm filter) 10 μm spectrum of RCW 38 IRS1 is presented in Persson, Frogel & Aaronson (1976). From simple two parameter fits to the spectrum they derive a dust temperature of 175 K and a modest absorption optical depth of $\tau_{9.7\mu m} = 0.4$.

From its NIR colours FP74 suggest that IRS2 represents an early O star (around O4) or group of stars, suffering 12.8 magnitudes of extinction. As noted by Furniss, Jennings and Moorwood (1975), the ionizing flux from such a star is more than sufficient to account for all the 5 GHz flux observed by Goss & Shaver (1970). They suggested that an O5 star and little or no dust absorption of the continuum photons in the ionised region could fit the known parameters of RCW 38. Mizutani et al. (1987) present a Brγ map of the region (15″ resolution) and find that Brγ emission largely follows the structure of the 10 μm images.

From their observations they deduce an electron temperature of about 8000 K. They argue that IRS2 represents three O6 (ZAMS) stars rather than a single O5 star, though they do not preclude the possibility of an O5 star with a cluster of embedded stars.

Storey & Bailey (1982) present a near-infrared K band image of the inner 2.'5 of RCW 38. Their image shows a number of discrete sources surrounded by extended nebulosity. NIR photometry indicates that all the bright sources in the field are highly reddened point sources, and they infer visual extinctions of up to 60 magnitudes. Allen & Meadows (1992) present a JHK' image of a larger region around IRS2. Their more sensitive observations show that the nebulosity is far more extended than indicated by the image of Storey & Bailey. The blue appearance of the nebulosity in the JHK' false colour image hints that the extinction toward the nebulosity is not high.

Ligori et al. (1994) imaged a region $\sim 1.5 \times 1.5$ arcmin^2 at JHK centred on IRS2 with a spatial resolution of 0.''89 pixel^{-1}. They resolve IRS2 into a cluster of at least 5 point sources within the central 16'', the beamsize used by FP74. The brightest source in this region dominates the observed flux and is saturated in their data. They also find a number of sources with large $H - K$ excess within their field of view which may also be young embedded sources. One of their reddest sources is tentatively identified with FP74's IRS 3, detected at 10 μm. From their data Ligori et al. construct a K band luminosity function, which they fit with a Miller–Scalo IMF to deduce a cluster age of ~ 2 Myr.

Due to the complex nature of this source, the large beam *IRAS* observations at 12 and 25 μm of this region do not provide much insight, though Kuiper et al. (1987) are able to extract useful 60 and 100 μm fluxes from which they deduce a cool dust temperature of 45 K and gas column density of 2×10^{20} cm^{-2}. However, from observations at 1-mm Cheung et al. (1980) derive a high column density of 8×10^{23} cm^{-2}, from which they infer a large visual extinction of 800 mag, indicating that RCW 38 lies at the front surface of a dense and massive (10^4 M$_\odot$) molecular cloud.

Detailed molecular observations of RCW 38 are rare. Gillespie, White & Watt (1979) mapped a region 1.0 × 0.5 deg^2 in the CO (1 → 0) line with a 3.′2 beam. They find that the CO is extended with a size of ∼ 20′ × 10′, which corresponds to a linear size of 10 × 5 pc at the adopted distance. The emission consists of 2 clumps connected by a bridge of material in an east–west direction. RCW 38E is associated with the H II region, while RCW 38W lies some 15′ away. Observations with higher spectral resolution in the CO (2 → 1) line by White & Phillips (1983) indicates that the CO emission suffers from large self-absorption in the direction of RCW 38E. More recently, Zinchenko, Mattila & Toriseva (1995) have mapped RCW 38E in CS (2 → 1). Their data shows the high density gas (> 10^4 cm^{-3}) to be clumpy and not peaked at IRS1, but rather appears in a shell-like structure surrounding it. A large velocity gradient is evident, running from NE to SW through IRS1. The CS velocity agrees with the dip in the CO emission, confirming that the dip is due to self-absorption by foreground gas. Zinchenko et al. estimate that the region traced by CS has a mass of 1.5 × 10^3 M$_\odot$. Howe, Snell & Bergin (in preparation) have mapped RCW 38E in ^{13}CO (2 → 1) and CS (2 → 1). Their data shows the gas to be very clumpy with multiple velocity components along the line of sight. Their data also indicates that the region around IRS2 does not contain much dense gas, and appears as a hole in their CS integrated intensity maps.

As part of a program aimed at studying the morphology and excitation of southern H II regions we have obtained both continuum and line mid-infrared images, as well as a spectrum, of RCW 38. Observations of another H II region, G333.6–0.2, have already been published by Fujiyoshi et al. (1997). In the following section we describe our observations of RCW 38 using a newly commissioned mid-infrared camera. In section A.3 we present our results and analysis of both the imaging and spectroscopic information, in terms of the excitation and density of the H II region, and the dust temperature. We discuss our results in section A.4, and finally present our conclusions in section A.5.

A.2. Observations

The imaging observations presented here were made with the Max–Planck–Institut für extraterrestrische Physik (MPE) mid–infrared (MIR) imaging system MANIAC (Mid And Near Infrared Array Camera) at the European Southern Observatory (ESO) 2.2–m telescope at La Silla in Chile. This instrument is based on a Rockwell 128 × 128 Si:As IBC array, with control and readout electronics provided by Wallace Electronics Inc. The instrument is designed to provide simultaneous imaging at both MIR and NIR wavelengths. So far however, only the mid-infrared channel has been completed in Phase I of the instrument construction project. The NIR channel (with a 256 × 256 InSb array) and an MIR Fabry–Perot etalon are to be added during Phase II, which is currently underway. More detail of the instrument construction and capabilities are provided by Böker et al. (1997). Work is currently in progress to improve the system efficiency and on-line data reduction procedures, as well as the major upgrades provided by the Phase II plan for this instrument. The Phase II upgrades to MANIAC are a joint undertaking between the MPE, UNSW, ADFA and Southern Cross University.

At the ESO 2.2–m telescope the instrument pixel size is 0.″345 with a 44″ clear field of view. Currently the instrument provides an *N*–band sensitivity of $1\sigma \simeq 2.5$ mJy arcsec^{-2} hr^{-1} on the 2.2–m telescope. At this telescope we experienced quite large chopping offsets and structure in the image that could only be removed by beamswitching. The exact cause of this chopping structure was not determined, but we attribute it to the fact that the secondary on the 2.2–m telescope is barely undersized, and with the 60″ or larger chops required with the field of view of MANIAC it is possible that we were chopping close to the edge of the primary mirror. Fortunately the beamswitch removed this structure to less than 1 per cent.

In MANIAC, each of the various filters appears not to be exactly parallel in the filter wheel, which introduces small spatial offsets (1–2″) when changing to different filters. The offset is quite stable, however, and is determined by

comparing the position on the array of a standard star in the various filters. These offsets are included when image registration and overlaying are used.

The observations were made on the nights 1996 October 30 & 31 and November 1. Throughout these nights the visible seeing was between 0.″3 and 0.″65, and well below the diffraction limit of 0.″96 at 10 μm and 1.″9 at 20 μm. The images of standard stars showed clearly diffraction limited structure, i.e. Airy rings, at all wavelengths used.

In addition to the image data we have spectroscopic observations of RCW 38 between 8–13 μm obtained using the UCL cooled grating spectrometer at the 3.9–m Anglo-Australian Telescope (AAT) on 1984 May 12. A description of the UCL spectrometer and observing procedures is presented by Aitken et al. (1985).

A.3. Results & Analysis

A.3.1. Broad band images

Fig. A.1 shows the *N*–band (8–13 μm) and *Q*–band (17.3–22.7 μm) images. The images were centred on the position quoted for IRS1 by FP74, but the absolute pointing is uncertain. *N*–band images were obtained on all three nights and Fig. A.1 is the sum of these images. It represents 680 seconds of integration including the chop and beamswitch overheads. The *Q*–band image was obtained on October 30 only, and represents 480 seconds integration (including chop/nod). Both images were obtained using a 60″north–south chop/nod. Flux calibration was made with respect to η Sgr, which was taken to have a flux of 196 Jy at *N* and 73.3 Jy at *Q*. The original images significantly oversample the diffraction limit (0.″345 pixel^{-1} and $\sim$ 1″ & 2″ diffraction FWHM at 10 & 20 μm, respectively), so the images in Fig. A.1 have been smoothed back to their respective diffraction limits with a Gaussian smoothing function.

Both the *N*– and *Q*–band images show similar extended emission in a ridge-

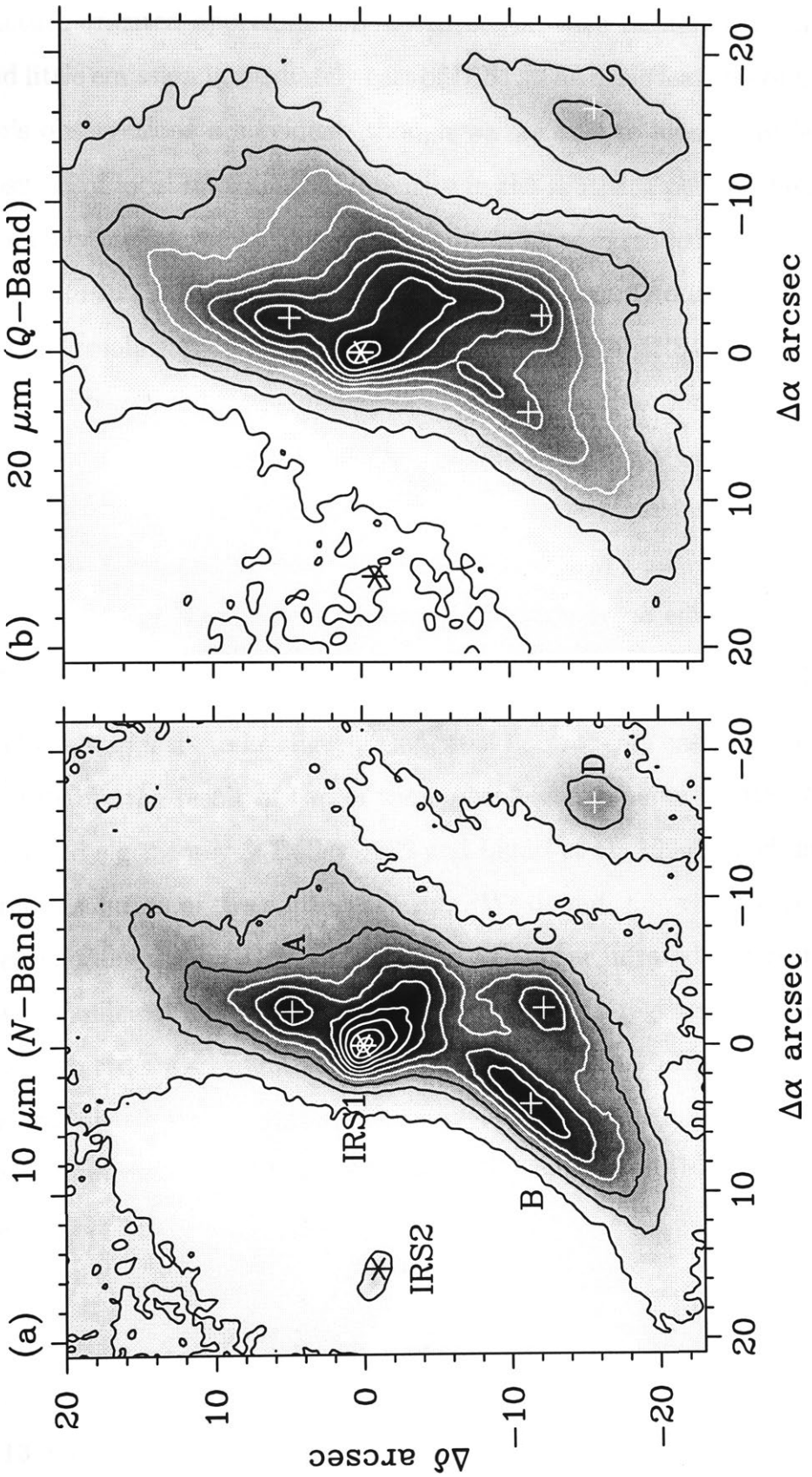

Figure A.1.— N– and Q–band image of RCW 38. Offsets are in arcsec from the peak of IRS1 which is labelled with an asterix, as is IRS2 $\sim 15\farcs5$ E of IRS1. Also labelled A–D are four 10 μm emission peaks, which will be referred to in subsequent figures. Contours superimposed on the images are 5, 15, 25, ..., 95 per cent of the peak of 1.44 Jy arcsec^{-2} (N–band) and 7.5 Jy arcsec^{-2} (Q–band).

like structure oriented approximately north–south, with fainter emission $\sim 20''$ west, and little emission immediately east of IRS1. The basic features of Epchtein & Turon's observations are evident, though we are able to identify at least one more position of local maximum of intensity in the southern part of the ridge at 10 μm, namely our source C. The ridge is a little more extended, or less peaked, at 20 μm than in the 10 μm image though it is important to keep in mind the lower spatial resolution of the 20 μm image. The peak of IRS1 in both the *N*– and *Q*–band images coincides to less than the 10 μm diffraction limit. We have tentatively identified the compact peak of emission $\sim 15''$ east of IRS1 with the bright NIR source IRS2. FP74's map suggests a separation between IRS1 and 2 of $\lesssim 10''$, but their spatial resolution was low and their positions are probably only good to $\pm 5''$ at best. There appears to be little or no emission from dust in the region immediately surrounding IRS2, a point we will come back to later.

IRS2 itself appears to be slightly elongated in a roughly east-west direction. This is probably the result of two of the multiple components of IRS2 (as seen in the *K* band e.g. Storey & Bailey 1982 and Ligori et al. 1994) which merge at the spatial resolution of these measurements. We do not, however, detect any of the other components of IRS2. Unfortunately the near infrared observations do not provide sufficient spatial information to allow us to register them with our images and so a detailed comparison of the mid– and near–infrared morphology and spectral distribution is impossible. However, such a comparison is one of the design requirements for MANIAC, and will become possible after a further upgrade.

A.3.2. 8–13 μm spectroscopy

The 8–13 μm spectrum is presented in Fig. A.2. This spectrum amounts to 26 minutes of integration, chop/nod included, and was made in a $4''.2$ circular aperture. A $60''$ north–south chop/nod was employed. The observation is centred on the 10 μm emission peak, which corresponds to the source labelled IRS1 by FP74. Flux calibration and correction for telluric absorption features are made

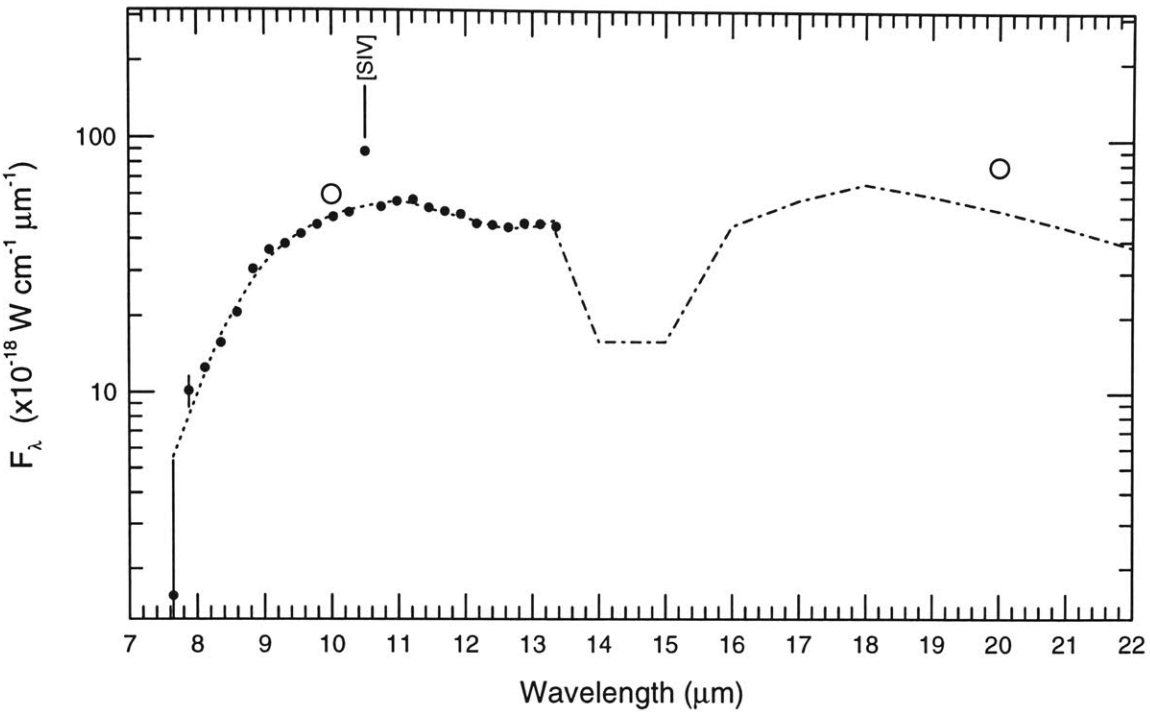

Figure A.2.— 8–13 μm spectrum of RCW 38 IRS1, obtained with the UCL spectrometer at the AAT. Filled circles show the observed spectroscopic data, and for all but a few points the error bars are smaller than the plotted point. The strong S IV emission feature is labelled and the dashed line shows a fit to the continuum spectrum as discussed in section A.3.2. The open circles show the *N*- and *Q*-band fluxes (from Fig. A.1) determined for a 4.″2 aperture centred on IRS1. The dot-dash line in the 13–22 μm region shows the extended fit using the dust temperature and absorptive optical depth determined from the 8–13 μm fit. The extended fitting is discussed in section A.3.4.

by reference to the standard star γ Cru with a flux at 10 μm of 4.5×10^{-15} W cm^{-2} μm^{-1}. The spectral resolution employed was R = 40, or 0.238 μm per resolving element.

The spectroscopic observation of RCW 38 was made as part of a polarimetric study of this source, and as a result of the long integrations required, the S/N ratio for the spectroscopic data is excellent at around 250 per point. In Fig. A.2 the error bars are only larger than the plotted point in a few cases at the very edge of the atmospheric window. The high S/N allows for fairly tight constraints to be placed on some of the dust parameters. The polarimetric data will be presented in detail elsewhere, but these observations show polarized emission at about the 2–3 per cent level with a position angle of 138°, as well as some evidence for a small absorptive polarization component with a position angle

of 75°. Accepting standard Davis–Greenstein type grain alignment theory, the polarimetry therefore indicates a magnetic field direction of between 48°and 75°, which is nearly normal to the elongated ridge in which IRS1 lies. Conversely the interstellar magnetic field direction, determined from optical polarimetry of field stars, lies at 170°(e.g. Axon & Ellis 1976, Klare & Neckel 1979), almost orthogonal to the MIR magnetic field and closely parallel to the dust ridge. The implications of this will be explored in a forthcoming paper, together with imaging polarimetry observations.

The rising spectral energy distribution (SED) indicates emission from relatively cool dust, plus the notable feature of the strong S IV fine structure emission line at 10.52 μm. We measure the S IV intensity as 8.2±0.5 × 10^{-18} W cm^{-2} in a 4.″2 aperture. On close examination of the spectrum the Ar III line at 8.99 μm is detected, though split over two detectors, with a line intensity of 1.3±0.4 × 10^{-18} W cm^{-2} and the Ne II line at 12.81 μm is also weakly present with a line intensity of 4±1 × 10^{-19} W cm^{-2}, both in a 4.″2 aperture. These line strengths are observed values and have not been corrected for extinction.

Emission line modelling

The presence of strong emission from S IV and only weak emission from Ne II and Ar III indicates a relatively strong ionizing radiation flux with an abundance of photons above the S III ionization potential of 34.83 eV (Genzel 1992). The ionization potential for Ne II is 40.96 eV and for Ar III it is 40.74 eV, and presumably most of the Ne and Ar has been ionized to the higher states, Ne III and Ar IV indicating a strong flux of photons with energies greater than 41 eV. On the other hand, the evident abundance of the S IV state (ionization potential = 47.3 eV) as indicated by the strong emission line, shows that photons with energies greater than 47.3 eV can not be so plentiful or these ions too would be ionized to the next higher state S V. Whilst we admittedly have no information on the abundances of the higher ionisation levels, we feel that the combination of weak Ne II and Ar III emission but strong S IV emission serve to constrain the bulk of the ionizing photons to the range 40.7–47.3 eV at the distance of IRS1.

To provide the required ionizing flux we estimate that a star with effective temperature $T_{\rm eff}$ of at least 40 000 K is needed. This rough estimate is made by simply comparing our observed line ratios in RCW 38 to those observed by other authors in different H II regions, and for which a $T_{\rm eff}$ was inferred (e.g. Rank et al. 1978 for G333.6–0.2 and G298.2–0.3; Lester, Dinerstein and Rank 1979 for K3-50A; Lacy, Beck and Geballe 1982 for G298.2–0.3, RCW57 and G29.9–0.0; Simpson and Rubin 1984 for G45.1+0.1 and G29.9–0.0; Colgan et al. 1991 for G45.1+0.1 and K3-50A). Compared to all these sources, RCW 38 has the highest observed S IV/Ar III and S IV/Ne II ratios. This estimate is consistent with near–infrared (FP74) and far–infrared (Furniss, Jennings & Moorwood, 1975) measurements which suggest a late O star or cluster of later type stars to be the exciting source. Similarly, the He I (λ = 2.06 μm)/Brγ ratio, which is often used as a constraint on massive star formation (e.g. Doyon, Puxley & Joseph 1992) is observed to be quite high in RCW 38 at 0.65 (Mizutani et al. 1987) which also suggests a minimum effective stellar temperature around 40 000 K.

Even though we have very limited information, with only two observed line ratios, in an attempt to confirm our arguments above and to perhaps investigate more fully the physics of RCW 38, we have used the CLOUDY photoionization code (version 90.03, Ferland 1993) to model our data. As input to the code we have used spectral energy distributions from photospheric LTE model atmospheres by Kurucz (1994) and non–LTE calculations by Pauldrach (1997). This allows us to investigate the affect of the adopted stellar SED shape. Assuming that IRS2 represents the exciting star(s) of the H II region, from our images we were able to constrain the inner radius of the ionized region to be around 0.12 pc, which is in fact the separation between IRS1 and IRS2. Whilst this is a projection of the real separation onto the plane of the sky, given that we interpret the ridge as part of a region forming an elliptical shell around IRS2 we believe that the actual value is very close to this.

With little *a priori* information on elemental abundances we assumed that they were all solar. There is however some justification for this assumption. For

instance, in a study of RCW 38 using far–infrared transitions of O III in a $2' \times 2'$ beam Takami et al. (1987) infer an oxygen abundance very close to solar. Whilst this does not necessarily imply that this is also the case for Ar, S and Ne, we also note that RCW 38 has a similar galactocentric distance as the Sun, so that it should not be subject to the radial abundance gradients known to exist within the Galaxy (e.g. Simpson et al. 1995). Since our images indicate the existence of dust in the ionised region we included dust in our models. The grains were of the Orion type as defined in Baldwin et al. (1991). The dust–to–gas ratio was such that 0.33% of the mass is contained in graphites and 0.52% in silicates (implying a gas–to–dust mass ratio of slightly more than 100). When comparing the model output to our observations we used extinction corrected line ratios. The correction was performed using an A_V of 10 mag (FP74), a Draine & Lee (1984) extinction law, and a screen–type geometry. Finally, the nebular hydrogen density and stellar luminosity were treated as free parameters in the models, the former being assumed constant within any one model.

Using the Kurucz SEDs we were able to fit both the extinction corrected S IV/Ar III and S IV/Ne II ratios with an effective temperature, $T_{\rm eff}$, of about 46 000±2000 K and density of $10^{4.0\pm0.1}$ cm^{-3} (which is in agreement with measured electron density estimates, e.g. Mizutani et al. 1987, Takami et al. 1987), essentially independent of the presence of dust. Including dust does however bring the line fluxes themselves a bit closer to the observed values, within a factor of a few. The uncertainties indicate the ranges in each quantity observed when sampling the line ratios at either the inner or outer face of the model cloud. For instance, at the inner face a $T_{\rm eff}$ of around 44 000 K is required, whereas at the outer face about 48 000 K is better. Lower density models, down to 10^2 cm^{-3}, and higher density models, up to $10^{5.5}$ cm^{-3}, provide progressively worse matches to the data. Our derived $T_{\rm eff}$ implies a single ZAMS star of spectral type between O5.5 and O4.5 as the ionizing source (Panagia 1973; Lang 1992; Hanson, Howarth & Conti 1997). Whilst we cannot exclude that a cluster of several lower $T_{\rm eff}$ stars could also provide a suitable match, the calculated ratios are very sensitive to the temperature and bolometric luminosity and $T_{\rm eff}$ could

only be lowered by about 1000 K for either face. The suggestion of Mizutani et al. (1987) of three O6 ZAMS stars ($T_{\rm eff} \sim 41\ 000$ K) is not consistent with our data. Indeed, between about 10 and 100 such stars would be required to fit just one of the ratios. However, their suggestion of a single O5 star plus a cluster of embedded stars is clearly not ruled out. Additionally, in $L_{\rm bol}$–$T_{\rm eff}$ space the solutions for our observed line ratios begin to diverge beyond the locus of ZAMS stars, i.e. with higher $L_{\rm bol}$ and lower $T_{\rm eff}$, so that an ionizing star above the main sequence is also inconsistent with our data. In anticipation of our model in section A.4.2 for the heating of the dust in RCW 38 we also ran a dust–free model, and found results in agreement with those above.

If instead the Pauldrach SEDs are used the extinction corrected line ratios can again be matched nicely, with the corresponding $T_{\rm eff}$ being in the range 45 000±2000 K and density again $10^{4.0\pm0.1}$ cm^{-3}. Obviously the implied spectral type of the ionising star is again between O4.5 and O5.5. In this case the solutions are not quite as sensitive to the temperature and bolometric luminosity, and at the inner face a model of three O6 ZAMS stars appears viable.

Unfortunately there is little other published information on fine structure line measurements of RCW 38 made in a similar beam size to ours, with which we might further constrain densities (e.g. electron density using lines from the same element and ionisation stage) and the exciting source and/or abundances (e.g. using lines from the same element but different ionisation stages). From optical observations in a $17'' \times 34''$ beam of S II and O II Danziger (1974) infers an electron density of 4×10^3 cm^{-3}, and Mizutani et al. (1987) derive 6×10^3 cm^{-3} from Brγ imaging, whilst Takami et al. (1987) infer an electron density of 10^4 cm^{-3} for their single component model, and 5×10^4 cm^{-3} clumps embedded in 150 cm^{-3} ambient gas for their two-component model. Our derived spectral type of the ionising star is similar to that inferred by other authors for RCW 38, as noted above and in our Introduction.

It is worth noting the similar $T_{\rm eff}$ results obtained for the Kurucz and Pauldrach model SEDs. Given that the Kurucz SEDs are calculated in LTE, and the Pauldrach SEDs include stellar winds and are non–LTE, the similarity is

striking. The implication may be that the most important physics is already contained within the LTE models. Further testing on different sources, with a larger line set and where other parameters such as the nebular density and inner radius are already constrained, would be advantageuous in determining whether observations of the type presented here can be used to test further developments in stellar atmosphere models.

To summarise, the best match between the model calculations and the observations, for both the Kurucz and Pauldrach SEDs, was for an inner radius of 0.12 pc, effective temperature of 43 000 to 48 000 K and hydrogen density of 10^4 cm^{-3}. Since we have set the inner radius of the model HII region to be the IRS1–IRS2 separation, and our spectral observations are centred on IRS1, we favour a $T_{\rm eff}$ at the low end of the quoted range, i.e. between 43 000 and 44 000 K, implying a spectral type of O5.5 V or O5 V.

Continuum emission modelling

Fitting the RCW 38 IRS1 SED to an optically thick black–body or optically thin silicate–like emissivity alone provides relatively poor fits to the spectrum (χ^2/n $\simeq$ 50). However a simple two component model fit with underlying optically thin silicate emission plus some silicate absorption by cold grains provides quite a good fit (χ^2/n $\simeq$ 2.6). The silicate dust emissivity function used in this case is derived from the deep absorption feature in W3 IRS 5 (Wright 1994). This emissivity function is similar to that for the Trapezium in Orion, but provides better fits to silicate emission/absorption from molecular cloud sources. The temperatures derived for the silicate dust from this fit are 175±6 K which is suffering a modest 0.56±0.03 optical depth at 9.7 μm from cold silicate dust absorption. Assuming an extinction ratio $A_{\rm V}/\tau_{9.7\mu{\rm m}}$ = 18.5 (Roche & Aitken 1984) we estimate the visual extinction towards IRS1 to be A_V = 10.4, which is in excellent agreement with the extinction of A_V = 10.7 over the extent of the H II region estimated by FP74. The resultant fit to the data is shown as a dashed line in Fig. A.2.

A.3.3. S IV image

On 1996 November 1 we obtained an image of RCW 38 in the S IV 10.52 μm fine structure line using a narrow band filter centered on 10.52 μm ($\Delta\lambda = 0.124$ μm) with MANIAC. The continuum is subtracted from the emission line using the *N*-band continuum image scaled to the continuum level at 10.5 μm. The scaling information is obtained from the spectroscopic data of Fig. A.2. Fluxes from corresponding 4.″2 apertures on the S IV and *N*–band images are scaled to those of the spectra in the line and continuum at 10.5 μm. This continuum subtraction technique relies upon the fact that the *N*–band image provides a reasonable representation of the 10.5 μm continuum, and that there are no extreme temperature or extinction variations across the image. The temperature map presented in section A.4.1 suggests that this assumption is reasonable at least for the regions of sufficient signal–to–noise (S/N) to be of interest. Three images are presented in Fig. A.3, the raw line plus continuum image, the *N*–band continuum used for subtraction and the continuum subtracted S IV image.

The S IV and dust thermal emission distributions are broadly similar, possibly indicating that the gas and dust are well mixed in the ionised zone of RCW 38. However, on closer inspection the two images do differ in their fine structure. For instance, the S IV image shows a very clear peak of 1.1×10^{-18} W cm^{-2} μm^{-1} arcsec^{-2} at a position $\Delta\alpha \simeq -2.''0$, $\Delta\delta \simeq +4.''0$ from IRS1 (near source A), and a second major peak of equal magnitude at a position $\Delta\alpha \simeq +2.''0$, $\Delta\delta \simeq -9.''0$. It is interesting to note that neither S IV peak coincides with a continuum peak in the ridge. Also the continuum peak D to the south-west corner does not show as a significant S IV peak, which is probably due to geometrical dilution and absorption of the photons capable of ionising sulfur to the S IV state.

Because the S IV image is unusual (e.g. IRS1 and the S IV peak are not coincident) great care was taken in registering the line and continuum images before subtraction. This was achieved by registering on the compact source IRS2 which was clearly present in both images. The registration is considered to be better than 1 pixel (0.″345). After the continuum subtraction, IRS2 was still

present in the S IV image so the positions of IRS2 and IRS1 in the line image are well defined. IRS2 was present though faint in the line image, but after smoothing (using a gaussian with FWHM $\sim$ 0.″8) it does not appear very clearly in the presented line image of Fig. A.3. The differences in the line and continuum images can actually be seen in the un–subtracted image of Fig. A.3, so the offset between the northern S IV peak and the continuum peak IRS1, for example, can not be an artifact of the continuum subtraction process.

A.3.4. 10/20 μm dust temperature map

From the spectroscopic data in section A.3.2 it is clear that the spectrum for RCW 38 shows evidence for emission and absorption from silicate–like dust grains. This means that to use the *N*– and *Q*–band images to produce a simple black-body colour temperature map would produce misleading results. The presence of the silicate absorptive and emissive components needs to be accounted for before a useful dust temperature map can be produced. Unfortunately we do not have any 20 μm spectroscopic data, nor is there any to be found in the literature or *IRAS* LRS catalogue.

We do not know the temperature of the absorptive material at 10 μm, but it is unlikely that this material would produce significant emission at 20 μm, so we have assumed that a proportional amount of absorption will occur at 20 μm. If we assume that the extinction is constant across the image then it is still possible to extract a reasonable dust temperature from *N*– and *Q*–band images. Although we do not have any 10 or 20 μm spatially resolved spectroscopic data to confirm this assumption, the 2.2 μm images of Allen & Meadows (1992) and Storey & Bailey (1982) do not show any significant variations that might be attributed to variable extinction across the image. Additionally, FP74 infer a similar amount of extinction towards IRS2 ($A_V \simeq 12.8$) as we find towards IRS1 ($A_V \simeq 10.4$), indicating that the extinction in this region is relatively constant.

To derive the dust temperature across the image, we first need to determine if the simple two component (single warm dust temperature) model is capable

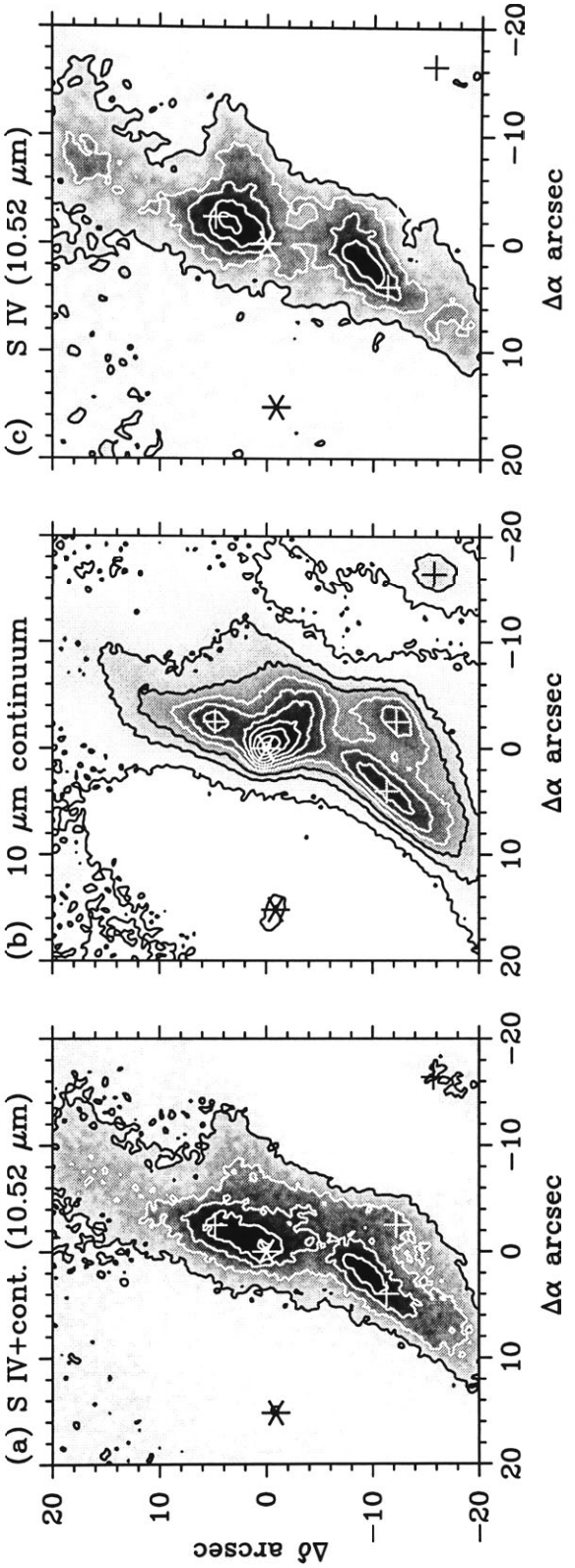

Figure A.3.— S IV image of RCW 38. From left to right the images are (a) the raw line plus continuum image (un–subtracted), (b) the N–band continuum used for subtraction and (c) the continuum subtracted S IV line image. Offsets are in arcsec from the peak of IRS1 in the N–band image. The positions of IRS1 and IRS2 are indicated with asterix (Fig. A.1), and the features A–D (Fig. A.1) are indicated with crosses. Contours superimposed on the images are 15, 35, ..., 95 per cent of the peak of 1.09×10^{-18} W cm^{-2} arcsec^{-2} (S IV image) and 5, 15, ..., 95 per cent of 1.44 Jy arcsec^{-2} (10 μm image).

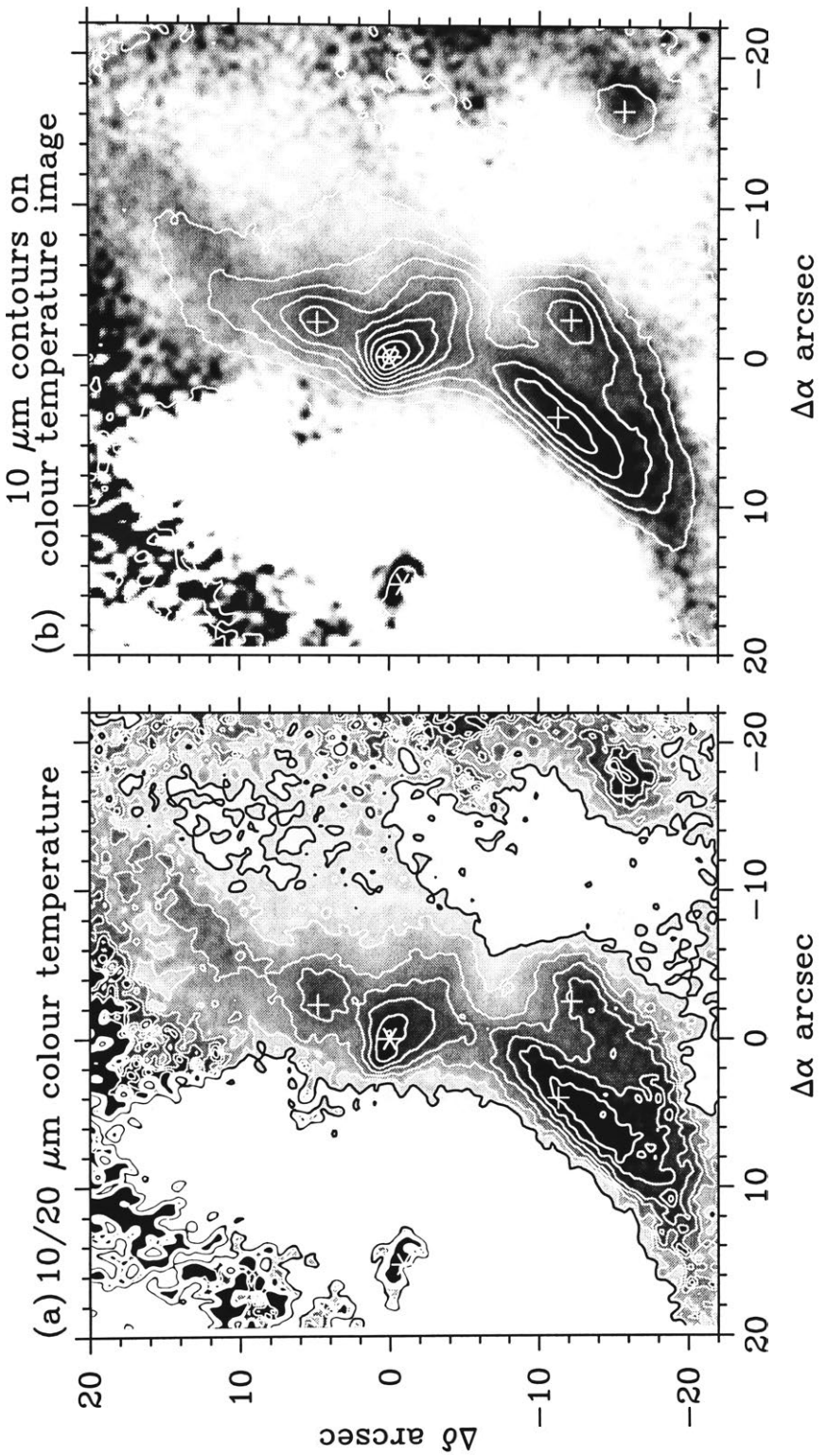

Figure A.4.— 10/20 μm colour temperature image of RCW 38. Offsets are in arcsec from the peak of IRS1 in the N–band image. In (a) we present the colour temperature image, while in (b) we present the same image with the 10 μm contours overlaid. The positions of IRS1 and IRS2 are indicated with asterix (Fig. A.1), and the features A–D (Fig. A.1) are indicated with crosses. The contour around the position of IRS1 is 170 K, and contours decrease in 5 K increments to the bottom contour of 145 K (shown in black). The maximum temperature contour around the peak to the south–east of IRS1 is 175 K. The 10 μm contour levels are the same as those in Fig. A.1.

of being extended to the 20 μm region. If not, a second cooler dust component may be needed, in which case it is impossible to extract any useful information from the limited amount of spectral information (i.e. 2 data points) in the two images. We have already assumed the extinction to be constant, and to make another assumption about a second cool dust component would be stretching the data beyond credibility.

If we extend the two component (single dust emission temperature) fit from section A.3.2 to longer wavelengths we obtain a prediction of the 20 μm flux that would result from a 4.″2 aperture around IRS1. We can then compare the fluxes obtained from the *N*– and *Q*–band images with those of the model. We have extended the silicate emissivity function beyond 13 μm in 1 μm steps out to 24 μm. As we do not have observed spectroscopic data for W3 IRS5 in the 20 μm window we have used emissivity data derived from the work of Scott & Duley (1997). This data is similar (though not identical) to other derived silicate emissivities (e.g. Draine & Lee 1984), but fortunately the shape of the silicate resonance in the 20 μm region is not so acutely dependent on the grain parameters as the 10 μm region. This extended model fit is included in Fig. A.2, and is shown by a dashed–dot line joining the 8–13 μm fit (short dashed line) at 13.5 μm. The model is defined by the equation

$$F_\lambda = \Omega\, \epsilon_\lambda\, B(\lambda, T)\, \mathrm{e}^{(-\tau_{9.7\mu\mathrm{m}}\, \epsilon_\lambda)} \qquad \text{(A1)}$$

where F_λ is the calculated flux, Ω is a parameter that normalises the derived flux to the observed flux at 10 μm, ϵ_λ is the silicate emissivity function, $B(\lambda, T)$ is the Planck function at dust temperature T, and $\tau_{9.7\mu\mathrm{m}}$ is the absorption optical depth at the peak of the silicate resonance. This model is not different from earlier simple two component fits (e.g. Aitken & Jones 1973, Gillett et al. 1975) but as it is to be used as the basis of the derived temperature map from the *N*– and *Q*–band images it is re–stated explicitly here.

From this model we obtain 10 and 20 μm broad band fluxes (i.e. integrating over the respective band) of 233 and 430 $\times$ 10^{-18} W cm^{-2} respectively. Equivalent fluxes extracted from a 4.″2 aperture centred on IRS1 from the *N*– and *Q*–band images provide fluxes of around 300 and 540 $\times$ 10^{-18} W cm^{-2} re-

spectively. Clearly there is a calibration difference between the two data sets of about 25 per cent, but it is the ratio between the 10 and 20 μm data that is important in the determination of the temperature. The absolute calibration of disparate data sets is always difficult without very careful photometric monitoring throughout a night, and we would rarely claim absolute calibration better than this 25 per cent difference anyway. The ratio of model data $F_{20\mu m}/F_{10\mu m}$ is 1.85 and from the broad band images it is about 1.8 which provides remarkably good agreement. We believe that this validates the simple two component model for use in the 20 μm window in this particular source.

Using a modified colour temperature (as described above) that takes account of the presence of silicate grains, we can derive a dust temperature for each common point in the *N*– and *Q*–band images, and Fig. A.4 shows the dust temperature map derived in this way. To ensure that the different spatial resolution in the *N*– and *Q*–band images does not produce spurious features the *N*–band image was smoothed to the *Q*–band diffraction limit before the colour temperature map was constructed. It should be remembered too, that we have made the assumption that the silicate extinction is the same over the whole image and that the chemical composition of the dust also remains more or less constant. For these reasons, plus the fact that a distribution of grain sizes might be expected, each of which perhaps attains a different equilibrium temperature, our temperature image is most useful for determining spatial trends in the dust temperature, rather than absolute values.

From Fig. A.4 we see that the temperature is highest in the centre of the ridge–like emitting region, and drops off rapidly to both the east and west. We do not attribute any significance to the high temperatures to the far north or far west of the map (except for source D at $\Delta\alpha \simeq -18'', \Delta\delta \simeq -16''$) as the S/N ratio in these regions of the *N*– and *Q*–band images is not sufficient to determine reliable temperatures.

In the region around IRS1 there is a reasonable temperature peak, with the peak contour of 170 K. There is also a slightly stronger dust temperature peak some 15″ to the south-east of IRS1. This temperature peak corresponds to

intensity peak B in the N–band image. Although it is only about 60 per cent as bright as IRS1, the temperature here is about 175–180 K compared with 170–175 K at IRS1. IRS2 appears as a hot source (> 200 K) about 15″ east of IRS1.

A.3.5. Dust opacity and mass

Having determined the dust temperature in the previous section it is now possible to calculate the emissive opacity and mass of the dust. Before doing so however, it is prudent to recognise the limitations of this calculation. In particular we assume that the previously calculated temperature represents a single and uniform grain temperature along the whole line of sight. Panagia (1975) and Natta and Panagia (1976) have presented criticisms of this assumption, which they say leads to an underestimate of the dust mass. As noted above, a distribution of temperatures might be expected on the basis of a distribution of grain sizes and/or compositions. Therefore, once again our opacity image is most useful in showing spatial trends. Nevertheless, with the above approximation in mind, we can at least obtain an estimate of the dust opacity, and so also the dust mass. Using the temperature distribution as determined previously and the observed flux from the N–band image we have determined the opacity distribution, using the following equation

$$\tau_{em,N} = F_N / B(N,T) \qquad \text{(A2)}$$

where $\tau_{em,N}$ is the emissive opacity in the N–band, F_N is the observed N–band flux and $B(N,T)$ is the blackbody flux at the derived colour temperature.

In section A.3.2 we noted that the spectrum of IRS1 shows an absorptive optical depth of $\tau_{9.7\mu\mathrm{m}} = 0.56$, which is attributed to a layer of cold silicate grains in front of the RCW 38 region. The 9.7 μm optical depth represents the peak of the absorption, but using the same silicate emissivity function as section A.3.2 we find that the average emissivity over the N-band is 0.61 of the peak 9.7 μm emissivity (ie. $\tau_{N-\mathrm{band}} = 0.61\tau_{9.7\mu\mathrm{m}}$). So to account for the absorbing material we de–redden the N–band fluxes by $e^{0.34}$. Given this correction the opacity distribution is presented in Fig A.5.

First it should be pointed out that the chain of high opacity points around the inner rim of the IRS1 ridge are undoubtedly an artifact caused by poorly determined temperatures in these regions of low signal to noise. Also the opacity image has been smoothed using a Gaussian smooth function with FWHM = 3 pixels. In the regions where the signal to noise in the original data is high, and where the dust temperatures are well determined (i.e. in the ridge) the opacities are also reasonably determined. We see in the opacity map that IRS1 does not appear as a significant peak, implying that this region is not simply a dust density enhancement. In fact the higher opacities occur on the outer edge of the ridge, i.e. away from IRS2. Apparently the bulk of the material is concentrated in the region away from the area of the most intense emission.

Given the opacities, it is also possible to determine a total dust mass. To achieve this we assume that all the grains are silicate, and use the silicate dust mass absorption coefficient (κ = 3000 cm^2 g^{-1} at 9.7 μm) from Draine (1985) and the distance d to the source of 1.7 kpc. We then determine a dust mass for each pixel using the following equation

$$M_{dust} = \tau_{em,N}\, d^2/\kappa \quad . \tag{A3}$$

Integrating over the ridge, an area of 350 square arcseconds, we obtain a total dust mass in the ridge of around 5.7 $\times$ 10^{-4} M$_\odot$. If we take a normal gas to dust ratio value of around 100:1 we find a total mass in the ridge of around 0.057 M$_\odot$ of gas and dust. However, as noted in section A.4.2, dust may be depleted in the region surrounding IRS2, and so this mass estimate may represent a lower limit to the true mass of the ridge.

A.4. Discussion

A.4.1. A wind blown cavity around IRS2

The region around IRS2 contains very little thermal emission, and almost no S IV emission, despite the proximity of the ionizing source, indicating that this space

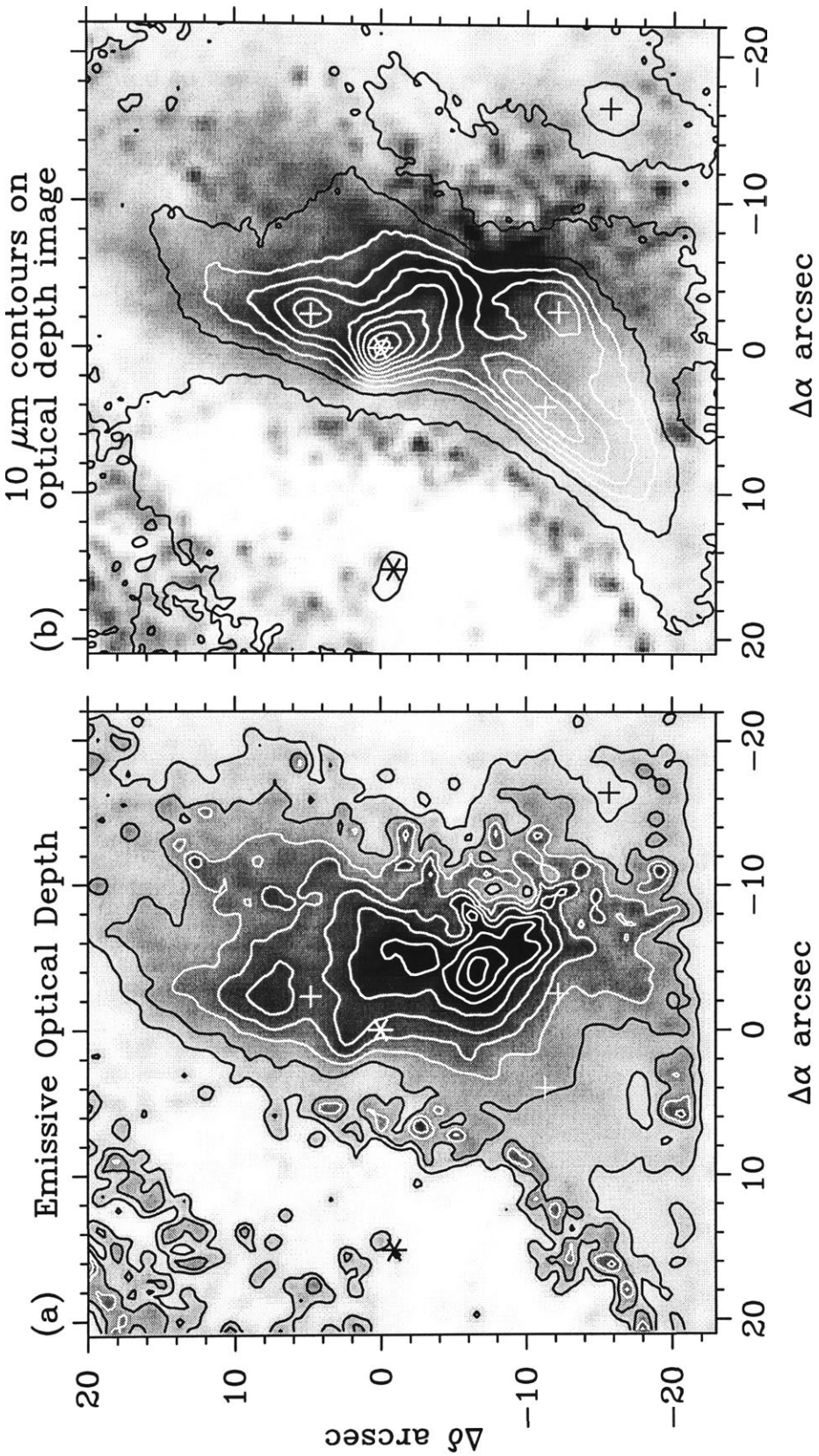

Figure A.5.— The emissive opacity distribution for RCW 38. Offsets are in arcsec from the peak of IRS1 in the N–band image. In (a) we present the emissive opacity image, while in (b) we present the same image with the 10 μm contours overlaid. The positions of IRS1 and IRS2 are indicated with asterix (Fig. A.1), and the features A–D (Fig. A.1) are indicated with crosses. The contours are 5, 15, ..., 95 per cent of the peak of 0.038 in the opacity image, and 1.44 Jy arcsec^{-2} in the N–band image.

is basically clear of dust and gas. From the 2.2 μm images we know that IRS2 is a hot source located to the east of IRS1. We propose that IRS2 is the powering source for the region and that the region around IRS2 represents a cavity blown out by the stellar wind of the young, hot star (or stars) inside IRS2. The ridge of emission around IRS1 shows the edge of the cleared cavity which has a higher density of material, and in fact represents the outer shell.

At the distance of RCW 38, the 15″ between IRS1 and IRS2 represents only 0.12 parsecs (projected on the sky). Now the terminal wind velocity of an O5 star is around 3000 $\mathrm{km\,s^{-1}}$ (e.g. Lamers, Snow & Lindholme 1995) and so a completely clear cavity between IRS1 and IRS2 could be crossed in just 39 years by the wind. The normal mass loss rate for this type of star is around 1×10^{-6} $\mathrm{M_\odot\ yr^{-1}}$ and could contribute at best a few percent of the observed mass in the ridge in the evolutionary timescales of this region. More likely the ridge of material around IRS1 results from preexisting dust and gas form the H II region being swept up by the wind into a shell.

If we assume an initial cloud density of 10^4 $\mathrm{cm^{-3}}$ (as implied by our emission line modelling), plus a mass loss rate and wind velocity as above, then by simple momentum transfer from the wind to the swept up region, we calculate a period of around 1.5×10^4 yr to sweep out the cavity to the outer radius of the IRS1 ridge. At this point the outward velocity of the shell is about 6 $\mathrm{km\,s^{-1}}$, and if the wind sweeps all material into the shell then the shell itself will have a mass of about 7.8 $\mathrm{M_\odot}$ by the time it reaches the radius of IRS1. If we assume the IRS1 ridge covers about a quarter of the total shell surrounding IRS2 then we would expect about 2 $\mathrm{M_\odot}$ in the IRS1 ridge. This mass estimate is consistent with that determined from the opacities earlier. We note that our picture for the cavity clearing process is different to that traditionally inferred for the expansion of dusty H II regions, namely the high pressure of the ionised gas and radiation pressure on dust grains (e.g. Mathews 1969).

It is interesting at this stage to compare our data with models of expanding H II regions. The molecular observations mentioned in our Introduction presented a picture of high density gas ($> 10^4$ $\mathrm{cm^{-3}}$) surrounding the region imaged

by ourselves, which itself does not contain much dense gas. This is typical for the expansion of s Strömgren ionization front and is similar to the models of Bodenheimer, Tenorio–Tagle & Yorke (1979), where ionization and shock fronts produced by a massive new-born star propagate into the ambient molecular cloud.

On the other hand, we may be seeing only the inner zone of a much more extended region. FP74 found 10 μm emission extended over a much larger region than we have imaged, as did Mizutani et al. in the Brackett γ line of hydrogen, and both our *N*– and *Q*–band images show what could be a second cavity and ridge (source D) about 10–15″ west of the IRS1 ridge. Perhaps the shell creation is an episodic event, with incomplete clearing of the cavity with each event.

Finally, we note that the shell is not spherical around IRS2, but rather elliptical. For instance, note the emission in the north–east corner of our N–band image. It may be that the presumed outflow finds it easier to expand toward the north–west and south–east of IRS2 due to lower density material along these directions. On the other hand, magnetic fields may also influence the shape of the cavity. For instance, the major axis of the ellipse is closely aligned with the interstellar magnetic field, yet almost orthogonal to the field determined from our spectropolarimetric observations.

A.4.2. Heating of the dust in the IRS1 ridge

A remarkable feature of our colour temperature image in Fig. A.4 is the relative constancy of the temperature over a large area. The variation is only ±15 K from the "average" of 160 K. There is a hint that this constancy extends over an even larger area in the work of FP74. Whilst they do not present a colour temperature map, they do state that the [10 μm] – [20 μm] colour does not change by more than 0.3 mag of the face of RCW 38. What mechanism can produce such a constant temperature, even though regions of the source are at significantly different projected separations from the presumed exciting star IRS2?

Direct heating of dust

Direct heating of the dust by IRS2 is undoubtedly occurring at some level. We investigate the contribution of this heating by using a radiation transfer model to determine what dust temperature one would expect from direct heating of a dust shell at the distance of IRS1 (0.12 pc) away from a central hot source (IRS2).

The model used is based on the quasi–diffusion method, in spherical geometry, of Leung (1975, 1976), as implemented by Mitchell & Robinson (1978, 1980). While spherical symmetry may not be entirely appropriate to RCW 38, given the optically thin nature of the dust distribution and the fact that the model of Leung solves the radiative transfer problem in spherical symmetry without significant approximation, the results obtained for the dust temperature are likely to be reasonable.

In the model we have assumed that the illuminating source is IRS2, of spectral type O5.5V, with $T_{\rm eff} = 44\,000$ K and luminosity $L = 6 \times 10^5$ L$_\odot$. The inner and outer boundaries of the dust shell were assumed to be located at 0.09 and 0.214 pc from IRS2 respectively, and the dust density distribution has been assumed to follow a power law, $\rho = \rho_0 r^n$, where the index n was treated as a free parameter. However, since the shell is not very extended, ($R_{max}/R_{min} \sim 2.4$), the value of n is not critical. The optical depth has been varied from optically thin to optically thick ($\tau_{10\mu{\rm m}} = 0.001$ to 20) to investigate the opacity's effect on the dust temperature and temperature distribution. While an optical depth of around 0.5 was previously determined for IRS1, this is a different line of sight from that which a photon from IRS2 sees, and so the wide range of opacities is required to fully investigate the parameter space. Models with a single grain species have been used, with the grain species being pure astronomical silicates and astronomical silicates coated with a water ice mantle (see Robinson et al. 1992 for more details of the assumed opacity law for these grains). The grain radius has been varied within the range $a = 0.01 - 2.0$ μm.

The temperature of pure astronomical silicate grains as a function of radial

distance for various grain sizes is shown in Table A.1 for the case $n = -2$ and $\tau_{10\mu m} = 0.05$. It may be seen that as the grain size increases the temperature at the inner boundary of the dust shell decreases significantly, as expected. In general the presence of a pure water ice mantle makes little difference to the grain temperature at the inner boundary of the shell but reduces it somewhat within the shell itself, and of course it will affect the spectral energy distribution significantly.

Table A.1. Grain temperature as a function of radial distance from IRS2

Grain radius	T (K)		
(μm)	$r = 0.09$ pc	$r = 0.15$ pc	$r = 0.21$ pc
0.01	224	108	83
0.02	206	116	87
0.05	168	126	102
0.10	142	118	101
0.10, 0.20[1]	141	100	77
0.20	122	105	92
0.50	100	89	79
1.00	87	78	69
2.00	74	67	59

[1]Core–mantle grain with silicate core of radius 0.10 μm and water ice mantle of radius 0.20 μm.

From these results we derive two important points. Firstly the population of small grains, which dominate the number density, are too hot at the inner edge of the shell compared with the temperatures observed, and secondly direct heating of the dust predicts a significant temperature gradient (on the order of 50 K) from the inner to outer edges of the dust shell. In the temperature map (Fig. A.4) there is very little evidence for such a temperature gradient.

The observed temperature is quite uniform (though with some small variations) given that parts of the dust ridge are further from IRS2 by at least a factor of 2 than the inner edge of the shell. As noted above, this can be readily explained with models of Lyman α absorption dominating the heating. Whilst we cannot exclude direct stellar radiation from contributing to the dust heating, it definitely cannot dominate it.

Dust heating due to trapped Ly–α photons

The Strömgren radius for a pure hydrogen nebula surrounding an O5.5 star is only about 0.2 pc if the nebula density is on the order of 10^4 cm^{-3} (and neglecting an inner cavity). This means that most of the $\sim 10^{49}$ Lyman–α producing photons per second from IRS2 are resonantly trapped within this volume, and ultimately are absorbed by dust grains. This can lead to a powerful heating mechanism for the dust in the IRS1 ridge, which lies within the Lyman-α trapping zone. Indeed, a hint that this may in fact be the case is provided by FP74. They find that the 1–25 μm luminosity is comparable to that of the Lyman α photons that are resonantly trapped within the ionised volume. Additionally, the inferred luminosity of IRS2 is consistent with that expected from a main sequence star whose ultraviolet output beyond the Lyman limit is not significantly different from that required to supply the observed radio flux, implying that the dust does not compete effectively with the gas for the primary ionising photons. Indeed, in our photoionization models we found that with a normal gas-to-dust ratio of 100 the 40% of the Lyman continuum photons are absorbed by the dust, which is inconsistent with the inferred Lyman continuum and observed ratio fluxes being equal. However, with a gas-to-dust ratio of 10^4 or higher, there is essentially no effective absorption of Lyman continuum photons by dust. FP74 infer that absorption by trapped Lyman α photons is the primary heating mechanism of the dust. We then use this as a working hypothesis and examine under what physical conditions the dust can be heated to the temperatures we observe.

We can estimate the heating effect of the Ly–α photons if we equate the

heating rate due to the Ly–α photons, $G_{L\alpha}$, with the cooling rate of the dust, $L_r(T_{\rm d})$, and then solve for the dust temperature, $T_{\rm d}$. We assume here that the energy radiated by the grain is essentially the same as that in thermodynamic equilibrium at temperature $T_{\rm d}$. Following the treatment of Spitzer (1978) we find that the dust heating due to Ly–α photons is given by:

$$G_{L\alpha} = Q_{L\alpha} F_{L\alpha} E_{L\alpha} \tag{A4}$$

where $Q_{L\alpha}$ is the dust grain efficiency factor for absorption of Ly–α photons, $F_{L\alpha}$ is the flux of Ly–α photons crossing the surface of a grain per unit projected area per second and $E_{L\alpha}$ is the energy of the Ly-α photon. The Ly–α flux is given by:

$$F_{L\alpha} = \frac{z_{L\alpha} n_{\rm e} n_{\rm p} \alpha^{(2)}}{\sigma_{\rm d} n_{\rm d} Q_{L\alpha}} \tag{A5}$$

where $z_{L\alpha}$ is the fraction of recombinations in levels $n \geq 2$ that lead to emission of a Ly–α photon (which we take to be 0.68 as given by Spitzer, but it could be higher at the density of RCW 38), $n_{\rm e}$ and $n_{\rm p}$ are the electron and proton number densities respectively, $\alpha^{(2)}$ is the recombination coefficient, (here equal to 3.1 $\times$ 10^{-13} cm^3 s^{-1}, again from Spitzer), $\sigma_{\rm d}$ is the dust grain geometrical cross–section (i.e. $\pi\, a^2$) and n_d is the dust grain number density. We will assume $n_{\rm e} = n_{\rm p} = n_{\rm H}$. This then leads to an expression for the heating rate:

$$G_{L\alpha} = \frac{z_{L\alpha} n_{\rm H}^2 \alpha^{(2)} E_{L\alpha}}{\sigma_{\rm d} n_{\rm d}} \tag{A6}$$

Our modelling of the radiation field in RCW 38 has previously indicated a gas density of around $n_{\rm H} \simeq 10^4$ cm^{-3}, so it remains to determine the dust cross–section and number density in order to evaluate $G_{L\alpha}$.

We assume that the grains are all spherical and of the same size, say 0.1 μm in radius. We can therefore find the volume of a grain, and using the density of silicates as 3 g cm^{-3}, also the mass of a single grain. Assuming that the gas is composed mostly of hydrogen, with 10% by number of helium, we can then write

$$R\, m_{\rm d}\, n_{\rm d} \;=\; 1.4\, m_{\rm H}\, n_{\rm H} \tag{A7}$$

where R is the gas–to–dust mass ratio, and $m_{\rm d}$ and $m_{\rm H}$ are the mass of a dust grain and a hydrogen atom respectively. Therefore the Lyman alpha heating

rate can be expressed as

$$G_{L\alpha} = \frac{z_{L\alpha}\alpha^{(2)}E_{L\alpha}m_{\rm d}}{1.4\sigma_{\rm d}m_{\rm H}}\,R\,n_{\rm H} \tag{A8}$$

To determine the equilibrium dust temperature we equate the heating rate to the cooling rate, L_r, which can be expressed in the following equation

$$L_r = 4\pi \iint Q_{abs}(a,\lambda)B(\lambda,T)d\lambda da \tag{A9}$$

where $Q_{abs}(a,\lambda)$ is the absorption efficiency factor for grains of radius a at wavelength λ. To solve this expression for the temperature $T_{\rm d}$ we again assume single sized grains, as well as that the efficiency factor is a constant and can be represented by a mean value in the MIR spectral region. This then leads to the simpler equation

$$L_r = 4\sigma_{SB}{T_{\rm d}}^4 < Q_{MIR} > \tag{A10}$$

where σ_{SB} is the Stefan–Boltzmann constant and $< Q_{MIR} >$ is the absorption efficiency factor in the MIR. Equating $G_{L\alpha}$ and L_r we find

$$T_{\rm d}^4 = \frac{z_{L\alpha}\alpha^{(2)}E_{L\alpha}m_{\rm d}}{5.6\sigma_{SB}\sigma_{\rm d}m_{\rm H} < Q_{MIR} >}\,R\,n_{\rm H} \tag{A11}$$

We take $< Q_{MIR} >$ here to be 0.04. This represents the mean of the efficiency factor from $\sim$ 6–25 μm, which we derived from the optical constants of various types of amorphous silicates (e.g. those of forsterite in Scott & Duley 1997, a pyroxene of approximate cosmic abundances in Jäger et al. 1994, glassy bronzite in Dorschner et al. 1988, astronomical silicate in Draine & Lee 1984, dunite in Penman 1976, and olivine and enstatite in Day 1979). Substituting in the relevant numbers then, i.e. $n_{\rm H} = 10^4$ cm^{-3} for IRS1, we find that with $R = 100$ the expected dust temperature is only of the order of 50 K. In order to get up to the temperatures we observe, namely $\sim$ 175 K at IRS1, the gas–to–dust mass ratio must be 1.5×10^4 for $n_{\rm H} = 10^4$ cm^{-3}.

We note that this is not affected by using a different grain size. As long as the Rayleigh approximation (i.e. $2\,\pi\,a \ll \lambda$) is valid the decreased/increased heating rate for a smaller/larger grain is offset by a similar change in the efficiency factor. However, if a grain size distribution is used it is probable that each size

will attain a different temperature. Additionally, it is affected if a different grain composition is used, such as graphite, which has been suggested by Tielens & de Jong (1979) to be an important contributor to the 5–15 μm continuum emission of H II regions. Graphite will attain a higher temperature because of its lower efficiency factor in the MIR than silicates, by about a factor of 3–4 (e.g. Draine & Lee 1984). In that case a gas–to–dust mass ratio of $\geq 10^4$ can produce the same temperature for IRS1 as given above. Also, if the silicates have a mantle of organic refractory material, as is postulated by Li & Greenberg (1997), the grains will be hotter for a given value of R. For example, with a mantle whose volume is the same as the silicate core, $< Q_{MIR} >$ is reduced by about a factor of about two, and so $R \simeq 8 \times 10^3$ cm^{-3} is required to reach 175 K for $n_{\rm H} = 10^4$ cm^{-3}. Nevertheless, the bottom line is that if resonant Ly-α absorption is the dominant heating source for the dust, a dust depletion of around 100 from the standard ISM gas–to–dust mass ratio of 100 is required within the RCW 38 ionised zone.

Such a large dust depletion has previously been inferred for the ionised zones of H II regions, and was the subject of much debate in the literature in the 1970's. For example, in his models of dusty H II regions Wright (1973) found that the dust had to be depleted by factors of order 1000 over the ISM value in order that Lyman α photons dominate the heating *and* that a constant temperature be produced in the ionised zone. In his undepleted model a temperature gradient exists with increasing distance from the central star, which we do not see here. Panagia (1975) and Natta & Panagia (1976) criticised observational findings of dust depletion on the basis that in some instances a direct comparison of the dust mass from MIR observations and gas mass from radio observations was used. They found that the common assumption of a single dust temperature leads to an underestimate of the dust mass, and when a more realistic temperature distribution is used a significant depletion is no longer found, if any at all.

Whilst this may be true, we note that our conclusions for RCW 38 are independent of the dust mass we derive. Rather they depend only on the relative invariance of the temperature throughout the RCW 38 ridge, a direct prediction

of Ly-α models. Indeed, even the value of the temperature itself is of only secondary importance. Tielens & de Jong (1979) reconciled the differences in the literature, and on the basis of a very detailed model of the spectral energy distribution of the W3A IRS1 H II region presented strong arguments for large dust depletions inside H II regions. They also proposed several mechanisms whereby the dust may be depleted, such as by radiation pressure from the central star or by sputtering by energetic particles. Hackwell et al. (1978) came to a similar conclusion of significant dust depletion for W3 IRS1, as did Aitken, Griffiths & Jones (1977) for G333.6–0.2, on the basis of mid–infrared emission and colour temperature maps, which are similar in nature to our images of RCW 38.

Application of Ly–α heating

Having concluded that the dominant dust heating mechanism may be absortion of resonantly trapped Lyman α photons, it remains to determine what might cause the slight, yet still apparent, temperature variations within the RCW 38 ridge, for example amongst the different clumps A–D. Looking at equation (A11) again, it can be seen that by changing either the gas–to–dust mass ratio R, whilst keeping the hydrogen density $n_{\rm H}$ constant, or changing $n_{\rm H}$ whilst keeping R constant, slight temperature variations can easily be produced. Of course changing both can also provide a similar result. Therefore, variations in these quantities could be responsible for the slight temperature changes observed throughout the ridge. This was also suggested by Wright (1973). However, we can go even further than this and use the Ly–α model to predict values for $n_{\rm H}$ and R for all the clumps, using equations (A6) and (A10), together with the following equation

$$dF_\lambda = \frac{\kappa m_{\rm d} dV}{d^2} n_{\rm d} B(\lambda, T) \qquad \text{(A12)}$$

where dF_λ is the flux observed at wavelength λ from a volume element dV, and all other quantities have previously been introduced. This is just a simple re–arrangement of equations (A2) and (A3), where $\kappa = 3Q_{abs}/4a\rho$, ρ is the density of silicates, and $M_{dust} = n_{\rm d} m_{\rm d} dV$.

The previous equations tells us that when comparing the fluxes of the differ-

ent clumps within RCW 38, the only important parameters are the dust number density and temperature of the clump. All other parameters can be assumed to be the same. Therefore, if we use IRS1 as a standard, for which we know the flux, dust density and temperature, we can express the flux of a particular clump, for which we only know its flux and temperature, as a fraction of the flux of IRS1, and thereby derive the number density of the dust for each clump. Since we know the temperature of the clump we can use equation (A10) to derive the heating rate (assuming it is equal to the cooling rate), and then use equation (A6) to solve for $n_{\rm H}$, the gas density. Doing so yields the values of $n_{\rm d}$, $G_{L\alpha}$, $n_{\rm H}$ and R for clumps A through D in Table A.2. It is reassuring that this Ly–α heating model is able to account for the difference in fluxes *and* temperatures between all the clumps within the ridge, e.g. IRS1 and source B, for which the temperatures are the same yet the fluxes differ by a factor of 2.

We can perform a similar calculation for the eastern and western rims of the ridge. Note that at the eastern rim the observed temperature is lower than in the middle of the ridge, despite the fact that it is closer to IRS2. Perhaps here, nearest the cavity, the gas density is lower and/or the gas–to–dust mass ratio higher than in the middle due to the proximity to IRS2 and its wind. Indeed, this is shown to be the case in Table A.2. With regard to the western rim, since its temperature is similar to that of the eastern rim it may be thought that its properties would be similar to those in the east. That may be true, perhaps strengthening the case for a 2nd cavity between the ridge and source D, but we must also be careful here. This is the region where our opacity image peaks, indicating perhaps an enhancement in the dust grain column density. As noted by Martin (1978), if there are too many grains the diffuse Lyman α flux does not build up and the grain temperatures are depressed.

Although all of our above treatment has made some fairly simplifying assumptions, e.g. a single grain size and a single dust temperature, we believe that it is the most direct and transparent way of presenting the effects of Lyman α heating. Additionally, we do not know what type of size distribution might exist within the ionised zones of H II regions, such as its form and the maximum

Table A.2. Gas densities and gas–to–dust mass ratios within the RCW 38 ridge

Source	Flux (N-band)	$T_{\rm d}$ (K)	$n_{\rm d}$ ($\times 10^{-11}$)	$G_{L\alpha}$ ($\times 10^{3}$)	$n_{\rm H}$ ($\times 10^{3}$)	R ($\times 10^{4}$)
IRS1	1.00	175	4.10	8.5	5.64	2.5
A	0.55	160	4.58	5.9	4.98	2.3
B	0.55	175	2.25	8.5	4.19	3.5
C	0.45	160	3.74	5.9	4.46	2.2
D	0.15	165	0.97	6.7	2.44	4.7
E&W	0.10	145	1.94	4.0	2.66	2.6
NSP	0.50	155	5.40	5.2	5.01	1.7
SSP	0.50	165	3.25	6.7	4.46	2.6

Note. — The N-band fluxes have been expressed relative to that at IRS1. The dust and gas number densities are expressed in terms of cm^{-3}, whilst $G_{L\alpha}$ is in units of erg s^{-1} cm^{-2}. For all sources the ratio of the Q–band flux to that at IRS1 is also consistent with the values quoted. E and W refer to the eastern and western rims of the ridge respectively, whilst NSP and SSP refer to the northern and southern S IV peaks respectively. The gas number density for IRS1 is determined in the same manner as the other sources, and not assumed to be 10^4 as in earlier sections.

and minimum sizes. It might be expected that the harshness of the environment there, in terms of both the particle and photon radiation as well as mechanical motions, would change these parameters from their interstellar counterparts as given by Mathis, Rumpl and Nordsieck (1977). We should re–iterate however that the numbers we present here for the dust temperature, and so $n_{\rm d}$, $n_{\rm H}$ and R are somewhat uncertain, perhaps by a factor of 2 for the latter three, but that their spatial trends and relative values should be quite reliable.

Ridge mass revisited

In this appendix we have used two methods to estimate the mass of material comprising the RCW 38 ridge. It is interesting to see if they arrive at a consistent result. In our cavity clearing scenario of section A.4.1 we estimated a mass of $\sim$ 2 $M_\odot$ in the ridge. From our observations in section A.3.5 we estimated a dust mass of $\sim 6 \times 10^{-4}$ $M_\odot$. Using a representative gas–to–dust mass ratio of $R \sim 10^4$, inferred from Table A.2, the mass in the ridge is $\sim$ 6 $M_\odot$, in reasonable agreement with the earlier estimate.

A.4.3. The nature of IRS1 and the S IV – continuum peaks

The preceding discussion presents the view that the ridge of emission is the outer shell of a wind blown cavity, illuminated by radiation from the young hot source IRS2. It would also seem that IRS2 can provide sufficient heating to the dust, via resonantly trapped Lyman–α photons, to explain most, perhaps all, of the thermal emission that we observe. Apart from IRS2, we have seen that IRS1, as well as being the brightest 10 μm source in our field, is also one of the warmest, along with the other MIR emission peaks B and D. However, IRS1 is *not* itself a peak of S IV emission. In fact, the northern S IV peak lies almost in the trough of continuum emission between source A and IRS1, and source B also does not coincide with the southern S IV emission peak. This may be thought to be counter intuitive, since it is expected that the gas and dust are

well mixed, and that their densities might vary in a similar way. Therefore, a peak of emission in one would show up as a peak in the other. How then might the relative offsets we observe be explained?

We showed in section A.4.2 that under the Lyman α heating model the gas–to–dust mass ratio must change throughout the length and breadth of the RCW 38 ridge to explain both the flux and temperature distribution. In other words, the gas and dust densities vary independently, so that it is possible to have a gas density peak, where the S IV emission might peak, located at a different position from the dust emission peak (which is however not necessarily a dust density peak). The question is, can we find a combination of $n_{\rm H}$ and R that matches the continuum flux and temperature at the S IV peaks, but also satisfies the criterion that the gas density is higher than at any other position?

We consider first the northern S IV peak, which we will abbreviate as NSP. If we take the continuum flux at the NSP as 50% of that at IRS1 (from Fig. A.1) and the temperature as 155 K (from Fig. A.4) then using the same procedure as in section A.4.2 we find from Table A.2 a gas density *below* that at IRS1. From Fig. A.3 we see that the S IV surface brightness at the NSP is about 1.1×10^{-18} W cm^{-2} arcsec^{-2}, whilst that at IRS1 is about 6.0×10^{-19} W cm^{-2} arcsec^{-2}. Using a statistical equilibrium and escape probability code, in the Large Velocity Gradient approximation, we would expect that since the surface brightness has increased by a factor of ~ 1.85 from IRS1 to the NSP, then the gas density should have increased by a factor of about 3.5. This assumes an electron temperature of 10 000 K and and electron density at IRS1 of 1.1×10^4 cm^{-3}, as indicated by our modelling. We note that this density is already approaching the critical density of the S IV 10.5 μm transition of 5.4×10^4 cm^{-3}, so that collisional de–excitation is starting to become important. Hence the quite large increase in the density required for a modest increase in the surface brightness. The critical density was calculated using an Einstein A–coefficient of 7.75×10^{-3} s^{-1} and collision strength at 10 000 K of 6.67, from Johnson, Kingston & Dufton (1986).

Therefore, since the gas density we predict at the NSP is below that observed at IRS1, our treatment falls a long way short of accounting for the difference in

the gas and dust emission distributions. With regard to the southern S IV peak (SSP), we see from Table A.2 that the gas density is again below that of IRS1, but that the S IV emission is again larger than at IRS1, about 8.2×10^{-19} W cm^{-2} arcsec^{-2}.

Perhaps the difference can be accounted for if it is assumed that a small fraction of the dust heating and emission throughout the ridge is provided by direct radiation from IRS2. For instance, if we say that the direct heating contribution is constant for all positions in the ridge, and then quite arbitrarily assume that the Ly–α contribution to the heating at IRS1 only raises the grains to a temperature of 160 K, whilst keeping the IRS1 and NSP Ly–α N–band flux ratios at 0.5, then the gas density at the NSP only increases to 9.3×10^3 cm^{-3}, still below that at IRS1.

Clearly then, an alternative explanation needs to be found for the differences in the dust and S IV emission distributions. Perhaps the most natural is to suppose that the S IV column density is locally enhanced at the respective S IV emission peaks. This might be produced within a shock, either from the IRS2 wind or internal motions within the ridge. Such a shock could have the dual affect of releasing sulfur back into the gas phase from its dust component (e.g. FeS or sulphur bearing ices), as well as providing further ionisation through collisions. This scenario is consistent with the reduced dust thermal emission at the NSP, although one might also expect that the dust temperature would increase there due to an enhanced population of small grains. However, we also note from section A.4.2 that the Ly–α heating mechanism can be independent of the grain size.

Another possible explanation for the separation of the S IV peak from the continuum peak arises if it is assumed that IRS1 contains a self–luminous source, albeit a relatively cool one compared to IRS2. The coolish nature of the source would mean that it contributes to the dust heating, but makes no contribution to the S IV distribution, as it emits no significant ionizing radiation. However, the main difficulty with this scenario is that the mid–infrared spectrum of IRS1 (Fig. A.2) shows no evidence for either an embedded source (e.g. the emission

is optically thin, with no sign of overlying deep absorption) or a revealed local source (e.g. no sign of any photospheric emission). Furthermore, the physical properties of the RCW 38 ridge, such as its relatively low mass and the expected high degree of turbulence, would seem to argue against the possibility of star formation. However, even if there is an embedded local source at IRS1, the problem of the difference in the S IV surface brightness between IRS1 and the NSP still exists. In other words, the problem transfers from being one of the offset between the dust and gas emission peaks, to one of how such a large enhancement in the S IV emission between IRS1 and the NSP is actually attained.

The final possibility we consider is that the NSP sees a greater radiation load from IRS2 than IRS1 does. However, this should increase both the gas and dust emission, and there is no evidence in any of our images, e.g. the optical depth image of Fig. A.5, to support an assumption that somehow IRS1 is shielded from IRS2.

In summary then, at this stage it is not really possible to differentiate unambiguously between the various proposed scenarios to explain the differences between the dust and S IV images. However, we believe an increased S IV column density caused by shock processing is the most likely. Similar narrow band imaging in the Ar III and Ne II lines, elements which may not be as prone to depletion on dust grains, or in a near–infrared recombination line of H I, would be helpful.

A.5. Conclusions

We have obtained 10 and 20 μm broad band images, 10 μm spectroscopy and a S IV image at 10.5 μm of the central region of RCW 38. The main results from our study are as follows.

(1). Modelling of the emission line structure at IRS1 indicates that the ionising radiation field characterises a star of type O5.5 or O5 with an effective temperature $T_{\rm eff} \simeq 45\,000$ K. The hydrogen number density is $n_{\rm H} \simeq 10^4$ cm^{-3} in

the IRS1 ridge.

(2). From fits to the 8–13 μm spectrum of IRS1 we find a dust colour temperature at this point of around 175 K.

(3). A dust temperature map is produced from the N– and Q–band continuum images and shows the ridge of emission, of which IRS1 is a part, to have a relatively uniform temperature structure, with an average of around 160 K. However there are a number of peaks in the dust temperature, up to 175 K, which correspond well with the intensity peaks in the N- and Q-band images. One of these peaks is situated at IRS1.

(4). From the temperature and continuum emission images we are able to derive an opacity map which shows material collecting at the western, or outer, edge of the ridge, which itself forms part of a shell around IRS2.

(5). We have proposed that the region can be explained in terms of a wind blown cavity, where the stellar wind from the hot young star in IRS2 has cleared a cavity about itself, and the ridge of emission we observe at IRS1 then represents the material which has been swept up into a shell around IRS2. The shell is not perfectly circular, which may indicate that the molecular cloud, into which the shell is being driven by the wind, is not uniformly distributed, but rather clumpy.

(6). Modelling the effects of direct heating on the dust shell predicts a large temperature gradient across the shell (50 K from inner to outer edges). We do not, however, see such a gradient in our temperature maps, indicating that this form of heating certainly does not dominate the region.

(7). We have estimated the heating effect of the Ly–α photons on the dust and conclude that if the gas density is $n_{\rm H} = 10^4$ cm^{-3}, as at IRS1, then silicate–type dust would reach an equilibrium temperature around 175 K if the gas–to–dust mass ratio R is of the order of a few times 10^4. Variations in $n_{\rm H}$ and R can produce both the subtle temperature and emission changes throughout the RCW 38 ridge. A significant dust depletion over normal interstellar values is

therefore required. We believe that this is the case in RCW 38 since Ly–α heating can only be dominant if such a depletion exists, and as far as we can ascertain it is the only heating mechanism which can explain the relatively constant dust temperatures seen throughout RCW 38, and the lack of any temperature gradient away from the central star.

(8). We estimate the mass of dust in the ridge around IRS1 to be about 5.7×10^{-4} $M_{\odot}$, and if we take a gas–to–dust mass ratio of around 10^4:1, as indicated by our Lyman α modelling, we find a total mass in the ridge of around 5.7 $M_{\odot}$ of gas and dust. This mass estimate is consistent with a mass estimate of the shell derived from modelling the IRS1 ridge as an expanding shell driven by the stellar wind, for which we estimate a mass of 2 $M_{\odot}$.

(9). An image in the S IV fine structure line at 10.52 μm shows structure whose large scale is similar to that of the dust emission, but whose peaks do not exactly coincide with the continuum emission or temperature distribution peaks. For instance, IRS1 is not the main S IV peak in the region. A variety of explanations for this observation are possible, but we favour one in which the S IV column density is locally enhanced by grain destruction and collisional ionisation in a fast shock.

REFERENCES

Aitken D.K., Jones B., 1973, ApJ, 184, 127

Aitken D.K., Griffiths J., Jones B., 1977, MNRAS, 179, 179

Aitken D.K., Bailey A.J., Roche P.F., Hough J.H., 1985, MNRAS, 215, 425

Allen D., Meadows V, 1992, Astronomy, 20, 38

Axon D.J., Ellis R.S., 1976, MNRAS, 177, 499

Baldwin J., Ferland G.J., Martin P.G., Corbin M., Cota S., Peterson B.M., Slettebak A., 1991, ApJ, 374, 580

Beck S.C., Fischer J., Smith H.A., 1991, ApJ, 383, 336

Bodenheimer, P., Tenorio–Tagle, G., Yorke, H. W., 1979, ApJ, 233, 85

Böker T., Storey J.W.V., Krabbe A., Lehmann T., 1997, PASP, 109, 827

Cheung L.H., Frogel J.A., Gezari D.Y., Hauser M.G., 1980, ApJ, 240, 74

Colgan S.W.J., Simpson J.P., Rubin R.J., Erickson E.F., Haas M.R., Wold J., 1991 ApJ., 366 172

Danziger I.J., 1974, ApJ., 193, 69

Day K.L., 1979, ApJ, 234, 158

Dorschner J., Friedemann C., Gürtler J., Henning T., 1988 A&A, 198, 223

Doyon R., Puxley P.J., Joseph R.D., 1992, ApJ, 397, 117

Draine B.T., 1985, ApJS, 57, 587

Draine B.T., Lee H.M., 1984, ApJ, 285, 89

Epchtein N., Turon P., 1979, A&A, 72, L4

Ferland G.J., 1993, Dept. of Physics and Astronomy Internal Report, Univ. Kentucky

Frogel J.A., Persson S.E., 1974, ApJ, 192, 351 (FP74)

Fujiyoshi T., et al., 1997, MNRAS, in press

Furniss I., Jennings R.E., Moorwood A.F.M., 1975, ApJ, 202, 400

Genzel R.G., 1992, in The Galactic Interstellar Medium, Saas–Fee Advanced Course 21, eds. D. Pfenniger & P. Bartholdi, Springer–Verlag

Gillespie A.R., White G.J., Watt G.D., 1979, MNRAS, 186, 383

Gillett F.C., Forrest W.J., Merrill K.M., Capps R.W., Soifer B.T., 1975, ApJ, 200, 609

Goss, W.M., Shaver, P.A., 1970, Aust. J. Phys. Suppl., 14, 1

Gum C.S., 1952, Observatory, 72, 151

Gum C.S., 1956, Observatory, 76, 150

Hackwell J.A., Gehrz R.D., Smith J.R., Briotta D.A., 1978, ApJ, 221, 797

Hanson M.M., Howarth I.D., Conti P.S., 1997, ApJ, 489, 698

Jäger C., Mutschke H., Begemann B., Dorschner J., Henning Th., 1994, A&A, 292, 641

Johnson C.T., Kingston A.E., Dufton P.L., 1986, MNRAS, 220, 155

Klare G., Neckel Th., 1977, A&A Supp., 27, 215

Kuiper T.B.H., Whiteoak J.B., Fowler J.W., Rice W., 1987, MNRAS, 227, 1013

Kurucz R.L., 1994, Smithsonian Astrophysical Observatory, Kurucz CD–ROM No. 19

Lacy J.H., Beck S.C., Geballe T.R., 1982, ApJ., 255, 510

Lamers, H. J. G. L. M., Snow T. P., Lindholme, D. M., 1995, ApJ, 455, 269

Lang K.R., 1992, Astrophysical Data: Planets and Stars, Springer–Verlag, New York

Lester D.F., Dinerstein H.L., Rank D.M., 1979, ApJ., 229, 981

Leung C.M., 1975, ApJ, 199, 340

Leung C.M., 1976, J. Quant. Spectrosc. Radiat. Transfer, 16, 559

Li A., Greenberg J.M., 1997, A&A, 323, 566

Ligori S., Moneti A., Robberto M., Guarnieri M.D., Zinnecker H., 1994, Mem. Soc. Astron. Ital., 65, 815

Martin P.G., 1978, Cosmic Dust, Oxford University Press, Oxford

Mathews W.G., 1969, ApJ, 157, 583

Mathis J.S., Rumpl W., Nordsieck K.H., 1977, ApJ, 217, 425

Mitchell R.M., Robinson G., 1978, ApJ, 220, 841

Mitchell R.M., Robinson G., 1980, MNRAS, 190, 669

Mizutani K., Suto H., Takami H., Maihara T., Sood R.K., Thomas J.A., Shibai H., Okuda H., 1987, MNRAS, 228, 721

Muzzio J.C., 1979, AJ, 84, 639

Natta A., Panagia N., 1976, A&A, 50, 191

Panagia N., 1973, AJ, 78, 929

Panagia N., 1975, A&A, 42, 139

Pauldrach A.W.A., 1997, private communication

Penman J.M., 1976, MNRAS, 175, 149

Persson S.E., Frogel J.A., Aaronson M., 1976, ApJ, 208, 753

Radhakrishnan V., Goss W.M., Murray J.D., Brook J.W., ApJ. Suppl, 24, 49

Rank D.M., Dinerstein H.L., Lester D.F., Bregman J.D., Aitken D.K., Jones B., 1978, MNRAS, 185, 179

Robinson G., Smith R.G., Hyland A.R., 1992, MNRAS, 256, 437

Roche P.F., Aitken D.K., 1984, MNRAS, 208, 481

Rodgers A.W., Campbell C.T., Whiteoak J.B., 1960, MNRAS, 121, 123

Scott A., Duley W.W., 1997, ApJS, 105, 401

Simpson J.P., Rubin R.H., 1984, ApJ., 281, 184

Simpson J.P., Colgan S.W.J., Rubin R.H., Erickson E.F., Haas M.R., 1995, in Haas M.R., Davidson J.A., Erickson E.F., eds, ASP Conf. Ser. Vol. 73, Airborne Astronomy Symposium on the Galactic Ecosystem, p. 53

Spitzer L., 1978, Physical Processes in the Interstellar Medium, Wiley, New York

Storey J.W.V., Bailey J., 1982, PASA, 4, 430

Takami H., et al., 1987, PASP, 99, 832

Tielens A.G.G.M., de Jong T., 1979, A&A, 75,326

White G.J., Phillips J.P., 1983, MNRAS, 202, 255

Wright C.M., 1994, PhD thesis, Univ. NSW

Wright E.L., 1973, ApJ, 185, 569

Zinchenko, I., Mattila, K., Toriseva, M, 1995, A&AS, 111, 95

Appendix B

CLASS Scripts used for Data Reduction of Zeeman Observations

In the following pages we present the CLASS scripts used in the reduction and analysis of the Zeeman data. The scripts are very interactive and forces the user to be very familiar with their data. The scripts are presented in order of use in the reduction pipeline. I'd like to thank Carl Heiles for the routines `crout` and `reler`, and the early version of the zeeman fitting routines, which I modified greatly to suit the current data formats. I'd also like to thank Mario Tafalla for help with the initial stages of some of these scripts and helping with the CLASS language.

Class script combine.class

```
!
!       combine.class
!
! Macro to read native class files created by cfits containing
! Parkes data, which were originally written to fits file in SPC
! Some header parameters need to be fixed after all this transforming
! of file types, see correct-header.class which is called in this macro
!
! usage:
!       LAS> @combine
!
! See the manual "Analysis of Parkes OH Zeeman data with CLASS"
! for a full description of what needs to be set up before this
! file is executed, and what inputs are required along the way
! (to be written!! Oct 27 1995)
!
! original M. Tafalla/T. Bourke 27/10/95
! updated T. Bourke 07/11/95
!
! update T. Bourke 10/10/96 fix integration time in header.  Value
! written by SPC is twice the actual value when pol. switching.
!
set align velocity      ! Alignment for averaging
set unit v f            ! On plots, Velocity on lower, Freq on upper
set weight time         ! Weight for averaging using "sum"
set var general read
set mode x tot
set mode y tot
set scan                ! refresh
!
define real first last total
define char inputfile*40 infile*40
define char outputfile*40 outfile*40
define char new-name*40
define char pol*1
def char ans*1
def real truetime
!
! Intro notes - tell the user they will be expected to identify
! the polarisation
!
say " "
say "-----------------------------------------------------------------"
say "This macro takes polarisation data that is in the form: "
say "   observation-num scan1 scan2 scan3 scan4"
say "                    A     B     B     A  "
say "averages together like polarisations for each observation,"
say "   ie scan1 and scan4 --> average"
say "and writes them to a new file"
say " "
say "You will be expected to identify the polarisation for each"
say "averaged pair, ie RCP or LCP.  This information will be appended"
say "to the telescope name in the output file"
say "-----------------------------------------------------------------"
say " "
!
! Open files for input and output
!
say " "
say "Enter input file name (.pks assumed) ..."
say " "
let inputfile =
let infile = 'inputfile'".pks"
file in 'infile'
say " "
say "Enter new output file name (.pks will be appended) ..."
say " "
let outputfile =
let outfile = 'outputfile'".pks"
file out 'outfile' new
!
! Loop through the file and get the first and last observation numbers
!
find/all
let total = found
get f
let first = num
for j 1 to total
if (j.eq.total) then
let last = num
!return
break
endif
get n
next
say "First observation = "'first'
say " Last observation = "'last'
!
! Now process the data
!
for i first to last
set scan i i
find/all
!
! Process polarisation "A"
!
if (found.ne.4) then
say " "
say "***Not 4 spectra - data not in required format***"
say " "
pause
endif
!
! Polarisation pairs are scan 1 & 4, and 2 & 3
!
drop i 2
drop i 3
sum
plot
!
! User must specify whether data is RCP or LCP
!
say " "
say "Identify polarisation - enter R or L"
say " "
let pol =
let new-name = 'telescope'"-"'pol'"CP"
modify telescope 'new-name'
modify line OH
!
```

Class script combine.class

```
! Modify some header items
!
@correct-header
!
! Correct the integration time.  Current value is twice actual value
!
let truetime = time|2
let time = truetime
!
say " "
say "Write to file?  (y/n)... "
say " "
let ans =
if ((ans.eq."y").or.(ans.eq."Y")) then
        write
else
endif
!
! Process polarisation "B"
!
find/all
if (found.ne.4) then
say " "
say "***Not 4 spectra - data not in required format***"
say " "
pause
endif
!
! Polarisation pairs are scan 1 & 4, and 2 & 3
!
drop i 1
drop i 4
sum
plot
!
! User must specify whether data is RCP or LCP
!
say " "
say "Identify polarisation - enter R or L"
say " "
let pol =
let new-name = 'telescope'"-"'pol'"CP"
modify telescope 'new-name'
modify line OH
!
! Modify some header items
!
@correct-header.class
!
! Correct the integration time.  Current value is twice actual value
!
let truetime = time|2
let time = truetime
!
say " "
say "Write to file?  (y/n)... "
say " "
let ans =
if ((ans.eq."y").or.(ans.eq."Y")) then
        write
else
endif
!
next
set scan                ! Resets the scan to all observations
!
! Remind user of current input and output files
!
show files
!
! End
!
```

Class script correct-header.class

```
!
!       correct-header.class
!
! Macro to correct a few header items which are either completely
! wrong (ie epoch) after creation of the fits file by SPC,
! or which need to be adjusted because some fits header items
! are interpreted differently by SPC and CFITS.
!
! Called by the macro combine.class
!
! original M. Tafalla/T. Bourke 27/10/95
! updated T. Bourke 07/11/95
!
set var position write
set var spectro write
!
! These items are wrong or non-existent, so fix them
!
let epoch = 1950.0
let proj = 7
!
! Redefine the reference channel and correct for frequency offset
! problem, caused by different interpretation of fits header items
!
define real vrefold
let vrefold = voff
let voff = vrefold+(1-(nchan|2))*vres
let rchan = nchan|2
let foff = 0.
!
! End
!
```

Class script sum-spectra.class

```
!
!       sum-spectra.class
!
! usage:
!       LAS> @sum-spectra
!
! See the manual "Analysis of Parkes OH Zeeman data with CLASS"
! for a full description of what needs to be set up before this
! file is executed, and what inputs are required along the way
! (to be written!! Oct 27 1995)
!
! Basically takes the result of combine.class and combines all the
! L spectra of a polarisation, writes to a file, then combines all
! the H spectra of the same polarisation and writes to the same file.
! The other polaristion is then processed in the same manner, the data
! written to a new file
!
! original T. Bourke 06/11/95
!
set align velocity      ! Alignment for averaging
set unit v f            ! On plots, Velocity on lower, Freq on upper
set weight time         ! Weight for averaging using "sum"
!
define char inputfile*40 outputfile*40
define char iname*40
define char oname*40[2]
define char sname*20
define char pol*1
!
! Remind user of current input and output files
! and allow them to reset them
!
show files
say " "
say "Set Output file to be Input file if you have just run combine"
say "else define a new input file"
say "Enter current output file name or new file name (.pks assumed) ..."
say " "
let inputfile =
let iname = 'inputfile'".pks"
file in 'iname'
!
! Loop through polarisation data and average
!
say " "
say "Enter a prefix for the new output file  ..."
say "File name will be prefix-pol.pks where pol = RCP or LCP"
say " "
let outputfile =
say " "
say "Set source name (suffix -L or -H will be added)..."
say " "
let sname =
!
! RCP
!
let pol = R
!let telescope = "64M-"'pol'"CP"
set telescope "64M-"'pol'"CP"
let oname[1] = 'outputfile'"-"'pol'"CP.pks"
file out 'oname[1]' new
show files
set source 'sname'"-L"
find/all
sum
write
set source 'sname'"-H"
find/all
sum
write
!
! LCP
!
let pol = L
set telescope "64M-"'pol'"CP"
say 'telescope'
let oname[2] = 'outputfile'"-"'pol'"CP.pks"
file out 'oname[2]' new
show files
set source 'sname'"-L"
say 'source'
find/all
sum
write
set source  'sname'"-H"
find/all
sum
write
say "RCP data written to "'oname[1]'
say "LCP data written to "'oname[2]'
!
! Reset source and telescope
!
set source
set telescope
!
! End
!
```

Class script fold-spc.class

```
!
!       fold-spc.class
!
! Class macro to create frequency switched like spectra and fold
! them.
! Data are from Parkes, and are taken at the same position, but with
! different central frequencies (since true freq switching is not
! possible at Parkes).
! The steps are discussed below.
!
! Two files are created, one containing RCP data, the other LCP data.
!
! See the manual, not yet written
!
! original M.Tafalla/T. Bourke 27/10/95
! updated T. Bourke 07/11/95
!
set unit v f
set var spectro write
set var position write
set align velocity
set source
set telescope
!
symbol  mx "set mode x"
!
define real t1 t2               ! for system temps
define real f1                  ! for frequency reset
define real chans chanref velref velres
define char inputfile*40[2] outfile*40[2]
define char fname*40[2] tname*40[2]
!
say " "
say "Current files are ..."
say " "
show files
say " "
say "Enter RCP file to open (.pks assumed) ..."
say " "
let inputfile[1] =
let fname[1] = 'inputfile[1]'".pks"
let outfile[1] = 'inputfile[1]'"-f.pks"
say " "
say "Enter LCP file to open (.pks assumed) ..."
say " "
let inputfile[2] =
let fname[2] = 'inputfile[2]'".pks"
let outfile[2] = 'inputfile[2]'"-f.pks"
say " "
say "Folded freq. switched spectrum will be written to ... "
say "RCP data : "'outfile[1]'
say "LCP data : "'outfile[2]'
say " "
!
! Big loop through the two polarisations
!
for poln 1 to 2
!
! first get rid of any *tmp* files
!
say " "
say "One moment please ... "
say " "
system "\rm *tmp*pks"
!
! open the input file
!
file in 'fname[poln]'
!
! open temp file for output
!
let tname[1] = 'inputfile[poln]'"-tmp1.pks"
let tname[2] = 'inputfile[poln]'"-tmp2.pks"
file out 'tname[1]' new
!
find/all
get first
let chans = nchan
let chanref = rchan
let velref = voff
let velres = vres
resample chans chanref velref velres vel
let vres = velres
write
!
get next
resample chans chanref velref velres vel
let vres = velres
write
!
file in 'tname[1]'
file out 'tname[2]' new
!
find/all
get f
let t1 = tsys
get next
let t2 = tsys
!
! Form quotient Q = [(S/R Tr/Ts) - 1]Ts
!
! divide performs current/previous
!
divide 0.001
multiply t1|t2
! correct for offset of 1 after division
say " "
say "Be patient, this takes time ... "
say " "
for i 1 to 8192
        let ry[i] = ry[i]-1
        if (abs(ry[i]).gt.1e3) then
        let ry[i] = 0
        endif
next
!
multiply t2
let tsys = t2
write
!
```

Class script fold-spc.class

```
find/all
get f
get next
let f1 = restf
let t1 = tsys
get f
let t2 = tsys
!
! Form quotient Q = [(S/R Tr/Ts) - 1]Ts
!
! divide performs current/previous
!
divide 0.001
multiply t1|t2
! correct for offset of 1 after division
say " "
say "Be patient, this takes time ... "
say " "
for i 1 to 8192
        let ry[i] = ry[i]-1
        if (abs(ry[i]).gt.1e3) then
        let ry[i] = 0
        endif
next
!
multiply t2
let tsys = t2
modify freq f1
write
!
show files
!
file in 'tname[2]'
file out 'outfile[poln]' new
find/all
set align velocity
sum
plot
say " "
say "If you are happy with the result shown in the plot then"
say "continue, otherwise make any changes and then continue ..."
say "Enter c to continue when done"
say " "
say "If data looks flat and y scale is huge, then there is a problem"
say "channel somewhere near the end channels which slipped through "
say "our net. To fix, reset the x axis to be within a few channels of"
say "the end, eg enter :"
say "   prompt> set unit c f"
say "   prompt> mx 0 20"
say "NB repeat mx command for the high end as well"
say "   prompt> plot"
say "   prompt> draw"
say "You will now be in cursor mode.  Place the cursor on the offending"
say "channel and hit <k> on the keyboard, to kill it."
say "Continue until all bad channels are out of there!"
say "To check reset the x axis to everything and plot"
say "   prompt> mx tot"
say " "
pause
say " "
say "Current source name is "'sourc'
say "If you want to change the name, enter: "
say "   prompt> let sourc = <new name>"
say "Whether you modify or not, enter c to continue when done ..."
say " "
pause
write
!
! Do the next polarisation
!
next
say " "
say "Done"
say " "
!
!End
!
```

Class script line-sep.class

```
!
!       line-sep.class
!
! Takes folded spectra (created by fold-spc.class) and corrects velocity
! offsets for each of the OH lines (only one of the lines is corrected
! in a spectra containing both lines.  Also baselines the data with user
! input.
!
! Two files are created, one containing 1665 data, the other 1667 data
!
!       preceeding file : fold-spc.class
!       next file       : get-ave.class
!
! original T. Bourke 07/11/95
!
set cursor on
set var spectro write
set var position write
set source
set telescope
set unit c f
!
symbol  b0      "base 0/plot"
symbol  b1      "base 1/plot"
symbol  b2      "base 2/plot"
symbol  b3      "base 3/plot"
symbol  b4      "base 4/plot"
symbol  b5      "base 5/plot"
symbol  b6      "base 6/plot"
symbol  b7      "base 7/plot"
symbol  b8      "base 8/plot"
symbol  b9      "base 9/plot"
symbol  b10     "base 10/plot"
symbol  b11     "base 11/plot"
symbol  b12     "base 12/plot"
symbol  dw      "draw window"
symbol  mx      "set mode x"
symbol  my      "set mode y"
symbol  sw      "set window"
!
define char inputfile*40 outputfile*40
define char infile*40[4] outfile*40[4]
define real fline ohline
define real fdiff deltachan
define char poln*10
!
say " "
say "Current file are :"
show files
say " "
say "Enter RCP file name (.pks assumed) ..."
say " "
let inputfile =
let infile[1] = 'inputfile'".pks"
say " "
say "Enter LCP file name (.pks assumed) ..."
say " "
let inputfile =
let infile[2] = 'inputfile'".pks"
!
! Big loop through the two OH lines
! Both polarisations done for each line
!
for line 1 to 2
if (line.eq.1) then
        let fline = 1665.40184000000
        let ohline = 1665
endif
if (line.eq.2) then
        let fline = 1667.35903000000
        let ohline = 1667
endif
!
! Slightly smaller loop through both polarisation for one OH line
!
for pol 1 to 2
!
! RCP pol = 1, LCP pol = 2
!
if (pol.eq.1) then
        poln = "RCP"
endif
if (pol.eq.2) then
        poln = "LCP"
endif
file in 'infile[pol]'
say " "
say "Processing "'poln'" data for "'ohline'" OH line"
say " "
!
find/all
get f
mx tot
set unit c f
plot
say " "
say "Baseline fitting ..."
say " "
say "Change the channel range plotted to include only the "'ohline'" line"
say "To do this enter: "
say "   prompt> mx first-channel last-channel"
say "and to see the result: "
say "   prompt> plot"
say " "
say "When happy with the range, enter c to continue ..."
say " "
pause
say " "
say "Now define windows to be excluded from the baseline fitting"
say "To do this, enter: "
say "   prompt> sw "
say "and use the cursor to define regions you don't want to include"
say "** use the space bar to set the regions **"
say " "
say "Use (e) to exit from cursor mode."
say " "
say "To see the resulting window, enter: "
say "   prompt> dw"
say " "
say "When you are happy with the the window, enter c to continue ..."
```

Class script line-sep.class

```
say " "
pause
say " "
say "For a zeroth order baseline, enter: "
say "   prompt> b0"
say "and b1 for 1st order, etc (12th is the highest allowed)."
say "The baselined data can be plotted by entering: "
say "   prompt> plot"
say "If you are not happy with the baseline, retrieve the original data ..."
say "   prompt> swap"
say "   prompt> plot"
say "Start baselining, when finished enter c to continue ..."
say " "
pause
say " "
say "Now correcting velocity and writing to file ..."
!
let fdiff = fline-restf
let deltachan = fdiff|fres
let rchan = rchan+deltachan
let restf = fline
!
! If pol = 2 then output file is already open, so skip this bit
!
if (pol.eq.1) then
say " "
say "Current line is "'ohline'" OH line"
say "Current file are :"
show files
say " "
say "File for output (.pks will be appended) ..."
say " "
let outputfile =
let outfile[line] = 'outputfile'".pks"
file out 'outfile[line]' new
endif
mx total
write
! Plot the processed data
set unit v f
mx voff-30 voff+30
plot
say " "
say "This is the result of the processing ..."
say "enter c to continue"
say " "
pause
!
! End of RCP processing for this line, onto the LCP data
!
next
!
! This is the end of the first OH line
! Let the user know what line was just processed, and ask
! them for the next line.
say " "
say 'ohline'" OH line processing finished, onto the next line ..."
say " "
next
! now remind the user of the new files
!
say "Final files are "
say "1665 OH line :- "'outfile[1]'
say "1667 OH line :- "'outfile[2]'
say " "
!
! End
!
```

Class script produce-v.class

```
!
!       produce-v.class
!
! This macro reads in the RCP and LCP components for the line of
! interest and produces the V and I/2 spectra
!
!       V = RCP - LCP
!       I/2 = (RCP + LCP)/2
!
! Assumes that one file contains both RCP and LCP for the 1665 line,
! and another contains the same data for the 1667 line
!
define char inputfile*40 infile*40[2]
define char outfile*40[2]
define char name*40 pol*40
define real scale t1
define integer fline
define char prefix*40 suffix*40
!
set weight equal
set var spectro write
set var position read
!
say " "
say "File containing 1665 line data (.pks assumed) ... "
say " "
let inputfile =
let infile[1] = 'inputfile'".pks"
say " "
say "File containing 1667 line data (.pks assumed) ... "
say " "
let inputfile =
let infile[2] = 'inputfile'".pks"
say " "
say "Enter scaling factor for data (1 for no scaling) ..."
say " "
let scale =
for line 1 to 2
if (line.eq.1) then
        fline = 1665
endif
if (line.eq.2) then
        fline = 1667
endif
file in 'infile[line]'
let name = 'sourc'
if (line.eq.1) then
say " "
say "Output file will be of the form"
say "   prefix-"'fline'"-suffix.pks"
say " "
say "Enter prefix ..."
say " "
let prefix =
say " "
say "Enter suffix ..."
say " "
let suffix =
endif
let outfile[line] = 'prefix'"-"'fline'"-"'suffix'".pks"
file out 'outfile[line]' new
!
! V
!
say " "
say "Determining V for "'fline'" line"
say " "
find/all
get f
let pol = 'telescope'
if (pol.eq."64M-RCP") then
        get f           ! RCP
        get n           ! LCP
        mult -1
        mult scale
        get f           ! RCP
        mult scale
        accum           ! RCP + (-LCP)
else if (pol.eq."64M-LCP") then
        get f           ! LCP
        mult -1
        mult scale
        get n           ! RCP
        mult scale
        accum           ! RCP + (-LCP)
endif
set mode x voff-20 voff+20
plot
say " "
say "V spectrum plotted - enter c to continue"
say " "
pause
set mode x tot
write
!
! I/2
!
say " "
say "Determining I/2 for "'fline'" line"
say " "
get f
mult scale
get n
mult scale
accum                   ! with weight equal, produces sum, ie I
let t1 = tsys
mult 0.5
let tsys = t1
set mode x voff-20 voff+20
plot
say " "
say "I/2 spectrum plotted - enter c to continue"
say " "
pause
set mode x tot
write
say " "
say "Data written to "'outfile[line]'
say " "
next
```

Class script zfit.class

```
!
!       zfit.class
!
! Class macro
! Fits derivative of line spectrum to V spectrum, assumes NO
! gaussian information - see zee-fit and zee-gfit for gaussian fitting
!
!       proceeding file :
!       next file       : there ain't none!
!
! original T. Bourke 10/11/95
! this version T. Bourke 04/12/95
!
! adapted from zgfit and zfit, originally by C.Heiles
!
! Includes gain term
!
! 26/02/97 allow user to determine direction of fitting, e.g. from
! low to high channels, or high to low channels.
!
! 04/09/97 allow for possibility that channels may decrease as the
! velocity increases (as is the case for S88B Arecibo data from Alyssa
! Goodman.
!
! 05/09/97 program has now been tested on S88B data, and found give
! consistent results.
!
! 10/2/98 write out individual parts of the model fit, ie the gain
! term and the scaled dI/df
!  Output file now contains
!    1. I spectrum
!    2. V spectrum
!    3. Overall fit to V spectrum
!    4  dI/df scaled ie z[1] * dI/df
!    5. gainterm ie z[2] * I
!    6. gain subtracted V spectrum
!
set var spectro write
set var plot write
set var gauss write
set var calibration write
set weight equal
set unit v c
!
def char inputfile*40 infile*40[2] ofile*40[2] suffix*40
def real gainterm
def int obs line fline chn1 chn2 gg
def int ntry nnfit pts bb jj jjj
def real gfact v[8192] t[8192] modelfit[8192]
def real ts[8192] dts[8192]
def real dvmin dvmax dchnmin dchnmax midchn
def real chnsp srsq srsqe brkt delp1 delm1 rsid ff
def real c[11] ht[10] cen[10] fwhm[10] cenv[10] fwhmv[10] width[10]
def real z[10] bfld[10] berr[10] d[10,10] err[10]
def real velocity-min velocity-max vmiddle
def real pi
def real a[10,10] x[10]
def integer m jp1 jm1 l ll mix j1 j2 tempchn nntry
def integer direction iprime naprime step jprime
!
let pi = 3.141592654
!
symbol mx "set mode x"
symbol my "set mode y"
!
say " "
say "One moment ... clearing up files ..."
say " "
system "\rm zee-temp*.pks"
!
say " "
say "Current files are :"
sh files
say " "
say "Enter file containing V and I data (.pks assumed) ... "
say " "
let inputfile =
let infile[1] = 'inputfile'".pks"
say " "
say "First observation assumed to be V, second is I"
say "If first observation is I, then enter (1) ..."
say " "
let obs =
file in 'infile[1]'
!
! Ask user to identify the line
!
say " "
say "Which OH line (1 = 1665, 2 = 1667) ?"
say " "
let line =
if (line.eq.1) then
        let fline = 1665
        let gfact = 3.27
else if (line.eq.2) then
        let fline = 1667
        let gfact = 1.96
endif
!
! Get the I spectrum and plot it.
! Then ask user to define limits.
!
if (obs.eq.1) then
        find/all
        get f
else
        find/all
        get f
        get n
endif
!
!
! Now set the limits of the plot and plot I
!
!mx tot
mx voff-15 voff+15
plot
say " "
say "Set x limits for Zeeman fitting - give plenty of baseline ..."
say " "
```

```
say "To reset x limits, enter :"
say "   prompt> mx (min) (max)"
say "   prompt> plot"
say "else enter (c) to continue ..."
say " "
pause
!
! Now ask the user for the approximate velocity limits of the
! range just set - haven't been able to automate this
!
say " "
say "Enter the approximate velocity limits of your plot ..."
say " "
let velocity-min =
let velocity-max =
let vmin = velocity-min
let vmax = velocity-max
!
! Now determine start and end channel numbers from this info
!
plot
let vmiddle = (vmax+vmin)|2
let dvmin = vmiddle-vmin
let dvmax = vmax-vmiddle
let dchnmin = dvmin|vres
let dchnmax = dvmax|vres
let midchn = rchan-((voff-vmiddle)|vres)
let chn1 = nint(midchn-dchnmin)
let chn2 = nint(dchnmax+midchn)
!say 'chn1' 'chn2'
!
! Now determine if chn1 > chn2 or chn2 > chn1.  This is needed to
! determine the step size for 'for' loops.
!
if (chn1.gt.chn2) then
        let step = -1
else
        let step = 1
endif
!
! Interested in the I array Gaussian information, so get it now
! since we are using the I spectrum at present
! Note that the cen and wid info is in velocity units
! Do we need to change to channels? Assume so here
!
let ntry = 1
let nntry = 2
let nnfit = 3
!
if (chn1.eq.1) then
        let chn1 = 2
endif
if (chn2.eq.nchan) then
        chn2 = nchan-1
endif
!
! Read the I and V data into arrays defined by the channel extremes
! v is the V data, t is the line (temperature) data
! Also get the line data resulting from the subtraction of
! the fitted gaussian to the line profile
!
! Prompt user for direction of fitting
!
say " "
say "Do you want to fit the spectrum from..."
say "   [1] low velocity to high velocity, or"
say "   [2] high velocity to low velocity"
say " "
say "Enter 1 or 2"
say " "
let direction =
!
if (obs.eq.1) then
        find/all
        if (direction.eq.2) then
        get f                   ! I spectrum
        for i chn1 to chn2 by step
                let iprime = chn1+chn2-i
                let t[iprime] = ry[i]
        next
        get n                   ! V spectrum
        for i chn1 to chn2 by step
                let iprime = chn1+chn2-i
                let v[iprime] = ry[i]
        next
        else
        get f                   ! I spectrum
        for i chn1 to chn2 by step
                let t[i] = ry[i]
        next
        get n                   ! V spectrum
        for i chn1 to chn2 by step
                let v[i] = ry[i]
        next
        endif
else
        find/all
        if (direction.eq.2) then
        get f                   ! V spectrum
        for i chn1 to chn2 by step
                let iprime = chn1+chn2-i
                let v[iprime] = ry[i]
        next
        get n                   ! I spectrum
        for i chn1 to chn2 by step
                let iprime = chn1+chn2-i
                let t[iprime] = ry[i]
        next
        else
        get f                   ! V spectrum
        for i chn1 to chn2 by step
                let v[i] = ry[i]
        next
        get n                   ! I spectrum
        for i chn1 to chn2 by step
                let t[i] = ry[i]
        next
        endif
endif
!
```

Class script zfit.class

```
! Determine channel separation in Hz
!
let chnsp = fres*1e6
!say "chnsp = "'chnsp'
!
! Zero the matrix
!
for na 1 to nnfit
        for nb 1 to na
                let d[na,nb] = 0.
        next
next
!
! Determine derivative of the I
!
say " "
say "Determining derivatives (takes time) ... "
say " "
!say 'chn1+1'" "'chn2-1'
!
!
for j chn1 to chn2 by step
!        let jprime = chn1+chn2-j
        let j1 = j+1
        let j2 = j-1
    if (chn1.gt.chn2) then
        let dts[j] = (t[j2]-t[j1])*0.5
    else
        let dts[j] = (t[j1]-t[j2])*0.5
    endif
    if (direction.eq.2) then
        let dts[j] = -1*dts[j]
    endif
!
! Note we want the V spectrum here
! Include the I term to determine contribution of gain differences
!
        let c[ntry] = dts[j]
        let c[nntry] = t[j]
        let c[nnfit] = v[j]
        for nb 1 to nnfit
                for nc 1 to nb
                        let d[nb,nc] = d[nb,nc]+c[nb]*c[nc]
                next
        next
next
say "Calling crout and reler"
!
! crout and reler
!
!!!!!!!!!!!!!!!!!!!!!!!!!!!!!!!!!!!!!!!!!!!!!!!!!!!!!!!!!!!!!!!!!!!!!!!
!       crout.class
!
! Called by zee-fit.class macro
! Original documentation given below
!
!      SUBROUTINE CROUT(A, X, N)
!      DIMENSION A(12,12),X(12)
!
! Note that A and N are passed to the subroutine, X is returned
!
! CROUT method for matrix equation ax=c where matrix a is symmetr
! see hildebrand page 503.  M is the order of the matrix equation
! n is m plus 1.  The matrix a is assumed to be partitioned as
! described by hildebrand.  No attempt has been made to make this
! subroutine fast or to minimize memory.  Such attempts might
! be fruitful.
! The input matrix a is obliterated by this subroutine
! matrix x is returned as the solution.  Written by c. heiles.
!
! Updated for class T. Bourke 13/11/95
!
!def real a[10,10] x[10]
!def integer  m jp1 jm1 l ll
!
let a = d
let m = nnfit-1
!
for i 2 to nnfit
        let a[1,i] = a[i,1]|a[1,1]
next
for j 2 to m
        let jp1 = j+1
        let jm1 = j-1
        for k 1 to jm1
                let a[j,j] = a[j,j]-a[j,k]*a[k,j]
        next
        for i jp1 to nnfit
                for k 1 to jm1
                        let a[i,j] = a[i,j]-a[i,k]*a[k,j]
                next
                let a[j,i] = a[i,j]|a[j,j]
        next
next
let x[m] = a[m,nnfit]
for i 2 to m
        let l = nnfit-i
        let x[l] = a[l,nnfit]
        let ll = l+1
        for k ll to m
                let x[l] = x[l]-a[l,k]*x[k]
        next
next
say "end CROUT"
!
! End crout.class
!
!!!!!!!!!!!!!!!!!!!!!!!!!!!!!!!!!!!!!!!!!!!!!!!!!!!!!!!!!!!!!!!!!!!!!!!
!
let z = x
!
!!!!!!!!!!!!!!!!!!!!!!!!!!!!!!!!!!!!!!!!!!!!!!!!!!!!!!!!!!!!!!!!!!!!!!!
!
!       reler.class
!
! From zfit by C. Helies
! Modified to class macro T. Bourke 13/11/95
!
!      SUBROUTINE RELER(A,X,N)
!      DIMENSION A(12,12),X(12)
```

Class script zfit.class

```
!
! Finds relative errors using crout method on an existing augmented matrix.
!
let m = nnfit-1
let a = d
!
for i 1 to m
        for j 1 to nnfit
                let a[nnfit,j] = 0
        next
        let a[nnfit,i] = 1.
        let a[1,nnfit] = a[nnfit,1]|a[1,1]
        for j 2 to m
                let jm1 = j-1
                for k 1 to jm1
                        let a[nnfit,j] = a[nnfit,j]-a[nnfit,k]*a[k,j]
                next
                let a[j,nnfit] = a[nnfit,j]|a[j,j]
        next
        let x[m] = a[m,nnfit]
        if (i.ne.m) then
                let mix = nnfit-i
                for lxl 2 to mix
                        let l = nnfit-mix
                        let x[l] = a[l,nnfit]
                        let ll = l+1
                        for k ll to m
                                let x[l] = x[l]-a[l,k]*x[k]
                        next
                next
        endif
next
say "end RELER"
!
! End reler.class
!
!!!!!!!!!!!!!!!!!!!!!!!!!!!!!!!!!!!!!!!!!!!!!!!!!!!!!!!!!!!!!!!!!!!!!!!
!
let err = x
!
!!!!!!!!!!!!!!!!!!!!!!!!!!!!!!!!!!!!!!!!!!!!!!!!!!!!!!!!!!!!!!!!!!!!!!!
!
! Values of z returned by crout relate to the derived B field.
! Values of err returned by reler relate to the errors in these fits
! Bfld = z * chnsp / gfact  (see zfit2.f)
!
! Here we derive the overall fit to the V spectrum
!
! modelfit = dT/df * z(1) + T * z(2)
! where T = line
!       d/df is the derivative
!       z(1) is the z returned by crout for Bfld
!       z(2) relates to the gain term
!
! thus modelfit can be directly compared to V
!
say " "
say "Fitting the V spectrum (takes time) ..."
say " "
for na chn1 to chn2 by step
        if (direction.eq.2) then
        let naprime = chn1+chn2-na
        let modelfit[naprime] = z[1]*dts[na]+z[2]*t[na]
        else
        let modelfit[na] = z[1]*dts[na]+z[2]*t[na]
        endif
next
!
! Keep track of the gainterm
!
let gainterm = z[2]
!
! Setting up values for Berr
!
let srsqe = 0.
let pts = abs(chn2-chn1+1)
let ff = 0.
for i chn1 to chn2 by step
  if (direction.eq.2) then
        let naprime = chn1+chn2-i
        let rsid = v[i]-modelfit[naprime]
  else
        let rsid = v[i]-modelfit[i]
  endif
  let srsqe = srsqe+(rsid*rsid)
next
let ff = srsqe|(pts-nnfit)
let ff = sqrt(ff)
!
! Determine Bfld and Beff
!
! Note that, in the current method for determining the dervitives, that
! if the user chooses option 2 for fitting, ie fit from the high
! velocity end of the spectrum, then the derivative is the negative
! of what it should be, by definition.  We fix it here by correcting
! for the sign of the B field in this case.
!
!       if (direction.eq.2) then
        if (chn1.gt.chn2) then
        let bfld[1] = -1*z[1]*chnsp|gfact
        else
        let bfld[1] = z[1]*chnsp|gfact
        endif
        let berr[1] = abs(ff*sqrt(err[1])*chnsp|gfact)
!
! Now report this information to the screen
!
say " "
say "B(los) = "'bfld[1]'" +/- "'berr[1]'" micro-G"
say " "
say "enter (c) to continue"
say " "
pause
!
! then would like to plot modelfit on V
! so need to get modelfit into a class scan
!
! method:
! get I - write to temp file
! get I again - write to same file
```

Class script zfit.class

```
! open that file
! get f
! mult -1
! get n
! accum with equal weighting
! this should create a spectrum with all 0's, but with header info
! relating to I.
! write this to the temp file
! reopen the temp file
! get the zero spectrum
! write the modelfit info to it
!       loop chn1 to chn2 by step
!            let ry[i] = modelfit[i]
! then write to a file, with the V and I data
! now can plot V and modelfit data.
!
! Get the I spectrum
!
if (obs.eq.1) then
        find/all
        get f
else
        find/all
        get f
        get n
endif
!
! Write the I spectrum to a temp file twice,
! then open the file and create the zero spectrum
! and write to another temp file
!
system "\rm zee-temp*.pks"
file out zee-temp1.pks new
write
write
file in zee-temp1.pks
find/all
get f
mult -1
get n
accum                   ! with weight equal, produces sum
write
!
! Ok, now just have to open zee-temp1.pks and get the third
! spectrum, whenever we want a zero spectrum to write new
! data to.
!
! Note - could also just get the I spectrum, write over the
! data, and write to a new file.  But that is a bit more messy.
!
! Ok, now write the model fit to a file
! Ask the user for extention
!
file in 'infile[1]'
say " "
say "Current files are"
say " "
sh files
say " "
say "Data and fit will be written to file of the form: "
say "   inputfile-suffix.pks"
say " "
say "Enter suffix ..."
say " "
let suffix =
let ofile[1] = 'inputfile'-'suffix'".pks"
file out 'ofile[1]' new
!
! write to new file I, then V, then fit to V
!
if (obs.eq.1) then              ! I is first spectrum
        find/all
        get f
        write
        get n
        write
else                            ! V is first spectrum
        find/all
        get f
        get n
        write
        get f
        write
endif
!
! Write the fit to the new file
!
file in zee-temp1.pks
find/all
get f
get n
get n
for i chn1 to chn2 by step
        let ry[i] = modelfit[i]
next
!
! Put the Bfld into the beam efficiency, beeff.
! Put the Berr into the forward efficientcy, feff
!
let beeff = bfld[1]
let foeff = berr[1]
write
!
! write dI/dv to the file
!
file in zee-temp1.pks
find/all
get f
get n
get n
for i chn1 to chn2 by step
        let ry[i] = z[1]*dts[i]
next
write
!
! write out the gain term spectrum
!
file in zee-temp1.pks
find/all
get f
```

Class script zfit.class

```
get n                                                                    !
get n
for i chn1 to chn2 by step
        let ry[i] = z[2]*t[i]
next
write
!
! write out the gain-subtracted V spectrum
!
file in zee-temp1.pks
find/all
get f
get n
get n
for i chn1 to chn2 by step
        let ry[i] = v[i]-(z[2]*t[i])
next
write
!
! Now open the new file and plot the V and fit data
!
file in 'ofile[1]'
say " "
say "File containing, in order, I, V and model fit spectrum, is ..."
sh files
find/all
get f
get n
!mx voff-15 voff+15
mx vmiddle-15 vmiddle+15
set unit v f
plot
say " "
say "Set y axis limits no."
say "   prompt> my lower upper"
say "   prompt> plot"
say "enter (c) to continue"
say " "
pause
get n
pencil/weight 5
spectrum
pencil/weight 1
say " "
say "Plotted is the V spectrum with the model Zeeman spectrum derived"
say "from the individual gaussian components"
say " "
!
! Write B data to screen
!
say " "
say "B(los) = "'beeff'" +/- "'foeff'" micro-G"
say " "
say "Gain term = "'gainterm'
say " "
say "Done"
say " "
my tot
!
! End
```

Class script zgfit.class

```
!
!       zgfit.class
!
! Class macro
! Fits gaussian components of line with Zeeman pattern and compares
! to true V spectrum.
! Assumes that the gaussian information is contained in the I spectrum
! header - if not run gauss.class first.
!
!       proceeding file : gauss.class
!       next file       : there ain't none!
!
! original T. Bourke 10/11/95
!
! adapted from zgfit by C.Heiles
!
! 26/8/97 added option to fit from low or high velocity end
! also added gain terms for each gaussian - hopefully this is correct!
! 7/10/97 removed gain terms for each gaussian, changed back to
! one gain term for whole line...currently the scaled I spectrum.
! Maybe change later to get the gain from the sum of gaussians
!
! 05/09/97 fix up all the little things - based on the fact that
! zfit.class is now working
!
! 08/10/97 now writes out the individual components of the fit into
! the output file.  After the overall fit (3rd spectrum in output file)
! the fit to the first gaussian is written, then the second gaussian...
! up to the 5th (and max) gaussian, then the gain contribution, and
! then the gain-corrected V spectrum
! So output file is:
!       1. I spectrum
!       2. V spectrum
!       3. Overall fit to V spectrum
!       4. contribution of 1st gaussian to fit to V spectrum
!       ... 8. = 5th gaussian
!       contribution of I term scaled by gain term
!       gain corrected V spectrum
!       residual = gain-corrected V - Gaussian derivative sum
!

set var spectro write
set var plot write
set var gauss write
set weight equal
set unit v c
!
def char inputfile*40 infile*40[2] ofile*40[2] suffix*40
def int obs line fline chn1 chn2 gg
def int ntry nnfit pts bb jj jjj nntry nn n jk
def real gfact v[8192] t[8192] modelfit[8192] gainfit[8192]
def real dvmin dvmax dchnmin dchnmax midchn
def real chnsp srsq srsqe brkt delp1 delm1 rsid ff cg
def real c[20] ht[20] cen[20] fwhm[20] cenv[20] fwhmv[20] width[20]
def real z[20] bfld[20] berr[20] d[20,20] err[20] gfit[20,8192]
def real gainterm gainerr low high
def real velocity-min velocity-max vmiddle
def real pi
def real a[20,20] x[20]
def integer m jp1 jm1 l ll mix g[5]
def integer direction iprime naprime step ngauss
!
let pi = 3.141592654
!
symbol mx "set mode x"
symbol my "set mode y"
!
say " "
say "One moment ... clearing up files ..."
say " "
system "\rm zee-temp*.pks"
!
say " "
say "Current files are :"
sh files
say " "
say "Enter file containing V and I data (.pks assumed) ... "
say " "
let inputfile =
let infile[1] = 'inputfile'".pks"
say " "
say "First observation assumed to be V, second is I"
say "If first observation is I, then enter (1) ..."
say " "
let obs =
file in 'infile[1]'
!
! Ask user to identify the line
!
say " "
say "Which OH line (1 = 1665, 2 = 1667) ?"
say " "
let line =
if (line.eq.1) then
        let fline = 1665
        let gfact = 3.27
else if (line.eq.2) then
        let fline = 1667
        let gfact = 1.96
endif
!
! Get the I spectrum and plot it.
! Then ask user to define limits.
!
if (obs.eq.1) then
        find/all
        get f
else
        find/all
        get f
        get n
endif
!
!
! Now set the limits of the plot and plot I
!
mx voff-15 voff+15
plot
say " "
say "Set x limits for Zeeman fitting - give plenty of baseline ..."
```

Class script zgfit.class

```
say " "
say "To reset x limits, enter :"
say "   prompt> mx (min) (max)"
say "   prompt> plot"
say "else enter (c) to continue ..."
say " "
pause
!
! Now ask the user for the approximate velocity limits of the
! range just set - haven't been able to automate this
!
say " "
say "Enter the approximate velocity limits of your plot ..."
say " "
let velocity-min =
let velocity-max =
let vmin = velocity-min
let vmax = velocity-max
!
! Now determine start and end channel numbers from this info
!
plot
let vmiddle = (vmax+vmin)|2
let dvmin = vmiddle-vmin
let dvmax = vmax-vmiddle
let dchnmin = dvmin|vres
let dchnmax = dvmax|vres
let midchn = rchan-((voff-vmiddle)|vres)
let chn1 = nint(midchn-dchnmin)
let chn2 = nint(dchnmax+midchn)
!
! Now determine if chn1 > chn2 or chn2 > chn1.  This is needed to
! determine the step size for 'for' loops.
!
if (chn1.gt.chn2) then
        let step = -1
else
        let step = 1
endif
!
! Interested in the I array Gaussian information, so get it now
! since we are using the I spectrum at present
! Note that the cen and wid info is in velocity units
! Do we need to change to channels? Assume so here
!
let ntry = nline
! ntry gaussians and ntry derivatives of gaussians
!let nntry = ntry+1
!let nnfit = ntry+2
!
let gg = 0
for j 1 to ntry
                let gg = 3*j-2
                let ht[j] = nfit[gg]
                let gg = gg+1
                let cenv[j] = nfit[gg]
                let gg = gg+1
                let fwhmv[j] = nfit[gg]
                ! convert area to intensity
                let ht[j] = (ht[j]|fwhmv[j])*sqrt((4*log(2))|pi)
! convert to channels
                let cen[j] = ((cenv[j]-voff)|vres)+rchan
                let fwhm[j] = fwhmv[j]|vres
                let width[j] = fwhm[j]|(2*sqrt(log(2)))
next
!
! Ok, now reject components outside the display window, clearly the user
! does not wish to fit them
!
ngauss = 0
for j 1 to ntry
        let low = cenv[j]-(fwhmv[j]|2)
        let high = cenv[j]+(fwhmv[j]|2)
        if (low.gt.vmin) then
         if (high.lt.vmax) then
          let ngauss = ngauss+1
          let g[ngauss] = j
         else
         endif
        else
        endif
next

say " "
say "Gaussians = "'ngauss'
say " "
let ntry = ngauss
let nntry = ntry+1
let nnfit = ntry+2

!
if (chn1.eq.1) then
        let chn1 = 2
endif
if (chn2.eq.nchan) then
        chn2 = nchan-1
endif
!
! Read the I and V data into arrays defined by the channel extremes
! v is the V data, t is the line (temperature) data
! Also get the line data resulting from the subtraction of
! the fitted gaussian to the line profile
!
! Prompt user for direction of fitting
!
say " "
say "Do you want to fit the spectrum from..."
say "   [1] low velocity to high velocity, or"
say "   [2] high velocity to low velocity"
say " "
say "Enter 1 or 2"
say " "
let direction =
!
if (obs.eq.1) then
        find/all
        if (direction.eq.2) then
        get f                   ! I spectrum
        for i chn1 to chn2 by step
                let iprime = chn1+chn2-i
```

```
                let t[iprime] = ry[i]
        next
        get n                   ! V spectrum
        for i chn1 to chn2 by step
                let iprime = chn1+chn2-i
                let v[iprime] = ry[i]
        next
        else
        get f                   ! I spectrum
        for i chn1 to chn2 by step
                let t[i] = ry[i]
        next
        get n                   ! V spectrum
        for i chn1 to chn2 by step
                let v[i] = ry[i]
        next
        endif
else
        find/all
        if (direction.eq.2) then
        get f                   ! V spectrum
        for i chn1 to chn2 by step
                let iprime = chn1+chn2-i
                let v[iprime] = ry[i]
        next
        get n                   ! I spectrum
        for i chn1 to chn2 by step
                let iprime = chn1+chn2-i
                let t[iprime] = ry[i]
        next
        else
        get f                   ! V spectrum
        for i chn1 to chn2 by step
                let v[i] = ry[i]
        next
        get n                   ! I spectrum
        for i chn1 to chn2 by step
                let t[i] = ry[i]
        next
        endif
endif
!
! Determine channel separation in Hz
!
let chnsp = fres*1e6
!
! Zero the matrix
!
for na 1 to nnfit
        for nb 1 to na
                let d[na,nb] = 0.
        next
next
say " "
say "Determining derivatives (takes time) ... "
say " "
!
! here we determine the derivatives of the fitting gaussians
! and set up the equtions of conditions
! for the max no of gaussians, c(1) - c(4) hold the current
! value of the respective gaussian, and c(nfit) = c(5) the value
! of the true V spectrum
! Max number of gaussian allowed in zgfit = 5.  This will be
! updated for class (But class only allows 5)
!
let n = 0
for na chn1 to chn2 by step
        for k 1 to ntry
          let n = g[k]
          if (direction.eq.2) then
                let naprime = chn1+chn2-na
                let delp1 = (naprime+1-cen[n])|width[n]
                let delm1 = (naprime-1-cen[n])|width[n]
          else
                let delp1 = (na+1-cen[n])|width[n]
                let delm1 = (na-1-cen[n])|width[n]
          endif
!
! determine derivative
!
        if (chn1.gt.chn2) then
                let c[k] = 0.5*ht[n]*((exp(-delm1*delm1))-(exp(-delp1*delp1)))
        else
                let c[k] = 0.5*ht[n]*((exp(-delp1*delp1))-(exp(-delm1*delm1)))
        endif
        next
!
! Note we want the V spectrum here
! Later will include I spectrum for a gain difference estimate
! Done
!
let c[nntry] = t[na]
let c[nnfit] = v[na]
!
        for nb 1 to nnfit
                for nc 1 to nb
                        let d[nb,nc] = d[nb,nc]+c[nb]*c[nc]
                next
        next
next
say "Calling crout and reler"
!
! crout and reler
!
!!!!!!!!!!!!!!!!!!!!!!!!!!!!!!!!!!!!!!!!!!!!!!!!!!!!!!!!!!!!!!!!!!!!!!!
!       crout.class
!
! Called by zee-fit.class macro
! Original documentation given below
!
!       SUBROUTINE CROUT(A, X, N)
!       DIMENSION A(12,12),X(12)
!
! Note that A and N are passed to the subroutine, X is returned
!
! CROUT method for matrix equation ax=c where matrix a is symmetr
! see hildebrand page 503.  M is the order of the matrix equation
! n is m plus 1.  The matrix a is assumed to be partitioned as
! described by hildebrand.  No attempt has been made to make this
! subroutine fast or to minimize memory.  Such attempts might
```

Class script zgfit.class

```
! be fruitful.
! The input matrix a is obliterated by this subroutine
! matrix x is returned as the solution.  Written by c. heiles.
!
! Updated for class T. Bourke 13/11/95
!
!def real a[10,10] x[10]
!def integer  m jp1 jm1 l ll
!
let a = d
let m = nnfit-1
!
for i 2 to nnfit
        let a[1,i] = a[i,1]|a[1,1]
next
for j 2 to m
        let jp1 = j+1
        let jm1 = j-1
        for k 1 to jm1
                let a[j,j] = a[j,j]-a[j,k]*a[k,j]
        next
        for i jp1 to nnfit
                for k 1 to jm1
                        let a[i,j] = a[i,j]-a[i,k]*a[k,j]
                next
                let a[j,i] = a[i,j]|a[j,j]
        next
next
let x[m] = a[m,nnfit]
for i 2 to m
        let l = nnfit-i
        let x[l] = a[l,nnfit]
        let ll = l+1
        for k ll to m
                let x[l] = x[l]-a[l,k]*x[k]
        next
next
say "end CROUT"
!
! End crout.class
!
!!!!!!!!!!!!!!!!!!!!!!!!!!!!!!!!!!!!!!!!!!!!!!!!!!!!!!!!!!!!!!!!!!!!!!!
!
let z = x
!
!!!!!!!!!!!!!!!!!!!!!!!!!!!!!!!!!!!!!!!!!!!!!!!!!!!!!!!!!!!!!!!!!!!!!!!
!
!       reler.class
!
! From zfit by C. Helies
! Modified to class macro T. Bourke 13/11/95
!
!      SUBROUTINE RELER(A,X,N)
!      DIMENSION A(12,12),X(12)
!
! Finds relative errors using crout method on an existing augmented matrix.
!
let m = nnfit-1
let a = d
!
for i 1 to m
        for j 1 to nnfit
                let a[nnfit,j] = 0
        next
        let a[nnfit,i] = 1.
        let a[1,nnfit] = a[nnfit,1]|a[1,1]
        for j 2 to m
                let jm1 = j-1
                for k 1 to jm1
                        let a[nnfit,j] = a[nnfit,j]-a[nnfit,k]*a[k,j]
                next
                let a[j,nnfit] = a[nnfit,j]|a[j,j]
        next
        let x[m] = a[m,nnfit]
        if (i.ne.m) then
                let mix = nnfit-i
                for lxl 2 to mix
                        let l = nnfit-mix
                        let x[l] = a[l,nnfit]
                        let ll = l+1
                        for k ll to m
                                let x[l] = x[l]-a[l,k]*x[k]
                        next
                next
        endif
next
say "end RELER"
!
! End reler.class
!
!!!!!!!!!!!!!!!!!!!!!!!!!!!!!!!!!!!!!!!!!!!!!!!!!!!!!!!!!!!!!!!!!!!!!!!
!
let err = x
!
!!!!!!!!!!!!!!!!!!!!!!!!!!!!!!!!!!!!!!!!!!!!!!!!!!!!!!!!!!!!!!!!!!!!!!!
!
! Values of z returned by crout relate to the derived B field.
! Values of err returned by reler relate to the errors in these fits
! Bfld = z * chnsp / gfact  (see zfit2.f)
!
! Here we derive the overall fit to the V spectrum from the
! gaussian information.
!
! modelfit = dg(1)/df * z(1) + dg(2)/df * z(2) ... + I * z(nntry)
! where g(1) = gaussian 1
!       d/df is the derivative
!       z(1) is the z returned by crout for g(1)
!
! thus modelfit can be directly compared to V
!
! Also add gain term
!
say " "
say "Fitting the V spectrum (takes time) ..."
say " "
let n = 0
for na chn1 to chn2 by step
  if (direction.eq.2) then
    let naprime = chn1+chn2-na
        let srsq = 0.
```

```
        for k 1 to ntry
          let n = g[k]
          let delp1 = (naprime+1-cen[n])|width[n]
          let delm1 = (naprime-1-cen[n])|width[n]
          if (chn1.gt.chn2) then
            let brkt = (exp(-delm1*delm1))-(exp(-delp1*delp1))
          else
            let brkt = (exp(-delp1*delp1))-(exp(-delm1*delm1))
          endif
!         let gfit[n,na] = z[n]*0.5*ht[n]*brkt
          let gfit[k,na] = z[k]*0.5*ht[n]*brkt
!         let srsq = srsq+z[n]*0.5*ht[n]*brkt
          let srsq = srsq+z[k]*0.5*ht[n]*brkt
        next
!
  else
        let srsq = 0.
        for k 1 to ntry
          let n = g[k]
          let delp1 = (na+1-cen[n])|width[n]
          let delm1 = (na-1-cen[n])|width[n]
          if (chn1.gt.chn2) then
            let brkt = (exp(-delm1*delm1))-(exp(-delp1*delp1))
          else
            let brkt = (exp(-delp1*delp1))-(exp(-delm1*delm1))
          endif
!         let gfit[n,na] = z[n]*0.5*ht[n]*brkt
          let gfit[k,na] = z[k]*0.5*ht[n]*brkt
!         let srsq = srsq+z[n]*0.5*ht[n]*brkt
          let srsq = srsq+z[k]*0.5*ht[n]*brkt
        next
!
  endif
        let gainfit[na] = z[nntry]*t[na]
        let modelfit[na] = gainfit[na]+srsq
next
!
!
! Keep track of the gainterm
!
let gainterm = z[nntry]
!
! Setting up values for Berr
!
let srsqe = 0.
let pts = abs(chn2-chn1+1)
let ff = 0.
for i chn1 to chn2
        let rsid = v[i]-modelfit[i]
        let srsqe = srsqe+(rsid*rsid)
next
let ff = srsqe|(pts-nnfit)
let ff = sqrt(ff)
!
! Determine Bfld and Beff for each gaussian
!
for j 1 to ntry
say 'z[j]'
    if (chn1.gt.chn2) then
        let bfld[j] = -1*z[j]*chnsp|gfact
    else
        let bfld[j] = z[j]*chnsp|gfact
    endif
        let berr[j] = abs(ff*sqrt(err[j])*chnsp|gfact)
next
!
! "Error" in gainterm
!
!gainerr = abs(ff*sqrt(err[nntry]))
!
! Now report this information to the screen
!
for k 1 to ntry
          let jk = g[k]
           say " "
           say "Gaussian "'jk'
           say "Temp = "'ht[jk]'", Vel = "'cenv[jk]'", FWHM = "'fwhmv[jk]'
           say "B(los) = "'bfld[k]'" +/- "'berr[k]'" micro-G"
next

say " "
say "enter (c) to continue"
say " "
pause

!
! then would like to plot modelfit on V
! so need to get modelfit into a class scan
!
! method:
! get I - write to temp file
! get I again - write to same file
! open that file
! get f
! mult -1
! get n
! accum with equal weighting
! this should create a spectrum with all 0's, but with header info
! relating to I.
! write this to the temp file
! reopen the temp file
! get the zero spectrum
! write the modelfit info to it
!       loop chn1 to chn2 by step
!            let ry[i] = modelfit[i]
! then write to a file, with the V and I data
! now can plot V and modelfit data.
!
! Get the I spectrum
!
if (obs.eq.1) then
        find/all
        get f
else
        find/all
        get f
        get n
endif
!
! Write the I spectrum to a temp file twice,
```

Class script zgfit.class

```
! then open the file and create the zero spectrum
! and write to another temp file
!
system "\rm zee-temp*.pks"
file out zee-temp1.pks new
write
write
file in zee-temp1.pks
find/all
get f
mult -1
get n
accum                   ! with weight equal, produces sum
write
!
! Ok, now just have to open zee-temp1.pks and get the third
! spectrum, whenever we want a zero spectrum to write new
! data to.
!
! Note - could also just get the I spectrum, write over the
! data, and write to a new file.  But that is a bit more messy.
!
! Ok, now write the model fit to a file
! Base its name on the input file containing V and I
!
file in 'infile[1]'
say " "
say "Current files are ..."
say " "
show files
say " "
say "Data and fit will be written to file of the form: "
say "   inputfile-suffix.pks"
say "Enter suffix ..."
let suffix =
let ofile[1] = 'inputfile'-'suffix'".pks"
file out 'ofile[1]' new
!
! write to new file I, then V, then fit to V
!
if (obs.eq.1) then              ! I is first spectrum
        find/all
        get f
        write
        get n
        write
else                            ! V is first spectrum
        find/all
        get f
        get n
        write
        get f
        write
endif
!
! Write the fit to the new file
!
file in zee-temp1.pks
find/all
get f
get n
get n
for i chn1 to chn2 by step
        let ry[i] = modelfit[i]
next
!
! Write the Bfld and Berr info to the Class header
! Store it in the Gauss fit results error array
!
for k 1 to ntry
        let jk = g[k]
        let bb = 3*jk-2
        let nerr[bb] = bfld[k]
        let bb = bb+1
        let nerr[bb] = berr[k]
        let bb = bb+1
        let nerr[bb] = 0
next
write
!
! Ok, now write the individual components of the fit to the file
! First the gaussian terms, then the gain term
!
file in zee-temp1.pks
find/all
get f
get n
get n
for k 1 to ntry
  for i chn1 to chn2 by step
        let ry[i] = gfit[k,i]
  next
  write
next
!
! write the gain term
!
file in zee-temp1.pks
find/all
get f
get n
get n
for i chn1 to chn2 by step
        let ry[i] = gainfit[i]
next
write
!
! write the gain subtracted V spectrum
!
file in zee-temp1.pks
find/all
get f
get n
get n
for i chn1 to chn2 by step
        let ry[i] = v[i]-gainfit[i]
next
write
!
! write the sum of the gaussian derivatives
```

Class script zgfit.class

```
!
file in zee-temp1.pks
find/all
get f
get n
get n
for i chn1 to chn2 by step
        let ry[i] = modelfit[i]-gainfit[i]
next
write
!
! write the residual
!
file in zee-temp1.pks
find/all
get f
get n
get n
for i chn1 to chn2 by step
        let ry[i] = v[i]-modelfit[i]
next
write

!
! Now open the new file and plot the V and fit data
!
file in 'ofile[1]'
say " "
say "File containing, in order, I, V and model fit spectrum, is ..."
sh files
find/all
get f
get n
!mx voff-15 voff+15
mx vmin vmax
set unit v f
plot
say " "
say "Set y axis limits no."
say "   prompt> my lower upper"
say "   prompt> plot"
say "enter (c) to continue"
say " "
pause
get n
pencil/weight 5
spectrum
pencil/weight 1
say " "
say "Plotted is the V spectrum with the model Zeeman spectrum derived"
say "from the individual gaussian components"
say " "
!
! Write B data to screen
!
say " "
say " Line                      B(los) micro-Gauss"
say "-----------------------------------------------------"
!for j 1 to ngauss
for k 1 to ntry
        let jk = g[k]
        let jj = 3*jk-2
        let jjj = jj+1
        say "  "'jk'"           "'nerr[jj]'" +/- "'nerr[jjj]'
next
say " "
say "Gainterm  = "'gainterm'
say " "
say "Done"
say " "
my tot
!
! End
!
```